Mechanisms of Action and Sources of Variability in Neurostimulation for Chronic Pain

by

Robert D. Graham

A dissertation submitted in partial fulfillment
of the requirements for the degree of
Doctor of Philosophy
(Biomedical Engineering)
in the University of Michigan
2022

Doctoral Committee:

Assistant Professor Scott F. Lempka, Chair
Associate Professor Tim M. Bruns
Clinical Associate Professor Srinivas Chiravuri
Assistant Professor Bo Duan

Robert D. Graham

rdgraham@umich.edu

ORCID iD: 0000-0002-9795-4614

Dedication

This dissertation is dedicated to:

my parents, Beth and Eric, for being loving, supportive, and understanding role models

my stepparents, Dino and Missy, for being just like my biological parents

and Shadow, for being the sweetest piece of organic matter in the universe. Though I knew our time together would be short, you were the best part of every day I got to spend with you.

Acknowledgements

If I was going to properly thank everyone who has supported me on my journey through life and school, the acknowledgements would be considerably longer than the rest of this dissertation. To anyone who knew me during the first quarter-ish (I hope!) of my life and finds their name missing here, I'm sorry that I had to cut this down. My life is likely better for having had you in it. I have been inexpressibly fortunate to have known so many amazing people. These acknowledgements are a summary of how lucky I am.

I should start by thanking Scott, for being an excellent advisor. Thank you for giving me so much opportunity in your lab, for encouragement and support through every career change, and for your patience and tolerance with my lack of professionalism, run-on sentences (like this one), and propensity to wear slippers (or socks) to lab. Thank you for inspiring a vision of how research should always push us towards improvements for patients, and for your patience when I'd spend (too much) time outside of the lab in student orgs. Most of all, thank you for your compassion and understanding when I found life was pulling me in multiple directions away from lab. You've been instrumental in my development as a scientist and as a human, and I will be forever grateful. Thank you.

I was exceptionally lucky to have a committee of brilliant, passionate, generous, and encouraging people. Tim, every meeting I had with you left me feeling excited and optimistic about science and the future. I don't think I would have gotten to Michigan if it wasn't for you. I'm glad we found a way to work together. Bo, thank you for being so generous with your endless knowledge of neuroscience, and for highlighting how much is left to discover. Your class was my

favorite I've ever taken and is one of the main reasons I want to pursue a postdoc in neuroscience. Srini, thank you for being so welcoming and letting me shadow in your clinic. Seeing the patients that are living with these disorders gave me a deeper appreciation for the humans on the other side of the electrode. I'll be lucky to understand anything half as well as you understand anatomy.

The Neuromodulation Lab has had a ton of great people pass through during my time here. Thank you to Sauradeep Bhowmick, Hans Zander, Nystha Baishya, Jessica Loechli, Evan Rogers, Meagan Brucker-Hahn, Luis Ruiz, Anagha Kotkar, Adrian Porras, Vish Sankarasubramanian, Vanessa Pruitt, Lianna Shimoun, and Hannah Soifer – an excellent group of people with whom to figure out which neurons nearest the electrode are being activated. I have to give special thanks to Carlos Anaya, Dr. Ehsan Mirzakhalili, and Amolak Jhand. Carlos is one of the kindest and most devoted human beings on the planet, is painfully funny, and is one of the best friends I've ever had. Ehsan is inspiringly brilliant, beyond generous with his time and advice, and his mentorship dramatically improved the contents of this dissertation. Amolak is both a great mentee and a great friend. Watching him grow as a scientist has been one of the most rewarding components of my time in grad school. All three of them have great taste in music. I'm going to miss doing science with them.

Thank you to everyone outside of the Neuromodulation Lab I've been lucky to have collaborated with: Kate Kish, Manorama Kadwani, Nishant Verma, and Drs. Ameya Nanivadekar, and Hankyu Lee. A huge thank you to Dr. Zach Sperry for being the driving force behind the histology work and BIONIC, both of which I happened to join at the right time. Thank you to everyone who has come through TNE over the past six years – I've loved learning from and with you all. A special thank you to Lauren Madden, who is a great collaborator, and an amazing person.

Thank you for making the last several months so special, and for making writing a dissertation bearable. I'm grateful for everything you've brought to my life.

Thank you to Skylar Woodman – a real-life superhero. If we all followed his example, the world would be a more beautiful place. Thank you to Pat Dorin for being a great friend, and for helping me in trying to follow Sky's example. Thank you Dr. Nadine Wong, Laura Charlick, and Lisa Moran, for making BI an enjoyable place to be, and thank you to the BME department's amazing administrative staff, in particular Maria Steele and Erik Keup. Maria is an angel in human form, and Erik's tech support facilitated a lot of the computational work presented in this dissertation. Thank you to StackExchange, and Drs. Michael Hines and Ted Carnevale on the NEURON forum for doing the legwork of this PhD.

Thank you Drs. Wilsaan Joiner and Ken Thompson. Dr. Joiner always gives great advice and was a huge source of support during grad school applications and beyond. Dr. Thompson is one of the most genuine and unfailingly kind people I have ever met. Thank you for believing in me and helping me discover a love of writing. Thank you to Judy Adkins, Josh Edgell, and Stephanie Kevan for making me feel like I was a smart kid even if my grades didn't show it.

Thank you to everyone from the GMU Neural Engineering lab, in particular Drs. Nathalia Peixoto and Joe Pancrazio. Dr. Pancrazio, thank you for always being generous with career and personal advice. Nathalia, thank you for letting a mediocre student with virtually no promise work in your lab. I have no idea where my life would have gone if you hadn't given me that opportunity. Thank you.

"They" say that you are the average of the people you spend the most time with, and so I owe much of what I have in life to my friends from Maryland, Mason, and Michigan. Thank you Joe Stack, Caleb Hammer, Matt Roderick, Jack Draper, Calvin Matson, Seamus O'Brien, Ria

Datta, Danah Koch, Andrew Leich, John Miller, Boomy Koo, Andrew Huang, Brendan Metzger, April Aralar, Ashley Willis, Chris Lee, Kory Davis, Michael Kurtzke, Jon Alston, Linh Ho, and Hunter Loveland. David Whyte says that "friendship is a mirror to presence," and y'all's steady presence despite my frequent absence means more to me than I'm able to express.

To the friends I've made at UM, thank you for being a part of my journey through grad school. Much love to Melissa Lemke, Katy Norman, Danny Quevedo, Barry Belmont, Paras Patel, Oskar Singer, Charles Lu, Elizabeth Bottorff, Dorsa Ghaffari, Tejas Navaratna, Dan Clough, Berenice Castillo, Meagan and Dalton Brucker-Hahn, Brian Macdonald, Jonathan Schwartz, and Akshay Bhardwaj. Thank you, Tiffany (Tiff) Nguyen, for being such a great mom to Shadow, and for teaching me maturity. Thank you, Ryan Kassel, for taking a parallel, but slightly phase shifted, journey with me. Thank you to Ravi Raghani and Dan Matera for bringing music back into my life. Thank you to Yves Nazon for being the type of person that it's impossible to feel anything other than joy around, and for always being there for me. Thank you, Aditya Varma, for being the most principled person I've ever met. I've benefited greatly from your example. Thank you, Dylan Neale, chef extraordinaire, for being the type of person than can somehow make moving a fun process, and for being one of the few people I immediately clicked with background-wise. Thank you, Phil Vu, for being the most fun person to talk about science with, and for always having an open ear that gives great advice. Thank you, Steven Chavez, for everything. Steven and I became friends almost instantly, and he's been an integral part of virtually every aspect of my time in graduate school. From science to fitness, concerts to nutrition, celebration to commiseration, Steven is an inspiring person and his motivation in every aspect of life is infectious. I am immensely grateful for his friendship. To everyone I've been fortunate enough to call a friend throughout my life, thank you for making my life brighter.

My family has always been supportive and understanding of my academic pursuits, and of all the missed birthdays, births, and holidays. Their love, generosity, and genuine interest in what I'm doing when I'm not at home have made traveling to both coasts for reunions an easy burden to bear. It takes a village, and I'm lucky that my family is approximately village sized, even if it keeps me from thanking everyone adequately here. Peep, thank you for being a second parent to me. Jackson, I am so proud of you. I've tried and often failed to be a role model for you, but if I can complete a PhD, I know you can achieve whatever brings you fulfillment. Tony and Danielle, if it wasn't for your examples, I don't think I would have gone to college. There's a strange, twisted irony that I gravitated towards therapies for neurological disorders, when a neurological disorder is the only reason you two are in my life in the first place. I am so grateful for the role you've both played in my life. I hope in return I can make a positive contribution to reducing the burden of such disorders on other families.

You're lucky if you get one great parent in life, and the universe gave me four. Thank you all for your unending love and support. I could write chapters on all the positive ways in which you've each influenced me as a person. I'll do my best to summarize with paragraphs.

My stepparents, Dino Gregorich and Missy Willis, deserve to be canonized for their patience and tolerance. I was a difficult teenager, and they both seemed to know exactly what capacity I needed from them. They both epitomize hard work, dedication, and putting family first. I love you both, and I appreciate so much having the two of you in my life.

My mom, Beth Gregorich, taught me the importance of empathy and compassion, of flexible intelligence and open-mindedness, and of forgiveness, acceptance, and perseverance. She's always been my biggest cheerleader. Her character was one of the initial forces that oriented

me towards working on problems that could help people. She was also an enormous help in reviewing several portions of this dissertation. Mom, I love you. I am truly grateful to be your son.

My dad, Eric Graham, is the hardest working, smartest, most humble person I've ever met. A farmer that flips burgers, nerves of steel but cool as a cucumber, he could have done twice the work in half the time it took me to complete this PhD. Unendingly selfless, genuine, and caring, his sacrifices are the reason I was able to pursue higher education in the first place. His character is the reason I was able to succeed. Dad, I love you. I am truly grateful to be your son.

Finally, Dr. Franz Hamilton, an exceptional mentor, a great friend, and the graduate student tasked with mentoring me when I first joined the Neural Engineering Lab at Mason. I joined the lab as Franz began the last year of his PhD, which I've come to learn is stressful enough without the added responsibility of an incompetent undergrad that asks too many questions. Franz could have used me to collect the final bits of data he needed to finish his dissertation, and then moved on to the next step of his career. Instead, he selflessly invested a significant chunk of his time in my development as a scientist, and as a person. Franz taught me many of the technical skills needed to perform science, but more importantly, he helped me cultivate my interest in science, taught me how to identify and positively address my shortcomings, and helped me develop the work ethic and persistence needed to be a scientist. His support and mentorship were the main reasons I applied to grad school. Howard Zinn said (paraphrased) that small acts multiplied across millions of people can change the world. Franz showed me that the seemingly small acts of a single person, multiplied by days, weeks, and months, can change someone's life. Franz, it is impossible for me to thank you enough; you changed my life.

Table of Contents

List of Tables

List of Figures

Abstract

Chronic pain is a debilitating neurological disorder which affects hundreds of millions of people worldwide. Neurostimulation therapies, such as spinal cord stimulation (SCS) and dorsal root ganglion stimulation (DRGS), are non-addictive alternatives for managing chronic neuropathic pain that is refractory to conventional medical management. SCS and DRGS apply sequences of brief electrical impulses to neural tissue. However, not all patients receiving these therapies obtain adequate pain relief, and patient outcomes are not improving despite decades of clinical experience and advancements in stimulation technology. This dissertation addresses two crucial knowledge gaps limiting the success of neurostimulation therapies: 1) we do not understand the physiological mechanisms of electrical stimulation-induced pain relief, and 2) we do not understand the sources of variability affecting the neural response to stimulation.

The first portion of this thesis examined the mechanisms of action of DRGS. We developed statistical models of neural element (i.e., cell bodies, axons) locations in histological samples of human dorsal root ganglia (DRG) tissue. Next, we employed a histologically informed field-cable modeling approach to study the neural response to DRGS. We coupled a finite element method model of the potential distribution generated by DRGS to multi-compartment cable models of DRG neurons to simulate which types of sensory neurons are activated by therapeutic DRGS. Our data suggest that clinical DRGS directly activates the subset of sensory neurons that code non-painful touch sensations, which may trigger pain-inhibition neural networks in the spinal cord dorsal horn.

The second portion of this thesis investigated how biological variability at different scales (e.g., single cells, patient anatomy) affected the neural response to stimulation. We implemented a Markov Chain Monte Carlo (MCMC) method to parametrize populations of neurons with heterogeneous ion channel expression profiles. We incorporated this approach in our field-cable model of DRGS and showed that variability in ion channel expression can affect the stimulation amplitude required to generate activity in target neurons. We further applied this population-modeling approach to investigate how pathology induced changes in ion channel expression can affect the behavior of neural circuits governing sensory transmission. Finally, we developed a framework for constructing patient-specific field-cable models of patients receiving SCS. This framework captured the effect of key anatomical details (e.g., the amount of cerebrospinal fluid between a patient's SCS electrode array and the spinal cord) on neural activation during stimulation. Furthermore, this patient-specific modeling framework allows the comparison of model predictions of neural activation during SCS with clinical data, such as patient-reported outcomes (e.g., pain relief).

The results of this dissertation suggest that DRGS may share mechanisms of action with other neurostimulation therapies for pain management, such as SCS. This dissertation also developed frameworks for studying the effect of biological variability on the nervous system's response to electrical stimulation. To develop safe and effective therapies for neurological disorders, it is crucial to understand both the physiological mechanisms of symptom relief, and how the neural response to therapy may vary across cells, circuits, and patients. This dissertation provides novel insights on both aspects as they relate to neurostimulation for chronic pain.

Chapter 1 – Introduction

Electrical stimulation of neural tissue via extracellular electrodes is a therapeutic approach for managing the symptoms of neurological disorders.[1] Such therapies are typically referred to as "neuromodulation therapies" or "neurostimulation therapies." Though other modalities of neurostimulation exist (e.g., mechanical stimulation via ultrasound, stimulation using infrared light),[2,3] many clinical neurostimulation therapies apply brief (on the order of tens to hundreds of microseconds) electrical impulses which modulate neural activity. This dissertation focuses on a subset of electrical neurostimulation therapies which manage chronic pain that is refractory to conventional medical management, specifically spinal cord stimulation (SCS) and dorsal root ganglion stimulation (DRGS).

1.1 Chronic pain

Pain is a useful signal that indicates behaviors or stimuli that are actively or potentially damaging to tissues and organs. For example, pain in response to touching a hot stove indicates the harmful nature of high temperatures on the skin. Chronic pain, pain that persists in the absence of noxious stimuli, is the experience of pain that does not have any informative utility. Clinically, pain is typically deemed to be chronic after persisting for 3-6 months and can take form as one or more of a myriad of chronic pain disorders.[4] Unfortunately, chronic pain is one of the largest public health challenges currently facing the world, with far reaching impacts manifesting at the individual, societal, and economic levels.

1.1.1 Individual, societal, and economic impacts of pain

The International Association for the Study of Pain currently defines pain as "An unpleasant sensory and emotional experience associated with, or resembling that associated with, actual or potential tissue damage.[5]" Experiencing chronic pain therefore can produce debilitating effects on the individual living with chronic pain. The neuromatrix theory of pain emphasizes that the experience of pain cannot be reduced to a purely sensory experience.[6] Rather, the pain experience is comprised of, and in return impacts, the individual's ongoing sensory milieu (e.g., the sensory experience of pain), the individual's affective-motivational state (e.g., the emotional response to pain), and the individual's evaluative-cognitive state (e.g., the attention the individual pays to their pain).

Chronic pain syndromes can produce a variety of aversive sensory experiences. The sensations produced by such syndromes include burning, sharp, crushing, and shooting pain to name a few.[7] Chronic pain disorders often negatively impact, and can be exacerbated by, a patient's emotional state. For example, depression, suicidal ideation, hopelessness, and anhedonia are commonly comorbid with chronic pain.[8] Furthermore, chronic pain patients often experience negative effects on executive function. Anxiety, attention disturbances, and pain catastrophizing (i.e., a magnified negative response to experienced or anticipated pain) are commonly reported by pain patients.[9] The multi-modal nature of pain across the spectrum of experience underscores both the enormity and complexity of the negative impacts of pain on an individual.

The debilitating effects of chronic pain extend beyond the individual. Hundreds of millions of people worldwide are living with chronic pain, with more than 100 million individuals suffering from chronic pain in the United States alone.[10] Though the individual experience of pain can vary in intensity, duration, and frequency of occurrence, more than 14 million Americans report living

with “a lot of pain” each day.[11] The prevalence of pain has contributed to the ongoing “opioid epidemic” in the United States. Opioids are a commonly used pharmaceutical treatment for pain. Over the past two decades, the prescription rate of opioids has quadrupled in an effort to mitigate the pain epidemic.[12] During the same time period, the rate of overdose deaths involving opioids increased by 200%,[13] and are projected to continue increasing as seen in recent years.[14]

With so many individuals affected by debilitating daily pain, chronic pain has an enormous impact on the economy. It is estimated that chronic pain accrues hundreds of billions of dollars in direct costs to the healthcare system each year (e.g., doctor’s visits, increased wait times).[15] Furthermore, chronic pain syndromes often prevent an individual from going about their activities of daily living or going to work, leading to negative impacts on the economy via a loss of workforce productivity. In total, the economic impact of pain on the United States is estimated to be greater than 600 billion dollars each year.[15] The cumulative effects of pain on the individual, society, and the economy, underscore that effective and non-addictive pain therapeutics could fill an enormous humanitarian, societal, and economic need.

1.1.2 Conventional medical management

The neurostimulation therapies discussed in this dissertation typically manage chronic neuropathic pain that is refractory to conventional medical management. In other words, most of the patients receiving these therapies have not received adequate pain relief with conventional treatments, leaving them with few remaining treatment options. For patients with neuropathic pain, pharmaceutical options including opioids, anticonvulsants, N-methyl-D-aspartate antagonists, and others are often first-line treatments.[16] If patients do not find relief from pharmaceutical treatments, interventions, such as nerve blocks,[17] radiofrequency ablation,[18] and surgical procedures (e.g.,

spinal fusion)[19] are possible alternatives. However, as the clinical algorithm is exhausted, neurostimulation therapies are alternative treatment options.

1.2 Neurostimulation for managing medically refractory chronic pain

1.2.1 History

Melzack and Wall's Gate Control Theory of Pain is the mechanistic basis for the genesis of clinical neurostimulation therapies (**Figure 1.1**).[20] The Gate Theory of Pain describes innocuous and painful sensory input into the spinal cord as the activity of large-diameter (L) and small-diameter (S) afferent fibers, respectively. Both L and S fibers induce activity in pain transmission (T) neurons within the spinal cord, leading to pain perception. However, activity in L fibers also excites inhibitory interneurons in the superficial dorsal horn (classically, this region is referred to as the substantia gelatinosa (SG)). In turn, the SG neurons presynaptically inhibit the transmission of afferent input onto T neurons. Finally, activating large-diameter afferents induces top-down modulation (so-called Central Control), which exerts further modulatory effects on the Gate Control System. Though unable to fully describe the specific physiology of pain processing in the spinal cord,[21] the Gate Control Theory of Pain provides an excellent mechanistic framework for understanding pain transmission. Regarding neurostimulation therapies for pain management, the key insight provided by the theory is that if one could artificially increase the activity of large-diameter afferents, it may be possible to reduce the pain experienced by an organism.

Only two years after the Gate Control Theory of Pain was published, two clinical reports emerged using electrical stimulation to treat pain. Wall and Sweet published a report demonstrating a reduction in pain via electrical stimulation of peripheral nerves.[22] They demonstrated stimulation-induced analgesia in eight patients with varying pain etiologies, with

four patients receiving prolonged pain relief even after stimulation was turned off. That same year, Shealy and Mortimer published the first report of electrical stimulation of the dorsal columns of the spinal cord in one patient.[23] Dorsal column stimulation immediately abolished the patient's pain, and when pain began to reemerge, changes to the stimulus pulse frequency quickly ameliorated the discomfort. These early reports formed the foundation of modern clinical neurostimulation therapies and kicked off several decades of study and innovation.

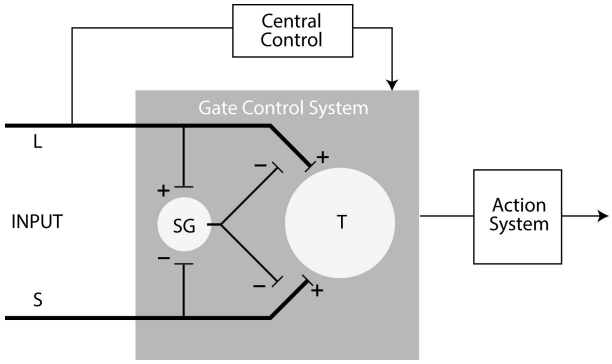

Figure 1.1 The Gate Control Theory of Pain. Small (S) pain-sensing fibers excite pain transmission neurons (T) and inhibit inhibitory interneurons in the substantia gelatinosa (SG). Large (L) touch-sensing fibers excite both T and SG neurons. The theory suggests repeated activation of SG neurons via L fiber stimulation may provide pain relief. Figure adapted from Melzack and Wall, 1965.[21]

1.2.2 Spinal cord stimulation

Five decades after Shealy and Mortimer demonstrated analgesia via dorsal column stimulation, spinal cord stimulation (SCS; **Figure 1.2**) has become the most prevalent clinical neurostimulation therapy with more than 50,000 implants per year.[24] SCS electrode arrays now come in one of two general forms: a cylindrical electrode array that can be implanted percutaneously, and a paddle electrode array which requires a laminotomy.[25] Most conventional forms of SCS apply stimulation with pulse frequencies typically between 40 and 60 Hz. However, several new waveform modalities have emerged over the past 10 years, such as applying stimulation in packets of high-frequency bursts, or applying stimulation at frequencies on the order of 1 to 10 kHz.[25] SCS is typically used to manage neuropathic limb pain syndromes that do not

respond to conventional medical management.[26,27] Unfortunately, the efficacy of SCS seems to wane over time,[28] and there is considerable variability both in success of SCS in individual patients and the success rates of SCS in clinical studies.[29] Some novel SCS technologies implement closed-loop control in an effort to induce more consistent pain relief.[30,31] However, continued longitudinal study of such technologies is needed to assess their efficacy in the long-term.

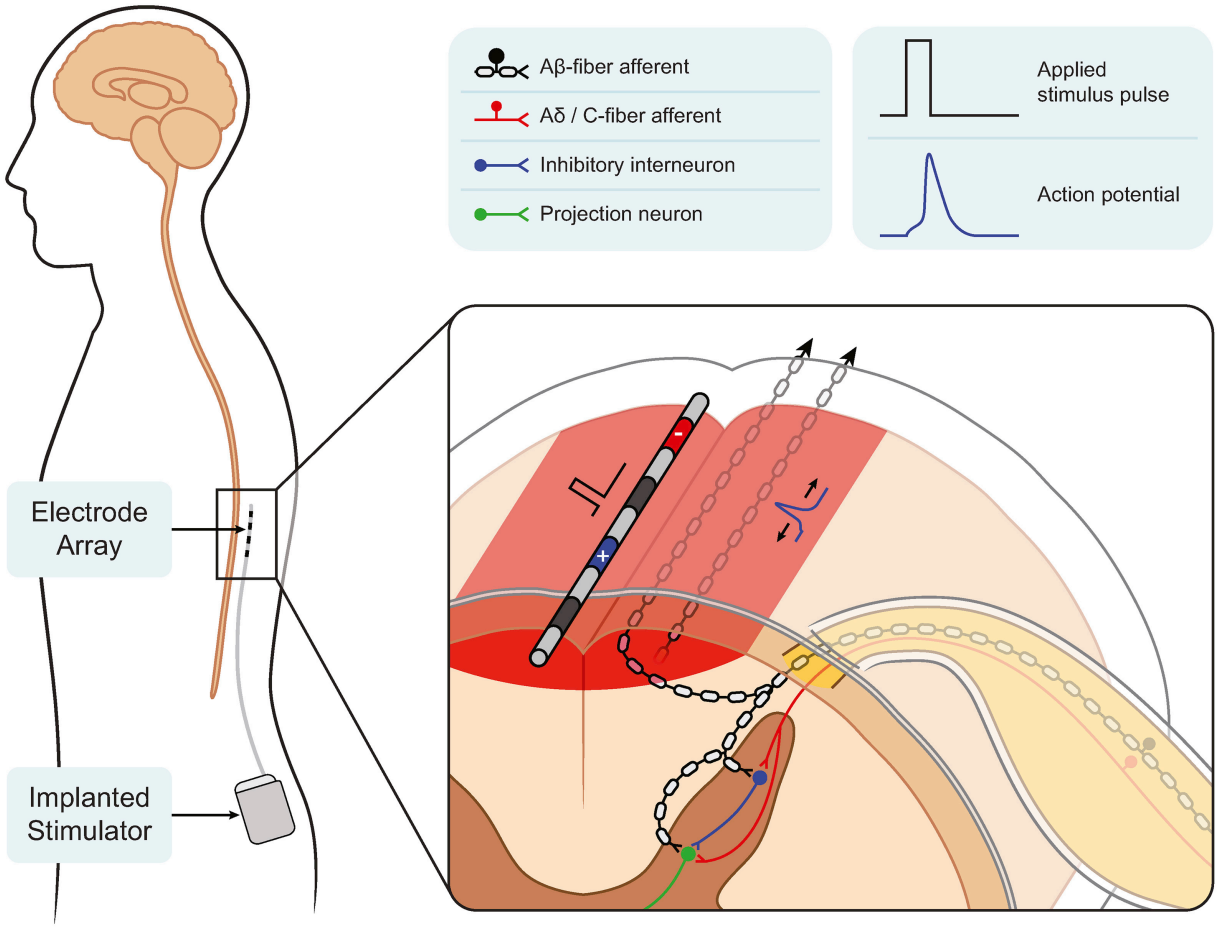

Figure 1.2 Spinal cord stimulation. An implanted stimulator and electrode array apply electrical stimulation to the dorsal columns of the spinal cord. SCS putatively activates large-diameter Aβ-axons in the dorsal columns, which induces antidromically propagating action potentials which activates circuitry in the dorsal horn. Figure adapted from Lempka and Patil, 2018.[25]

Conventional SCS, like Shealy and Mortimer's dorsal column stimulation, is hypothesized to provide pain relief by electrically stimulating the large-diameter Aβ-afferents in the dorsal columns.[32] Electrically driving the activity of the large-diameter afferents is hypothesized to

increase the inhibitory tone of networks in the dorsal horn of the spinal cord, thus "closing the gate" and preventing pain transmission neurons from sending signals to the brain. However, newer SCS waveform modalities may provide pain relief via other mechanisms. For example, modeling studies suggest that at stimulus pulse amplitudes used clinically, it is unlikely that 10 kHz SCS activates many, if any, axons in the dorsal columns.[32,33] Instead, many novel forms of SCS are hypothesized to provide pain relief via mechanisms including: modulating inhibitory interneurons in the spinal cord,[34] modulating the activity of glial cells,[35] inducing increases in temperature which alter neural activity,[36] and modulating the coupling between neurons and the vasculature.[37]

1.2.3 Dorsal root ganglion stimulation

Though SCS is a mainstay therapy for managing intractable pain, the complex anatomy of the spinal column (e.g., the presence of highly conductive CSF) makes it difficult to target pain in certain regions of the body (e.g., the feet and groin).[38] As each dorsal root ganglion (DRG) contains sensory neurons (**Figure 1.3C,D**) innervating a particular dermatome (i.e., region of the body), it was hypothesized that dorsal root ganglion stimulation (DRGS) may be able to provide focal pain relief in dermatomes that are traditionally difficult to target with SCS.

DRGS is achieved by placing an electrode array in the intraforaminal space of the spinal column and applying brief electrical impulses to a DRG (**Figure 1.3A,B**). DRGS received approval by the United States Food and Drug Administration for the management of complex regional pain syndrome (CRPS) in the lower limbs in 2016.[39] The ACCURATE clinical trial demonstrated that compared to traditional SCS, DRGS provided greater pain relief over the course of one year in patients with lower limb CRPS. Furthermore, preliminary studies indicate that DRGS may be effective in managing other chronic pain etiologies, such as diabetic neuropathy,[40] phantom limb pain,[41] groin pain,[42] and others. However, approximately 30% of the DRGS cohort

in the ACCURATE study did not receive adequate pain relief from DRGS (i.e., did not respond to the therapy).[43] Furthermore, preliminary long-term data on DRGS pain relief suggest that DRGS-induced analgesia may decrease over time.[42,44] Due to the novelty of DRGS, the physiological mechanisms of DRGS-induced pain relief are unknown, preventing us from both understanding why some patients do not respond to DRGS, and from innovating the therapy to specifically target analgesic mechanisms.

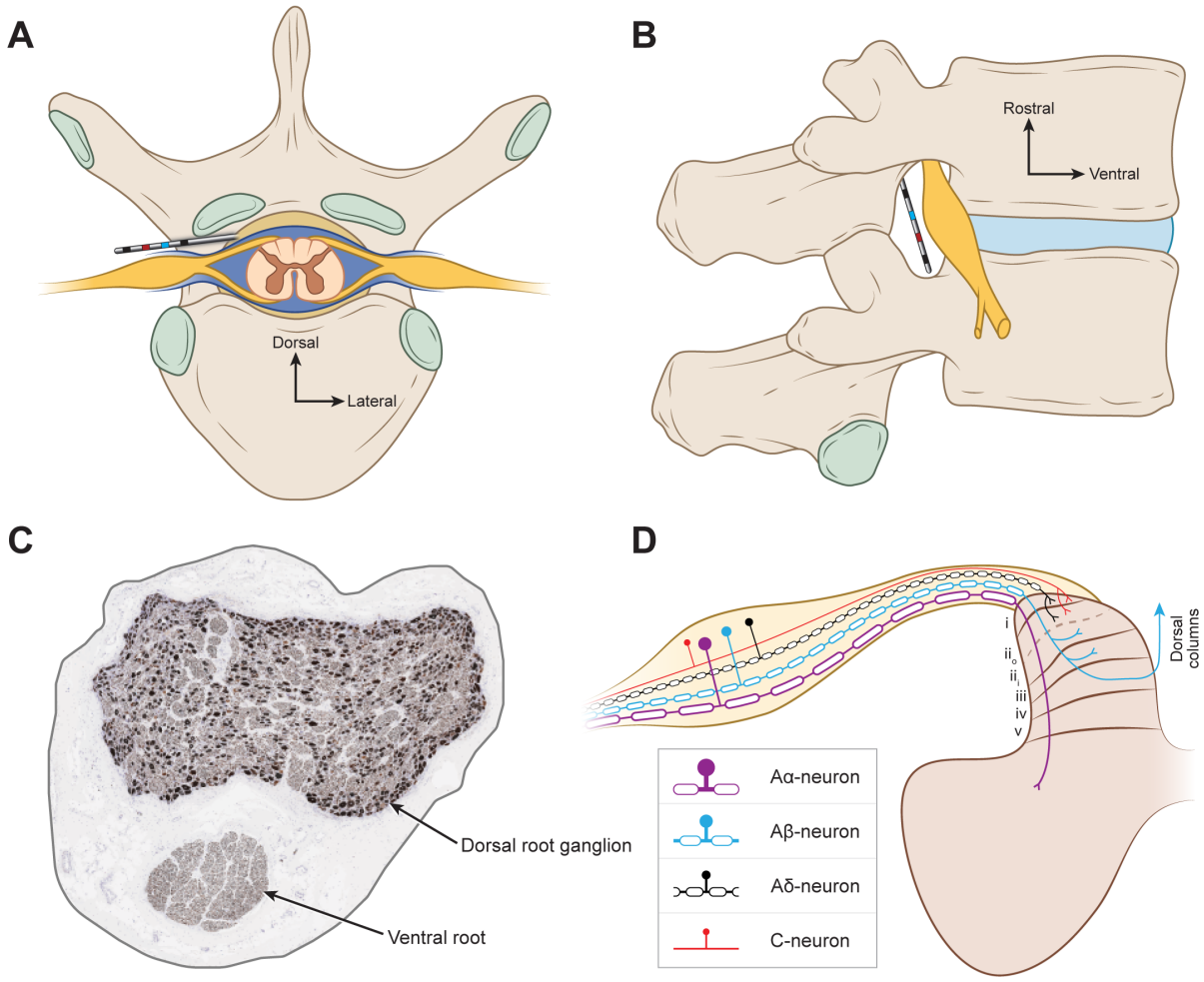

Figure 1.3 Dorsal root ganglion stimulation (DRGS). Axial (A) and lateral (B) views of the dorsal root ganglion (DRG), surrounding anatomy, and cylindrical electrode array. (C) Representative histology slice of a human lumbar DRG.[45] (D) Example primary sensory neurons and their axonal projections to the spinal cord dorsal horn. Figure adapted from Graham et al., 2021.[46]

Early *in vitro* and *in vivo* studies hypothesized that due to DRG containing the cell bodies of all sensory neurons innervating a given dermatome, DRGS may engage different analgesic mechanisms than SCS. Specifically, it was hypothesized that the ability to specifically stimulate cell bodies, and the ability to directly modulate the activity of nonmyelinated nociceptive neurons (i.e., C-neurons) may enable DRGS to provide superior pain relief relative to SCS.[47–49] However, conventional neurostimulation theory (see below) suggests that axons are the primary target of extracellular stimulation, while cell bodies are more difficult to excite.[50,51] Furthermore, it is well established that myelinated cells are activated at much lower current amplitudes than nonmyelinated cells.[50] Therefore, continued investigation is needed to assess whether these proposed mechanisms are engaged by clinical DRGS, and to discover if other analgesic mechanisms are concurrently utilized by the therapy.

1.3 Computational modeling of extracellular electrical stimulation

Computational modeling is an important tool for designing and studying the mechanisms of action of neurostimulation therapies. Computational approaches to studying neuromodulation therapies commonly involve modeling the electric field generated by the therapy (e.g., using a volume conductor model), and simulating neural activity in response to stimulation (e.g., using multi-compartment cable models). These techniques have been applied to studying several modern neurostimulation therapies, such as deep brain stimulation,[52] transcranial direct current stimulation,[53] and peripheral nerve stimulation.[54] Furthermore, these techniques can be leveraged to aid in the design and analysis of novel stimulation technologies (e.g., injectable electrodes).[55]

1.3.1 Foundations

Alan Hodgkin and Andrew Huxley's conductance-based (**Figure 1.4**) formalism describing action potential initiation and propagation in the squid giant axon laid the foundation on which many modern applications of computational modeling in neuroscience are built.[56] The Hodgkin-Huxley formalism represents a neural membrane as a parallel circuit with a capacitor representing the membrane capacitance, a resistor representing a linear leak conductance, and voltage- and time-dependent conductances representing active ion channels. Using this formalism, one can simulate how an arbitrary combination of ion channels present in a neural membrane produces the diversity of signals neurons use to communicate in response to injected current.

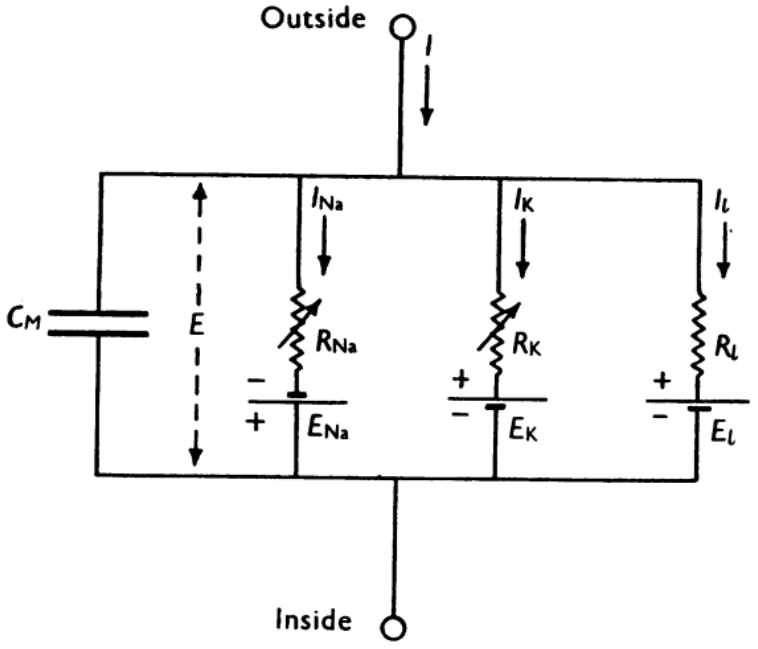

Figure 1.4 The Hodgkin-Huxley model. The Hodgkin-Huxley model represents neural membranes with a parallel capacitance, a passive leak channel (R_L), and voltage- and time-dependent conductances which represent active ion channels. Figure adapted from Hodgkin and Huxley, 1952.[56]

In the years following Hodgkin and Huxley, several studies examined the effect of extra- or juxta-cellular stimulation on the axonal response to stimulation. However, those studies only examined the steady-state response of neural membranes (i.e., in response to infinite duration pulses), whereas emerging clinical technologies at the time utilized short duration pulses to excite nerves. The seminal work of McNeal was the first study to examine the response of a myelinated

axon to finite-duration stimulus pulses.[57] McNeal demonstrated that membrane currents (and therefore, membrane voltages) at the nodes of Ranvier vary dramatically through time in response to a finite-duration stimulus pulse from a point-source electrode. Importantly, McNeal's model corroborated experimentally measured strength-duration curves and increased action potential thresholds with decreased fiber diameters. Such findings underscored the utility of such models to interpreting existing experimental data and suggested that this modeling approach could be used to examine the neural response to complex electrode geometries like those used clinically.

Building upon McNeal's work, Rattay provided intuition to understand the influence of extracellular electrical stimulation on the initiation and propagation of action potentials. Rattay derived the activating function: the second spatial derivative (nonmyelinated axons) or second spatial difference (myelinated axons) of the extracellular potentials produced by an electrode sitting outside the neural membrane.[58] The activating function is a powerful tool for determining the most likely location of action potential initiation in an axon. Building upon this work, Rattay then demonstrated that in neuron models with somata, dendrites, and axons (both myelinated and nonmyelinated) action potentials generally initiate in the axon.[50] Furthermore, the polarity of the stimulus pulse (i.e., a negative or positive current) and the position of the electrode relative to different neural elements (i.e., somata, dendrites, axons) greatly affect the threshold current needed to initiate an action potential (i.e., the activation threshold of a neuron). Such intuitions are critical to designing clinical neurostimulation therapies and understanding how such therapies induce or disrupt ongoing activity in their neural targets.

As neurostimulation therapies became more prevalent and expanded to treating other disorders (e.g., the approval of deep brain stimulation for managing tremor in the 1990's)[59], it became even more pressing to understand how electricity interacts with the nervous system. The

work of McIntyre and Grill further advanced our understanding of neural excitation in response to extracellular electric fields,[51] and how stimulus parameters can affect which neural elements are being modulated near an electrode.[60] Continued development of these methods led to the modern form of the field-cable modeling approach.

The field-cable modeling approach couples the extracellular potentials generated by an electrode – typically calculated using the finite element method – to multi-compartment cable models of neurons. This approach enabled the simulation of the neural response to an arbitrary extracellular stimulus pulse from a finite electrode of arbitrary geometry, placed within a geometrically complex volume conductor, such as the brain or spine.[52,61] Applying the field-cable modeling approach to neurostimulation therapies which manage chronic pain has provided insights into the neural substrates of stimulation-induced pain relief. Continued study using these methods is critical to painting a holistic picture of pain relief mechanisms.

1.3.2 Computational modeling of spinal cord stimulation

The work of Coburn and Sin developed the first series of SCS models in the 1980s. Their early work provided the first insights into the electric fields generated by SCS,[62–64] and the effect of SCS on myelinated axons in the dorsal columns.[65] Interestingly, Coburn found that the model-predicted thresholds for generating action potentials in dorsal column axons matched closely with clinically reported values.[65] The ability to compare biophysical predictions with clinical data underscores the utility of the field-cable modeling approach in understanding therapeutic mechanisms and suggests field-cable modeling may be useful in aiding the design of novel technologies to better target these mechanisms.

The work of Holsheimer and colleagues increased our understanding of both the mechanisms of SCS and of the technical factors affecting the neural response to SCS. For example,

they demonstrated that therapeutic SCS likely activates large-diameter dorsal column axons in the most superficial aspect of the dorsal columns, while uncomfortable sensations resulting from SCS may be due to activation of dorsal root axons.[66,67] They also examined how the placement of anodes and cathodes affected neural recruitment[68] and paresthesia coverage,[69] and examined the utility of novel electrode configurations in improving dorsal column activation.[70,71] These contributions were critical in establishing the conventional use of bipolar and tripolar configurations in therapeutic SCS to maximize dorsal column activation while minimizing dorsal root activation.

Recent SCS modeling work has examined the mechanisms of novel forms of SCS[33] and explored the uses of SCS for applications other than managing chronic pain, such as restoring motor control.[72] The latest generation of SCS models have taken a patient-specific approach, both to understand the mechanisms of action of the therapy for pain relief,[73] but also for the personalized development of stimulation protocols for targeted restoration of function.[74] Continued development of the patient-specific approach paired with advances in computing techniques (e.g., automating the creation of models from patient imaging data) may lead to clinical decision support systems for the implementation of SCS. Such systems could assist in calculating optimal stimulation parameters (e.g., stimulus pulse width, amplitude, frequency, stimulation configuration) to maximize pain relief in all patients.

1.3.3 Computational modeling of dorsal root ganglion stimulation

Due to the novelty of DRGS, there are few prior computational studies examining the neural response to DRGS. Bourbeau and colleagues examined the response of axons in the DRG to electrical stimulation via a point source electrode.[75] The goal of their work was to examine whether a microelectrode implanted in the DRG could achieve selective activation of small-

diameter axons over large-diameter axons. They found that due to small-diameter axons having shorter internode distances, and therefore more nodes of Ranvier over a given length than large-diameter axons, intragangliar microstimulation of the DRG can achieve selective activation of small-diameter myelinated afferents. However, it was unclear if this trend would hold during DRGS utilizing macroelectrodes like those used clinically, and if this trend would extend to nonmyelinated DRG neurons.

Kent and colleagues used a field-cable modeling approach to study the influence of DRGS on nociceptive, nonmyelinated C-neurons.[76] They demonstrated that DRGS can induce action potentials in the somata of C-neurons, triggering potassium efflux from the soma via calcium-activated potassium channels. Potassium efflux produces a slow hyperpolarization at the soma, which electrotonically spreads to the T-junction, preventing action potentials from propagating into the spinally projecting axon, putatively inducing pain relief. However, the stimulation amplitudes required to produce this filtering of action potentials at the T-junction were large (> 9 mA) compared to the amplitudes typically used clinically (≤ 1 mA).[43,77] This suggests that either: 1) augmentation of T-junction filtering may not be a primary mechanism of DRGS in clinical scenarios, or 2) there is a feature of C-neurons not accounted for in current models that enable filtering in response to considerably lower DRGS amplitudes.

1.4 Problem statement

Two fundamental knowledge gaps precluding the improvement of neurostimulation therapies for chronic pain are: 1) we do not understand the physiological mechanisms of action of neurostimulation-induced pain relief, and 2) we do not understand the sources of variability in the patient experience of neurostimulation therapies. Without a clear understanding of both how pain

relief is achieved and how interpatient variability may affect their response to a therapy, we cannot improve the design and implementation of the therapies to maximize pain relief.

1.4.1 Mechanisms of action

Without understanding the mechanisms governing how a therapy achieves clinical benefit, we cannot innovate the therapy to engage these mechanisms more safely and effectively. Despite tens of thousands of implants per year, the mechanisms of action of neurostimulation therapies for chronic pain remain poorly understood.[25,46] Though the mechanisms of action of SCS have been studied in both computational and preclinical models for several decades,[32,33,67,78–81] there is relatively little work on the mechanisms of DRGS due to its novelty. Preliminary studies have suggested that DRGS may exert action directly on the somata of nonmyelinated C-neurons.[49,76,82] However, conventional neurostimulation theory suggests nonmyelinated cells and somata would be much more difficult to exert action on than myelinated axons. Therefore, comparing the neural response of myelinated afferents and nonmyelinated afferents in the DRG is warranted. Furthermore, we are not sure where different neural elements, such as cell bodies and axons, are located within human DRG. However, previous work in cat DRG suggests cell bodies may preferentially congregate around the outer edge of the structure,[83] presumably where DRGS-induced currents would be strongest.

1.4.2 Sources of variability

There is considerable heterogeneity in the amount of pain relief reported by patients receiving neurostimulation therapies to manage their chronic pain. For example, a long-term prospective study of DRGS in 62 patients showed considerable variability in pain ratings post implant.[44] Similarly, the success rates of SCS across clinical trials are highly variable, and

outcomes do not seem to be improving with time.[29] We currently do not understand why some patients receive adequate pain relief from these therapies while others do not. Furthermore, variability which affects the success of a therapy in a patient could manifest at multiple scales. For example, there could be variability in the gross anatomy of the spinal column between patients. Differences in the amount of highly conductive cerebrospinal fluid surrounding the spinal cord could produce more current-shunting in some patients than in others.[67,84] Or, there could be genetic variability affecting the spatiotemporal distribution of ion channels in particular cells. Such variability could affect the direct neural response to stimulation, the processing of natural and artificially induced neural signals in downstream circuits, or both.[85–87]

1.5 Dissertation goals

The goal of this dissertation was to provide insight into the mechanisms of action of DRGS. Furthermore, this dissertation sought to provide frameworks for studying the effects of variability on neural processes that are important to the neural response to therapeutic electrical stimulation.

1.5.1 Mechanisms of action of DRGS

One goal of this study was to provide insight into the mechanisms of action of DRGS, a recently developed neurostimulation therapy for managing neuropathic pain. First, this project aimed to determine where different neural elements affected by DRGS (e.g., somata, axons) are located in human DRG. Then, this project aimed to determine which subtypes of DRG neurons were being activated during clinical DRGS. This project also studied how varying clinically controllable parameters (e.g., stimulus pulse width, electrode configuration) affected neural activation during DRGS. Finally, this project examined potential modulatory effects of DRGS on

nonmyelinated C-neurons. Understanding the DRG neurons activated during DRGS is the first step to understanding how DRGS alters neural activity to provide pain relief.

1.5.2 Sources of variability in neurostimulation for chronic pain

The overall goal of this study was to understand how variability at multiple scales may affect the neural response to therapeutic neurostimulation. This project first examined how variability in ion channel expression could affect a neuron's response to DRGS. This project then developed a framework to study neural activation during SCS using patient-specific computer models. Such models could be used to compare neural activation profiles across patients (e.g., between responders and non-responders to SCS). Finally, this project developed a method for parametrizing populations of biophysical neuron models to study how variability in a cellular population could affect the pathogenesis of neurological disorders. Understanding how variability in cells, circuits, and patients contributes to the neural response to electrical stimulation may inform the design of new clinical neurotechnologies.

Chapter 2 – Dorsal Root Ganglion Stimulation for Chronic Pain: Hypothesized Mechanisms of Action

The work presented in this chapter is published as:

Graham RD, Sankarasubramanian V, Lempka SF. Dorsal root ganglion stimulation for chronic pain: Hypothesized mechanisms of action. *The Journal of Pain*. 2021;23:196-211.[46]

2.1 Abstract

Dorsal root ganglion stimulation (DRGS) is a neuromodulation therapy for chronic pain that is refractory to conventional medical management. Currently, the mechanisms of action of DRGS-induced pain relief are unknown, precluding both our understanding of why DRGS fails to provide pain relief to some patients and the design of neurostimulation technologies that directly target these mechanisms to maximize pain relief in all patients. Due to the heterogeneity of sensory neurons in the dorsal root ganglion (DRG), the analgesic mechanisms could be attributed to the modulation of one or many cell types within the DRG and the numerous brain regions that process sensory information. Here, we summarize the leading hypotheses of the mechanisms of DRGS-induced analgesia, and propose areas of future study that will be vital to improving the clinical implementation of DRGS.

2.2 Introduction

Chronic pain remains one of the world's largest public health challenges, affecting hundreds of millions of people throughout the world.[10] Neurostimulation therapies are important

tools in a pain physician's clinical toolbox to manage chronic pain conditions that are refractory to conventional medical management. Spinal cord stimulation (SCS) has been a mainstay neurostimulation therapy for chronic pain for more than 50 years, and is an effective tool in managing intractable neuropathic pain in the lower limbs.[25] Despite the overall success of SCS in treating many chronic pain conditions (e.g., failed back surgery syndrome), pain in specific areas, such as the groin, foot, low back, and knee, are difficult to accurately target with SCS. The complex anatomy of the spinal column, posture-related motion of the spinal cord in the thecal sac, and shunting of electrical current in the cerebrospinal fluid can limit the delivery of stimulation to the target fibers within the spinal cord.[88] Therefore, patients with intractable pain in regions that are difficult to target with SCS are often left with few alternatives, presenting a large need for innovations in neurostimulation for pain management.

Dorsal root ganglion stimulation (DRGS) is a novel neurostimulation therapy for managing medically refractory chronic pain.[89] As a single dorsal root ganglion (DRG) receives sensory information from a discrete region of the body, it was hypothesized that DRGS could be an effective strategy for managing pain in regions that are difficult to target with SCS. DRGS was approved by the United States Food and Drug Administration (FDA) in 2016 for the treatment of refractory complex regional pain syndrome (CRPS) in the lower limbs.[39] Despite currently only having FDA approval for CRPS in the lower limbs, DRGS has shown promise in managing other pain etiologies, such as painful diabetic neuropathy,[40] phantom limb pain,[41] and groin pain.[42] The ACCURATE clinical trial compared the safety and efficacy of SCS and DRGS in treating patients with intractable CRPS at 3 and 12 months post-implantation, and demonstrated that more patients were considered treatment successes (i.e., received $\geq$ 50% reduction in pain intensity) with DRGS than SCS.[90] However, a 50% reduction in pain intensity (measured via the visual analog scale

(VAS)) does not always lead to an improved quality of life, or facilitate a patient returning to their activities of daily living.[91] Furthermore, more than a quarter of patients were not deemed treatment successes with DRGS, leaving them with few other pain management options because neurostimulation therapies are often a last-resort therapy in a clinician's treatment algorithm.[92] Presently, we do not have a clear scientific understanding of the physiological mechanisms of DRGS-induced pain relief. We believe that it is vital to elucidate these mechanisms, to: 1) understand why DRGS fails in some patients, to improve patient selection, and 2) innovate DRGS technologies to specifically target these mechanisms, to maximize pain relief in all patients.

Recently, there was an excellent review of human DRG anatomy;[93] therefore, we will highlight only the anatomy essential to understanding DRGS. The DRG is a swelling in the dorsal spinal root, which houses the cell bodies of all primary sensory neurons (PSNs) (**Figure 2.1**) innervating a specific dermatome (i.e., region of the body). There are bilateral pairs of DRG at each vertebral level (**Figure 2.1A**), which receive information from roughly the same dermatome on opposite sides of the body. All DRG are encased by the meninges of the spinal cord as the meninges transition into the epineurium surrounding peripheral nerves.[94] DRG reside in the neuroforamina (**Figure 2.1B**), but the relative position of the DRG within the foramen may vary depending on the spinal level.[95] During the implantation of a DRGS system, electrode lead bodies are percutaneously inserted using a Touhy needle, guided through the epidural space of the spinal column using X-ray fluoroscopy, and routed into the intraforaminal space where the array of electrode contacts are placed along the dorsal side of the DRG (**Figure 2.1A,B**). The electrode lead(s) are connected to an implanted pulse generator, which resides in a body cavity usually around the posterior lateral flank.[77]

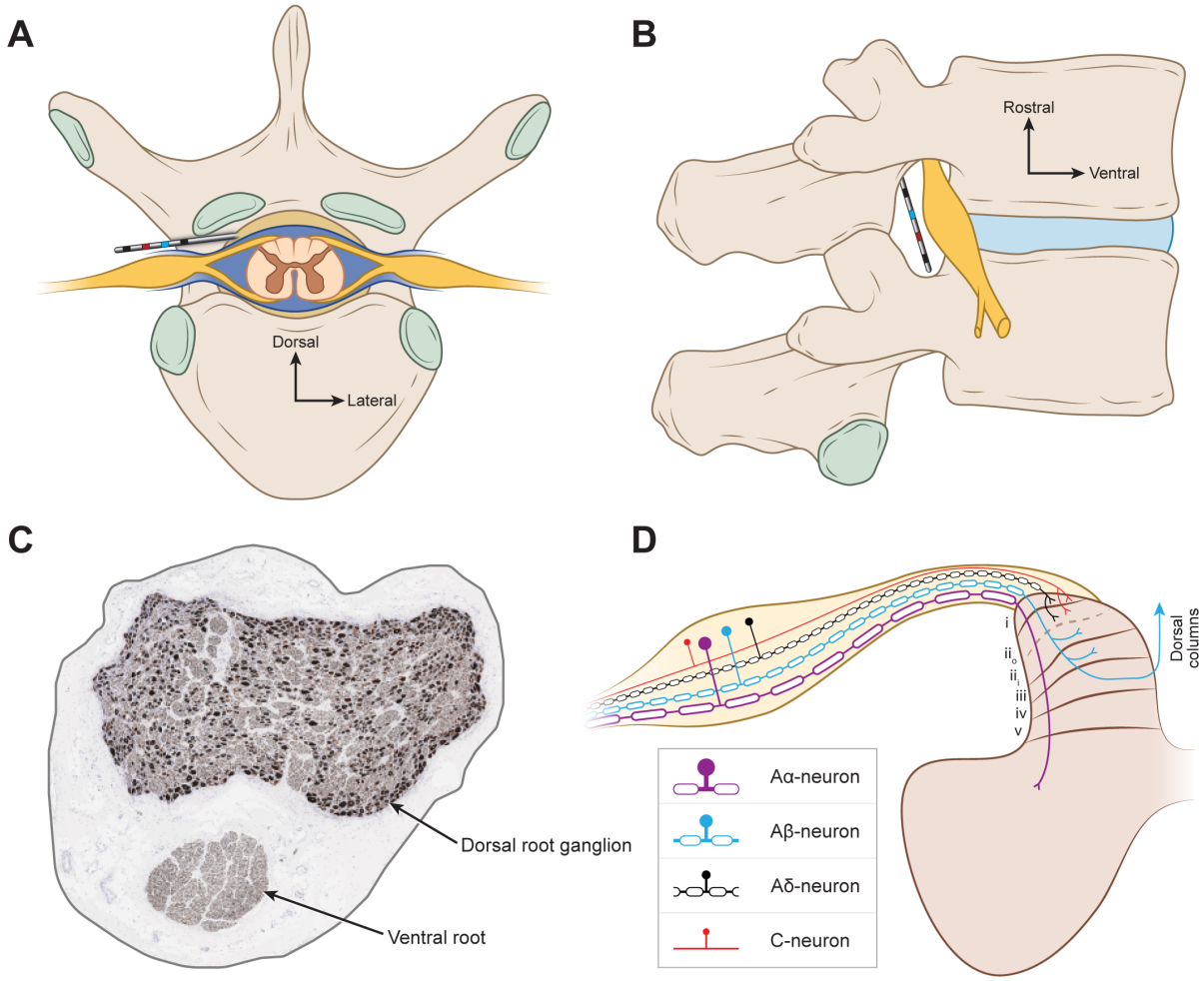

Figure 2.1 DRGS and surrounding anatomy. A) Axial view of a human spinal column with a DRGS electrode array in place. B) Sagittal view of a DRGS electrode array in the foramen. C) Histology image of a human lumbar DRG stained for 200 kDa neurofilament.[45] Axons appear as miniscule dots; cell bodies appear as larger dark spots. D) Sensory neuron types in the DRG and their projections into the spinal cord. The first five lamina of the dorsal horn are labeled to indicate where different sensory neuron types send axon collaterals.

Extracellular electrical stimulation, like that utilized by DRGS, can affect different neural structures (e.g., cell bodies, axons, presynaptic terminals) depending on the parameters of the stimulus pulse (e.g., amplitude, frequency, pulse width, polarity).[51] Therefore, the morphological characteristics of DRG neurons, and their location in the DRG relative to the stimulating electrodes, will greatly affect which cells are being modulated by DRGS. Clinically, DRGS is typically applied with a bipolar stimulation configuration and a tonic pulse train with a pulse frequency around 20 Hz, a pulse duration between 200 and 300 ms, and a pulse amplitude on the

order of several hundred mA to a few mA.[77] DRGS four-contact cylindrical electrode arrays are 1mm in diameter with 1.25 mm long contacts, comparatively smaller than traditional SCS cylindrical electrode arrays.[96] The electrode is typically placed within the foramen such that the second and third contacts span the pedicle, with the second and third contacts typically assigned as the cathode and anode, respectively.[77] PSNs, the cells within the DRG, are pseudounipolar, i.e., their cell bodies have a single axon process called the stem axon, which bifurcates at a region called the T-junction into an axon that projects to the spinal cord (centrally projecting axon) and an axon that projects to the peripheral nervous system (peripherally projecting axon) (**Figure 2.1D**).[97] Recent histological results demonstrated that in human lumbar DRG, cell bodies typically organize around the dorsomedial region of the ganglion, while axons of passage are more homogeneously distributed throughout the rest of the ganglion.[45] DRG cytoarchitecture is of great importance to the clinical implementation of DRGS (**Figure 2.1C**). As distance from the stimulating electrode increases, extracellular potentials exponentially decrease, and therefore DRGS-induced activity may be focused on the most superficial neural elements. Such knowledge is crucial to designing stimulus waveforms that target the neural elements and PSN subtypes responsible for the pain-relieving effects of DRGS.

PSNs are a diverse class of neurons, with different types of neurons conveying different sensory modalities (e.g., touch, pain, itch). PSN axons are commonly classified as A-fibers (myelinated axons) and C-fibers (nonmyelinated axons). In this review, we will refer to DRG neurons with myelinated axons as A-neurons, and DRG neurons with nonmyelinated axons as C-neurons. C-neurons are traditionally thought to be nociceptors, though it is known that C-neurons consist of several molecularly defined subpopulations that convey a myriad of sensations, including innocuous or painful touch,[98] innocuous and painful thermal sensations,[99,100] chemical

itch,[101] pleasant touch,[102] and some C-neurons code multiple types of sensations (i.e., polymodal C-neurons).[98,100] A-neurons are further stratified into Aα-, Aβ-, and Aδ-neurons. Aα-neurons are thickly myelinated, large-diameter muscle afferents, and can be further classified as group Ia neurons, which innervate muscle spindles and code muscle stretch, and Ib neurons which innervate golgi tendon organs and code muscle tension.[103] Aβ-neurons are also thickly myelinated, large-diameter afferents, though they are smaller in diameter than Aα-neurons. Aβ-neurons typically convey non-painful tactile stimuli,[104] though there have been reports of nociceptive signals conducted in the Aβ-fiber conduction velocity range,[105,106] and a subset of Aβ-neurons are important in transmitting mechanical itch.[107] Aδ-neurons are thinly myelinated, medium-diameter afferents, that typically convey innocuous or painful touch[108] or thermal sensations.[99] The peripherally-projecting axon of a PSN terminates in a sensory end organ, depending on the type of sensations conveyed by that neuron.[104] The centrally-projecting axon enters the spinal cord (**Figure 2.1D**), where it can send collaterals into the grey matter to form excitatory synapses with spinal neurons (e.g., interneurons in the dorsal horn), enter a white matter tract and project caudally or rostrally (e.g., to the brain stem), or project to both spinal and supraspinal targets.[109,110]

Previous reviews have covered several aspects of DRGS, including *in vivo* and *in vitro* studies of DRGS,[111] the DRG as a target for neurostimulation therapies,[112,113] and clinical evidence of DRGS efficacy.[114] However, to our knowledge, there has not been a review of the evidence supporting the current hypotheses of the physiological mechanisms of DRGS-induced pain relief. Therefore, our goal in this review is to summarize the evidence supporting the current. hypotheses of DRGS mechanisms, and to provide an outlook on the scientific insight needed to facilitate technological innovations that will improve the efficacy of DRGS. We consider both the direct neural response to DRGS (i.e., the neuronal processes that are transiently modulated by DRGS-

generated electric fields) and the indirect effects of DRGS (e.g., postsynaptic activation of neural circuits in the central nervous system, modulating the activity of non-neuronal targets). Due to the novelty of DRGS, there are few studies of the indirect effects of DRGS; therefore, much of our discussion will focus on the direct neural response to stimulation. We conclude by suggesting future research avenues towards painting the holistic picture of DRGS mechanisms.

2.3 Direct neural response to DRGS

Similar to other clinical neurostimulation therapies, DRGS interfaces with the body by generating spatiotemporally varying electric fields. These electric fields can perturb a cell's transmembrane voltage, and can lead to the opening or closing of voltage-sensitive ion channels. Stimuli of sufficient intensity can induce an action potential (AP), while subthreshold stimuli would result in a transient change in membrane potential that does not induce an AP. However, it is possible that subthreshold stimuli have modulatory effects, such as integrating or disrupting ongoing neural activity, or by influencing voltage-sensitive channels whose dynamic ranges are below the AP threshold. In this paper, we define the direct neural response to DRGS as any voltage-sensitive neurophysiological process that is induced, prevented, or characteristically altered by the transient electrical stimuli generated by DRGS. This definition includes effects such as generating APs in a particular cell type leading to neurotransmitter release from presynaptic terminals, or intracellular second messenger systems that are triggered by voltage-sensitive processes (e.g., calcium influx through voltage-sensitive calcium channels). We believe that there are three primary hypotheses on the direct neural response to DRGS: 1) the driving of feed-forward pain-inhibition circuitry, 2) augmenting low-pass filtering mechanisms at the T-junction of PSNs, and 3) suppressing the hyperexcitability of PSNs generated by chronic pain states.

2.3.1 Driving input into pain-gating networks

In their seminal paper in 1965, Melzack and Wall proposed the gate control theory of pain,[20] which states that activating large-diameter tactile afferents gates pain signals to the brain by driving inhibitory networks in the spinal cord, while also being modulated by top-down control from supraspinal structures. Only two years later, Wall and Sweet used this theory to demonstrate temporary analgesia in humans by electrically stimulating peripheral nerves, and Shealy et al. developed the first clinical usage of SCS.[22,23] By stimulating the large diameter afferents in peripheral nerves and the dorsal columns of the spinal cord, respectively, these groups demonstrated the ability of exogenous electric fields to drive pain inhibition in humans, putatively by artificially driving feed-forward pain-inhibition networks in the spinal dorsal horn.[21] As many of the Aβ-axons that constitute the dorsal columns originate in the DRG,[115] and extracellular electrical stimulation preferentially activates large-diameter myelinated axons over small-diameter nonmyelinated axons,[58,116] DRGS may share mechanisms of action with SCS.

Computational modeling is an important tool in uncovering the mechanisms of neurostimulation therapies.[117] Bourbeau and colleagues used a combined biophysical and analytical model to study activation thresholds during microstimulation of the DRG with penetrating microelectrodes.[75] Their results suggest myelinated afferent activation thresholds would be on the order of microamperes, and that microstimulation can preferentially activate small-diameter myelinated afferents over large-diameter myelinated afferents. This finding is contrary to conventional understanding that larger-diameter axons have lower activation thresholds than smaller-diameter axons.[57] The authors suggested that this selectivity for small-diameter axons was due to smaller axons having more closely spaced nodes of Ranvier, increasing the probability that a node would be present near the penetrating microelectrode. However, their

modeling framework was not designed to study clinical DRGS performed with non-penetrating macroelectrodes placed in the intraforaminal tissue, and it did not account for factors, such as the anatomy surrounding the DRG, which would affect the electric field delivered to DRG neurons. Furthermore, that study only modeled the axons in the DRG, assuming that cell bodies would not be excitable by extracellular stimulation, and it did not examine the effects on C-neurons. It is currently unclear if this selectivity is achievable with extragangliar electrodes, like those used in clinical DRGS.

Work from our laboratory implemented a field-cable modeling approach to study clinical DRGS, and compare the activation thresholds of Aβ-neurons with C-neurons.[118] We showed that when applying DRGS with clinical leads and stimulation parameters, DRGS drives the activity of Aβ-neurons without affecting the activity of C-neurons (**Figure 2.2**). Our follow-up study further examined the effect of DRGS on Aα- and Aδ-neurons.[119] We showed that with clinical stimulation parameters, DRGS may activate Aδ-neurons that sense innocuous touch, without activating Aδ-neurons that sense mechanical pain. Furthermore, we showed that Aα-neurons may be widely activated during DRGS, but their low population within the DRG makes it difficult to determine their extent of activation in clinical scenarios.[45] However, our models did not account for calcium channels or dynamics in DRG neurons, which may affect a neuron's activation threshold, and likely affects the DRGS-influenced neural dynamics which operate on time-scales lasting seconds or longer,[120] suggesting that additional mechanisms might be at play. Though computer models provide an excellent framework with which to probe the mechanisms of DRGS, there are several limitations to the computational approach, such as simplified cellular morphologies, and a lack of experimental data (e.g., spatiotemporal ion channel expression profiles) from which to build the models.

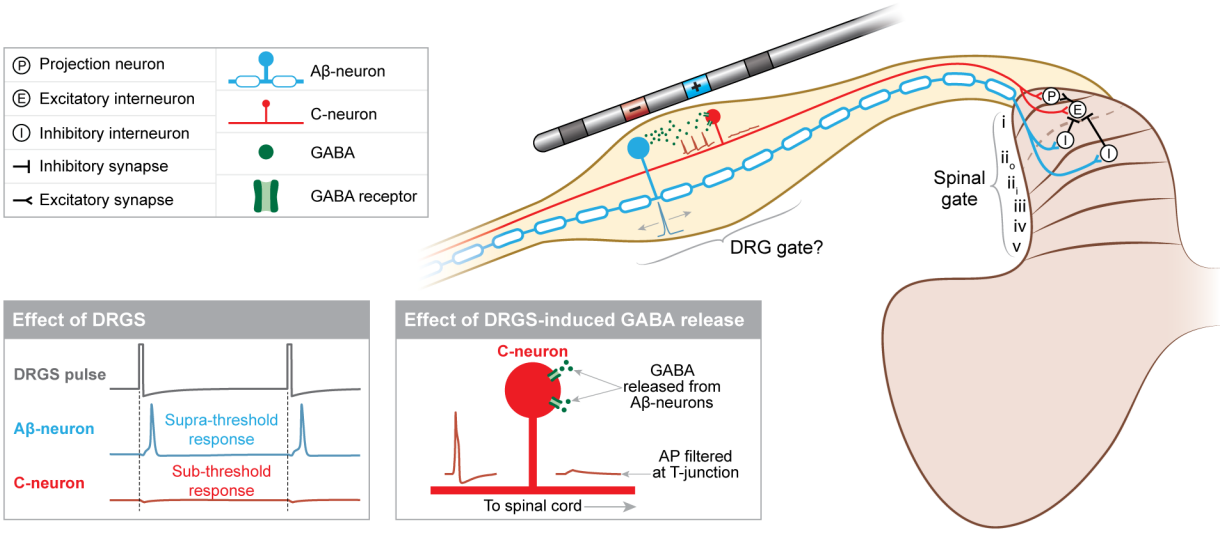

Figure 2.2 DRGS may drive pain-gating mechanisms in the spinal cord dorsal horn, the DRG, or both. DRGS applies trains of electrical pulses which induce APs in Aβ-neurons, which activate inhibitory interneurons in lamina ii_i and iii in the dorsal horn. Concurrently, Aβ-neurons may release GABA within the DRG, which can act on C-neurons and potentially prevent ectopic APs from propagating into the spinal cord.

Currently, there are a few in vivo studies of DRGS mechanisms, specifically in the context of neurostimulation for pain. However, these initial studies have provided interesting results. Using a rat model of DRGS, Chao and colleagues confirmed our modeling predictions that Aβ-neurons have the lowest activation thresholds during DRGS.[121] Koetsier and colleagues showed that in rats, DRGS did not affect intracellular levels of gamma-aminobutyric acid (GABA) in the spinal cord dorsal horn, suggesting DRGS does not drive inhibitory circuitry in the spinal cord.[122] Instead, the authors suggested that DRGS may drive GABAergic pain-gating circuits local to the DRG. Du and colleagues recently found that many DRG neurons possess the cellular machinery necessary to synthesize and release GABA, including large-diameter 200 kDa neurofilament-positive neurons, such as Aβ-neurons.[123] They also demonstrated that optogenetically depolarizing these neurons caused behavioral changes indicative of reduced acute and chronic pain. Therefore, it is possible that clinical DRGS directly activates myelinated afferents, leading to a release of GABA within the DRG itself to inhibit pain perception (**Figure 2.2**). However, these findings are

preliminary, and more work is needed to understand the physiological consequences of in vivo GABA release in DRG, and whether clinical DRGS is capable of inducing somatic GABA release.

Furthermore, these data have not ruled out pain-gating inhibition in the dorsal horn as a mechanism of DRGS. Alternatively, DRGS may drive the release of other inhibitory neurotransmitters, such as glycine, in the dorsal horn. Aβ-neurons in the DRG have axonal projections to lamina ii_i and iii of the dorsal horn,[109] where they form feed-forward circuits with glycinergic interneurons that gate mechanical allodynia, a common phenotype of neuropathic pain.[124] It is possible that DRGS drives the activity of Aβ-projections to the dorsal horn, thereby increasing the glycinergic inhibitory tone in the spinal cord to gate neuropathic pain. Continued study of the complex pain-processing networks in the central nervous system is crucial to fully elucidating how DRGS-generated peripheral inputs reduce pain.

Additional studies have examined DRGS through the lens of other neurorehabilitation therapies, such as controlling bladder function,[125] or as a target to provide somatosensory feedback and control in neuroprosthetic systems.[126] Though these studies were not designed to provide evidence on the mechanisms of DRGS for pain relief, they still give insight into which types of DRG neurons respond to extracellular stimulation. For example, some studies found that low-amplitude intragangliar stimulation with penetrating microelectrodes elicits antidromic compound action potentials (CAPs) with conduction velocities in the Aβ- to Aα-range.[127–129] Other studies showed similar findings with an electrode array placed on the surface of the ganglion.[130] However, due to the small diameter of Aδ- and C-neuron axons, their APs can be difficult to resolve on CAP recordings, leaving the extent to which small-diameter axons are recruited during DRGS an open question.

2.3.2 Augmenting T-junction filtering

Several sources of experimental data have suggested that T-junction filtering could be a primary mechanism of DRGS-induced analgesia. Following frequency, the maximum frequency train of APs that can be conducted through an axonal branch point, is used as a measure of T-junction filtering in PSNs. Gemes and colleagues showed that in excised rat DRG, A-neurons have significantly larger following frequencies than C-neurons, i.e., A-neurons can transmit higher frequency trains of APs across the T-junction than C-neurons.[48] Interestingly, peripheral nerve injury decreased the following frequency in A-neurons, but increased the following frequency in C-neurons, suggesting that in chronic pain states there is a coincident decrease of pain-gating signals and increase of painful signals entering the spinal cord. They also found that in C-neurons, increasing current through calcium-dependent ion channels (e.g., small conductance calcium-activated potassium (SK) channels) reduced the following frequency. This result suggests that a therapy designed to trigger calcium influx into C-neurons may enhance T-junction filtering and block pain signals from entering the central nervous system.

The T-junction, the region where the stem axon bifurcates into a spinally projecting axon and a peripherally projecting axon, is a morphological peculiarity nearly unique to DRG neurons (and the sensory neurons of the trigeminal ganglion).[97] The T-junction is a large node of Ranvier,[131] and the peripherally projecting axon is typically larger in diameter than the spinally projecting axon, though there may be differences in this diameter mismatch across cell types.[132] Furthermore, the cell bodies of DRG neurons have active ion channels, which allow peripherally generated APs to invade the soma.[133] These peculiarities can affect the transmission of afferent signals from the peripheral axon to the dorsal root axon. For example, in myelinated afferents, orthodromically propagating APs can generate ‘extra’ spikes in the initial segment, which rebound towards the T-junction and may occlude other orthodromic APs.[134] This self-generated occlusion

seems to increase the number of short and long inter-spike intervals, while decreasing the number of intermediate inter-spike intervals. In nonmyelinated afferents, combinations of morphological and electrophysiological features, such as stem axon length and slow hyperpolarizing conductances, can produce a low-pass filtering effect on orthodromically propagating APs.[135] DRGS may provide analgesia by augmenting this filtering property in the DRG neurons responsible for pain pathophysiology.

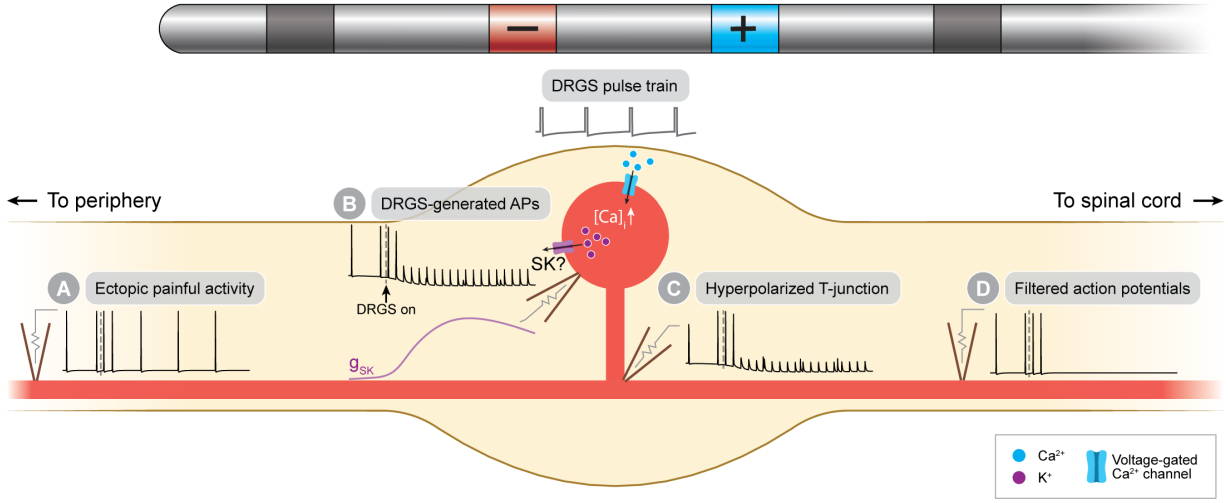

Figure 2.3 DRGS may augment the low-pass filtering properties of nociceptive C-neurons. A) Ectopic APs indicative of spontaneous pain propagate along the peripheral axons of C-neurons towards the central nervous system. B) The DRGS pulse train induces APs in or near C-neuron somata causing calcium influx through voltage-gated calcium channels, putatively triggering potassium efflux through calcium-activated SK channels. C) Potassium efflux hyperpolarizes the soma, which electrotonically hyperpolarizes the T-junction. D) Orthodromically propagating APs are unable to propagate passed the hyperpolarized T-junction into the spinal axon.

The first computational study of clinical DRGS mechanisms examined the effect of DRGS on putatively nociceptive C-neurons. Kent and colleagues used a field-cable modeling approach to show that DRGS generates APs in C-neuron somata, which produces a net hyperpolarization by increasing the current through SK channels (**Figure 2.3B**).[76] Somatic hyperpolarization electrotonically hyperpolarized the stem axon and T-junction (**Figure 2.3C**) to an extent that blocked AP propagation into the dorsal root axon (**Figure 2.3D**), both painful APs from the periphery (**Figure 2.3A**) and DRGS-generated APs from the soma. However, to produce the T-

junction filtering effect, it was necessary to apply DRGS with a stimulation amplitude greater than 9 mA, which is far greater than typical clinical stimulation amplitudes (1 mA on average).[77] It is important to note that anatomical simplifications and parameter selection (e.g., tissue conductivities, ion channel conductances) used in the field-cable model can dramatically affect the thresholds necessary to generate APs in modeled neurons.[136] Therefore, future studies should examine which parameters affect the fidelity with which DRGS can augment T-junction filtering.

Koopmeiners and colleagues utilized an in vitro approach to study the effect of extracellular electrical stimulation on Aδ- and C-neurons in excised rat DRG.[47] They demonstrated that field stimulation of excised DRG reduced the following frequency of putatively nociceptive neurons, while producing large transient increases in intracellular calcium concentration. Pan and colleagues then provided the first in vivo recordings of T-junction filtering in a rat model of DRGS for rheumatoid arthritis, though in this case, DRGS filtered antidromically propagating APs initiated via dorsal root stimulation and recorded via teased fiber recordings from the sural nerve.[82] These results add further evidence that DRGS may provide pain relief by filtering the transmission of APs at the T-junction, and that this phenomenon is likely either calcium-dependent or calcium-sensitive.

Recently, Chao and colleagues used an in vivo rat model to study the mechanisms of action of DRGS.[121] Using teased fiber dorsal root recordings, they demonstrated that when stimulating the sciatic nerve, the stimulation amplitude needed to activate nonmyelinated C-axons is more than 50 times greater than the amplitude needed to activate myelinated Aβ-axons, in agreement with conventional neurostimulation theory. However, when stimulating the DRG, the C-neuron activation threshold was only 1.5 times the Aβ-neuron threshold, contrary to previous modeling results.[118] Furthermore, they found that within approximately 30 seconds of starting DRGS applied

at 80% of motor threshold, the orthodromically propagating C-component of the teased fiber recording disappeared, suggesting that prolonged DRGS augments T-junction filtering in nociceptive neurons after a brief wash-in period. These experimental results are exciting, and imply that DRGS activates many types of neurons simultaneously, suggesting multiple pain-relieving mechanisms may be happening concurrently.

As with all animal models of human technology, it is critical to ensure that in vivo models accurately recapitulate clinical scenarios. Therefore, the electric fields generated by DRGS in preclinical studies must adequately approximate the electric fields generated by clinical DRGS systems to ensure the conclusions of experimental studies accurately inform our clinical understanding of the technology. In this way, there are three interrelated factors that we think are worth careful consideration when designing future experimental studies of DRGS: 1) the dimensions of the stimulating electrode contacts, 2) the dimensions of the animal model's DRG and surrounding anatomy, and 3) the choice in stimulation parameters, particularly the pulse amplitude. Chao and colleagues used an in-house made electrode to apply bipolar DRGS that is necessarily smaller than the electrode leads used clinically, because the rat neuroforamina are considerably smaller than human neuroforamina. However, smaller electrode contacts will generate larger current densities in stimulated tissues compared to larger contacts for a given pulse amplitude, potentially lowering the activation threshold of small neurons (e.g., C-neurons). Furthermore, smaller neuroforamina, i.e., a more enclosed space surrounded by a bony structure, implies more current will enter the more conductive neural tissue, compared to the minimally conductive bone. A recent study of anatomical factors affecting the activation thresholds of neurons in the spinal cord dorsal columns emphasizes the importance of this latter point.[136]

Comparatively larger current densities resulting from smaller electrode contacts and neuroforamina make the already difficult task of choosing clinically relevant pulse amplitudes for in vivo DRGS studies even more challenging. Koetsier and colleagues applied DRGS using an intensity of 66.7% motor threshold (i.e., the minimum amplitude at which DRGS causes muscle activation in the patient's or animal's stimulated myotome), whereas Chao and colleagues suggested that 80% motor threshold was the optimal stimulating intensity.[121,122] However, preliminary clinical data suggest that sensory thresholds (i.e., the minimum stimulation amplitude at which a human patient reports feeling paresthesias) can be between 33% and 70% of the motor threshold value.[137] This finding, taken with the clinical reports that some DRGS patients utilize sub-perception DRGS (i.e., DRGS with amplitudes that do not produce paresthesias) and achieve successful pain relief,[138,139] indicates further study is needed to determine how the 'optimal' pulse amplitude should be calculated in experimental studies to most accurately recapitulate clinical DRGS. Determining this relationship between experimental and clinical pulse amplitudes is a challenging problem because there are currently no clinically analogous methods for determining sensory thresholds in animal models.

Furthermore, neural activation generated when stimulating at a particular percent motor threshold in a preclinical model may not be directly analogous to the neural activation generated by stimulating at the same percent motor threshold in a human study, because of differences in DRG size across species. Muscle twitches resulting from DRGS are likely caused by: 1) direct activation of Ia afferents in the DRG causing postsynaptic activation of motor neurons in the ventral horn,[72] or 2) direct activation of motor axons in the ventral root. Because Ia afferents have low populations in both rodent[140] and human[45] DRG, activation of sufficient numbers of Ia afferents to produce a muscle twitch could suggest widespread neural activation throughout the

DRG. Similarly, assuming the stimulating electrode is placed on the dorsal side of the DRG, direct activation of the ventral root − a structure farther from the stimulating electrode than the DRG − would suggest that DRGS was applied with a large pulse amplitude, thereby likely causing widespread activation throughout the DRG.

However, rat DRG are much smaller than human DRG. In the dorsal-ventral axis, lumbar rat DRG are likely less than 1 mm wide[141,142] while human lumbar DRG are approximately 6 mm wide,[93] placing rodent ventral roots and Ia afferents much closer to the stimulating electrode contact than in clinical scenarios. Because the voltage at a given point in space is inversely proportional to its distance from a current source, a given percent of a motor threshold in a rat likely causes more neural activation in the DRG than the same percent motor threshold would cause in a DRGS patient. Future work should develop rigorous methodologies for selecting stimulation parameters in both clinical and preclinical DRGS experiments which allow for direct comparison between the two types of data.

2.3.3 Suppressing PSN hyperexcitability

Spontaneous firing of APs despite a lack of sensory input and increased firing of APs in response to peripheral stimuli, are thought to be two biomarkers of several chronic pain etiologies. For example, ongoing input into nociceptive C-neurons, generated perhaps from a peripheral neuroma, may lead to pain perception without an external noxious stimulus.[143] Spontaneous activity in Aβ-neurons, which typically don't convey pain signals, is thought to underly allodynia, a clinical symptom of neuropathic pain whereby previously non-painful stimuli cause pain.[144,145] Current evidence suggests that the DRG can be responsible for the development of neuropathic pain through hyperexcitability and spontaneous ectopic firing of PSNs. One proposed mechanism of DRGS is that electrical stimulation rectifies this hyperexcitability and aberrant activity.

Koopmeiners and colleagues measured the number of APs generated in response to current-clamp stimulation in excised DRG from healthy rats.[47] They demonstrated that putatively nociceptive neurons generate fewer APs in response to current clamp stimulation after exposure to 90 seconds of DRGS compared to before receiving DRGS, suggesting that DRGS reduces membrane excitability. Given that DRGS applied at an intensity that reduced membrane excitability also produced large increases in intracellular calcium, the authors hypothesized that the reduction of membrane excitability may be calcium-dependent or calcium-sensitive. It is currently unclear how different chronic pain etiologies affect neural dynamics and the response to DRGS, but these data provide evidence that justifies further study of DRGS' ability to suppress neuronal excitability.

In a tibial nerve-injured (TNI) rat model of DRGS, Chao and colleagues showed that DRGS raised the mechanical threshold to elicit AP firing in both C- and Aδ-neurons, and significantly reduced the firing frequency of C- and Aδ-neurons in response to mechanical stimulation.[121] As these data come from teased fiber recordings of dorsal root axons, it is difficult to ascertain whether these changes resulted from suppressing the excitability of the recorded cell, or from inducing T-junction filtering of orthodromically propagating APs (see previous section). However, the authors also showed that after DRGS, the average spontaneous firing frequency of C-neurons decreased, and other studies have shown that DRGS reduces spontaneous pain behavior in TNI rats,[49,146] suggesting that excitability suppression is a possible culprit of the reduction in nociceptor activity.

To date, there are relatively few studies explicitly examining the hypothesis of hyperexcitability suppression, and the biophysical mechanisms through which excitability suppression is achieved are unclear. Extracellular electrical stimuli with durations lasting on the order of 1 ms or shorter, such as those utilized by DRGS, are conventionally believed to induce

neural activity by transiently perturbing voltage-gated sodium channels to generate action potentials, counterintuitive to the idea of stimulation-induced suppression of excitability. Therefore, it is likely that DRGS-induced reductions in membrane excitability are due to voltage-sensitive intracellular secondary messenger cascades.[147]

2.4 Indirect effects of DRGS

Though the direct response to electrical stimulation is usually the generation of an AP in a target cell, the ultimate goal of neuromodulation therapies is to cause the release of neurotransmitters that modulate downstream neural activity which produces clinical benefit − so-called indirect effects of stimulation. Indirect effects are likely widely distributed throughout the neuraxis, particularly when stimulated tissue projects to many structures throughout the nervous system. Furthermore, the indirect effects of neuromodulation therapies may extend to non-neuronal targets, such as glial cells. Due to the novelty of DRGS, and the importance of first understanding which cells are directly affected by stimulation, there are as of yet few studies on the indirect effects DRGS. However, preliminary evidence suggests that DRGS may share indirect effects with conventional SCS, though continued study is vital to delineate the specific mechanisms unique to each therapy. Such knowledge may help improve patient selection and allow therapy assignment to be tuned to the pathophysiological differences across chronic pain etiologies.

2.4.1 Spinal/segmental effects

The goal of DRGS − to stimulate a particular DRG to provide dermatome-specific pain relief − places fundamental importance on the effects of stimulation at the particular spinal

segment receiving sensory information from a patient's painful region. A wide range of experimental techniques exist to objectively characterize the segmental effects of neurostimulation. For example, quantitative sensory testing (QST) and standard clinical electrophysiological assessments (e.g., electromyography) have proven useful in characterizing the mechanisms of action of SCS (for review, see [148]). Application of these techniques to patients receiving DRGS treatment could provide critical insight into the segmental effects of DRGS, and can be utilized in longitudinal studies to examine how the therapeutic effects of stimulation change over time, which are difficult to recapitulate using computational and preclinical models.

QST can assess a patient's sensory capacity and has been used to characterize SCS and DRGS patients' responses to both static stimuli (i.e., single transitory sensory stimuli) and dynamic stimuli (i.e., multiple stimuli). To date, there have been three studies using such experimental techniques to characterize the mechanisms of DRGS.[139,149,150] All three studies found that DRGS increased patients' pain thresholds in response to pressure stimuli localized to the patients' painful regions, though Kinfe and colleagues noted that the increase they observed was not statistically significant. A localized increase in pressure pain threshold suggests that DRGS modulates patients' perception of acute nociceptive pain, possibly through central mechanisms (e.g., segmental inhibition in the dorsal horn), or though peripheral mechanisms (e.g., suppression of nociceptive PSN activity), or both. DRGS may also affect patients' abilities to detect non-painful mechanical stimuli by modulating the activity of large-diameter Aβ-neurons. Kinfe and colleagues found that DRGS lowered detection thresholds in response to non-painful punctate stimuli,[150] while Chapman and colleagues found a similar, but non-statistically significant trend.[149] However, work from our laboratory found that in patients receiving DRGS or SCS treatment, vibration detection thresholds did not change during stimulation compared to pre-treatment values,[139] suggesting that continued

study is needed to determine the effect of DRGS on patients' perception of innocuous mechanical stimuli.

Furthermore, these early studies showed that DRGS reduces temporal summation (TS).[139,150] TS is a dynamic QST metric that is typically measured by taking the difference between a patient's reported pain intensity in response to a train of noxious stimuli and their reported pain intensity in response to a single noxious stimulus of equal magnitude. TS is a proxy to measure the "windup" phenomenon in humans. Wind-up is an increased firing rate of dorsal horn neurons in response to painful stimuli, believed to be mediated by activation of Nmethyl- D-aspartic acid (NMDA) receptors on wide dynamic range neurons in the dorsal horn.[151] Therefore, a reduction in TS by DRGS suggests stimulation provides pain relief in part by reducing the firing rate of pain-coding neurons in the central nervous system. It is reasonable to expect that DRGS may reduce TS by activating inhibitory circuits in the spinal cord dorsal horn, by causing nociceptive signals to be filtered out within the DRG, or a combination of the two. Interestingly, patients receiving SCS that demonstrate enhanced TS prior to implantation reported less overall pain after implantation.[152] If SCS and DRGS both provide pain relief in part by driving the activity of Aβ-neurons, preimplantation TS levels could similarly predict patients that will respond well to DRGS. Taken together, these preliminary studies indicate that DRGS may exert several concurrent effects on segmental pain processing, and demonstrate the utility of QST in studying the mechanisms of DRGS. Future work should include larger patient cohorts, examine the effects of pain etiology on changes in QST metrics, and determine if clinically quantifiable factors can be used as predictors for patient success with DRGS.

SCS has been shown to reduce the amplitude of some spinal cord reflex arcs, such as the H-reflex,[153] a mono-synaptic reflex mediated by large-diameter muscle afferents, and the

nociceptive flexor withdrawal reflex (also known as the RIII-reflex),[153–155] a poly-synaptic reflex mediated by small-diameter nociceptors. Similar to TS, the nociceptive flexor withdrawal reflex is a proxy for assessing spinal excitability in humans. From these results, it is generally interpreted that SCS increases the inhibitory tone of the spinal cord, thereby decreasing the amplitude of the nociceptive reflex arc, and may reduce the amplitude of the H-reflex by causing AP collision in muscle afferents. Interestingly, the magnitude of attenuation of the nociceptive flexor withdrawal reflex correlates with SCS-induced pain relief, suggesting that the success of the therapy is at least partially attributable to facilitating segmental inhibition. We hypothesize one would see similar results using these measures to study DRGS, as computational and preclinical studies demonstrate that DRGS also generates APs in large-diameter afferents.[118,119,121] However, it may be possible that DRGS exerts a larger attenuating effect on the nociceptive flexor withdrawal reflex, through the combined mechanisms of increasing inhibitory tone in the spinal cord, and reducing the net small-diameter input entering the spinal cord via T-junction filtering.

2.4.2 Supraspinal effects of DRGS

The original gate control theory of pain emphasized the importance of 'central control' – descending efferent fibers which modulate the gate control system − to the experience of pain, and stimulation-induced neural activity likely modulates brain regions involved in descending control. For example, SCS-induced activation of Aβ-axons in the dorsal columns activates neurons in brainstem regions, such as the rostroventral medulla and locus coeruleus,[79,156] which in turn drive descending inhibition via serotonergic and noradrenergic efferents.[157,158] As DRGS likely also drives the activation of Aβ-neurons,[118,119,121] it may modulate similar supraspinal regions to SCS. However, as experimental data also suggest DRGS may directly affect the activity of small-

diameter PSNs,[121] there may be considerable differences in the brain regions engaged by SCS and DRGS.

In the first study of the supraspinal regions involved in DRGS, Pawela and colleagues performed functional magnetic resonance imaging (fMRI) in a rat model of DRGS to examine the effect of DRGS on the blood oxygen- level dependent (BOLD) signal evoked by noxious electrical stimulation of the hindpaw.[159] They found that DRGS reduced the magnitude of the BOLD response in regions associated with the sensory-discriminative component of pain, such as the somatosensory cortices and the ventral posterolateral and ventral posteromedial nuclei of the thalamus, similar to findings from studies performing fMRI during SCS.[160–162] Interestingly, they also found that DRGS reduced the magnitude of the BOLD response in the nucleus accumbens − a limbic structure that may play a role in the motivational aspect of chronic pain − which was recently implicated as a potential supraspinal target of SCS in a rat fMRI study.[163] These results suggest that DRGS may provide pain relief through similar mechanisms to tonic SCS, though additional supraspinal mechanisms may also be at work. Continued study of the supraspinal mechanisms of DRGS will be critical, particularly studies performed in humans, as anesthesia used in non-human functional imaging studies adds additional confounds to interpreting results.

Parker and colleagues recently used magnetoencephalography (MEG) to study the effect of DRGS-induced pain relief on cognitive performance.[164] They found that patients receiving pain relief from DRGS displayed a reduction in gamma-band (30-45 Hz) activity in the somatosensory and anterior cingulate cortices (ACC) − brain structures that have been shown to be implicated in the pain-relieving effects of conventional tonic SCS and burst SCS, respectively.[165] It is hypothesized that burst SCS − a type of SCS that applies stimulation in high-frequency bursts − provides pain relief in part by modulating the medial spinothalamic pain pathway. This pathway

flows from C-neurons in the DRG which project to lamina i of the dorsal horn,[109] to several brain regions including the ACC, and is associated with the affective and attentional components of pain. Therefore, Parker and colleagues' observation that DRGS-induced pain relief is accompanied by modulation of the ACC adds additional evidence that DRGS may directly act upon C-neurons, as suggested by previous computational and animal studies.[76,121] Interestingly, Parker and colleagues found a reduction in gamma-band activity in the ACC, while De Ridder and colleagues found an increase in alpha-band activity (8-10 Hz) in the ACC,[166] but neither study considered the effects of stimulation across the full power spectrum of neural activity. More work is needed to understand how different patterns of peripheral input affect the activity of different functional brain networks. This understanding could lead to the design of DRGS stimulation patterns that directly target different components of the pain matrix (i.e., sensory, affective, cognitive), allowing for the personalized design of a patient's stimulation parameters based on their individual needs.

Studying the effect of DRGS on somatosensory evoked potentials (SSEPs) may also give insight into the supraspinal effects of the therapy, and SSEPs have been used for several decades to characterize the effects of SCS. SSEPs consist of positive and negative voltage deflections as a sensory-stimulus travels through the nervous system. SSEPs are often obtained by recording electroencephalogram signals from the scalp in response to an external stimulus (e.g., percutaneous nerve stimulation), and can provide insight into how a therapy affects sensory processing. Generally, SCS-induced activation of Aβ-axons in the dorsal columns decreases the amplitude of SSEPs,[167–170] and as DRGS likely acts in part through similar mechanisms, we may expect similar findings. A recent study of the effect of DRGS on laser evoked potentials (LEPs) − an SSEP measured in response to noxious laser stimulation of the skin − showed that DRGS increases the N2-P2 amplitude of LEPs, and that larger N2-P2 amplitudes may be correlated with lower pain

ratings.[171] Given that LEPs are designed to only study the cortical response to noxious stimulation, and that there are possible coincident effects of DRGS on small-diameter afferents which may produce different effects on SSEPs, continued investigation into the cortical effects of DRGS is necessary. A multi-modal approach to studying the supraspinal effects of DRGS will be necessary not only to understand the mechanisms of action of the therapy, but to also understand its effects on patients across pain etiologies and comorbidities.

2.4.3 Effects on glia

Historically, the non-neuronal effects of neurostimulation technologies have largely been ignored, except in the context of the foreign body response to implanted materials.[172] An area of basic research that remains underexplored is the effect of DRGS on satellite glial cells (SGCs), the glial cells present in the DRG.[173] SGCs are known to be important in the development and maintenance of chronic pain.[174] Though they do not generate APs, SGCs possess voltage-sensitive ion channels, and communicate directly with neurons in the DRG,[175] suggesting that they may be directly influenced by the DRGS-generated electric fields, or indirectly by DRGS-induced activity in PSNs. Though the effects of stimulation on glial cells have not yet been studied in the context of DRGS, early studies in SCS suggest it is an avenue well worth exploring.

SCS is most commonly applied to the lower thoracic spinal cord, where there are approximately 20 glial cells for every neuron.[176] A high density of glial cells around common SCS targets indicates that SCS-generated electric fields could modulate glial activity, depending on the electrophysiological characteristics of glial cells and how those characteristics are affected by SCS stimulus waveforms.[177] Differential targeted multiplexed programming-SCS (DTMP-SCS) was developed to concurrently drive neuronal and glial mechanisms of pain relief, by concurrently delivering a low-frequency SCS waveform (~50 Hz) and a high-frequency SCS waveform (~1200

Hz). Vallejo and colleagues demonstrated that in rats with spared nerve injuries, DTMP-SCS provided a greater reversal in chronic pain behavioral metrics, such as mechanical and thermal hypersensitivity, relative to low-frequency or high-frequency SCS alone.[35] Furthermore, spared nerve injury affected the expression levels of many glia-related genes, and DTMP-SCS drove the expression level of many of those genes back towards naïve levels. These results suggest that simultaneously modulating the neuronal and glial components of pain may lead to greater pain relief than modulating the neuronal component alone.

It is currently unclear how DRGS modulates the SGC component of pain. However, SGCs being the singular glial cell type in the DRG may make DRGS an ideal use case to study the differential effects of neurostimulation on neurons versus glia, and how communication between neurons and glia are modulated by extracellular stimulation. It is worth investigating the extent to which current clinical DRGS stimulation waveforms affect SGC physiology, and if further innovation is necessary to modulate the SGC component of pain (e.g., by multiplexing DRGS, similar to DTMP-SCS). Finally, in addition to the importance of glia in stimulation-induced pain relief, these studies also highlight the nascent but important study of omics, both to understand the mechanisms of neurostimulation therapies and as potential biomarkers of various chronic pain states.[178,179]

2.5 Looking forward

Several decades after helping construct the gate control theory of pain, Melzack synthesized a wide body of work across the medical and biological sciences into a new theory, the so-called neuromatrix theory. The neuromatrix theory places greater emphasis on not only the sensory component of pain, but also on the role of cognitive and affective components.[6] Much as

the foundation of this new theory drew from evidence across several disciplines, so too should our approach towards elucidating the mechanisms of action of neurostimulation therapies to manage pain. We believe that it is unlikely that these therapies provide pain relief through a single mechanism, and that a holistic understanding of electrical stimulation-induced pain relief is vital towards successful and consistent implementation of these therapies. Therefore, much work remains to be done through the combined efforts of basic neuroscience, engineering, and clinical pain research.

Presently, there is considerable disagreement between the conceptual understanding of neurostimulation biophysics and the available experimental data of DRGS mechanisms. One of the most striking results of the work of Chao and colleagues is that the ratio of C-neuron to Aβ-neuron activation threshold was dramatically lower than the corresponding ratios when stimulating the sciatic and saphenous nerves.[121] This result contrasts greatly with modeling studies comparing Aβ- and C-neuron activation thresholds.[118,119] These conflicting results suggest several potential explanations that warrant further study. Firstly, the recent discovery of GABAergic communication within the DRG, suggests possible synaptic action within the DRG itself.[123] Because GABA depolarizes C-neurons due to the atypical higher concentration of chloride within C-neurons than the extracellular space,[180] it is possible that DRGS drives GABA release from Aβ-neurons, which then depolarizes C-neurons to induce T-junction filtering as described above. However, it is unclear if GABAergic activation alone is sufficient to induce filtering. Secondly, there could be one or more features of the soma and stem axon complex of C-neurons that are missing from existing computer models that significantly reduce the activation thresholds of these neurons.

For example, much of our intuition of extracellular stimulation-induced neural activation comes from modeling studies of the peripheral nerve, characterized by long, straight axons.[57,58,181] In reality, DRG neurons have complex, winding stem axon trajectories[131,182–184] that haven't been accounted for in previous models. These trajectories could produce complex spatiotemporal profiles of depolarization and hyperpolarization in response to DRGS, making prediction of neural activation difficult. In simplified models of retinal ganglion cells, the presence of a 90-degree bend in an axon was sufficient to produce complex spatial distributions of activation thresholds,[185] suggesting that more complex trajectories may require a new conceptual framework to predict neural activation. Furthermore, the effects of ephaptic coupling (i.e., transmembrane currents contributing to the extracellular potential at other parts of the cell) are typically ignored, but could be on the order of several millivolts.[186] Because DRG neurons have tightly coiled stem axons closely apposed to large cell bodies (which would produce large transmembrane currents), intra- and inter-cellular ephaptic effects in the DRG could be significant. Future modeling work should aim to develop new intuitions of neural activation when stimulating cells with complex morphologies and axon trajectories, and use these novel intuitions to assist in interpreting experimental data of DRGS. Such intuitions will be critical to understanding not only the mechanisms of DRGS, but the mechanisms of other clinical neuromodulation therapies, including SCS.

In addition to complex stem axon trajectories, DRG neurons have active ion channels in their somata. Typically, APs are thought to be rarely generated in the soma,[51] but the presence of active ion channels in DRG somata, and the computer modeling predictions that some APs may initiate in the somata of DRG neurons,[76,118] suggest that this intuition may not apply to DRGS. There is a myriad of sodium[187] and potassium[188] channel isoforms important to physiological and

pathological pain processing, many of which are expressed in DRG. In a recent study from our lab, we implemented two models of Aδ-neurons that were morphologically and electrically identical, except for the voltage-gated sodium channels that they expressed.[119] Aδ-neurons that expressed $Na_v1.6$ had lower activation thresholds than Aδ-neurons that expressed $Na_v1.7$ and $Na_v1.8$, suggesting that in addition to morphological properties, the electrophysiological properties of a given neuron are crucial in determining its response to extracellular stimulation. Future experimental data summarizing the types, densities, and spatial distributions of ion channels in DRG neurons will be critical to developing accurate computer models with which to study the mechanisms of DRGS.

In addition to accurately representing the electrophysiological characteristics of the neural systems under study, computational and experimental studies of neuromodulation therapies must utilize electric fields that are representative of the fields generated during clinical implementation of the therapies. Patient-specific modeling is a powerful technique in understanding and developing neurostimulation therapies, and for ensuring computer models mimic clinical implementation of the therapy.[189] This approach has already proven useful in investigating the mechanisms of SCS for pain.[73] Patient-specific DRGS models could provide evidence for why DRGS fails in some patients but not others, or serve as the basis for a clinical decision-support system to accelerate the time-consuming process of titrating an individual patient's stimulation parameters.

There is good agreement between experimental[121] and clinical[77] studies of preferred DRGS parameters, particularly that the preferred stimulation frequency is 20 Hz in both human patients and rats. The work of Gemes and colleagues showed that when stimulating *ex vivo* rat DRG, Aδ- and C-neurons typically produced the largest calcium transients in response to frequencies between

3-7 Hz, while Aβ-neurons produced the largest calcium transients in response to 20-50 Hz stimulation.[120] Furthermore, the calcium transients in putative nociceptors (i.e., Aδ- and C-neurons) had larger amplitudes and slower decay time constants than the Aβ-neurons. These results may suggest different calcium-dependent mechanisms of stimulation on different functional groups of DRG neurons. Augmented T-junction filtering of nociceptive signals is believed to be achieved through triggering of calcium-activated slow hyperpolarizing currents, which may suggest that larger amplitude, slowly decaying levels of internal calcium may be more conducive to sustained filtering in nociceptors (**Figure 2.3**). It is also possible that the release of GABA within the DRG from Aβ-neuron somata (**Figure 2.2**) requires comparatively smaller increases in intracellular calcium and benefits from faster decay times to allow somatic neurotransmitter resources to quickly reprime for the next release event. Could 20 Hz DRGS then be a 'happy medium' between the optimal frequencies to produce the necessary diversity of somatic calcium transients in both nociceptive and non-nociceptive DRG neurons? Such a finding would further suggest DRGS provides pain relief by directly activating multiple types of PSNs.

In the more than five decades since Melzack and Wall proposed the gate control theory, a superb amount of effort has gone in to elucidating the specific neural circuits which govern pain processing and transmission in the dorsal horn (for review, see [109,190,191]). Much of the currently available data on DRGS mechanisms give evidence for the direct effects of stimulation, but it remains an open question as to how DRGS-induced peripheral input is integrated by neural networks in the central nervous system. With the advent of preclinical techniques to dissect neural circuits, such as optogenetics, calcium imaging in awake behaving animals, and transsynaptic tracing, it is now possible to elucidate the network dynamics that lead to chronic pain phenotypes. Applying these techniques to preclinical studies of DRGS could provide mechanistic knowledge

into the systems-level effects of stimulation, and inform the design of novel DRGS technologies to specifically target these mechanisms.

To fully elucidate the mechanisms of DRGS, we must also understand how DRGS affects an individual patient's pain experience (e.g., time course of pain relief, pain diagnosis, sensory profile). There is a dearth of clinical data on the temporal features of DRGS-induced analgesia, such as how long it takes for analgesia to onset (i.e., wash-in time) and offset (i.e., wash-out time). Preliminary clinical studies suggest that wash-in and wash-out times for DRGS are on the order of minutes,[121] with DRGS possibly having faster wash-out times than SCS.[192] Studying these phenomena in humans and comparing these temporal characteristics with clinical outcomes could provide insight into whether the analgesic effects of DRGS predominantly rely on faster mechanisms (e.g., transient induction or interruption of neural firing patterns), or slower mechanisms (e.g., inducing changes in synaptic plasticity).

Finally, using a mechanistic understanding of DRGS to design prospective clinical studies examining DRGS outcomes in patients with specific pain etiologies will be critical to determine which patient populations are best managed with DRGS. Determining if there are clinically measurable sensory features (e.g., mechanical allodynia, cold hypersensitivity) that correlate with DRGS-induced pain relief (e.g., through clinical studies performing QST), could not only provide further insights into the mechanisms of action of DRGS, but also improve patient selection. Furthermore, functional neuroimaging (e.g., fMRI, MEG) and clinical electrophysiology (e.g., electroencephalography) studies will be critical to investigating how DRGS modulates brain regions associated not just with the sensory component of pain, but also with the affective and cognitive components of pain. As DRGS has been shown to provide greater improvement in depression- and mood-related metrics than tonic SCS,[90] improving our understanding of how

DRGS modulates the non-sensory components of the pain neuromatrix may further assist in patient stratification between neurostimulation therapies. Continued study of the clinical manifestations of the effect of DRGS on the nervous system will be crucial to bridging the gap between our mechanistic understanding of DRGS-induced analgesia and improvements in patients' quality of life.

2.6 Conclusion

Dorsal root ganglion stimulation is an important tool in a pain physician's toolbox for managing intractable chronic pain. It is unlikely that any neuromodulation therapy acts through a single mechanism alone, and the growing body of evidence suggests that DRGS is no exception. Current evidence suggests that DRGS may provide pain relief by post-synaptic activation of pain-gating circuitry in the dorsal horn and possibly the DRG itself, by augmenting the lowpass filtering of painful signals at the T-junction of nociceptive neurons, and by reducing the intrinsic excitability of DRG neurons. Continued study of the mechanisms of action of DRGS, particularly into the supraspinal effects of DRGS, as well as the role of cognitive and affective networks in the patient response to DRGS, is warranted. DRGS is an excellent use case to develop new intuitions on the morphological and electrophysiological factors contributing to neural activation, which will be invaluable in innovating current, and developing novel, neurostimulation therapies for neurological disorders. Such innovation will be crucial to reduce the world-wide impact of chronic pain.

Chapter 3 – Spatial Models of Cell Distribution in Human Lumbar Dorsal Root Ganglia

The work presented in this chapter was in collaboration with Nicholas Peck-Dimit, and Drs. Zachariah J. Sperry and Tim M. Bruns. This work is published as:

Sperry ZJ*, **Graham RD***, Peck-Dimit N, Lempka SF^, Bruns TM^. Spatial models of cell distribution in human lumbar dorsal root ganglia. *Journal of Comparative Neurology*. 2020;528:1644-1659. **(*co-first author**; ^co-senior author).[45]

3.1 Abstract

Dorsal root ganglia (DRG), which contain the somata of primary sensory neurons, have increasingly been considered as novel targets for clinical neural interfaces, both for neuroprosthetic and pain applications. Effective use of either neural recording or stimulation technologies requires an appropriate spatial position relative to the target neural element, whether axon or cell body. However, the internal three-dimensional spatial organization of human DRG neural fibers and somata has not been quantitatively described. In this study, we analyzed 202 cross-sectional images across the length of 31 human L4 and L5 DRG from 10 donors. We used a custom semiautomated graphical user interface to identify the locations of neural elements in the images and normalize the output to a consistent spatial reference for direct comparison by spinal level. By applying a recursive partitioning algorithm, we found that the highest density of cell bodies at both spinal levels could be found in the inner 85% of DRG length, the outer-most 25–30% radially, and the dorsal-most 69–76%. While axonal density was fairly homogeneous across the DRG length, there was a distinct low density region in the outer 7–11% radially. These findings are consistent with previous qualitative reports of neural distribution in DRG. The quantitative measurements we

provide will enable improved targeting of future neural interface technologies and DRG-focused pharmaceutical therapies, and provide a rigorous anatomical description of the bridge between the central and peripheral nervous systems.

3.2 Introduction

Dorsal root ganglia (DRG) are regions of the posterior spinal roots, which contain the cell bodies of all primary sensory neurons innervating a specific dermatome of the body or end organ.[97] Recently, DRG have been increasingly investigated as sources from which to record control signals for neuroprosthetic devices, for applications ranging from treating bladder dysfunction to providing limb prosthetic control and sensory feedback.[193–197] While most studies have used penetrating electrode arrays to record from neurons in the interior of the DRG, recent work has demonstrated that afferent signals can be recorded from neurons near the exterior of DRG using surface recording arrays[198,199] and that microelectrodes can be used for low-current microstimulation of DRG neurons.[125–127] Additionally, dorsal root ganglion stimulation (DRGS) is an emerging therapy for chronic neuropathic pain,[90] providing a nonaddictive alternative to opioids for pain management. Although these technologies have the potential to provide dramatic improvements in quality of life for a diverse range of patients, preliminary clinical studies have demonstrated limited success thus far. Commonly reported issues include inconsistencies in the quality of elicited sensations, and variable amounts of pain relief across patients.[114] These technologies rely on either the accurate recording or delivery of electric currents to specific types of DRG neurons (e.g., recording from bladder afferents, stimulating sensory inputs to reflex circuits). However, we have a limited understanding of the three-dimensional (3D) spatial distribution of primary afferents throughout human DRG. Describing the 3D cellular anatomy of

DRG could inform the clinical implementation of these technologies (e.g., DRGS electrode placement relative to the ganglion, selection of penetrating or surface recording arrays to target different cells), which may lead to improved and more consistent clinical outcomes.

DRG contains both the cell bodies and portions of the axons of primary sensory afferents. Neural recording technologies detect neural activity through the voltages generated by the transmembrane currents generated by neural signal propagation.[200] The largest transmembrane currents, which would contribute to the bulk of the recorded signal, are thought to originate from the cell body and axon initial segment of recordable cells.[201] In contrast, extracellular stimulation technologies are thought to primarily induce neural activation in axons[51], with modeling studies suggesting that DRGS electrodes primarily activate the axons of large myelinated tactile afferents.[118] Although the specific roles of subgroups of primary afferents are complex, DRG cells can be roughly broken into functional groups based on the cell body and axon size.[183] C-fibers are small unmyelinated cells that typically conduct thermal or noxious sensation.[202,203] Myelinated A-fibers, which are typically mechanoreceptive or proprioceptive, are larger than C-fibers and typically have thinly- to thickly myelinated axons. A-fibers can be further stratified into Aα-, Aβ-, and Aδ-fiber classes, which are listed in order of descending conduction velocity and fiber size.[204] Although this classification scheme is commonly used throughout the literature, there is a dearth of studies examining the spatial distribution of these fibers throughout the DRG.

The effectiveness of both recording and stimulating neural interface technologies relies heavily on the spatial relationship between the interface electrode and particular neuron types of interest. However, few studies have examined the spatial organization of neurons in DRG, and to our knowledge, no studies exist in human literature. Various studies have discussed a weak functional somatotopy for the DRG in animal studies based on nerve tracing, with rostral-caudal,

medial-lateral, and ventral-dorsal divisions all present to a certain degree.[142,205–210] Few studies have examined the distribution of neural structures (e.g., cell bodies, axons) in DRG. Only a few anecdotal references exist, including studies showing superficial cell bodies or a "central fiber stream" in the DRG,[211,212] and a neural recording study in feline DRG reported the largest density of cell bodies at a depth between 0 and 100 μm.[213] There is a general consensus that most cell bodies are found around the circumferential edge of the ganglion. That idea was supported by our previous study, in which a quantitative analysis of feline lumbosacral DRG showed that the highest density of cell bodies in medial sections could be found in the outer 24% radially and on the dorsal-most side of the ganglion.[83] However, in this previous study, we only examined neuronal distribution in medial sections of the DRG, while clinical neurotechnologies would likely act upon neurons distributed along the entire DRG.

In this work, we sectioned human lumbar DRG specimens at 1 mm increments along the nerve root axis. We stained these sections with neurofilament and imaged the sections for high-contrast identification of neural cell bodies and axons. We developed software to automatically segment and characterize the spatial location and size of neural elements. Finally, we used a recursive partitioning algorithm to model the 3D spatial densities of the neural elements. We also analyzed high-level donor demographic and anatomical trends in our data set. These analyses provide key insights for future neural interface technologies and therapies with human DRG.

3.3 Methods

3.3.1 Gross tissue processing

This study utilized human tissue donated by de-identified deceased individuals, and was, therefore, determined to be "Not Regulated" by the University of Michigan Institutional Review

Board [HUM00109152]. We received bilateral human lumbar spinal roots (RRID:SCR_005043) from the L4 and/or L5 spinal levels from the National Disease Research Interchange (NDRI, Philadelphia, PA) from the deceased donors within 72 hr of aortic cross-clamp. We chose to study L4 and L5 DRG because these DRG are common DRGS targets for managing chronic pain in the feet and lower legs.[77] We excluded donors that had a history of diabetes, cancer, herpes zoster, a peripheral nerve condition, spinal cord injury, previous spine surgery, or opiate abuse. NDRI stored the tissue in 10% neutral-buffered formalin and shipped it at ambient temperature. Upon receipt, we used calipers to measure the DRG portion of each root at 1 mm increments to determine the gross tissue dimensions. We then used a razor blade to cut the DRG in half and removed two 1 cm segments constituting the approximate proximal (i.e., nearest the spinal cord) and distal (i.e., nearest the peripheral nerve) DRG halves (**Figure 3.1**). We placed the cut sides of each DRG half face-down in a histology cassette to preserve DRG orientation across slides. If visual inspection indicated that the remaining tissue contained gray matter, we removed additional segments to obtain samples of the entire DRG region. We stored the cassettes in 70% ethanol to halt fixation, and shipped them to an external histopathology lab (Histowiz Inc., Brooklyn, NY) for histological processing.

3.3.2 Histological processing and imaging

The histopathology lab embedded the tissue samples in paraffin (Leica EG 1150 H&C) and cut 4–5 μm thick sections at 1 mm steps (~20 sections per DRG) (Leica RM2235 microtome). They mounted the sections on slides and stained with a 1:3000 dilution of rabbit monoclonal antibody for neurofilament heavy polypeptide (NF200, ab40796, Abcam, Cambridge, UK, RRID:AB_2149620) which stains both A- and C-type fibers in humans.[214,215] They also counterstained for hematoxylin to identify nuclei. They imaged the slides at 40 with a brightfield

slide scanner, with a resolution of four pixels per micron (Leica Aperio AT2). The resulting images had neural cell bodies and axons visible in dark brown and cell nuclei visible in blue (**Figure 3.1c**). The nuclei of other DRG cellular types were also visible, including satellite cells and some endothelial vascular cells. The neural cellular elements were typically arranged into at least two fascicular regions. We considered the regions containing cell bodies (or continuous with cell-body containing regions across images) as DRG. We considered all other regions as the ventral root (VR). To the extent analyzed, the VR was considered separately from the DRG. We screened images for quality issues, including excessive tearing or folding, and poor quality regions were excluded from analysis.

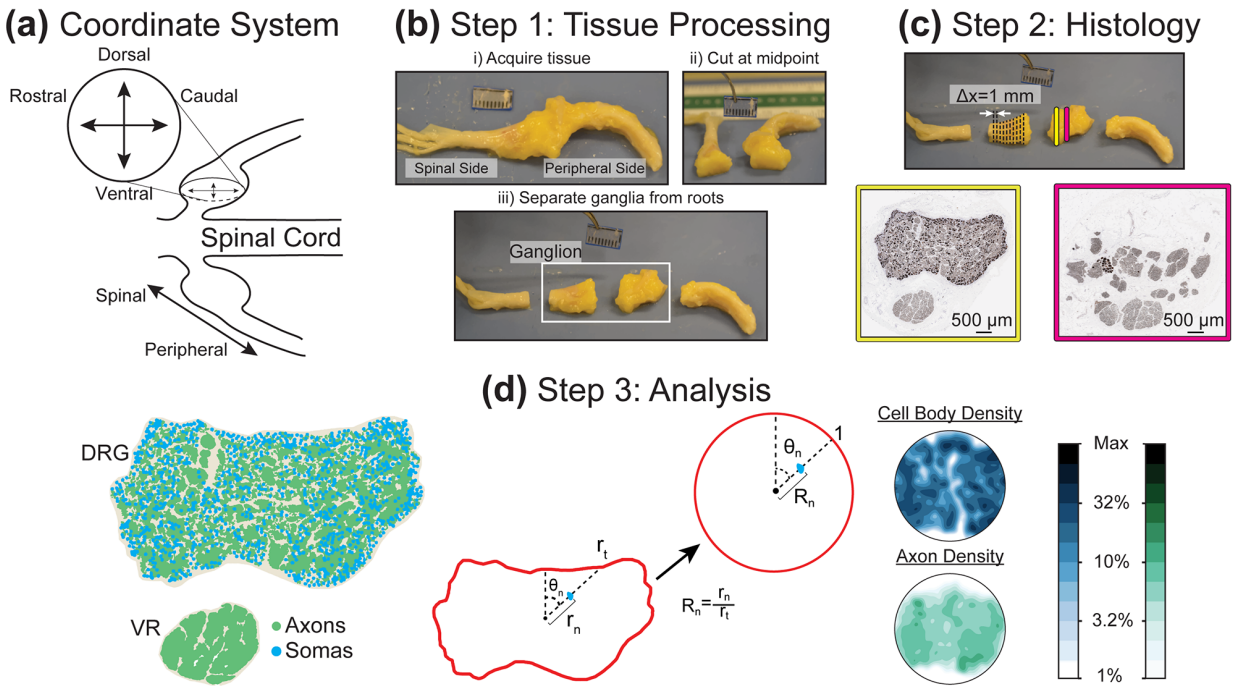

Figure 3.1 Tissue processing and image analysis methods. (a) Illustration of coordinate system for DRG cross-section images. (b) Initial tissue processing. (c) Representation of sample locations and NF200-stained samples (dark brown). We counterstained each sample with hematoxylin, resulting in blue cell nuclei (not visible at displayed image size). (d) Analysis of histological data. (left) DRG cross section after automated processing, with identified axon and soma locations highlighted. (center) Diagram of polar normalization, demonstrating transformation from perimeter and internal features to unit circle. (right) Contour plots generated from polar normalization of DRG, with logarithmic color scale at right.

3.3.3 Image processing software

Lumbar DRG contain ~35,000 neurons.[216] Therefore, to identify each neural element we developed a custom semi-automated graphical user interface (GUI) using MATLAB and its Image Processing Toolbox (MathWorks Inc., Natick, MA, RRID: SCR_001622). After loading the image, the GUI allows the user to identify the DRG, VR, and nonneural outer tissue and then calculates an optimal rotation to align the DRG above the ventral root in the upper half of the image. The GUI white-balances the image and converts it to binary using a series of thresholding steps and morphological operations. We extracted the shapes and locations of all neural elements in the original image from the resulting binary image for analysis.

In order to validate the GUI results, we selected four validation images pseudo-randomly from the final image set, to balance for inclusion from different donors, spinal levels, and sidedness (i.e., right DRG or left DRG). We randomly selected a 1 mm square region containing both axons and cell bodies from each validation image. Following consultation from a neuropathologist, the first three authors each traced the neural cell elements in the validation sub-images using the ImageJ (RRID:SCR_003070, https://imagej.nih.gov/ij/) plug-in ObjectJ (https://sils.fnwi.uva.nl/bcb/objectj/index.html, Vischer, N. & Nastase, S. University of Amsterdam).

For automated processing, we first converted all validation images to grayscale, and white balanced each image against background luminescence for each color channel (red = R, green = G, and blue = B). These grayscale images were converted to binary (black and white) using a threshold determined to minimize the difference between the initially detected object number and the number of objects determined by each human validator. A threshold of 0.78 minimized the difference between the computer- and human-identified objects, therefore we used a threshold of 0.78 for all black-white thresholding steps. We discovered that a simple threshold tended to split

large lightly-stained cell bodies into many smaller objects, but that intact cell bodies could be recovered by utilizing the ratio between R and B channels. Specifically, an R/B-B/R threshold of 0.5 consistently returned an image with intact cell bodies. This step was effective because the neurofilament stain tended to have a high R value and a low B value, while hematoxylin had a strong B value and weak R value. This RB ratio transformation was noisy outside of the cell bodies, so only objects with an area greater than 600 μm2 were retained (roughly corresponds to circular objects with diameter 14 μm). The logical disjunction of the RB ratio image and the original binary image (RB Ratio OR Binary), denoised with a morphological "open" and with holes filled, served as the final image for automated neural element identification with MATLAB's Image Processing (MathWorks, Natick, MA) toolbox.

To compare the automated system and human performance, we found the pixel overlap between the output images and calculated the precision and recall of the automated system, using the human segmented images as ground truth. Precision is the ratio between true positives and total positives (true positives + false positives), and is a measure of how often the program incorrectly labeled a pixel as belonging to a neuron. Recall is the ratio between true positives and ground truth positives (true positives + false negatives), and is a measure of how often the program missed a neuron pixel it should have labeled. Both ratios range from 0 to 1, with a higher value being a better score.[217,218]

The precision of the algorithm was 0.92 ± 0.04 and the recall was 0.81 ± 0.05. While this is short of perfection, these values are consistent with other well-performing cell segmentation programs.[217,219,220] In comparison, the inter-human precision was 0.84 ± 0.06 (significantly lower than the human vs. algorithm, Student's t test; $p = .0021$), and inter-human recall was 0.86 ± 0.07 (Student's t test; $p = .1075$). These values suggest that the algorithm is behaving overall like an

average human validator, and on the basis of precision and recall would likely be indistinguishable. The absolute difference in object count between human and algorithm was 5.43 ± 4.21% (nonabsolute difference: 1.45 ± 6.89%, not significantly different than zero [Student's t test; p = .4806]). The standard deviation of inter-human count for a given image as percentage of the mean was 5.43 ± 4.21%. Ultimately, the goal of the program was not to perfectly label all cells but to reduce the time to adequately label an image so that trends could be quantified. Each human annotation of a 1 mm2 image took ~6–10 hr depending on the number of objects, and there was considerable variation in duration between annotators. The same images took only ~1 min for the program. Considerable time savings, along with the positive performance metrics, suggests that the program was a significant improvement over manual image labeling.

Figure 3.2 shows a portion of a raw validation image between the automated and human segmentation for comparison. In the full version of this image, the program identified 5277/5359 objects identified by the average human, a difference of −1.53%. The precision in this image was 0.95 and recall was 0.80. A note on human versus automated performance is the tendency of human segmenters to label an object with a border larger than the actual object (oversegmentation). This explains the evident difference in some object sizes between the two images.

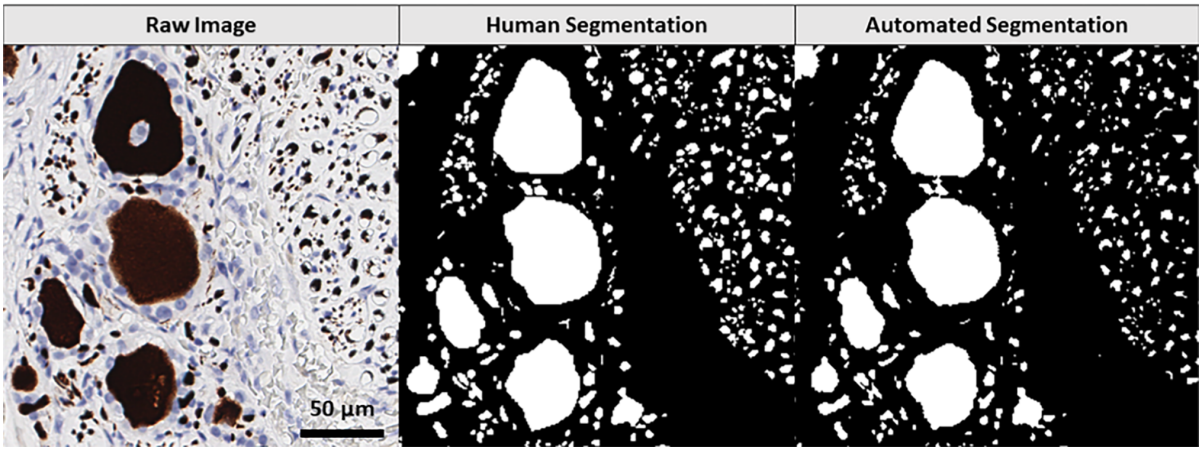

Figure 3.2 Comparing human and automated segmentation. Comparing (left) Raw portion of validation image. (center) Binarization of human segmented image. (right) Binarization of automatically segmented image.

3.3.4 DRG reconstruction

We reconstructed the 3D profiles of individual ganglia regions by converting manually-traced 2D profiles of DRG, VR, and compact outer tissue to .svg files in MATLAB, then stacking and interpolating (lofting) between the curves using the computer-aided design (CAD) program Audodesk Fusion 360 (Autodesk, San Rafael, CA), slightly adjusting image alignment as needed (**Figure 3.3**). We used these 3D reconstructions to analyze the mean geometric properties (e.g., aspect ratio, length, width) of root regions (e.g., dorsal root, ventral root).

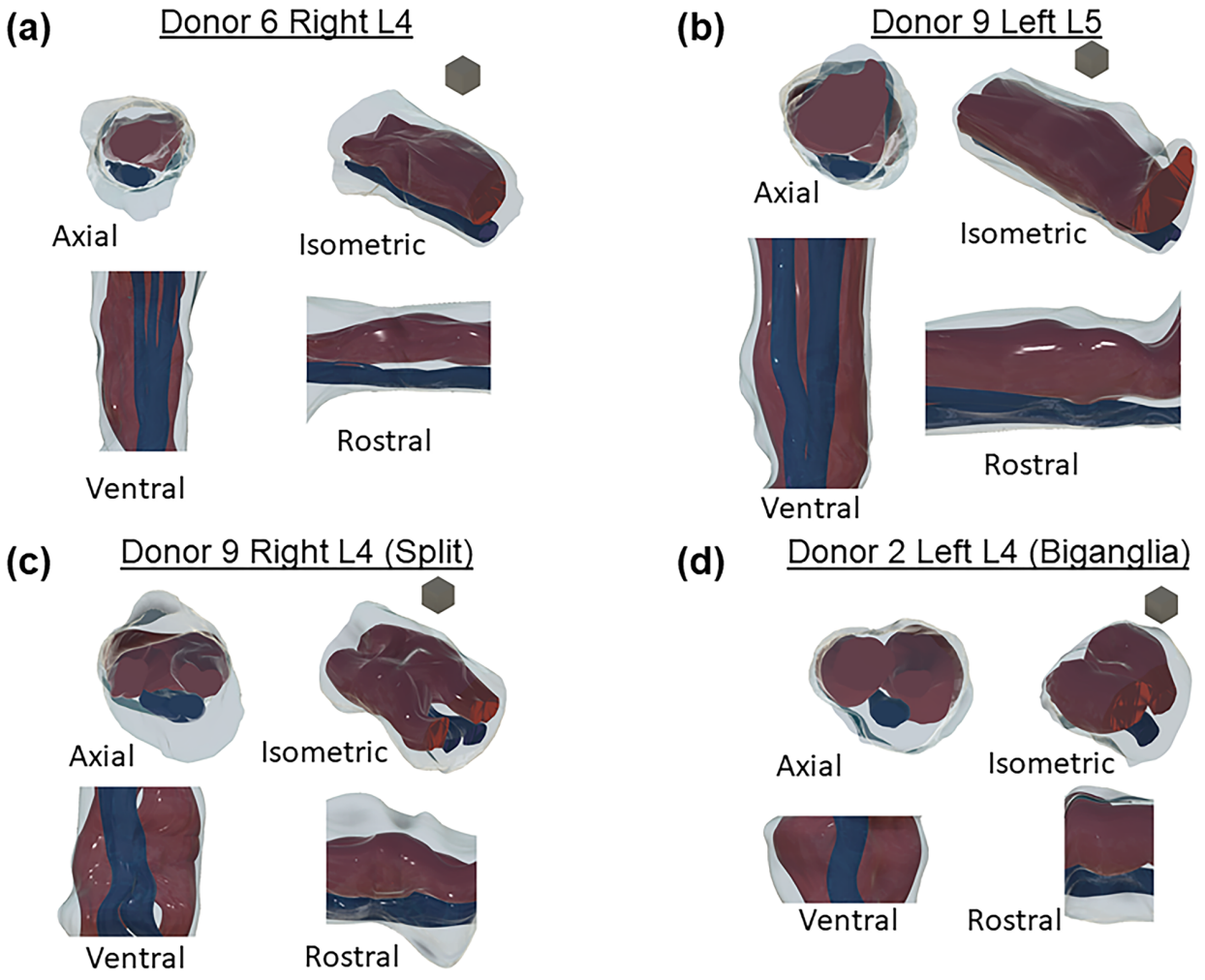

Figure 3.3 DRG reconstructions. Four views of reconstructed specimens. Dark red is dorsal root ganglion, blue is ventral root, gray is epineurial tissue. In each group views are (clockwise from top left): axial (face closest to spine [spinal face] visible), isometric (spinal face right), rostral (spinal face right), and ventral (spinal face down). Blocks shown for scale have 1 mm edges. (a) L4 monoganglia (b) L5 monoganglia (c) near biganglia (d) full biganglia.

3.3.5 Image analysis

Following parameter optimization and comparison of GUI results to human performance, we analyzed each image containing at least 10 visible soma[221] in the GUI to determine neural element size, shape, and location. We identified inplane axons as elements exceeding a geometric eccentricity of 0.9 (i.e., their shape dramatically deviated from circularity), and excluded them from population size analysis. We defined a mean diameter as the average of the major and minor axis. Based on values previously reported,[204] we used a mean diameter cutoff of 20 μm to distinguish larger axons from smaller cell bodies. We found that objects larger than 110 μm in diameter were typically detritus, and we removed them from the data set.

Note that for the purposes of this study, we will refer to the three spatial dimensions of the DRG as follows: the axial position refers to the location of an image along the nerve trajectory, and may be either spinal (close to the spinal cord) or peripheral (away from the spinal cord); cross-sections are oriented with the dorsal side up and the ventral side down; the axis perpendicular to both these axes, and horizontal in cross-sections, is the rostral-caudal axis (**Figure 3.1a**). We determined this final label by considering the in situ anatomy of lower lumbar nerve roots, which exit the spinal cord slightly more perpendicular than parallel,[222] and therefore to align the third axis with the rostral-caudal bodily axis. If the nerve roots were parallel to the spinal cord, it would be appropriate to refer to our rostral-caudal axis as lateral-medial, respectively. A previous computational modeling study of lower lumbar DRG also used this nomenclature, shown visually in the Coordinate System section of **Figure 3.1**.[118]

3.3.6 Cell density mapping

In order to quantify neural cell densities across DRG, we normalized the location of each identified cell body and axon within an image to polar coordinates using a method similar to our

prior work.[83] We set the centroid of the user-defined DRG region as the origin for determining the polar angle of neuron n (θ_n). We defined θ_n to equal 0 at the vertical (i.e., dorsal) normal vector calculated from the user-defined DRG region. We determined radial location (r_n) by calculating the ratio of the distance from the DRG centroid of neuron n and the distance from the DRG centroid to the DRG edge along θ_n. The end result is a circular map with the circumference representing the DRG edge and all neurons located inside the circle. In cases where we observed multiple ganglionic regions (i.e., multiple cell body-containing fascicles) in a single slice, we combined all regions into a single region using built-in MATLAB image processing functions. To combine all ganglionic regions into a single region, we first found the perimeter of each ganglionic region (MATLAB command: bwperim). Then, we calculated the outline of a shape which formed a boundary encompassing the entirety of each ganglionic region's perimeter (MATLAB command: boundary). Lastly, we converted the resulting boundary into a mask (MATLAB command: poly2mask), which represented the entire cell bodycontaining region of the slice.

We used the normalized circular maps described above to calculate cellular densities. First, we divided the circular map into concentric annular sectors of equal width and increasing radii. Next, we divided each annular sector into wedges of constant area, to create a circular grid of wedge sectors defined by a radius from the center of the circular map, and an angle from the vertical normal vector. To calculate cellular density of a wedge sector, we divided the number of cellular elements (i.e., somas or axons) in the wedge by the nonnormalized area of that wedge (i.e., the area of the original image represented by the wedge sector). A shortcoming of the method used previously was very high variance in calculated densities in sectors at the center of normalized DRG, the result of very small sectors produced by using wedges of constant angular size.[83] Holding wedge sector area constant, and varying the number of wedge sectors in each annulus overcame

that issue (i.e., annuli with smaller circumferences closer to the center of the circular map have fewer wedge sectors, but each wedge sector has the same area). Given that the largest expected cell bodies in human and other large mammal DRG have a diameter of about 100 μm,[183,223] we chose annulus width and sector area to accommodate approximately four large cell bodies packed in each sector. We chose this size after trial and error as a compromise between fine and coarse resolution for the final maps. **Figure 3.1d** shows a summary of image analysis steps.

To determine axial position of each image, we fit a 3rd-degree polynomial curve to the DRG fascicle areas considering the known distance between sequential images. We took the axial position corresponding to the maximum value of the fit curve as 0 μm (i.e., the middle of the DRG). We assigned a negative axial position value to images on the spinal side of the midpoint, and a positive value to images on the peripheral side. We did not assign an axial position to images from ganglia without a clear center (i.e., fascicle areas with no peak value). These images were included only in analyses that did not rely on axial position.

3.3.7 Donor demographic trend analysis

We performed all statistical analyses for this study using JMP Pro 14 statistical software (SAS Institute, Cary, NC, RRID:SCR_014242). We tested the effect of various donor demographic and anatomical characteristics on mean neuron count and density in each DRG. We evaluated the two-factor effects (sex [male/female], side [left/right], and spinal level [L4/L5]) with a Student's t test. For all tests, we set the significance threshold at $p = .01$. We evaluated the effect of donor size by calculating body mass index (BMI), sorting donors into "normal," "overweight," and "obese" categories (group divisions at 25 and 30), [224] then performing an analysis of variance (ANOVA) test for significance followed by a Tukey honest significant difference (HSD) test. We evaluated

the effect of donor age by fitting a line to the density (or count) versus donor age data and assessed the significance of the slope estimate (Student's t test, H_0: slope = 0).

3.3.8 Spatial density modeling

The goal of spatial density modeling is to provide a partitioned map of neural elements throughout a DRG. We used JMP to fit separate partition models for normalized densities by spinal level (L4 and L5), and neural element type (soma and axons) for a total of four models. We further stratified the axon models by size (large [≥5 μm diameter] and small [<5 μm diameter]). Partition models split a distribution of dependent variables (e.g., cell body density) into sub-populations of distribution based on the values of one or more independent variables (e.g., axial location). This splitting operation is performed recursively, and splits distributions at values of independent variables which maximizes model fit. The result of a partition model is a decision tree that maximally captures sub-populations of distributions within a dependent variable (e.g., identifying regions of large or small cell body density based on axial location in the DRG). We used 10-fold cross-validation of the model at each split to avoid overfitting. We terminated splitting at the stage when 10 additional splits failed to improve the model R^2 by at least 0.05. We additionally restricted the model to only produce groups containing more than 5% of data points, leading to a theoretical maximum of 20 groups in the model. As in Ostrowski et al. (2017) we used radial location and vertical angle as model inputs, defining vertical angle as the angle measured from the top (dorsal-most) point of the circle reflected across the dorsal-ventral midline of each image. For our partition models, we also added the axial position as model input. We assessed the output models by performing an ANOVA and Tukey HSD test on the measured densities in the identified spatial regions. Where relevant, results are presented as mean ± standard deviation.

3.4 Results

All DRG images, software, summary data, and CAD models referenced in this study are available online at the Open Science Framework.[225]

3.4.1 Donors and specimens

We collected a total of 34 DRG from 10 human donors. **Table 3.1** provides demographics for each donor. This included seven males and three females, of which seven were Caucasian, two Hispanic and one Black. Ages ranged from 25 to 59 years (47.2 ± 10.3 years). BMI ranged from 24 to 38 kg/m2 (30.1 ± 4.5 kg/m2). Based on typically reported ranges, two of the donor BMIs were considered "Normal," four were considered "Overweight," and four were considered "Obese." Seven of the donors died from natural causes (cardiovascular or stroke), and three died from external causes (trauma or asphyxiation).

We collected bilateral L5 DRG from all donors, and bilateral L4 DRG from all but three donors (D3, D5, and D8). In all but D10, the DRG were identifiable as either left or right upon receipt. Therefore, D10 was excluded from all left–right analyses, but was used when comparing features across levels (i.e., L4 vs. L5). All but one of the DRG had images suitable for inclusion in this study. Tissue slices in all images from Donor 1's Right L5 DRG were torn and therefore unusable. **Table 3.1** reports the DRG collected and used in this study.

The majority of DRG in our data set (28/33) could be defined as monoganglia, that is, at some point we observed an image containing a single compact DRG fascicle. All of these DRG split at either the spinal or peripheral side into multiple fascicles, and in some cases were split into two primary fascicles throughout most of the region of interest. The remaining five DRG were biganglia, that is, the minimum number of observed DRG fascicles was two. It is possible that these DRG had a merged region in between images not captured by our sectioning, but the

maximum length of this region would necessarily be less than 1 mm due to our sampling method. Of the biganglia, three were L4 DRG and two were L5 DRG. **Figure 3.3** shows four samples of donor specimens reconstructed from histological images (one each of monoganglia L4 and L5, a near biganglia, and a full biganglia).

The number of images used from each DRG ranged from 3 to 10 (6.1 ± 1.8; 202 total), varying due to anatomical differences and the quality of the final images. Considering both image quality and inclusion of only cell-body containing images, this represented ~25% of the overall images acquired. We imaged 17 complete DRG, identified based on a distinct continuous axial region with soma-containing images bounded by images with only axon-containing images. An additional seven DRG were considered "nearly complete," with the region of soma-containing images bounded on one side by axon-only images and on the other by highly fascicular images with few cell bodies. The remaining nine DRG were incomplete (i.e., the DRG image set did not include a non-soma-containing sample at the outer axial positions), but still had images useable for the study. Completeness and number of images used is also reported by DRG in **Table 3.1**.

3.4.2 Measurements and reconstructions

Within the complete DRG, there was a nonsignificant trend toward L5 being longer than L4 ($p = .0244$). L4 DRG had length 5.2 ± 1.9 mm while L5 DRG had length 7.1 ± 2.4 mm, measured as the length of the soma-containing region. Within the DRG containing a peak area, there was no apparent difference between L4 and L5 in maximum rostralcaudal width, and the overall width was 5.8 ± 1.0 mm. In these same DRG, there was a nonsignificant trend toward L5 having a larger maximum dorsal-ventral width than L4 ($p = 0.0228$). L5 had a maximum dorsal-ventral width of 4.5 ± 1.2 mm while L4 was 3.7 ± 0.8 mm.

Table 3.1 Detailed donor information.

Donor	Age (yr)	Sex	Wt. (kg)	Ht. (m)	BMI (kg/m^2)	Race	Cause of Death	DRG
D1	25	F	70	1.64	24.2	C	Cardiovascular	LL5(4), RL5(0)
D2	46	M	81	1.67	27.2	C	Arrhythmia	LL4(5), RL4(5-i), LL5(6), RL5(5-i)
D3	57	M	91	1.62	32.4	C	ICH/Stroke	LL4(6-i), RL4(5-i), LL5(5-i), RL5(5)
D4	49	M	112	1.69	36.5	H	Head Trauma	LL4(3-i), RL4(8), LL5(7), RL5(4-i)
D5	50	F	94	1.52	37.9	C	ICH/Stroke	LL5(6), RL5(6)
D6	54	M	97	1.76	29.0	C	ICH/Stroke	LL4(6), RL4(8), LL5(8), RL5(8)
D7	59	M	93	1.74	28.6	C	Head Trauma	LL4(5), RL4(5), LL5(3), RL5(7)
D8	46	M	88	1.81	24.9	C	Head Trauma	LL5(10), RL5(9)
D9	51	F	92	1.64	31.2	B	Cardiovascular	LL4(5), RL4(7), LL5(8), RL5(9)
D10	35	M	87	1.67	29.2	H	Asphyxiation	XL4(4-i), XL4(5), XL5(8-i), XL5(7)

F=female, M=male, C=Caucasian, H=Hispanic, B=Black. ICH=intracranial hemorrhage. All DRG collected are listed in the "DRG" column, first letter is side (L=left, R=right, X=not specified). Number of images included from each DRG is included in parentheses, with an "-I" indicating inclusion of an incomplete DRG (i.e., DRG image set did not include a non-soma-containing sample at the extreme axial positions).

Our polar model transforms the DRG fascicular area to a perfect circle of radius 1, but it is useful to understand the typical shape of our actual samples. We found that the actual mean aspect ratio of the DRG fascicular regions (as rostral-caudal width over dorsal-ventral width) was 1.52 0.47, significantly different than the unit aspect ratio of a perfect circle (Student's t test, $p < .0001$). When considering the number of DRG fascicles, we found that the mean aspect ratio of biganglia DRG fascicle cross sections (1.78 0.44) was significantly higher ($p = .0004$) than for monoganglia DRG (1.47 0.45). This feature of the DRG fascicle cross sections does not extend to the full tissue cross-section including VR, which had an aspect ratio of 1.04 0.21 which, while significantly greater than one (Student's t test, $p = .0077$), is an aspect ratio close to the aspect ratio

of a perfect circle. Our polar model does not rely on any assumptions of aspect ratio, but these geometric trends may be of interest for future models of DRG.

3.4.3 Neural counts and densities

We observed several trends in cell body and axon count related to spinal level. L5 DRG had significantly higher mean axon count in each image (33,643 ± 11,007) as compared to L4 (27,868 ± 10,846), with p = .0002. However, the mean density of axons did not differ significantly by spinal level, and the combined mean was $2.36 \times 10^{-3} \pm 8.50 \times 10^{-4}$ axons per μm^2. There was no significant difference in the number of cell bodies in each image by spinal level, though there was a slightly higher mean cell body density in L4 ($3.78 \times 10^{-5} \pm 1.98 \times 10^{-5}$ cells per μm^2) than in L5 ($3.24 \times 10^{-5} \pm 1.71 \times 10^{-5}$ cells per μm^2), with p = .0492. The combined mean number of cells per image was 469 ± 303. The apparent disparity between a difference in fiber count and a non-difference in by-image cell count appears to be the result of the additional length of L5 to contain the additional cell bodies. From this point, all figures and models will consider L4 and L5 separately.

Comparing the spinal and peripheral sides of each DRG (splitting at the center axial location), we observed that the peripheral side had significantly more axons than the spinal side at both spinal levels (difference at L4: 6,002 ± 5,917 axons, p = .0033; L5: 7,758 ± 6,398 axons, p = .0002). This trend was true of 24/29 individual DRG where axial location was determined. For large fibers, this represents a mean increase of 4,007 ± 4,118 fibers (or 62.16 ± 76.24%) from the spinal to peripheral side, and an increase of 2,964 ± 2,825 small fibers (15.4 ± 15.5%). This trend was not accompanied by a significant increase in per-image cell body count. However, when considering cell bodies by size, there was a significant increase in confirmed (nucleated) large cell bodies on the peripheral side versus the spinal side (9 ± 15 cells, or 51.5 ± 77.7%). The large cell

body trend was true of 21/29 DRG, although there was not enough data to determine if this trend was related to DRG level.

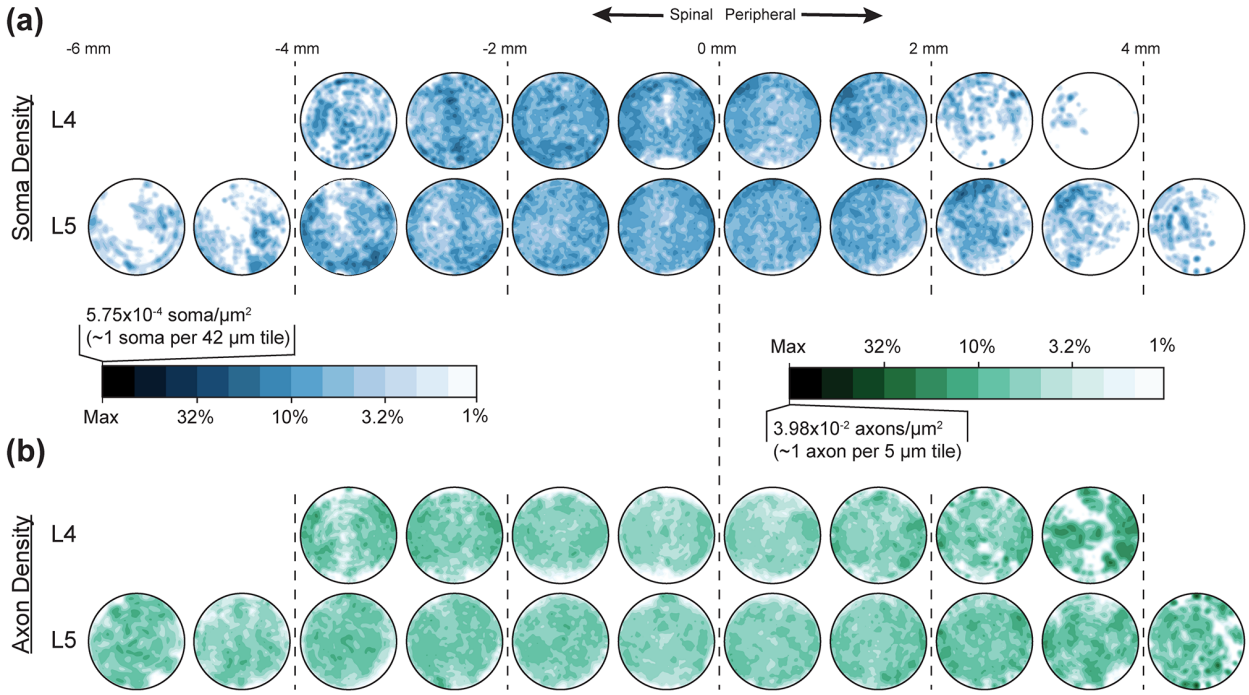

Figure 3.4 Spatial densities in L4 and L5 DRG. Polarized mean (a) cell body (blue) and (b) axon (green) spatial densities in each millimeter of L4 (upper) and L5 (lower) dorsal root ganglia fascicular region. Inset scale provides reference for color, which is on a logarithmic scale decreasing from maximum density to 1% of maximum (tile refers to square with given dimension per side).

It should be noted that large cell bodies represented only about 32.4 ± 18.0% of nucleated cell bodies, and that nucleated cells represented 27.3 ± 8.6% of all cell bodies identified in each image. Medium and small cells, respectively represented 43.7 ± 12.6% and 23.9 ± 11.3% of nucleated cells identified. The mean axon diameter was 4.37 ± 1.79 µm. The mean cell body diameter was 44.94 ± 15.13 µm. No axial trend was observed in either axon or cell body density (other than count) at any size. Possible reasons for these observations are enumerated in the Discussion section of this chapter.

The most significant trend related to patient demographics was that obese donors had a higher L5 DRG axon count (38,298 ± 8,783) than normal patients (30,934 ± 8,522; p = .0047).

Overweight donors overlapped both groups (33,113 ± 9,609). This trend was also observed in L4, although there were no normal BMI L4 donors (obese: 31,171 ± 10,383; overweight 26,499 ± 9,280; p = .0219). Obese donors had a higher cell body count in each L4 image than overweight donors (p = .0367), and higher than overweight and normal donors at L5 (p = .0073 and p = .0404, respectively). There was no significant cell body count or density trend related to BMI (i.e., the mean cell body counts and densities were not significantly different between donors categorized with different BMIs). Female donors had both higher mean L5 cell body count and cell body density than males in each image (p = .0179 and p = .0019, respectively).

Table 3.2 Summary of DRG density models by neural element and spinal level.

Neural Element	Spinal Level	R^2	Axial Proportion	Radial Proportion	Angular Proportion
Cell Bodies	L4	0.0659	0.57	0.21	0.22
	L5	0.0453	0.60	0.28	0.12
Axons	L4	0.1399	0.04	0.61	0.35
	L5	0.0942	0.14	0.81	0.05
Small Axons	L5	0.0835	0.17	0.76	0.07
Large Axons		0.1003	0.26	0.70	0.04

R^2 values indicate the amount of variance captured by the partition model for a neural element (i.e., cell bodies or axons) at a given spinal level. Proportion columns indicate the relative contribution of a given variable (e.g., axial position, radial distance from center) to the overall model on a scale from 0-1; proportions for a given model sum to 1.

Figure 3.4 shows the mean polarized densities of cell bodies and axons for each spinal level with axial position divisions at 1 mm intervals. While a full spatial description of VR axons is outside of the primary scope of this study, a few observations are relevant in comparison with the DRG. We counted 5,983 ± 1,474 axons in L4 VR, and 6,417 ± 1,564 axons in L5 VR, although the difference was not significant. There was no relationship between axon count and axial location

in the VR. In each image, the number of large axons in the VR was significantly fewer ($p < .0001$) than the number of small axons by 37.4 ± 35.8%, with no relationship to spinal level. The ratio of large-to-small axons was significantly higher ($p < .0001$) in VR as compared to the DRG, in which the same proportion was 42.4 ± 16.5% ($p < .0001$). This matched our qualitative observation that it was possible to visually discern a VR fascicle from a DRG fascicle based solely on the different axon population size.

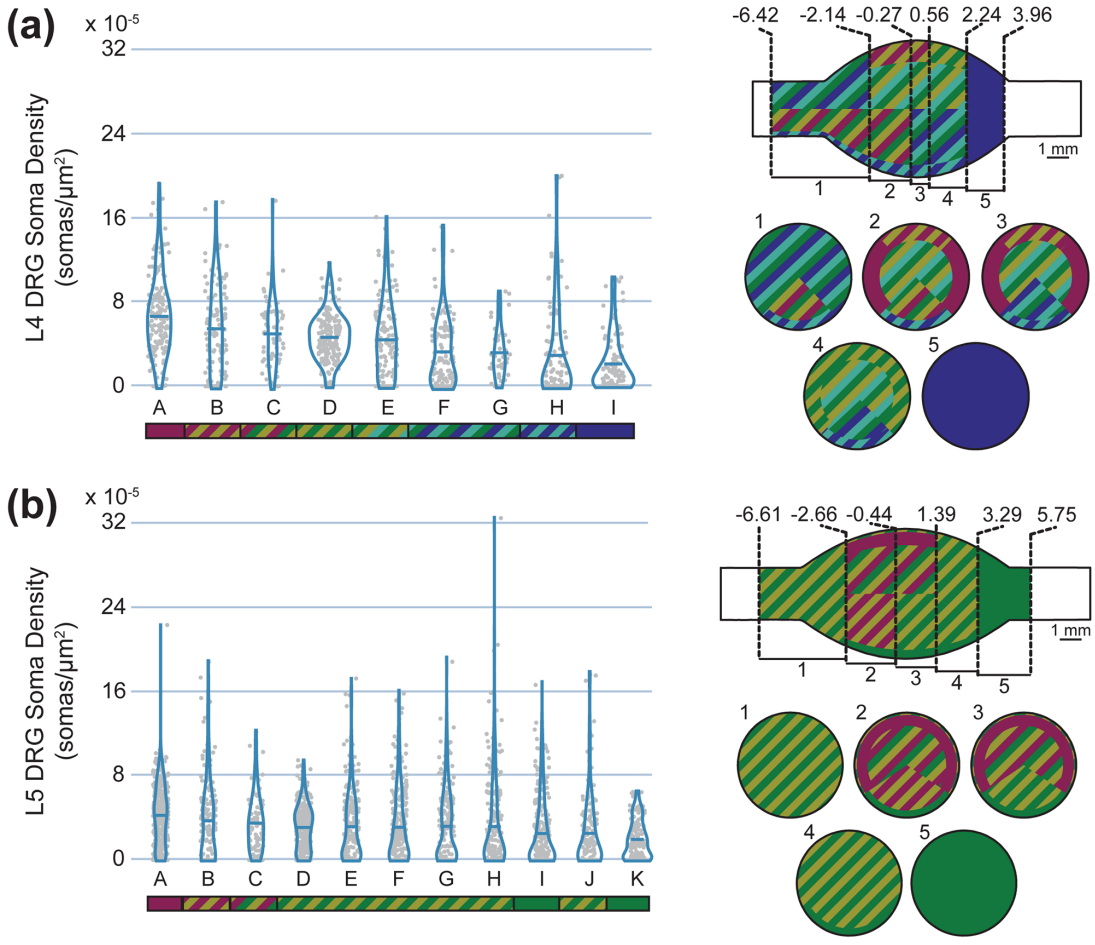

Figure 3.5 Cell body densities in human lumbar DRG. Cell body densities (left) and spatial representations of cell body density (right) of (a) L4 and (b) L5 DRG. Density data are summarized with a violin plot and a mean bar. Letters are unique to each violin plot, although the mean in each group is descending left to right. The colored bar below each plot represents statistical significance. Groups not connected by the same color (either solid or striped) are significantly different from each other. For example, in the top left graph, group A is significantly different from all groups other than B and C, which share its magenta color. The top view of each spatial representation is a view of the DRG with the spinal side left and dorsal side up. Within each uniquely described axial region, a cross-sectional slice with corresponding number label is shown below, with the dorsal side up (e.g., for L4, slice 1 represents cell body densities at axial locations between -6.42 and -2.14 mm from the middle of the ganglion). Values along the axial axis of the DRG have units of mm.

The axon and cell densities for each level were modeled using a recursive partition algorithm, which had radial, axial, and angular position as inputs. **Table 3.2** summarizes the performance of the partition models and the contribution of each input variable to the overall model as a proportion of the total R^2. For the cell body models, axial position was the most important variable, while the radial position was most important for the axon models. Both the L4 cell body and axon models had a higher R^2 than the corresponding L5 models, although as in Ostrowski et al., the trends described by the model represent a relatively small portion of the overall variation.[83] The axon models also had higher R^2 than the associated cell body models.

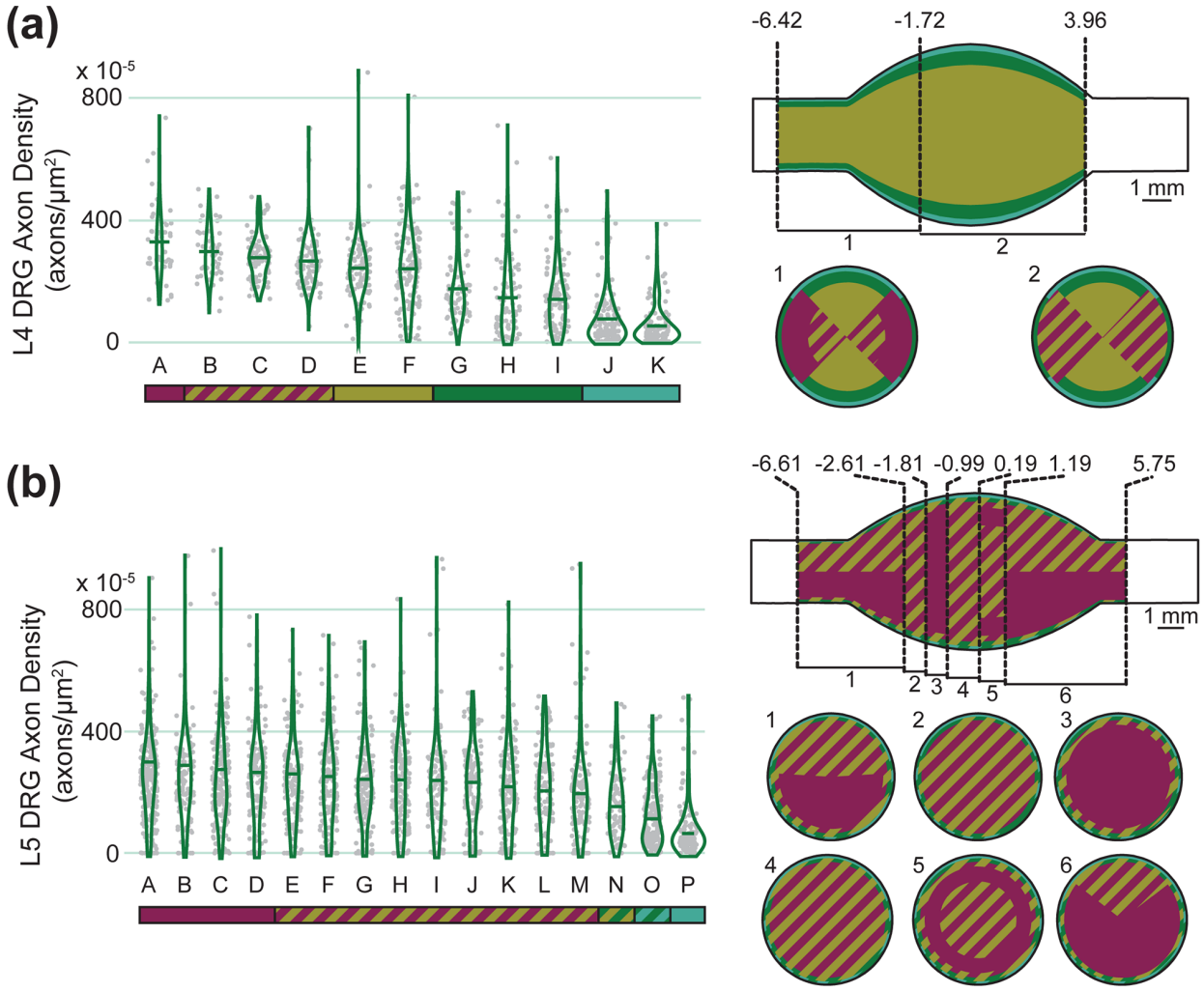

Figure 3.6 Axon densities in human lumbar DRG. Axon densities (left) and spatial representations of axon density (right) of (a) L4 and (b) L5 DRG. See **Figure 3.5** for specific information on the types of figures shown.

Figure 3.5 summarizes the measured cell body densities in each spatial region identified by the recursive partition algorithm models and describes the statistical relationships between regions. **Figure 3.6** shows the measured axon densities in each spatial region identified by the same recursive partition algorithm and describes the statistical relationship between those regions. Each model successfully identified regions with significantly different neural densities, with a minimum ratio of ~2x between the highest and lowest density regions (L5 cell bodies) and a maximum ratio of ~7x between the highest and lowest density regions (L4 axons).

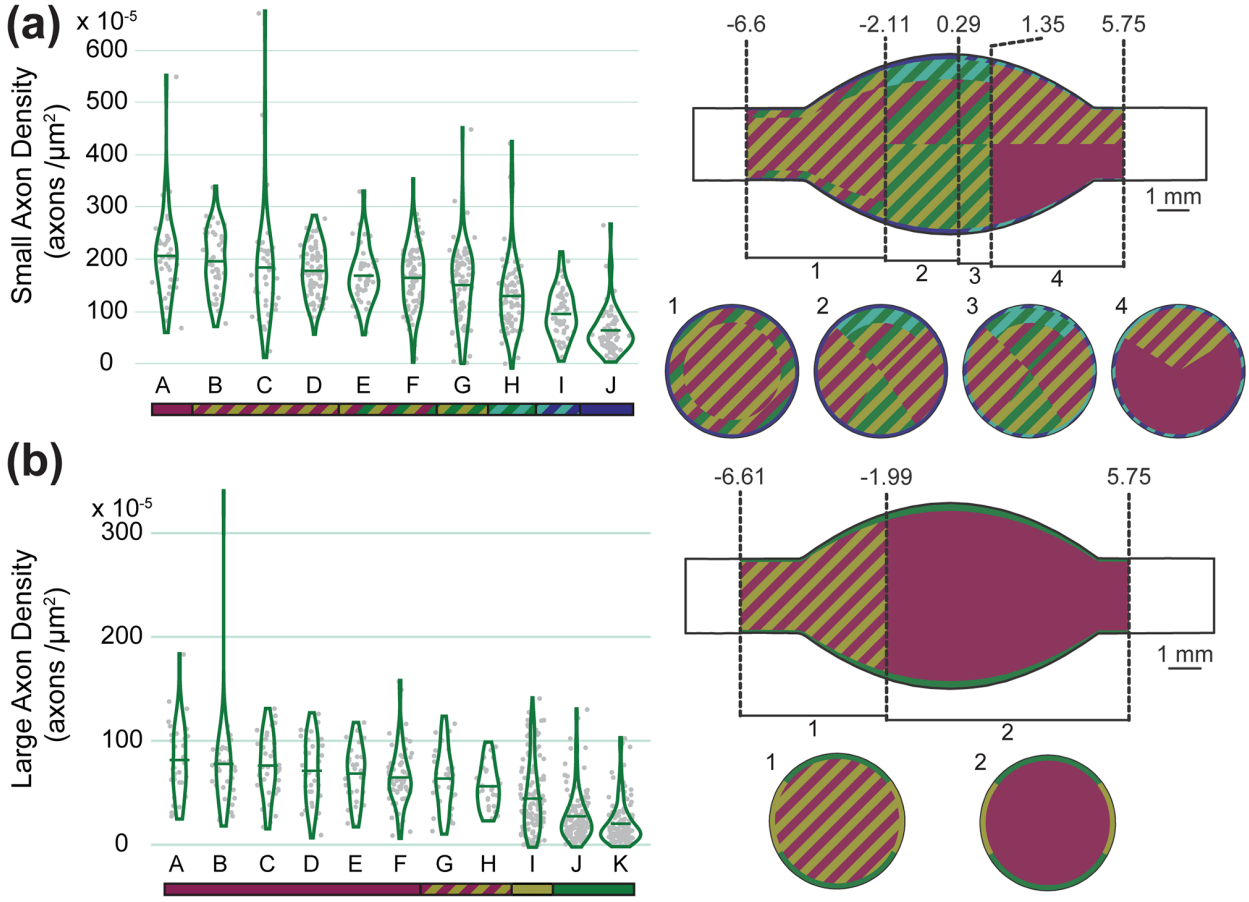

Figure 3.7 Differences in small- and large-diameter axon densities in L5 DRG. Axon densities (left) and spatial representations of axon density (right) of (a) small and (b) large axon density models for L5 DRG. See Figure 5 for specific information on the types of figures shown.

Axial position was the strongest contributor to the cell body models. In L4, the highest soma densities were in the inner ~4.4 mm, and in L5 the highest soma densities were within the

inner ~6 mm. These values both correspond to about 85% of the mean full length of the soma-containing region. For L4, the highest soma density region was in the dorsal-most 76% angularly and the outer-most 30% radially. The lowest soma density region (in the inner axial portion of the DRG) was the ventral-most 24% angularly and the outer-most 18% radially. For L5, the highest soma density region was similarly in the dorsal-most 69% angularly and the outer-most 25% radially, although the outer-most 5% radially was characterized by slightly lower soma density. The lowest soma density region was the ventral-most 31% angularly and the outer-most 14% radially. For both levels, the interior was a more homogeneous region. In contrast to the cell body models, radial position was the most important component of the axon models at both levels. Taken together, the highest axon density regions in the model were within 89% (L5) to 93% (L4) radially. The outer 11 and 7% (respectively) had significantly lower axon densities. In L4, the medial angles (43º–136º) had the highest density, while in L5 angle played almost no role in the final model.

We also considered differences in modeled densities with neural element size. There were not enough nucleated cell bodies to make size models at either level. At L4, the small and large axon density models were almost identical to the overall axon density model. In L5, however, considering fiber sizes separately changed the model in a few significant ways. The contribution of each input variable to each model and the density distribution in the large axon model were fairly similar to the overall axon model (see **Table 3.2** for variable contributions and model R^2). For large axons, the model predicted low density regions throughout the outer-most 8% radially, particularly in the dorsal- and ventral-most 30–35% angularly, and a homogeneously higher density region throughout the inner 92% radially. The small axon model, while retaining an outer low density region (outer-most 6%), had a unique low-density region at the medial dorsal aspect (−2.11 to 1.35 mm axially, dorsal-most 25% angularly, 28% radially). This dorsal region is

particularly important for DRGS applications, so a paucity of small axons in the area may be an important characteristic for ongoing research in the area. **Figure 3.7** shows both models as violin plots and spatial models.

3.5 Discussion

In this study, we analyzed 202 cross sections across the full span of 33 human L4 and L5 DRG collected from 10 donors. To our knowledge, this represents the largest such collection of human DRG images included in a single study. Additionally, while this study was limited to a description of DRG, the full library of images produced includes over 900 images of human spinal roots, both stained and unstained, for use in potential future studies. We utilized a custom semiautomated GUI to aid in this analysis and greatly reduced processing time compared to manual image segmentation. This GUI, which relied on the high contrast neural staining provided by the use of NF200 (rather than hematoxylin & eosin), represented a significant improvement relative to our previous study of feline DRG.[83]

Considering our donor demographics, the main effect we found was that the overall number of axons increases categorically with increasing BMI. To our knowledge, there is no conclusive evidence regarding the role of body size on sensory neuron counts. A previous study in frogs[226] demonstrated that larger frogs had more DRG neurons than smaller frogs, however, few studies have examined the effect of body size or weight on DRG neuron counts in mammals. One study demonstrated that in male rats, which continue to grow in body mass throughout adult life, DRG neuron count increases with age and size.[227] Other studies in rats refute this,[228] claiming that DRG neuron counts do not increase with age. However, that study did not report the sex of their animals, and it is understood that female rats level off in body size, unlike male rats. Future studies should

examine the role of body size, and the presence of obesity, on DRG neuron counts in humans. As obesity is a common comorbidity to chronic pain, obese patients receiving DRGS may have different neuroanatomical makeups than nonobese patients. It is currently unclear if increased axon counts would have an impact on DRGS outcomes.

In contrast to previous studies, we did not find evidence that neuronal numbers increase with age.[141] However, our study was likely underpowered to determine this relationship because our sample only included two donors under the age of 35. One study in cats[229] showed that DRG neuron count did not increase with age, however, the authors reported a slight increase in axon counts with age.

A high-level anatomic trend that we observed was the significant increase in axon and cell body number in peripheral DRG compared to the spinal side. This trend is likely related to axonal branching of DRG neurons which has been observed in rat and cat studies, with branching ratios similar to those in our data.[230–233] Other explanations may include our underestimation of the number of small C-fiber axons present in our tissue samples, particularly considering that unmyelinated axons account for approximately two-thirds of axons in the DRG.[234] Alternatively, it has been observed that the peripheral side of pseudounipolar DRG neuron axons are slightly larger than their spinal counterparts.[133] Lee and colleagues demonstrated that nearly 13% of spinal axons in A-fibers have diameters less than 2 μm, suggesting they would not be detected by our algorithm.[183] We found ~22% more fibers on the peripheral side of the DRG than the spinal side, a slightly larger portion than Lee and colleagues' findings would suggest. It is possible that because our analysis could not detect very small fibers, there is a population of cells, which can only be detected on their peripheral side.

We found a mean 33,643 ± 11,007 axons in L5 DRG and 27,868 ± 10,846 in L4 DRG. These counts are consistent with a recent study by Liu et al. which counted human dorsal root fibers and found 34,455 ± 2,740 in L5 and 31,175 ± 2,740 in L4.[216] In both cases, our mean counts are slightly lower, which may be a result of the variance in our data or our undercount of small unmyelinated fibers. However, both our study and Liu et al. stained spinal root tissue with NF200 and used computer programs to determine the number of fibers present, suggesting Liu and colleagues may have also underestimated the number of unmyelinated fibers. Davenport and Bothe reported 59,000 cells in human L3 DRG, with 25,000 unmyelinated fibers contributing to their total population.[235] Davenport and Bothe's estimation of the number of unmyelinated fibers in lumbar DRG approximately accounts for the difference in their estimate of total cellular population with the estimates made by our study and Liu et al. This suggests that both our study and Liu et al. accurately captured the population of myelinated axons in DRG, but underestimated the number of unmyelinated axons. Considering the sizes of the identified axons, there was a sharp drop-off in counted axons with mean diameter below 2 μm (only 0.018% of identified axons). We, therefore, concluded that our imaging and analysis method was not capable of consistently measuring unmyelinated C fiber axons, which have a typical diameter < 1.6 μm.[204] We also may be undercounting small myelinated fibers (Aδ), which have a minimum diameter of 1 μm.[204] This was likely a result of a denoising step in our image analysis, which could not distinguish very small axons from other cellular detritus.

For our primary quantification of human DRG spatial organization, we utilized a recursive partitioning algorithm to model axon and soma densities in normalized DRG cross sections by axial, radial, and angular position. We found that the highest somatic densities were within about 2 mm of the widest point of L4 DRG and within 3 mm of the widest point of L5 DRG. Within

these regions, both the highest and lowest cell body densities were found in the outermost 20–25% radially, with the dorsalmost 75% having the highest overall density and the ventral-most 25% having the lowest overall density by angle. We found that axial position had a very minimal effect on axon density, which was much more affected by radial position. The outer ~10% at either level had a very low axon density, while the interior ~90% was relatively high.

Our findings related to soma density are consistent with our previous findings in Ostrowski et al. in feline lumbosacral DRG. That study found the highest density of cell bodies in the outer 25% radially and on the dorsal aspect.[83] As this was a study including DRG from a different spinal region (sacral), it suggests that our general characterization in human lumbar DRG can potentially be extended to other spinal levels.

3.5.1 Implications for clinical neurotechnologies

The location of different types of neurons within the DRG is vital to designing clinical neurotechnologies with the goal of treating disease. For example, dorsal root ganglion stimulation (DRGS) delivers electrical stimulation to the DRG with the goal of providing patients with pain relief. Presently, the physiological mechanisms of DRGS-induced pain relief are unknown, though previous studies have suggested that DRGS targets large myelinated DRG neurons,[118] while other studies have suggested DRGS targets small unmyelinated afferents.[47,76] As the mechanisms of DRGS become more clear, precisely targeting the cells responsible for pain relief, while avoiding cells that convey painful sensations, will be vital to the success of DRGS and to patient livelihood. Our results indicate that large axons are homogeneously distributed throughout human DRG. However, our data indicate that the density of smaller myelinated axons is lowest in the dorsal region of the middle of the DRG. Therefore, DRGS applied near the middle of the ganglion may simultaneously target the pain-relieving large axons, while minimizing the activation of small

myelinated nociceptive fibers (e.g., Aδ-fibers). Furthermore, our data demonstrate the presence of biganglia in human lower lumbar DRG, supporting the findings of.[236] It is currently unclear if the presence of bi- or triganglia would affect the accurate delivery of electrical stimulation to DRG neurons, or if the separate ganglia are functionally distinct. We can speculate that distinct regions of connective tissue between multi-ganglia, which tend to have higher impedance than the neuron containing region,[237] could affect the spread of current in the DRG. Shen and colleagues showed that biganglia are most commonly found at L4,[236] a common DRGS target to manage chronic pain in the foot and lower leg.[77] Future studies should explore the existence of functionally-distinct biganglia, which may inform the placement of the electrode lead for DRGS.

For neurotechnologies that record signals from the DRG, the location of cell bodies is crucial to obtaining an adequate signal, as cell bodies and their initial segments produce most of the transmembrane currents that lead to recordable neural signals. Such technologies would need to be placed in close proximity to those structures to ensure obtaining a viable signal.[238] Our results support previous findings in cats[83] that cell bodies typically organize around the dorsal aspect of the ganglion. However, our results further demonstrate that this phenomenon is present not only at the most medial portion of the DRG, but over a span of several millimeters around the middle of the ganglion for human lumbar DRG. Therefore, to maximize the likelihood of achieving a viable signal, technologies seeking to record signals from the DRG should target the dorsal-middle portion of the DRG, unless future work should determine a particular somatotopy for the desired sensory modality. However, as described above, our method is likely underestimating the presence of small unmyelinated fibers in DRG. Many physiological signals of interest to neuroprosthetic technologies (e.g., bladder signals, nociception) are carried by small fibers.[202,239] Therefore, future

implementations of our method must be mindful of the type of neuron carrying a signal of interest, and design their identification paradigm to successfully capture the target neural elements.

3.5.2 Limitations and future work

While our results provide a unique quantitative description of human DRG anatomy, there were several limitations to our study design. Firstly, we collected a histological slice at 1 mm increments along the nerve root axis. Human lower lumbar DRG on average range between 7.8 and 11.58 mm in length along the nerve root axis,[93] meaning we were limited to approximately between 7 and 11 samples per DRG. Ideally, we would have sectioned an entire DRG with 5 μm slices, to enable a complete reconstruction of the entire cellular population of a ganglion. However, this would dramatically increase the cost of processing even a single DRG, which would have limited us from making comparisons across lumbar levels and across donors. Therefore, we believe that sacrificing slice resolution to enable statistical comparisons was an appropriate choice for our study, as we wanted to gain a rough picture of the stereotactic distribution of neurons in the DRG. Future studies should consider sectioning multiple DRG at a higher resolution, as the monetary and time costs of high-throughput histological processing decrease. Newer tissue clearing and light sheet microscopy techniques may offer opportunities to image DRG cells with minimal sectioning required.

Secondly, we collected DRG from 10 individual donors. As described above, we sacrificed spatial resolution along the nerve root axis to obtain specimens from multiple donors. However, with a sample size of 10 donors, it is unlikely that we are sufficiently powered to make strong statistical claims relating demographic data to the number and distribution of primary afferents in human DRG. Previous work in rats demonstrated an increased number of DRG neurons with increased age and body size,[141,227] and we were able to demonstrate body size differences (but not

age differences) in our human data set. A previous study showed that sensory neuron count in human cervical DRG linearly increased with DRG volume, but DRG volume was not shown to correlate with any demographic data (e.g., height, weight) other than a significant sex difference in DRG volume,[240] a parameter that we did not directly quantify.

Staining our slides with only NF200 precluded us from making strong conclusions about the functional distribution of afferents in lumbar DRG. NF200 stains for cytoskeletal proteins present in all primary afferents in humans.[214,215] We believe that NF200 was the most appropriate choice in stain, as it provided sharp contrast between neural elements (which appeared brown in brightfield microscopy) and background tissue. However, the presence of NF200 did not assign a specific sensory function to a neuron (e.g., mechanoreception, nociception). Without information about sensory function, we were unable to make strong claims about the presence of functional somatotopy in human DRG. Co-staining our slides with other neurochemical markers more indicative of sensory function (e.g., TRPV1 or peripherin to stain small nociceptors[241]) would provide more convincing evidence of sensory function, and would allow us to test for the presence of functional somatotopy. Future work may utilize co-staining as an opportunity to examine out both sensory function and anatomical distribution of primary afferents.

Finally, the morphological operations our algorithm used to identify cell location may have individually or in tandem limited our ability to detect the location of very small axon fibers (i.e., < 2 μm in diameter). Unmyelinated C-fiber axons can be as small as 0.2 μm in diameter in cats (Lee et al., 1986). The morphology operations our algorithm used to accurately detect the location and diameter of stand-alone neural structures occasionally filtered out objects below 2 μm. However, the range of C-fiber axon diameters in humans is currently unknown. Therefore, it was difficult to estimate how many small neural structures were not captured by our framework. With

algorithmic adjustments and images scanned at higher magnification, however, it may be possible to examine C-fiber population distributions using the same GUI and methods described herein.

3.6 Conclusion

The spatial distribution of neural elements in human DRG is important to clinical neurotechnologies seeking to treat neurological disease. We developed a semi-automated algorithm to identify the location of different neural elements in human DRG. We demonstrated that, at lower-lumbar levels, cell bodies preferentially organize around the dorsalmost region of the ganglion, while axons are homogeneously distributed throughout the interior 90% of the ganglion. We also presented a method to reconstruct 3D-models of human DRG based on histological images. Future studies could extend our identification algorithm to probe the presence of functional somatotopy in human DRG, or use 3D-model reconstructions as an in situ platform for developing novel DRG-interface technologies.

Chapter 4 – Dorsal Root Ganglion Stimulation for Chronic Pain Modulates Aβ-fiber Activity but not C-fiber Activity: A Computational Modeling Study

The work presented in this chapter is published as:

Graham RD, Bruns TM, Duan B, Lempka SF. Dorsal root ganglion stimulation for chronic pain modulates Aβ-fiber activity but not C-fiber activity: A computational modeling study. *Clinical Neurophysiology*. 2019;130:941951.[118]

4.1 Abstract

Objective:

The goal of this project was to use computational models to investigate which types of primary sensory neurons are modulated by dorsal root ganglion stimulation (DRGS) to provide pain relief.

Methods:

We modeled DRGS by coupling an anatomical finite element model of a human L5 dorsal root ganglion to biophysical models of primary sensory neurons. We calculated the stimulation amplitude needed to elicit an action potential in each neuron, and examined how DRGS affected sensory neuron activity.

Results:

We showed that within clinical ranges of stimulation parameters, DRGS drives the activity of large myelinated Ab-fibers but does not directly activate small nonmyelinated C-fibers. We also showed that the position of the active and return electrodes and the polarity of the stimulus pulse influence neural activation.

Conclusions:

Our results indicate that DRGS may provide pain relief by activating pain-gating mechanisms in the dorsal horn via repeated activation of large myelinated afferents.

Significance:

Understanding the mechanisms of action of DRGS-induced pain relief may lead to innovations in stimulation technologies that improve patient outcomes.

4.2 Introduction

Chronic pain is a debilitating disorder that affects over 100 million Americans and accounts for $560–635 billion in healthcare and productivity costs in the United States each year.[15] For patients with chronic pain that is refractory to conventional medical management (e.g., pharmaceuticals, orthopedic surgery), neurostimulation therapies, such as spinal cord stimulation (SCS) and dorsal root ganglion stimulation (DRGS), are alternative treatment options. SCS has been a mainstay of refractory pain management for decades, and is achieved by implanting electrode arrays in the epidural space dorsal to the spinal cord.[25] To reduce pain, the goal of conventional SCS is to apply electrical impulses to the region of the spinal cord that innervates the patient's painful regions, which evokes paresthetic (i.e., tingling) sensations in those regions. Unfortunately, the anatomy of the spinal column makes it difficult for SCS to target certain regions of the body (e.g., the bladder, feet), and has contributed to the limited success of SCS in treating focal pain etiologies.[38] Furthermore, the presence of highly conductive cerebrospinal fluid (CSF) around the spinal cord can shunt electrical current away from the targeted region.[67] SCS leads are prone to migration over time, and changes in posture can affect the position of the spinal cord relative to the electrode lead, both of which further affect the accurate delivery of electrical

stimulation to the spinal cord.[25] With these shortcomings in mind, DRGS was developed to provide a new therapy for patients with refractory focal pain.

In contrast to SCS, DRGS is achieved by implanting a cylindrical stimulating electrode in the intraforaminal epidural space above a dorsal root ganglion (DRG). Due to the compactness of the intraforaminal space and scarcity of CSF around the ganglion,[94] DRGS electrode leads consistently remain in close proximity to the DRG without much migration, and are less prone to the postural effects that hamper SCS leads.[242] Since a DRG innervates a single dermatome of the body, electrical stimulation of a DRG could provide dermatome-specific pain relief, suggesting that DRGS may be effective for patients with pain that is difficult to target with conventional SCS (e.g. bladder pain, focal foot pain). DRGS was approved by the Food and Drug Administration in 2016 to treat intractable complex regional pain syndrome (CRPS) of the lower limbs,[39] and has been used off-label for several other pain etiologies (e.g. phantom limb pain, painful diabetic neuropathy, groin pain).[40,41,243,244] Though preliminary clinical studies report success in many patients (approximately 75%),[90] not all patients receive adequate pain relief from DRGS. One contributing factor to the limited success rate of DRGS is that we do not understand the mechanisms of action by which DRGS provides pain relief. Without a mechanistic understanding of DRGS, we cannot optimize clinical parameters (e.g. stimulation amplitude, electrode lead position) to maximize pain relief in all patients.

The DRG is a bulge in the posterior spinal root, located bilaterally in the intraforaminal space at each spinal vertebral level. Each DRG contains the cell bodies of all the primary sensory neurons (PSNs) innervating the dermatome governed by its spinal segmental level (e.g. the left L5 DRG innervates the left foot). PSNs are pseudounipolar – the soma has a single axon process (the stem axon) that bifurcates at a large node of Ranvier called the T-junction. One axon projects

centrally and terminates in the spinal cord, while the other projects to the periphery and terminates in a nerve ending.[97,131,132] Two types of PSNs commonly examined in pain pathophysiology studies are the large myelinated Aβ-fiber and the small nonmyelinated C-fiber.[97,245,246] Aβ-fibers typically convey innocuous tactile stimuli, but have been shown to generate ectopic action potentials (APs) in some chronic pain models, and are known to contribute to the development of tactile allodynia.[145,245,247–250] C-fibers typically convey noxious stimuli. In some chronic pain conditions, peripheral sensitization of C-fibers may generate aberrant action potentials at the site of a neuroma or tissue damage.[248,251–253] The importance of the DRG in the development and maintenance of chronic pain is well understood, making it an attractive target for neurostimulation therapies. However, our limited understanding of the therapeutic mechanisms of DRGS precludes the design of stimulation technologies (e.g. stimulus waveforms, electrode designs) to take full advantage of these mechanisms.

To understand the mechanisms of DRGS, it is imperative to first understand which neural elements are directly modulated by DRGS. Currently, there are several hypotheses to explain the therapeutic mechanisms of DRGS, ranging from filtering nociceptive impulses before they reach the spinal cord, to suppressing aberrant electrical activity of PSNs.[254] However, there is no clinical evidence directly supporting any one hypothesis. *In-vitro* studies have shown that C-type fibers exhibit a low-pass filtering effect at the T-junction that prevents some peripherally generated noxious afferent signals from reaching the central axon branch leading to the spinal cord. These studies also suggest that extracellular electrical stimulation can enhance this filtering effect.[47,48] The only previously-published computer modeling study of DRGS showed that clinical DRGS may provide pain relief by augmenting this mechanism.[76] However, the stimulation amplitudes required to produce filtering (approximately 9.5 mA) were far outside clinical ranges (typically

1 mA),[90] suggesting that DRGS provides pain relief through other mechanisms in clinical contexts. It is well understood that extracellular stimulation preferentially activates large-diameter myelinated axons over small nonmyelinated axons[58] and this trend suggests that Aβ-fibers and not C-fibers may be directly stimulated by DRGS.

In this work, we developed a computer model of clinical DRGS to investigate the mechanisms by which DRGS provides pain relief. We developed a volume conductor model of a human L5 DRG, a common stimulation target to manage chronic foot pain.[40,41,255] We coupled this anatomical model to multi-compartment models of Aβ- and C-fibers. We validated these cell models against experimental data. We developed the first computer model examining the effects of DRGS on both myelinated and nonmyelinated afferents, and showed that at stimulation amplitudes within typical clinical ranges, electrical stimulation is driving the activity of Aβ-fibers but not activating C-fibers. These results suggest that DRGS may provide pain relief by activating pain-gating mechanisms within the dorsal horn. Lastly, we examined the effect of electrode location on DRGS-induced neural activation, and suggest that straddling the active and return electrodes over the ganglion may be the optimal electrode configuration for activating neural tissue.

4.3 Methods

We developed computer models to investigate how DRGS affects sensory neurons in the DRG. We coupled multicompartment models of primary sensory neurons to a three-dimensional finite element model (FEM) of a human L5 DRG. We calculated the voltage distribution generated by DRGS throughout the DRG and surrounding anatomy. We applied these voltages to the multi-

compartment models of sensory neurons within the DRG, and examined how different sensory neuron types (i.e., mechanoreceptors and nociceptors) responded to DRGS.

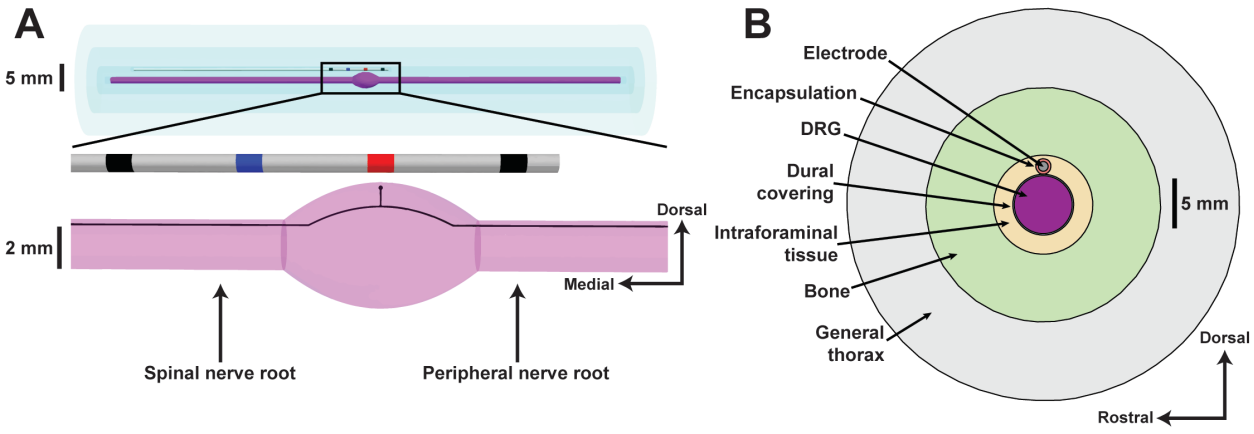

Figure 4.1 Finite element model of human L5 DRG. Anatomy of the finite element model of a human L5 DRG and stimulating electrode. (A) Side view of the DRG with the DRG stimulating electrode oriented above the ganglion (red: active electrode, blue: return electrode, black: inactive electrode). An example primary sensory neuron trajectory is shown in black with the soma below the active electrode. (B) Cross sectional view through the middle of the DRG.

4.3.1 Step 1: Calculate the extracellular voltages generated by DRGS

We constructed a three-dimensional FEM based on experimentally measured values to create an anatomically and electrically accurate volume conductor model of a human L5 DRG (**Figure 4.1** and **Table 4.1**). The geometry of the model was based on published cadaver and imaging studies of the DRG and surrounding anatomy (e.g., dural covering, intraforaminal tissue, bone).[95,222,256,257] The electrical conductivity of each tissue was based on values used in previous computational studies of neurostimulation for pain, and experimentally measured tissue resistivities.[33,258–260] Each conductivity was modeled as isotropic, except the nerve root, which was two-dimensionally anisotropic white matter (**Table 4.2**). The FEM was built in the commercially available software 3-matic Module within the Mimic Innovations Suite (Materialise, Belgium). We included a model of the four-contact Abbott AxiumTM DRG electrode array (Abbott Laboratories, USA) oriented above the DRG such that the active electrode was centered directly above the middle of the ganglion. We wanted to examine the effect of electrode lead position on

neural activation. Therefore, in some simulations (where noted below) we shifted the electrode so that the active and return electrodes straddled the DRG such that the halfway point between the middle of the two electrodes was directly above the middle of the ganglion. We shifted the electrode 3.125 mm along the nerve root (i.e., half of the distance from the middle of one contact to the middle of an adjacent contact). We encased the electrode in a 300-μm thick encapsulation layer to represent the typical foreign body response to implanted materials.[259]

Table 4.1 Anatomical parameters used to build the finite element model of a human L5 DRG.

Parameter	Value	Reference
DRG Length	9.4 mm	[95]
DRG Width	5.9 mm	[95]
Nerve Root Radius	1.19 mm	[256]
Dural Sheath Thickness	150 μm	[257]
Foramen Height	17.3 mm	[95]
Encapsulation Layer	0.3 mm	[259]
Electrode Contact Length	1.25 mm	[96]
Electrode Radius	0.5 mm	[96]

Abbreviations: DRG, dorsal root ganglion

We imported the FEM into COMSOL Multiphysics (COMSOL, Inc., USA). Clinically, DRGS utilizes a bipolar electrode configuration (Kramer et al., 2015). To model bipolar DRGS, we applied boundary conditions at the active electrode (i.e. current stimulation) and the return electrode (i.e. ground; 0 V). We modeled the electrode shaft as a perfect insulator. We modeled inactive electrode contacts as equipotential with zero net current across their surface. To model DRGS, we calculated the voltage distribution generated by a unitary stimulus current (i.e. 1A) using the conjugate gradient method to solve the Laplace's equation:

$$\nabla \cdot (\sigma \cdot \nabla \Phi) = 0 \quad (4.1)$$

where σ is the tissue stiffness matrix and Φ is the calculated voltage distribution. We used Ohm's law to calculate the impedance of the bipolar stimulation configurations by measuring the average voltage generated at the active electrode and dividing by the applied stimulus current. We then compared our average model impedances to clinically measured impedances. The model's average impedance (1500 Ω) was within clinically reported impedance ranges.[77]

Table 4.2 Electrical conductivities used in the finite element model.

Parameter	Value	Reference
Gray Matter	0.23 S/m	[258]
White Matter (longitudinal)	0.6 S/m	[258]
White Matter (transverse)	0.083 S/m	[258]
Dural covering	0.6 S/m	[33]
Bone	0.02 S/m	[260]
Thorax	0.25 S/m	[258]
Encapsulation	0.17 S/m	[259]

4.3.2 Step 2: Define sensory neuron models in the DRG

We used the freely-available software package, NEURON (v7.4),[261] to construct all multi-compartment models of primary sensory neurons described below.

Aβ-fiber model

We developed a model of an Aβ-fiber (**Figure 4.2**) based on morphological parameters from previous studies (**Table 4.3**).[133,262] We extended a model of a mammalian axon – the MRG model[263] – to describe the pseudounipolar morphology of Aβ-fibers. The MRG model is a double-cable model of a mammalian motor axon with nodes of Ranvier separated by three distinct finite

impedance myelin segments: the myelin attachment segment, a paranode main segment, and internode regions. We accounted for two features of Aβ-fiber internode regions not accounted for in the original MRG model (**Figure 4.2**): (1) the internode regions of the stem axon become increasingly myelinated near the bifurcation node, and (2) the first several internodes of the central and peripheral axons increase in length moving distally from the T-junction until they reach a consistent value.[133] The spinal axons of PSNs are smaller in diameter than the peripheral axons.[132] Therefore, we set our Aβ-fiber model central axon diameter to 5.7 μm and the peripheral axon diameter to 7.3 μm.[183] The myelinated compartments were made of two concentric layers containing linear leak conductances with a parallel membrane capacitance. The nodes of Ranvier contained the parallel active nodal conductances of the sensory-specific axons described by Gaines and colleagues: fast Na+, persistent Na+, fast K+, and slow K+ ion channels.[264] The active nodal conductances were in parallel with a linear leakage conductance and membrane capacitance (**Table 4.3**). We increased the model's leak conductance from 6 to 8 mS/cm^2 to reduce membrane potential fluctuation at simulation onset. We increased the slow K+ channel's β rate constant's A parameter from 0.03 to 0.06 ms^{-1} to better fit the experimental values of AHP amplitude and duration.[265,266] The soma and initial segment contained the same active ion channels as the nodes, but with sodium channel densities of 300 channels/μm^2 and 500 channels/μm^2, respectively.[267] Note that we used an initial segment channel density of 500 channels/μm^2, which is slightly lower than the ~800 particles/μm^2 reported by Matsumoto and Rosenbluth,[267] but was necessary to prevent the cell from generating spontaneous action potentials at the initial segment. We believe this is a reasonable modification, as the Aβ-fiber model reproduced many action potential characteristics seen in literature (**Table 4.4**).

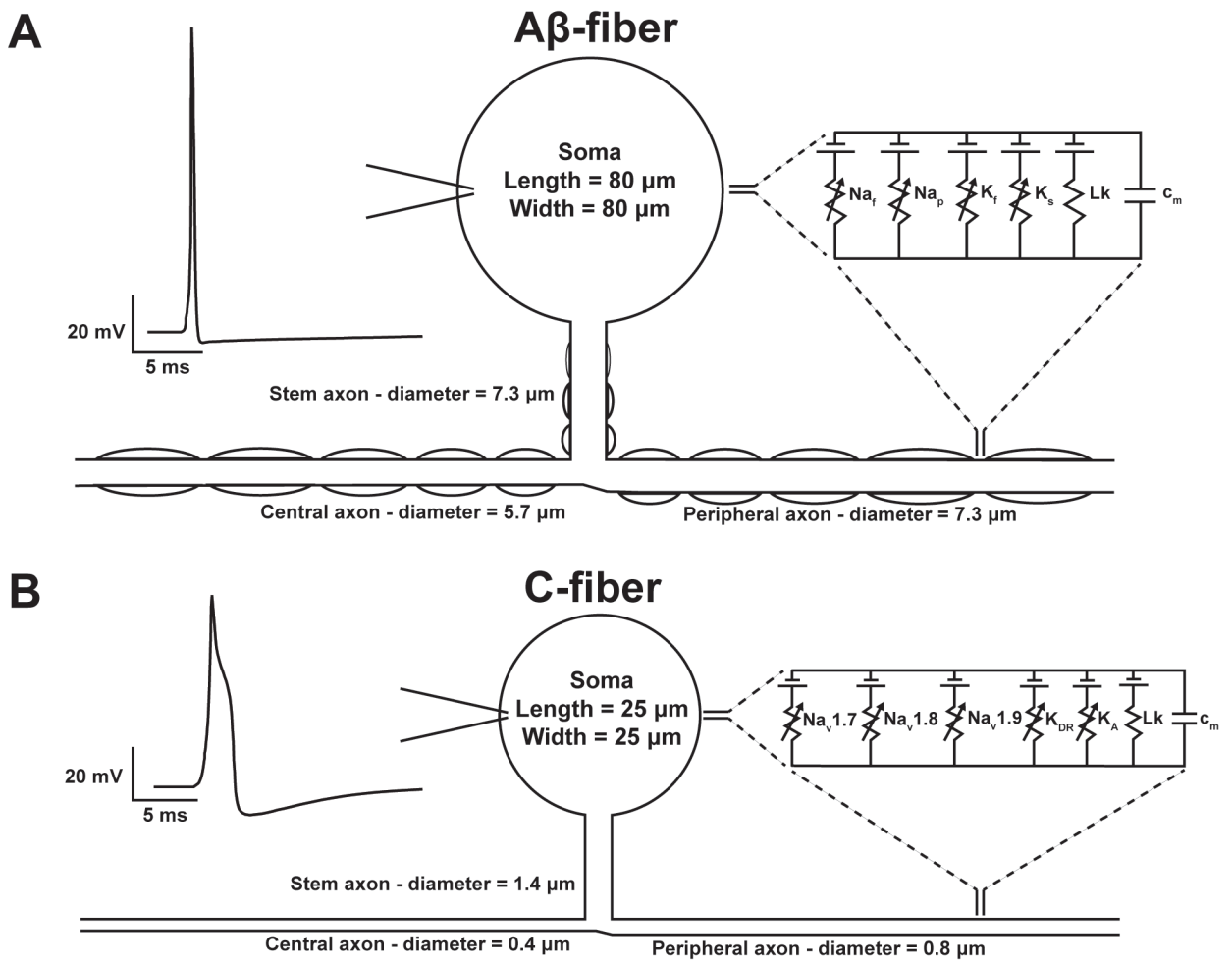

Figure 4.2 Multi-compartment DRG neuron models. (A) We modified a previously-published model of a mammalian sensory neuronto represent the pseudounipolar morphology of an Aβ-fiber.[133,263,264] An example action potential is shown on the left. The equivalent circuit diagram with active ion conductances included in the nodal, initial segment, and soma compartments is shown on the right. (B) we constructed a model of a C-fiber based on morphological parameters and electrophysiological parameters from previous studies.[135,268,269] An example action potential is shown on the left. The equivalent circuit diagram with active ion conductances included in all membrane compartments is shown on the right.

C-fiber model

We implemented a model of a nonmyelinated C-fiber (**Figure 4.2** and **Table 4.3**) based on morphological values described by Sundt and colleagues.[135] The C-fiber membrane contained active conductances commonly seen in C-type nociceptors, and are studied as targets in pharmacological pain treatment. Specifically, we implemented the active ion channels and corresponding channel densities described in by Sheets and colleagues: TTX-Sensitive Nav1.7,

TTX-Resistant Nav1.8, a delayed rectifier K+ channel, and a transient A-type K+ channel.[268] We also included the slow TTX-Resistant Nav1.9 from Huang and colleagues.[269] We included a passive leak channel with a conductance set to balance the resting membrane potential at -55 mV.[135] All compartments contained equal distributions of each ion channel type, as nonmyelinated axons have largely homogeneous membrane structures.[270] To reduce computational demand while still ensuring model accuracy, we set the compartment lengths in the peripheral and spinal axons to 10 μm for compartments within 20 mm of the bifurcation point (i.e., near the stimulating electrode) and 500 μm elsewhere along the axon.[76] The stem axon was divided into 100 compartments of equal length (8.4 μm).[135] The C-fiber model matched well with experimental somatic action potential values (**Table 4.4**).

Table 4.3 Cell morphology parameters used to construct Aβ- and C-fiber multi-compartment models.

Parameter	Aβ-fiber Value	C-Fiber Value	Reference
Fiber diameter (peripheral)	7.3 μm	0.8 μm	[132,183]
Fiber diameter (central)	5.7 μm	0.4 μm	[132,183]
Fiber diameter (stem)	7.3 μm	1.4 μm	[135,183]
Stem axon length	789 μm	844 μm	[133,135,262]
Soma length	80 μm	25 μm	[133,135,262]
Soma diameter	80 μm	25 μm	[133,135,262]
Node length	1.0 μm	-	[263]
Heminode diameter	5 μm	-	[133,262]
Initial segment length	200 μm	-	[133,262]
Initial segment diameter	5 μm	-	[133,262]
Paranode length	3.0 μm	-	[263]
Juxtaparanode length	Variable	-	[263]
Internode length	Variable	-	[133,263]

Spontaneously active fibers

In a subset of simulations, we modified the Aβ-fiber and C-fiber models to produce spontaneous activity – a feature of some chronic pain states – to examine how DRGS affects pain-state sensory neurons. Aβ-fibers fire ectopic action potentials generated in the soma in some models of chronic pain.[144,145,245,249,271] This phenomenon is mediated in part by a decrease in somatic potassium conductance,[272–274] and an increase in sodium conductance.[275–277] We therefore decreased somatic potassium conductance by 20% and increased sodium conductance by 50% so the model generated ectopic action potentials in the soma at frequencies reported in experimental studies (28 Hz).[247,271,273]

C-fibers rarely generate ectopic APs in their somata.[144,248,278,279] Instead, pain-state C-fiber activity often arises as aberrant signals coming from the periphery, usually at the site of tissue damage (e.g., neuroma, inflammation).[248,251–253] Therefore, we modeled pain-state C-fibers by introducing synaptic events in the peripheral axon to simulate painful APs generated in painful tissue (NEURON's NetStim class, 50 ms spike period).

We next placed the sensory neurons models within the DRG. A recent study showed that in mammalian DRG, cell bodies are preferentially located around the dorsal edge of the ganglion,[83] but the spatial distribution of Aβ- and C-fibers within the DRG is unknown. Therefore, we homogeneously distributed each cell type throughout the DRG. We placed the somata of both sensory neuron models on a 2D regular grid within the sagittal and transverse planes of the DRG (**Figure 4.3**; **Figure 4.4A**, gray shaded areas) with 100 μm spacing in all directions. Stem axons projected towards the midline of the ganglion, then bifurcated into central and peripheral processes that curved ventrally to enter the nerve root. The stem axon and soma totaled 869 μm in length for both cell models.[133] **Figure 4.1** and **Figure 4.3** show an example axon trajectory within the FEM.

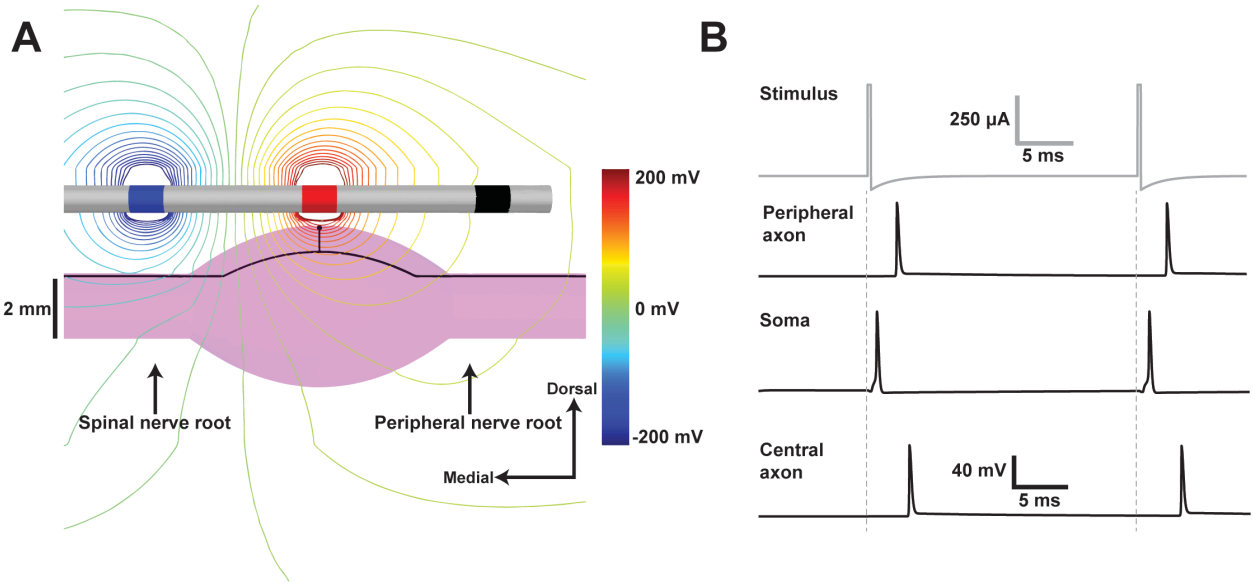

Figure 4.3 Coupled DRGS model. Coupling the finite element model (FEM) of a human L5 DRG to the multi-compartment models of primary sensory neurons. (A) Isopotential lines of the extracellular voltages generated by bipolar DRGS calculated from the FEM. (B) Time-dependent transmembrane voltages resulting from stimulating an example Aβ-fiber with a 500 µA anodic DRGS pulse (top trace, gray). The action potential initiates near the soma and then propagates into the central and peripheral axons (bottom three traces, black).

4.3.3 Step 3: Determine the cellular response to DRGS

We interpolated the extracellular voltages calculated from the FEM (Eq. (1)) onto the center of each neuron compartment. We used the NEURON simulation environment (v7.4) within the Python programming language to apply the extracellular voltages to both cell models using NEURON's extracellular mechanism.[261,280] For each simulation, we calculated each neural compartment's time-varying membrane potential, Vm, by using a backward Euler implicit integration method with a time step of 0.005 ms to solve the cable equation:

$$r_i c_m \frac{\partial V_m}{\partial t} = \frac{\partial^2 V_m}{\partial x^2} + \frac{\partial^2 V_e}{\partial x^2} - \frac{r_i}{r_m} \sum I_{ion} \tag{4.2}$$

where r_m is the membrane resistance, r_i is the intracellular resistance, V_e is the extracellular voltage, and c_m is the membrane capacitance. The ΣI_{ion} term represents the sum of all ionic currents through a given compartment. The ionic current for a generic ion (e.g., sodium, potassium) is represented by the Hodgkin-Huxley formalism:

$$I_{ion} = \bar{g}_{ion} s(V_m - E_{ion}) \quad (4.3)$$

where $\bar{g}_{ion}$ is the maximal ionic conductance, s is a state variable, and E_{ion} is the ionic reversal potential. Some ionic currents have more than one state variable. For the full formulation of each ion channel's current equation, we refer the reader to their original manuscripts.[264,268,269] Because the FEM tissue conductivities were linear, the voltage distribution generated by a given stimulus amplitude was a scalar multiple of the voltage distribution generated by a unit stimulus (i.e., a 1 A stimulus).[238]

We examined sensory neuron response to DRGS (**Figure 4.3**). We calculated the minimum stimulation amplitude to elicit one or more action potentials (i.e., the activation threshold) in both fiber types. All pulses were biphasic with a stimulus pulse followed by a passive discharge phase. To mimic common parameter values used in clinical DRGS, we used a stimulus pulse width of 300 μs, an interphase interval of 20 μs (i.e., delay between the end of a stimulus pulse and the start of the passive discharge phase), and a pulse frequency of 40 Hz.[76,90,281] We calculated activation thresholds for both anodic- and cathodic-first stimulus pulses. We used a binary search algorithm to find the activation thresholds to within 0.1 μA.

4.4 Results

4.4.1 Cell model validation

We created multi-compartment models of two types of sensory neurons that are important in pain processing: a myelinated Aβ-fiber and a nonmyelinated C-fiber. Both the Aβ-fiber and C-fiber models reproduced somatic action potential characteristics observed in experimental studies.[133,265,266,271,282–285] The Aβ-fiber model matched experimental ranges of AP amplitude, AP

duration, AHP amplitude, AHP half duration, resting membrane potential, and conduction velocity (CV). The C-fiber model matched experimental ranges of AP amplitude, AP duration, rise time, fall time, AHP amplitude, AHP half duration, resting membrane potential, and CV. The action potential rise and fall times of the Aβ-fiber model were slightly outside of the experimental range, however the total duration of the action potential matched experimental data. **Table 4.4** summarizes the somatic action potential characteristics of our models and how they compared to values reported in literature.

Table 4.4 Validation metrics for our multi-compartment models against experimental data.

Aβ-Fiber			
Parameter	**Our Value**	**Literature Ranges**	**Reference**
Soma AP amplitude	107.7 mV	109.72 +/- 11.21 mV	[133,282]
AP duration	1.225 ms	1.29 +/- 0.59 ms	[265,283]
Rise time	0.775 ms	0.61 +/- 0.13	[283]
Fall time	0.45 ms	0.89 +/- 0.41	[283]
AHP amplitude	4.2 mV	7.9 +/- 4.2 mV	[265]
AHP half-amplitude duration	14.7 ms	10.1 +/- 11.0 ms	[266]
Resting potential	-79.1 mV	-80 mV	[285]
Ectopic spiking frequency	28 Hz	10-50 Hz	[271]
CV (peripheral axon)	25.00 m/s	14-30 m/s	[286]
CV (central axon)	17.02 m/s	14-30 m/s	[286]
C-Fiber			
Parameter	**Our Value**	**Literature Ranges**	**Reference**
Soma AP amplitude	76.5 mV	81.6 +/- 6.9	[265]

AP duration (base)	3.5 ms	4.97 +/- 2.16	[265]
Rise time	1.675 ms	2.5+/- 0.89	[283]
Fall time	1.825 ms	4.61 +/- 3.5	[283]
Resting potential	-55 mV	-48.6 +/- 9.2	[265]
AHP amplitude	10.9 mV	8.2 +/- 5.1 mV	[265]
AHP 80	9.5 ms	14.4 +/- 9.2 ms	[283]
AHP half amplitude duration	5.2 ms	12.87 +/- 8.4 ms	[265]
CV(peripheral axon)	0.28 m/s	< 1.4 m/s, 0.2-0.8 m/s	[284]
CV (central axon)	0.21 m/s	< 1.4 m/s, 0.2-0.8 m/s	[284]
CV (stem axon)	0.39 m/s	< 1.4 m/s, 0.2-0.8 m/s	[284]

Abbreviations: AP, action potential; AHP, afterhyperpolarization; CV, conduction velocity

4.4.2 Activation thresholds

DRG contain several types of primary sensory neurons that convey different sensory modalities (e.g., touch, pain). Large myelinated fibers, such as Aβ-fibers, typically convey innocuous touch stimuli, while small nonmyelinated fibers, such as C-fibers, typically convey noxious stimuli.[97] We wanted to determine which types of sensory neurons are likely being activated by DRGS. Therefore, we calculated the stimulation amplitudes necessary to elicit one or more action potentials in the multicompartment models of Aβ- and C-fibers.

In Aβ-fibers, cathodic and anodic DRGS typically caused APs to initiate in either the peripheral or central axon – whichever was closer to the cathode. In C-fibers, most APs initiated in the stem axon when the cell body was near the anode, while APs were typically generated in the soma when the cell body was near the cathode. **Figure 4.4B** shows contour plots of the activation thresholds for Aβ- and C-fibers. Aβ-fiber thresholds were lower than C-fiber thresholds.

Anodic thresholds were consistently lower than cathodic thresholds for both cell types. PSNs with cell bodies below an anode had lower thresholds than PSNs with cell bodies below a cathode. Activation thresholds increased with distance from the active and return electrodes. The minimum stimulation amplitude needed to elicit an action potential in an Aβ-fiber was 0.36 and 0.24 mA for cathodic and anodic DRGS, respectively. The minimum stimulation amplitude needed to elicit an action potential in a C-fiber was 4.38 and 4.09 mA for cathodic and anodic DRGS, respectively. On average, DRGS amplitudes used in clinical practice do not exceed 1 mA.[90] With a 1 mA pulse amplitude, cathodic DRGS activated 29.5% of the modeled Aβ-fibers in the DRG, while anodic DRGS activated 74.6% of Aβ-fibers in our DRG model. Interestingly, there were no C-fibers activated within clinical amplitude ranges. These results suggest that, with standard clinical amplitudes, DRGS directly activated myelinated Aβ-fibers without activating nonmyelinated C-fibers.

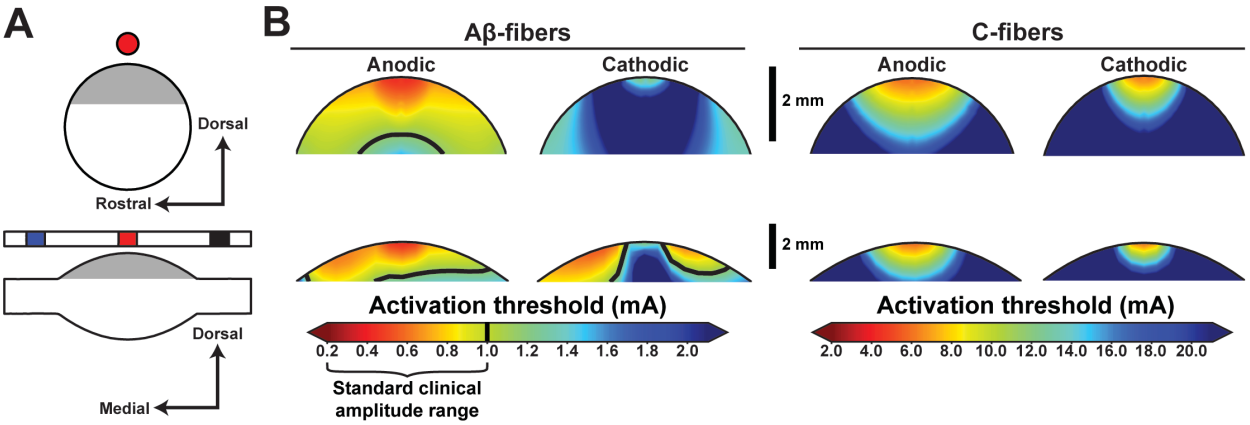

Figure 4.4 Activation thresholds with active electrode centered above DRG. DRGS amplitudes required to elicit one or more action potentials (activation threshold) in primary sensory neurons (PSNs) for anodic- and cathodic-first DRGS. (A) Sagittal (top) and transverse (bottom) DRG cross sections used to construct the threshold plots in B. Gray shaded regions indicate the locations of PSN somata. Electrode contacts are color coded such that: red = active electrode, blue = return electrode, black = inactive contact, white = insulated lead body. (B) Activation threshold plots for Aβ- and C-fibers. Black contour lines indicate the cutoff for clinical DRGS amplitude ranges (≤ 1 mA). Note the difference in color bar scales between the Aβ- and C-fibers.

4.4.3 DRGS drives regular firing of Aβ-fibers

Primary sensory neurons may go through quiescent periods in which they do not fire action potentials (e.g., when they do not receive sensory input). PSNs may also experience periods of spontaneous activity, such as in response to sensory stimuli or in some chronic pain states. Currently, we do not know how DRGS modulates the activity of sensory neurons in either state to provide analgesia. One theory suggests that DRGS provides analgesia by suppressing PSN hyperexcitability, or otherwise silencing abnormal electrical patterns of DRG neurons brought about by chronic pain.[254] Conversely, the gate control theory of pain suggests that stimulation-induced pain relief is achieved by repeatedly activating large myelinated somatosensory fibers, activating inhibitory interneurons in the dorsal horn that silence transmission neurons.[20,109]

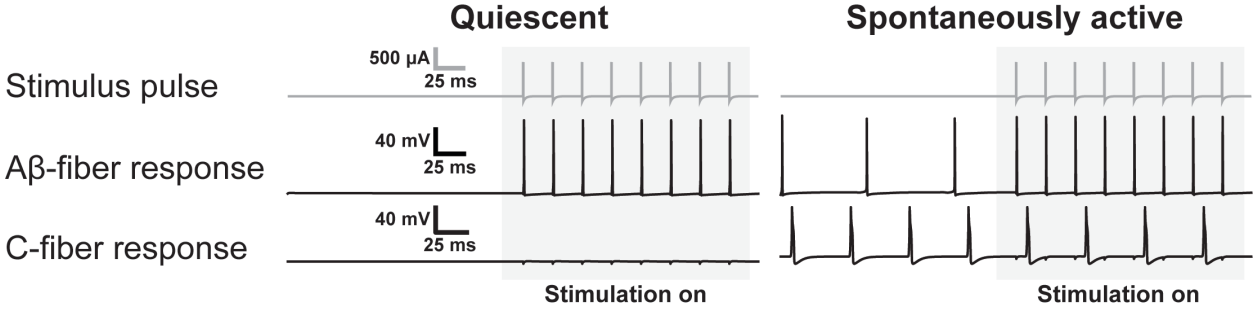

Figure 4.5 Neural response to DRGS pulse trains. Applying DRGS to quiescent and spontaneously-active primary sensory neurons. We applied an anodic DRGS pulse (top trace, gray) with an amplitude of 750 µA, a pulse width of 300 µs, and a pulse frequency of 40 Hz to example quiescent and spontaneously-active Aβ- and C-fibers. The somatic membrane potential traces (bottom traces, black) of an example Aβ- and C-fibers before and during DRGS are shown. Gray shaded regions indicate when DRGS is applied.

We tested these theories by examining how DRGS modulate PSN activity under quiescent and spontaneously active conditions. We implemented a pain-state model of an Aβ-fiber that generates ectopic action potentials from its soma (a feature of tactile allodynia),[245] and a pain-state model of a C-fiber that generates action potentials in the peripheral axon (e.g., in response to tissue damage). We then applied suprathreshold clinical DRGS (0.75 mA pulse amplitude, 300 µs pulse width, 40 Hz pulse frequency) to examine the effect of stimulation on quiescent and spontaneously

active fibers (**Figure 4.5**). Stimulating both quiescent and spontaneously active Aβ-fibers caused the fiber to fire one action potential in response to every stimulus pulse (i.e., one-to-one activation). DRGS did not elicit any action potentials in quiescent C-fibers. When stimulating spontaneously active C-fibers, DRGS did not suppress or drive activity. Instead, the cell continued to fire at its original frequency, and DRGS only evoked subthreshold responses. These results further suggest that clinical DRGS directly drives the activity of large myelinated Aβ-fibers without modulating C-fiber activity.

4.4.4 Effect of lead location

DRGS leads are implanted percutaneously, and guided into the intraforaminal space above the DRG.[287] Clinicians use fluoroscopic imaging to visualize lead location during implantation, but fluoroscopy cannot resolve neural tissue. Therefore, the position of active and return electrodes relative to the DRG is difficult to ascertain during implantation. With variations in patient anatomy, it is possible that electrode location with respect to the ganglion is inconsistent across patients, and could potentially lead to differences in patient outcomes. We examined the effect of electrode position on PSN activation thresholds to determine how lead placement altered neural activation.

After shifting the electrode along the nerve root 3.125 mm (i.e., half the distance from the middle of one contact to the middle of an adjacent contact) so that the active and return electrodes straddled the ganglion, cathodic and anodic DRGS again caused APs to typically initiate in the axon closest to the cathode for Aβ-fibers. For both cathodic and anodic DRGS, C-fiber APs usually initiated in the soma when the cell body was below a cathode, and the stem axon when the cell body was below an anode. When the cell body was halfway between the anode and cathode, C-fiber APs were generated in either the peripheral or central axon. **Figure 4.6** shows the activation

thresholds for Aβ- and C-fibers when the active and return electrodes straddled the DRG. With the active and return electrodes straddling the ganglion, most cathodic thresholds were lower than anodic thresholds. The minimum amplitudes needed to elicit an action potential in an Aβ-fiber was 0.27 and 0.34 mA for cathodic and anodic DRGS, respectively. The minimum amplitude to elicit an action potential in a C-fiber was 8.51 and 6.72 mA for cathodic and anodic DRGS, respectively. For Aβ-fibers, slightly fewer cells had anodic activation thresholds within clinical ranges when the active and return electrodes straddled the ganglion compared to when the active electrode is centered over the ganglion: 72.4% of cells vs 74.6% of cells, respectively. However, there were more Aβ-fibers with cathodic activation thresholds within clinical ranges when the active and return electrodes straddled the ganglion compared to the active electrode centered over the ganglion: 86.6% of cells vs. 29.5%, respectively. Straddling the active and return electrodes across the ganglion did not produce any C-fiber activation within clinical ranges. These results indicate that both stimulus polarity and the positioning of anodes and cathodes relative to the ganglia may alter the number of neurons activated by DRGS.

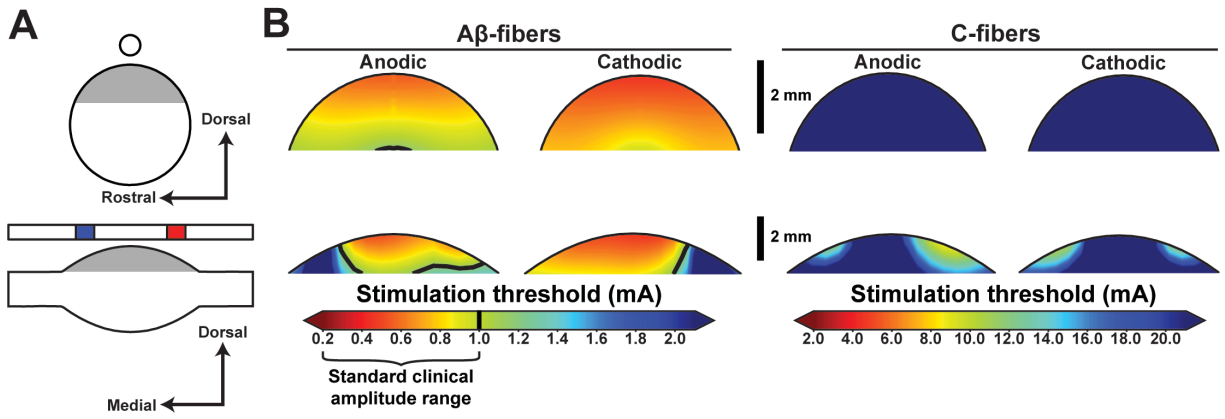

Figure 4.6 Activation thresholds with active and return contacts straddling DRG. DRGS amplitudes required to elicit one or more action potentials (activation threshold) in primary sensory neurons (PSNs) after shifting the electrode lead such that the active and return contacts straddle the ganglion. (A) Sagittal (top) and transverse (bottom) DRG cross sections used to construct the threshold plots in B. Gray shaded regions indicate the locations of PSN somata. The electrode lead is color coded such that: red = active electrode, blue = return electrode, black = inactive contact, white = insulated lead body. (B) Activation threshold plots for Aβ- and C-fibers. Black contour lines indicate the cutoff for clinical DRGS amplitude ranges (≤ 1 mA). Note the difference in color bar scales between the Aβ- and C-fibers.

4.5 Discussion

DRGS is a promising therapy for chronic intractable pain. However, not all patients receive sufficient pain relief from DRGS. There are several factors that may contribute to these shortcomings, such as inconsistencies in lead positioning, stimulation parameter selection, and possible differences in mechanisms of action of chronic pain between different pain etiologies. Another likely contributing factor is that the physiological mechanisms of stimulation-induced pain relief are unknown. This knowledge gap prevents the design of stimulation therapies to specifically target these mechanisms. Uncovering these physiological mechanisms will be essential in maximizing pain relief in all patient populations. The data presented in this study are an important next step towards this goal. Our results suggest that within the range of clinical stimulation parameters, DRGS activates large myelinated Aβ-fibers but not small nonmyelinated C-fibers. Therefore, we conclude that a primary mechanism of DRGS-induced pain relief may be the activation of pain-gating mechanisms in the dorsal horn. Furthermore, our data suggest that cathodic DRGS applied with the active and return electrodes straddling the ganglion may activate more Aβ-fibers than other electrode configurations.

4.5.1 Potential mechanism of clinical DRGS

We employed a computer modeling approach to study the mechanisms of DRGS on PSNs. DRG contain several types of sensory neurons: large myelinated proprioceptive and mechanoreceptive fibers (e.g., Aβ-fibers), small thinly myelinated mechanoreceptive, thermoceptive, and nociceptive fibers (e.g., Aδ-fibers), and small nonmyelinated mechanoreceptive and nociceptive fibers (e.g., C-fibers). In our model, we considered two sensory

neurons commonly studied in chronic pain – the large myelinated mechanoreceptive Aβ-fiber, and the small nonmyelinated nociceptive C-fiber. Our results suggest that DRGS within clinical ranges of stimulation parameters (e.g., amplitude, pulse width) are directly activating Aβ-fibers, but not C-fibers (**Figure 4.4**). We observed this result irrespective of lead placement and stimulation configuration (**Figure 4.6**). DRGS caused one-to-one activation of Aβ-fibers, regardless of the fiber's activity before DRGS was turned on (**Figure 4.5**). Repeated activation of large myelinated Aβ-fibers suggests that DRGS may provide pain relief by activating pain-gating mechanisms within the spinal cord.[20] This aligns well with the current theories on the mechanisms of action of SCS for pain, where SCS activates the large myelinated Aβ-fibers of the dorsal columns, which activate inhibitory interneurons in the dorsal horn.[25,67,288]

A recent computational study of DRGS examined the effect of stimulation on C-fibers.[76] Kent and colleagues showed that DRGS activates C-fibers with stimulation amplitudes on the order of several milliamps, similar to the ranges reported in this study. We also corroborated their finding that action potentials typically initiate around the soma or stem axon in C-fibers. Their results suggest that DRGS could potentially generate analgesia by blocking painful afferent signals from propagating into the spinal axon by enhancing low-pass filtering of noxious afferent signals at C-fiber T-junctions. However, the stimulation amplitudes reported to elicit sustained block were far outside clinical ranges (>9.5 mA). Therefore, we believe that in clinical scenarios, T-junction filtering is unlikely to be the primary mechanism of DRGS-induced pain relief, though it is likely important in normal physiologic pain processing.[47,48] Instead, our results suggest that DRGS within clinical parameter ranges directly activates large myelinated afferent fibers.

In this work, we used a computer model to examine the direct effects of DRGS on primary sensory neurons within the DRG. However, more work is needed to fully elucidate the pain-relief

mechanisms of DRGS, particularly the downstream effects of stimulation. Recent studies have provided insight into the complexity of the spinal networks that govern pain transmission, highlighting that Aβ-afferents synapse onto both excitatory and inhibitory interneurons in the dorsal horn, which mediate the activity of projection neurons that carry sensory signals to the brain.[190,289,290] It is currently unknown: (1) how different chronic pain etiologies sensitize or disinhibit the various components of this network, (2) how the prolonged driving of Aβ-fiber activity with DRGS may induce changes in this network, (3) how Aβ-fiber and dorsal horn network response to stimulation may change in response to chronic DRGS, and (4) how long-term DRGS-induced changes in network dynamics vary between chronic pain etiologies. Experiments designed to answer these questions may provide insight into which pain etiologies are likely to receive therapeutic benefit from DRGS,[114] and why the therapeutic efficacy of DRGS appears to decrease over time.[41,44] Furthermore, the results of those studies may inform the design of future computer models of DRGS to examine the effects of DRGS on dorsal horn circuitry. Such models could be used to optimize stimulation parameters to provide maximal pain relief.

4.5.2 Effect of electrode lead placement on neural activation

Because x-ray fluoroscopy cannot resolve neural tissue, it is difficult to determine the position of DRGS electrodes relative to the ganglion during implantation. It is possible that electrode placement with respect to the ganglion could be variable across patients, which may be a factor in the limited success of DRGS. To determine how this may affect the neural activation produced by DRGS, we examined the effect of lead position relative to the ganglion on DRGS-induced neural activation (**Figure 4.6**). We showed that regardless of lead position, clinical DRGS activates Aβ-fibers but not C-fibers. When the active and return electrodes straddled the ganglion, cathodic DRGS activated significantly more Aβ-fibers than when the active electrode was centered

above the ganglion (86.6% and 29.5% of Aβ-fibers within the ganglion, respectively). This result is likely due to the cathode being closer to the nerve root, which contains the axons of PSNs but not cell bodies. It is well understood that cathodic extracellular stimulation has lower thresholds when the cathode is near an axon compared to near a cell body.[51,291] Interestingly, when the active and return electrodes straddled the ganglion, the number of cells activated by clinical ranges of anodic DRGS only decreased by 2.2%, possibly because the active electrode remained close enough to the ganglion to directly stimulate cells with somata around the dorsal edge of the ganglion.

These results suggest that if DRGS provides pain relief by activating Aβ-fibers, the optimal stimulation parameters may be to have the active and return electrodes straddle the DRG and to apply cathodic DRGS. This is consistent with previous clinical reports that suggested straddling the second and third electrodes across the pedicle was the ideal electrode lead location.[41] Lumbar ganglia are typically located under the pedicle in the 'foraminal region,' suggesting that electrode location with respect to the pedicle may be a good proxy for electrode location with respect to the ganglia at those levels.[95,222,292]

Our model suggests that a straddled electrode configuration would activate the largest number of Aβ-fibers for a given stimulation amplitude, thus minimizing power consumption. It is important to note that our model assumed a homogeneous distribution of each afferent type throughout the DRG, while the spatial distribution of different types of PSNs in human DRG is unknown. Previous studies in rats suggest that two-thirds of L5 DRG neurons are C-type fibers,[293] and that lumbar DRG may show digit-specific organization.[208] However, it is unclear if DRG neurons also organize based on sensory modality, though it has been suggested.[142] Deciphering

the location of Aβ-fibers within human DRG may inform the ideal location in which to place the electrode lead to effectively target these populations.

4.5.3 Limitations

We used a computer model to investigate which cells are directly stimulated by DRGS. Computer modeling has been a powerful tool in understanding the mechanisms of action of other neurostimulation therapies, such as deep brain stimulation and SCS.[52,66,294,295] However, it will be imperative to confirm our findings with experimental data, and to use those data to validate and refine our model design. Furthermore, there are several limitations to our approach with regards to studying DRGS-induced pain relief. First, we examined only two sensory neurons found within human DRG: Aβ- and C-fibers. Though Aβ-fibers and C-fibers are crucial in the development and maintenance of chronic pain, other cell types, such as Aα-proprioceptors and Aδ-thermoceptors and nociceptors, may also play important roles.[97] In particular, Aδ-fibers are of interest, as Aδ-fibers typically convey thermal or mechanical pain.[99,110,296] Since Aδ-fibers are myelinated, albeit thinly, it is possible that DRGS will directly affect their firing patterns compared to the nonmyelinated C-fibers. However, we excluded these fibers from our analyses because of a paucity of experimental data necessary to describe Aδ-fiber ion channel physiology. Because Aδ-fibers are known to play an important role in several forms of chronic pain,[99,110,247] future computational modeling studies should consider the effects of DRGS on Aδ-fibers.

We made several simplifications with regards to the ion channels included in our multi-compartment sensory neuron models. Sensory neurons express a myriad of ion channels, but due to computational demands and limited experimental data, it is not possible to model every ion channel type present in sensory neurons. Therefore, we focused on the major ion channels necessary to reproduce the somatic action potential characteristics described in previous

experimental studies. Future DRGS studies could consider a more complete model of PSN ion channel physiology, particularly with regards to the long-term effects of stimulation (e.g., calcium sequestration, synaptic transmitter release).

We developed a simplified representation of a human DRG using a cylindrical volume conductor model, a similar approach used previously to study the mechanisms of action of neurostimulation therapies.[33,52,53,294] We assumed an idealized trajectory for axons within the ganglion. In our models, stem axons projected towards the midline of the ganglion and nerve root, then bifurcated into central and peripheral axons which curved ventrally before entering the nerve root and following straight trajectories. In reality, stem axons are complex and winding, forming tightly packed glomeruli around somata before reaching bifurcating nodes.[97] The impact of tightly coiled stem axons on DRGS thresholds is currently unclear. Future studies should examine the effects of complex stem axon trajectories on neuronal activation, and the extent to which ephaptic phenomena may influence DRGS outcomes.

4.6 Conclusions

DRGS is a promising therapy for chronic intractable pain. We examined which cell types in the DRG are directly stimulated by DRGS within clinical ranges of stimulation parameters. The results of this study suggest that large myelinated PSNs are directly driven by DRGS, indicating that DRGS-induced analgesia may be achieved by activating pain-gating mechanisms in the dorsal horn. We demonstrated that the position of the active and return electrodes can influence neural activation. Our results suggest that cathodic DRGS applied when the active and return electrodes straddle the ganglia activates more large myelinated afferents than electrodes placed over the medial aspect of the DRG

Chapter 5 – The Effect of Clinically Controllable Factors on Neural Activation During Dorsal Root Ganglion Stimulation

The work presented in this chapter is published as:

Graham RD, Bruns TM, Duan B, Lempka SF. The effect of clinically controllable factors on neural activation during dorsal root ganglion stimulation. *Neuromodulation*. 2021;24:655-671.[119]

5.1 Abstract

Objective:

Dorsal root ganglion stimulation (DRGS) is an effective therapy for chronic pain, though its mechanisms of action are unknown. Currently, we do not understand how clinically controllable parameters (e.g., electrode position, stimulus pulse width) affect the direct neural response to DRGS. Therefore, the goal of this study was to utilize a computational modeling approach to characterize how varying clinically controllable parameters changed neural activation profiles during DRGS.

Methods:

We coupled a finite element model of a human L5 DRG to multicompartment models of primary sensory neurons (i.e., Aα-, Aβ-, Aδ-, and C-neurons). We calculated the stimulation amplitudes necessary to elicit one or more action potentials in each neuron, and examined how neural activation profiles were affected by varying clinically controllable parameters.

Results:

In general, DRGS predominantly activated large myelinated Aα- and Aβ-neurons. Shifting the electrode more than 2 mm away from the ganglion abolished most DRGS-induced neural

activation. Increasing the stimulus pulse width to 500 μs or greater increased the number of activated Aδ-neurons, while shorter pulse widths typically only activated Aα- and Aβ-neurons. Placing a cathode near a nerve root, or an anode near the ganglion body, maximized Aβ-mechanoreceptor activation. Guarded active contact configurations did not activate more Aβ-mechanoreceptors than conventional bipolar configurations.

Conclusions:

Our results suggest that DRGS applied with stimulation parameters within typical clinical ranges predominantly activates Aβ-mechanoreceptors. In general, varying clinically controllable parameters affects the number of Aβ- mechanoreceptors activated, although longer pulse widths can increase Aδ-neuron activation. Our data support several Neuromodulation Appropriateness Consensus Committee guidelines on the clinical implementation of DRGS.

5.2 Introduction

Chronic pain poses one of the greatest public health challenges currently facing the United States, with more than 14 million Americans reporting they live with "a lot of pain" on a daily basis.[11] In an effort to combat the pain epidemic, the prescription rate of opioids, a common pharmacologic pain management strategy, quadrupled over the past 20 years.[12] Over the same timeframe, there was a 200% increase in the rate of overdose deaths involving opioids.[13] As the death rates from opioid-related drug overdoses have continued to climb in recent years,[14] the need for nonaddictive pain therapies has become even more pressing.

Neurostimulation therapies are effective, nonaddictive treatment strategies for chronic pain that is refractory to conventional medical management. Spinal cord stimulation (SCS) is a neurostimulation therapy primarily used to treat intractable neuropathic pain in the lower limbs

(e.g., failed back surgery syndrome).[27] SCS is achieved by implanting an electrode lead in the spinal epidural space, and applying brief electrical impulses to the dorsal columns (DCs).[281] However, due to the complex anatomy of the spinal column, SCS struggles to treat certain pain etiologies, particularly pain that is highly focalized to specific dermatomes (i.e., regions of the body), such as the groin and foot.[38]

Dorsal root ganglion stimulation (DRGS) was approved by the U.S. Food and Drug Administration in early 2016 for the treatment of intractable complex regional pain syndrome in the lower limbs,[39,90] and has shown success at treating several other focal pain indications (e.g., phantom limb pain, painful diabetic neuropathy, groin pain).[40–42] In contrast to SCS, DRGS electrodes are placed in the intraforaminal space, where they apply electrical stimulation to a single DRG. There are bilateral pairs of DRG at each level of the spinal cord, with each DRG containing the cell bodies, and a portion of the axons, of all the primary sensory neurons innervating a single dermatome.[93] DRG neurons are pseudounipolar: a single axon process extends from the soma, bifurcates at a large node of Ranvier called the T-junction, and forms an axon that projects to the spinal cord and an axon that extends to the periphery.[97] Due to the precise targeting of a single dermatome's primary afferents, DRGS is rationalized to provide patients with focal, dermatome-specific pain relief.

Although preliminary clinical results indicate that DRGS provides adequate pain relief for many patients, approximately 20–30% of patients do not receive sufficient pain relief from DRGS.[90] Furthermore, long-term studies showed that DRGS may lose efficacy over time,[42,44] a trend also found in long-term clinical studies of SCS.[28,297] These two shortcomings of DRGS can partially be attributed to the fact that we do not have a clear understanding of the physiologic mechanisms of action of DRGS. Uncovering the mechanisms by which DRGS provides pain relief

will allow scientists and engineers to innovate the technology to specifically target these mechanisms to ultimately improve clinical outcomes.

A recent computational modeling study suggested that DRGS may provide pain relief by augmenting a low-pass filtering mechanism at the T-junction, preventing nociceptive impulses from propagating from the periphery to the spinal cord.[76] However, the stimulation amplitudes necessary to augment T-junction filtering (> 9 mA) were far greater than the amplitudes used clinically (≤ 1 mA on average). Using a similar computational modeling approach, we recently showed that for stimulation parameters used clinically, DRGS may directly activate large-diameter myelinated Aβ low-threshold mechanoreceptors (Aβ-LTMRs; putative innocuous touch-sensing neurons), but not small-diameter nonmyelinated C-nociceptors.[118] However, this study did not examine the effect of DRGS on Aα-neurons, large myelinated afferents that innervate muscles,[103] or Aδ-neurons, a diverse class of medium-diameter, thinly-myelinated afferents that can convey noxious or innocuous sensations.[104] Furthermore, there are several clinical factors which affect the delivery of electrical stimulation to neural tissue, such as the placement of the electrode lead relative to the neural target[31,51,118] and the choice of stimulation parameters (e.g., pulse width, pulse frequency).[33,298] Currently, it remains unclear how these clinically controllable parameters affect the recruitment of different types of primary afferents for pain relief during DRGS. It is vital to understand how factors under clinical control influence neural activation, as these factors likely directly influence the efficacy of DRGS. Therefore, these factors are key in ensuring positive patient outcomes.

In this work, we employed a computer model of DRGS to study how clinical factors, such as electrode position and stimulation parameter selection, affect primary afferent recruitment. We coupled a finite element model (FEM) of a human L5 DRG to multicompartment models of

primary sensory neurons to study how these clinically controllable factors affected neural activation during DRGS. We considered our results in context with the recommendations of the Neuromodulation Appropriateness Consensus Committee (NACC) on best practices for DRGS.[77]

5.3 Methods

Building upon our prior work,[118] we developed a computer model of DRGS to investigate how clinically controllable factors (e.g., electrode position, stimulus parameter selection) affect neural activation in the DRG. We coupled an FEM of a human L5 DRG to multicompartment models of sensory neurons. We used the FEM to calculate the voltage distribution generated by DRGS, and applied these voltages to the multicompartment models. We examined which types of neurons generated action potentials in response to DRGS, and how neural activation patterns changed as we varied electrode position and stimulation parameters (i.e., pulse width, pulse frequency, stimulus configuration).

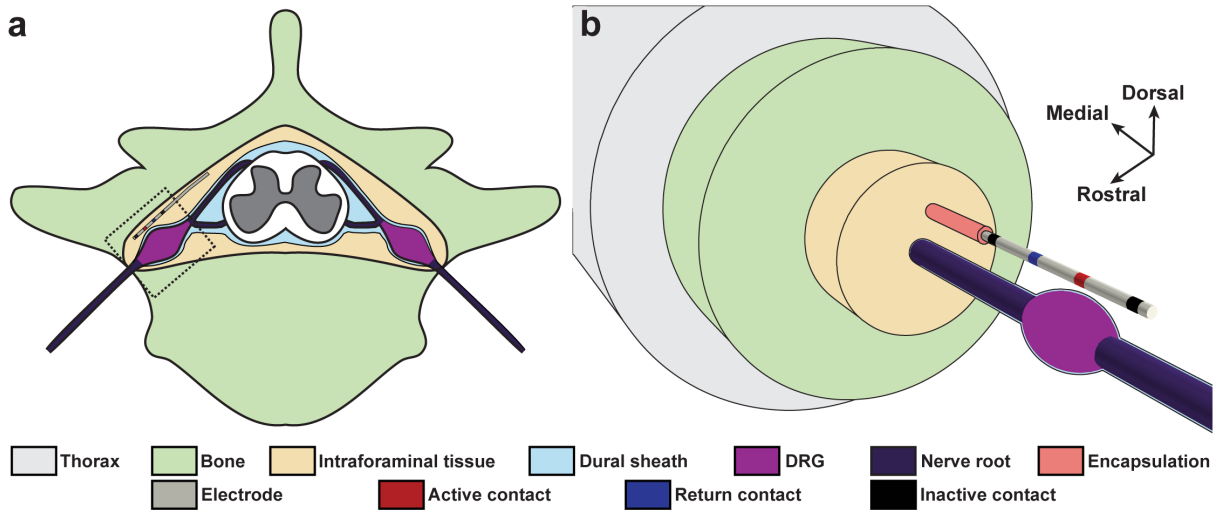

Figure 5.1 FEM of human L5 DRG and surrounding anatomy. a. Representative schematic of the human L5 spinal column, dorsal root ganglion, surrounding anatomy, and four-contact DRGS electrode lead. The dashed box represents the general area represented by the FEM. b. Exploded view of the concentric cylindrical domains used to create the FEM. On the four-contact DRGS electrode lead, the red contact indicates the active contact, the blue contact is the return contact, and the black contacts are inactive. DRGS, dorsal root ganglion stimulation; FEM, finite element model.

Table 5.1 Dimensions of the finite element model of a human L5 dorsal root ganglion (DRG).

Parameter	Value	Reference
DRG length	9.4 mm	[95]
DRG width	5.9 mm	[95]
Nerve root radius	1.19 mm	[256]
Dural sheath thickness	150 μm	[257]
Foramen height	17.1 mm	[95]
Encapsulation layer	300 μm	[259]
Electrode contact length	1.25 mm	[96]
Electrode radius	0.5 mm	[96]
Electrode contact spacing	5 mm	[96]

5.3.1 Step 1: Calculate the voltage distribution generated by DRGS

We constructed an FEM of a human L5 DRG and its surrounding anatomy (e.g., intraforaminal tissue, foraminal bone) based on experimentally measured values (**Table 5.1**, **Figure 5.1**). We based the geometry of the model on imaging and cadaver studies of human DRG and foraminal tissues.[95,96,256,257] We wanted to examine the effect of electrode lead position relative to the ganglia, and the effect of lead distance from the ganglia on primary afferent recruitment. Therefore, we used a larger measured value for foraminal height (17.1 mm) in this model than in our previous model to allow a greater range of distances to be tested.[95] We set the electrical conductivity of each tissue (**Table 5.2**) to the values used in our previous study of DRGS.[118,258–260] We modeled all conductivities as isotropic, with the exception of the nerve root, which we modeled as anisotropic white matter.[118] We built the FEM in the commercially available software 3-matic Module within the Mimics Innovation Suite (Materialise, Brussels, Belgium). We included an explicit representation of a four-contact DRGS electrode array in the FEM, with the second electrode contact centered above the middle of the DRG. In some simulations, we shifted

the electrode 3.125 mm laterally along the nerve root axis, such that the midpoint between the second and third contacts was centered above the middle of the DRG (i.e., so the second and third contacts straddled the ganglion). We surrounded the electrode with a 300-μm encapsulation layer to represent the foreign body response to implanted materials.[259]

Table 5.2 Electrical conductivities assigned to the anatomical compartments of the finite element model.

Parameter	Value	Reference
Gray matter	0.23 S/m	[258]
White matter (longitudinal)	0.6 S/m	[258]
White matter (transverse)	0.083 S/m	[258]
Dural covering	0.6 S/m	[118]
Bone	0.02 S/m	[260]
General tissue	0.25 S/m	[258]
Encapsulation	0.17 S/m	[259]

We imported the FEM into COMSOL Multiphysics (COMSOL, Inc., Burlington, MA, USA). To simulate bipolar DRGS,[77] we applied a unit current stimulation boundary condition (i.e., 1 A) to the active electrode contact and grounded (i.e., 0 V) the return contact. To improve stimulation selectivity, clinical SCS sometimes utilizes a guarded cathode stimulation configuration: two electrode contacts adjacent to the active contact are used as return contacts.[69,299,300] To our knowledge, the use of a guarded cathode stimulation configuration in DRGS has not been reported. To explore the utility of the guarded cathode configuration in DRGS, we applied current stimulation to either the second or third contact, and grounded the contacts immediately adjacent to the active contact (e.g., grounding the first and third contacts for an active second contact). In all simulations, we modeled the electrode lead shaft as a perfect insulator, and inactive contacts as equipotential with zero net current across their surface. To calculate the voltage

distribution generated by DRGS, we used the conjugate gradient method to solve Laplace's equation:

$$\nabla \cdot (\sigma \cdot \nabla \Phi) = 0 \tag{5.1}$$

where σ is the tissue conductivity tensor, and Φ is the calculated voltage distribution. **Figure 5.2** shows voltage distributions generated by DRGS using example stimulation configurations. We validated the FEM by its ability to produce bipolar impedances similar to impedances reported clinically.[77] To calculate model impedance, we divided the average voltage across the active contact's surface by the applied stimulus current. From the ACCURATE clinical trial, average bipolar DRGS electrode impedances one year post-implant were 1458.9 ± 714.5 Ω.[77] Our models produced a minimum bipolar impedance of 1358 Ω, when the active contact was centered immediately above the DRG and the return contact was adjacent to the active electrode and more proximal to the spinal cord. Our models produced a maximum bipolar impedance of 1552 Ω when the most distal contact and most proximal contact formed a longitudinal bipole pair. All model bipolar impedances fell within clinical range.

Table 5.3 Validation metrics for the Aα-neuron model.

Aα-fiber			
Parameter	**Our Value**	**Literature Ranges**	**Reference**
Soma AP Amplitude (mV)	108.6	109.72 +/- 11.21	[282]
AP duration (base) (ms)	1.075	0.98 +/- 0.2	[265]
Rise time (ms)*	0.675	0.46 +/- 0.13	[283]
Fall time (ms)*	0.4	0.89 +/- 0.41	[283]
AHP amplitude (mV)	3.68	6.5 +/- 4.2	[301]
AHP half-amplitude duration (ms)	12.175	10.9 +/- 11.0	[266]

Resting potential (mV)	-79.2	-80.0	[285]
CV (m/s)	90.4	89.7 +/- 7.6	[103]
CV (m/s)	83.5	89.7 +/- 7.6	[103]

*AP, action potential; AHP, afterhyperpolarization; CV, conduction velocity. *Indicates a model value outside of the previously reported experimental ranges.*

5.3.2 Step 2: Develop multi-compartment models of primary sensory neurons

We implemented multicompartment models of primary sensory neurons found in human DRG using the NEURON simulation environment (v7.4).[261] We implemented previously published models of an Aβ-LTMR and C-nociceptor (**Figure 5.3a,d**).[118] We developed a model of an Aα-afferent by extending the previously published model of an Aβ-LTMR to include large-diameter (i.e., 15–16 μm) axons. Because Aα- and Aβ-neurons share electrophysiologic characteristics,[283] we implemented the membrane dynamics of our previously published Aβ-LTMR in our Aα-neuron model (**Figure 5.3a**). The Aα-neuron reproduced many action potential (AP) and conduction velocity (CV) data seen in experimental literature(e.g., AP height, duration) (**Table 5.3**). We developed two distinct multicompartment models of Aδ-neurons: an LTMR (**Figure 5.3b**) and a high-threshold mechanoreceptor (HTMR) (**Figure 5.3c**).[104] Aδ- LTMRs and Aδ-HTMRs express distinct voltage-gated sodium channel profiles.[187] Aδ-LTMRs mainly express Nav1.6, similar to other non-nociceptive myelinated mechanoreceptors,[302] while Aδ-HTMRs express Nav1.7 and Nav1.8, similar to C-nociceptors.[303,304] Therefore, we developed two Aδ-neuron models, an LTMR and an HTMR model, distinguished by their active voltagegated sodium channels. Both models had the same morphology. Each model had a soma 29 μm long and 34 μm wide, connected to a 3.0-μm stem axon.[184] The Aδ-neuron axon morphologies (**Table 5.4**) were based on the McIntyre-Richardson-Grill (MRG) model of a mammalian peripheral axon.[263] The stem axon extended 840 μm to match the total stem axon and soma length of the Aα-neuron, Aβ-

LTMR, and C-nociceptor models (i.e., 869 μm), before splitting into two axons. One axon projected towards the spinal cord, with a diameter of 2.0 μm,[52,184] while the other projected to the periphery and had the same diameter as the stem axon (i.e., 3.0 μm).[132,184] The original MRG axon model was parametrized for axons of specific diameters (e.g., 2.0, 5.7, 7.3 μm). To implement an axon with a diameter not included in the original model, such as the 3.0-μm stem and peripheral axons used in the Aδ-neuron models, we performed a linear regression to calculate the values of each parameter (e.g., number of myelin lamellae, internodal length) for a given axon diameter.[305]

The nodes of Ranvier in the myelinated axon models were separated by three distinct finite impedance myelin segments: two myelin attachment sections, two paranode main segments, and six internodal segments.[264] To reduce computational demand of the Aδ-neuron models (i.e., medium diameter myelinated axons with short internode distances), we modeled the internodal segments farther than 20 mm from the active electrode with only a single compartment. This simplification did not produce significant differences in the activation thresholds (data not shown). The nodes of Ranvier contained active sodium and potassium conductances, and a linear leak conductance. Both models contained an A-type and delayed rectifier potassium conductance.[268] The Aδ-LTMR model nodes contained a Nav1.6 conductance,[306] while the Aδ-HTMR model nodes contained a Nav1.7 and Nav1.8 conductance.[268] We set all nodal sodium conductances to 3.0 S/cm2 (52). We set the LTMR model's somatic Nav1.6 conductance to 1.0 S/cm2, to best reproduce electrophysiologic data reported by literature. To best reproduce electrophysiologic data, we set the HTMR model's somatic Nav1.8 conductance to 0.3 S/cm2, A-type potassium conductance to 0.28 S/cm2, delayed rectifier potassium conductance to 6 mS/cm2, and all compartments' leak conductance to 2 mS/cm2. We validated the models based on their ability to reproduce AP and CV data reported in the literature (**Table 5.5**).[283,301,307]

Next, we distributed our multicompartment models of primary afferent neurons throughout the DRG FEM as described previously.[118] Previous histologic studies of mammalian and human DRG showed that cell bodies preferentially organize around the dorsal edge of the ganglion.[45,83] Therefore, we generated two two-dimensional regular grids—one intersecting the midpoint of the ganglion in the sagittal plane, and the other in the transverse plane—with 100-μm spacing in all directions, resulting in 2304 points. We used each point on the grid as a seed point for the somata of the cell models described in step 2. From each seed point, the stem axon projected toward the midline of the ganglion, then bifurcated into central and peripheral axon processes that curved ventrally to enter the nerve root (**Figure 5.1a**).

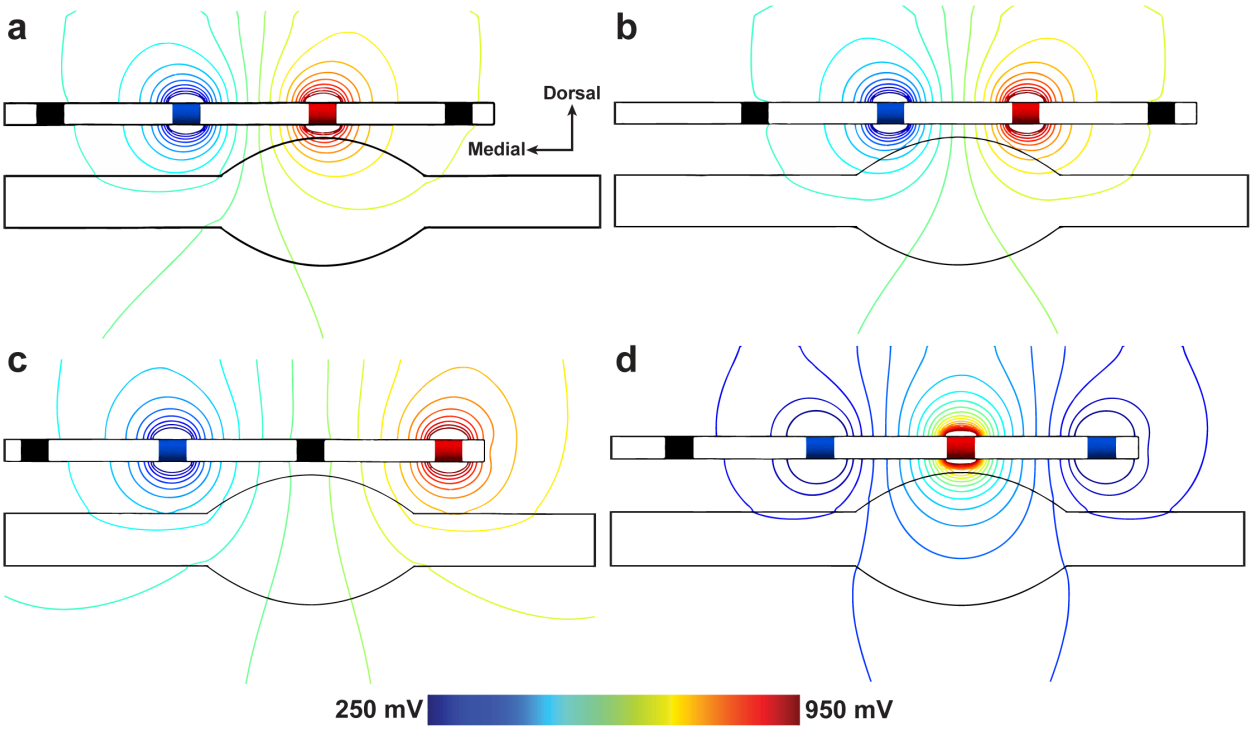

Figure 5.2 DRGS stimulation configurations. Isopotential lines of the voltage distributions generated by DRGS using example stimulation configuration: a. adjacent bipole with the active contact centered above the ganglion, b. adjacent bipole with the active and return contacts straddling the ganglion, c. separated bipole, and d. guarded contact with the active contact centered above the ganglion. Red contacts are active contacts, blue contacts are return contacts, black contacts are inactive.

5.3.3 Step 3: Simulate the neural response to DRGS

We interpolated the extracellular potentials calculated in Equation (1) onto the middle of each compartment of the cell models generated in step 2. We applied the extracellular potentials to the multicompartment models using NEURON's extracellular mechanism within the Python programming language.[280] We calculated each compartment's time-varying membrane voltage in response to DRGS by using a backward Euler implicit integration method with a time step of 5 μs (**Figure 5.4b**). The tissue conductivities of the FEM were linear. Therefore, the voltage distribution generated by a specific DRGS amplitude was a scalar multiple of the voltage distribution generated by a unit stimulus (i.e., a 1 A stimulus).[238]

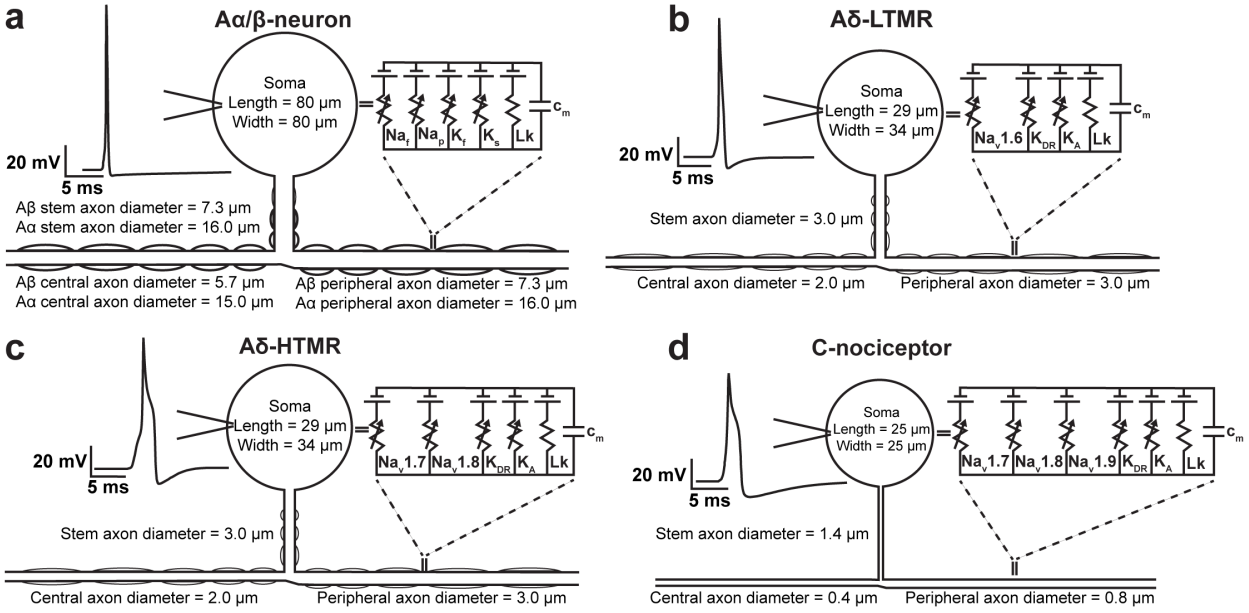

Figure 5.3 Multicompartment models of DRG sensory neurons. We implemented models of five types of sensory neurons found in DRG: (a) large-diameter, myelinated Aα- and Aβ-neurons; (b) a small-diameter, thinly myelinated Aδ-LTMR; (c) a small-diameter, thinly myelinated Aδ-HTMR; and (d) a small-diameter, nonmyelinated C-nociceptor. The Aα-neuron, Aβ-LTMR, and Aδ-LTMR putatively convey innocuous sensory information, while the Aδ-HTMR and C-nociceptor are putatively nociceptive. For each cell model, the equivalent circuit diagrams show the active voltage-gated ion channels included in each cell type and a linear leak conductance. Inset action potentials represent the somatic membrane response to a brief intracellular current pulse applied to the peripheral axon. DRGS, dorsal root ganglion stimulation; HTMR, high-threshold mechanoreceptor; LTMR, low-threshold mechanoreceptor.

Our goal was to study how clinically controllable factors (e.g., electrode lead position, stimulus parameters) affected neural activation in the DRG. Therefore, for each simulation, we calculated the minimum stimulus amplitude necessary to elicit one or more action potentials in

each neuron type (i.e., the activation threshold). Each stimulus pulse was a charge-balanced, biphasic pulse with an active stimulus phase and a passive discharge phase with an interphase interval of 20 μs.[76,281] Unless otherwise noted, we calculated activation thresholds in response to a single stimulus pulse with a 300-μs active phase (the approximate average pulse width reported by the ACCURATE clinical trial[90]), with the electrode lead positioned directly above the ganglion (i.e., with a 0-mm electrode shift). We calculated activation thresholds for both anodic- and cathodic-first pulses (i.e., stimulus pulses with a positive active phase and negative active phase, respectively), using a binary search algorithm with a resolution of 0.1 μA.

Table 5.4 Morphologic parameters for both Aδ-neuron models.

Parameter	Value	Reference
Fiber diameter (peripheral)	3.0 μm	184
Fiber diameter (central)	2.0 μm	184
Fiber diameter (stem)	3.0 μm	135,184
Stem axon length	840 μm	133,135,262
Soma length	29 μm	184
Soma diameter	34 μm	184
Node length	1.0 μm	263
Paranode length	3.0 μm	263
Juxtaparanode length	Variable	263
Internode length	Variable	133,263

We sought to identify which types of primary afferents (i.e., Aα-neurons, Aβ-LTMRs, Aδ-neurons, C-nociceptors) are likely activated by DRGS within parameter ranges used clinically. Therefore, we defined a maximum clinical amplitude of 2.0 mA, which is approximately the mean DRGS amplitude plus two standard deviations at one-year postimplant reported by the ACCURATE clinical study.[77] We considered any neuron with an activation threshold less than or equal to this maximum clinical amplitude (i.e., 2 mA) as activated within clinical ranges of

stimulation parameters (i.e., clinical DRGS). When examining the effect of stimulus pulse frequency, we simulated 200 ms of DRGS with a pulse amplitude of 1 mA, and a pulse width of 300 μs. Then, we calculated the response frequency, that is, the frequency of action potentials generated in response to DRGS of different pulse frequencies, of different types of neural compartments (e.g., the soma, the spinally projecting axon, etc.).

Table 5.5 Validation metrics for the Aδ-neuron models.

Low threshold mechanoreceptor (LTMR)			
Parameter	**Our Value**	**Literature Ranges**	**Reference**
Soma AP Amplitude (mV)	95.6	98.0 +/- 4.0	[301]
AP duration (base) (ms)	1.9	1.76 +/- 0.28	[283]
Rise time (ms)	0.9*	0.68 +/- 0.094	[283]
Fall time (ms)	1.0	1.07 +/- 0.22	[283]
AHP amplitude (mV)	7.9	9.5 +/- 3.7	[307]
AHP half-amplitude duration (ms)	1.6	3.0 +/- 2.6	[307]
Resting potential (mV)	-53.6	-55.2 +/- 9.6	[307]
CV (peripheral axon) (m/s)	5.3	1.3 – 12	[307]
CV (central axon) (m/s)	2.5	1.3 – 12	[307]
High threshold mechanoreceptor (HTMR)			
Parameter	**Our Value**	**Literature Ranges**	**Reference**
Soma AP Amplitude (mV)	85.86	77.0 +/- 13.2	[307]
AP duration (base) (ms)	3.65	3.0 +/- 0.72	[283]
Rise time (ms)	1.85*	1.18 +/- 0.31	[283]

Fall time (ms)	1.8	1.9 +/- 0.6	283
AHP amplitude (mV)	10.0	12.3 +/- 4.1	307
AHP half-amplitude duration (ms)	2.0	9.2 +/- 9.0	307
Resting potential (mV)	-55.06	54.1 +/- 10.1	307
CV (peripheral axon) (m/s)	3.72	1.3 – 12	307
CV (central axon) (m/s)	1.71	1.3 – 12	307

AHP, afterhyperpolarization; CV, conduction velocity; *a model value outside of the previously reported experimental ranges

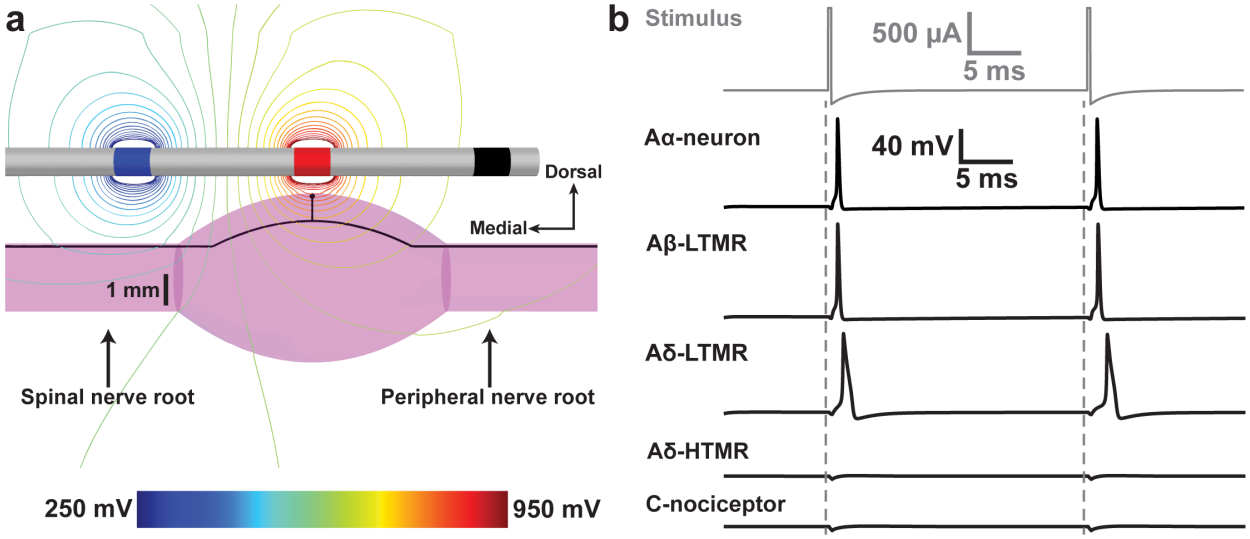

Figure 5.4 Simulating the neural response to DRGS. a. Isopotential lines of the voltage distribution generated by bipolar DRGS. The black trace in the DRG represents an example cell trajectory for a pseudounipolar primary sensory neuron. The red contact is the active contact, the blue contact is the return contact, and black contacts are inactive. b. Simulating the time-varying membrane potential of each sensory neuron cell type in response to a 1 mA anodic-first DRGS stimulus train (top trace, gray). The five black traces represent the somatic membrane potential of each type of sensory neuron with the example trajectory shown in part (a). Note that the putatively innocuous neurons (the Aα-neuron, Aβ-LTMR, and Aδ-LTMR) fire action potentials in response to a clinical DRGS pulse, while the putatively nociceptive models (the Aδ-HTMR and C-nociceptor) do not. DRGS, dorsal root ganglion stimulation; HTMR, high-threshold mechanoreceptor; LTMR, low-threshold mechanoreceptor.

5.4 Results

5.4.1 Effect of electrode position

Recent clinical studies have highlighted the importance of the electrode location relative to the ganglion to DRGS-induced pain relief.[308,309] To examine the effect of electrode position on DRGS-induced neural activation, we calculated activation thresholds for each cell type in response to DRGS applied with several electrode locations relative to the ganglion. **Figure 5.5** shows the percentage of modeled neurons with activation thresholds within clinical range (i.e., ≤ 2 mA) as distance between the lead and the DRG increased, both when the active electrode contact was centered above the ganglion and when the active and return contacts straddled the ganglion.

In general, for all electrode lead positions, clinical DRGS only activated myelinated afferents (i.e., Aα-, Aβ-, and Aδ-neurons) and did not activate nonmyelinated C-nociceptors (**Figure 5.5**). As the distance between the active contact and the ganglion increased, the percentage of myelinated afferents activated by clinical DRGS decreased. Generally, straddling the active and return contacts across the ganglion activated a larger percentage of Aβ-LTMRs than centering the active contact above the ganglion.

When the active contact was centered directly above the ganglion (i.e., with a 0-mm electrode shift), anodic-first DRGS (**Figure 5.5a**) activated 12% of Aδ-LTMRs, while cathodic-first DRGS (**Figure 5.5c**) activated less than 1% of modeled Aδ-LTMRs. When the active and return contacts straddled the ganglion, anodic-first (**Figure 5.5b**) and cathodic-first (**Figure 5.5d**) DRGS activated 2 and 3% of modeled Aδ-LTMRs, respectively. However, shifting the electrode lead 1 mm dorsally abolished activation of all Aδ-LTMRs. We observed minimal activation in Aδ-HTMRs. Anodic-first DRGS activated 3% of modeled Aδ-HTMRs only during anodic-first DRGS when the active contact was centered directly above the ganglion (**Figure 5.5a**). Shifting the electrode lead 1 mm dorsally abolished all Aδ-HTMR activation. We did not observe Aδ-HTMR activation during cathodic-first DRGS (**Figure 5.5a,d**), nor during anodic-first DRGS when the

active and return contacts straddled the ganglion (**Figure 5.5b**). We always observed a larger percentage of Aβ-LTMR activation than Aδ-neuron activation.

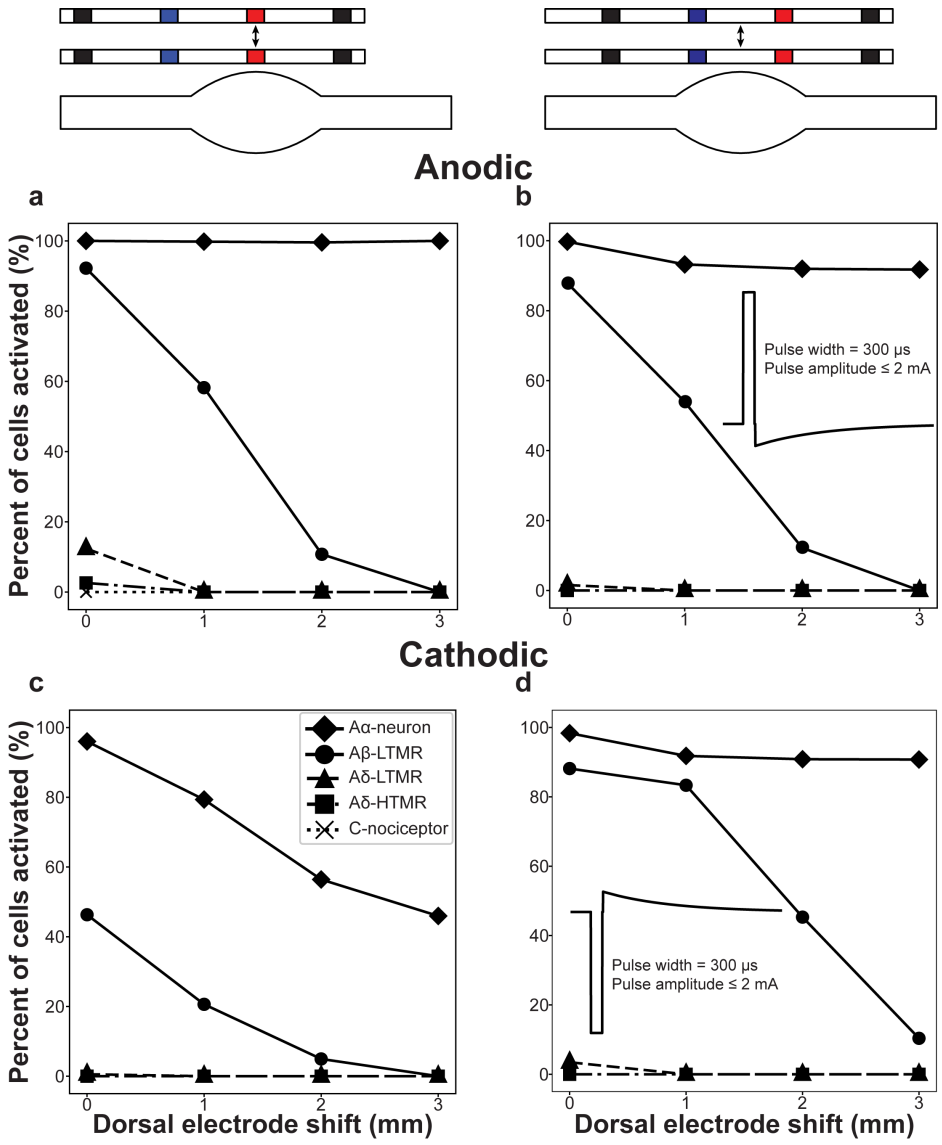

Figure 5.5 Effect of electrode position on neural activation during DRGS. Each plot show the percentage of each neuron type that generated action potentials in response to DRGS with a pulse width of 300 µs and an amplitude 2 mA or less (i.e., clinical DRGS), as the distance between the electrode lead and the ganglion increased. We examined the effect of electrode position relative to the ganglion for several electrode positions and stimulus polarities. a,c The active (red) contact centered above the ganglion. b,d The active and return (blue) contacts straddling the ganglion. a,b Anodic-first DRGS. c,d Cathodic-first DRGS. DRGS, dorsal root ganglion stimulation.

We observed Aα-neuron and Aβ-LTMR activation for all electrode positions. When the active contact was centered directly above the ganglion, anodic-first DRGS activated 100% and 92% of modeled Aα- and Aβ-neurons, respectively (**Figure 5.5a**), while cathodic-first DRGS

activated 99% and 46% of modeled Aα- and Aβ-neurons, respectively (**Figure 5.5c**). When the active and return contacts straddled the DRG, anodic- and cathodic-first DRGS both activated 88% of modeled Aβ-LTMRs and more than 98% of modeled Aα-neurons (**Figure 5.5b,d**). Increasing the distance between the active contact and the ganglion decreased the percentage of both Aα- and Aβ-neurons activated by clinical DRGS. When the electrode lead was shifted dorsally 1 mm or greater from the ganglion, cathodic-first DRGS applied with the active and return contacts straddling the ganglion produced the greatest Aβ-LTMR activation (**Figure 5.5d**). When the electrode lead was shifted dorsally 3 mm from the ganglion, we only observed Aβ-LTMR activation when cathodic-first DRGS was applied with the active and return contacts straddled the ganglion (**Figure 5.5d**). We observed Aα-neuron activation regardless of the distance from the electrode lead distance to the ganglion.

5.4.2 Effect of stimulus pulse width

Stimulus pulse width is a critical parameter when programming a patient's DRGS system, and has been shown to affect neural activation[298] and paresthesia distribution[310] during SCS. Interestingly, increasing SCS pulse width lowered the activation threshold of small-diameter myelinated DC axons.[298] However, the effect of stimulus pulse width on neural activation during DRGS has not been rigorously studied. Therefore, we calculated primary afferent activation thresholds for several pulse widths (i.e., 100, 200, 300, 500, and 1000 μs) both when the active contact was centered above the ganglion, and when the active and return contacts straddled the DRG. **Figure 5.6** shows the percentage of modeled neurons with activation thresholds in clinical range (i.e., ≤ 2 mA) as the stimulus pulse width increased, both when the active contact was centered above the ganglion, and when the active and return contacts straddled the ganglion.

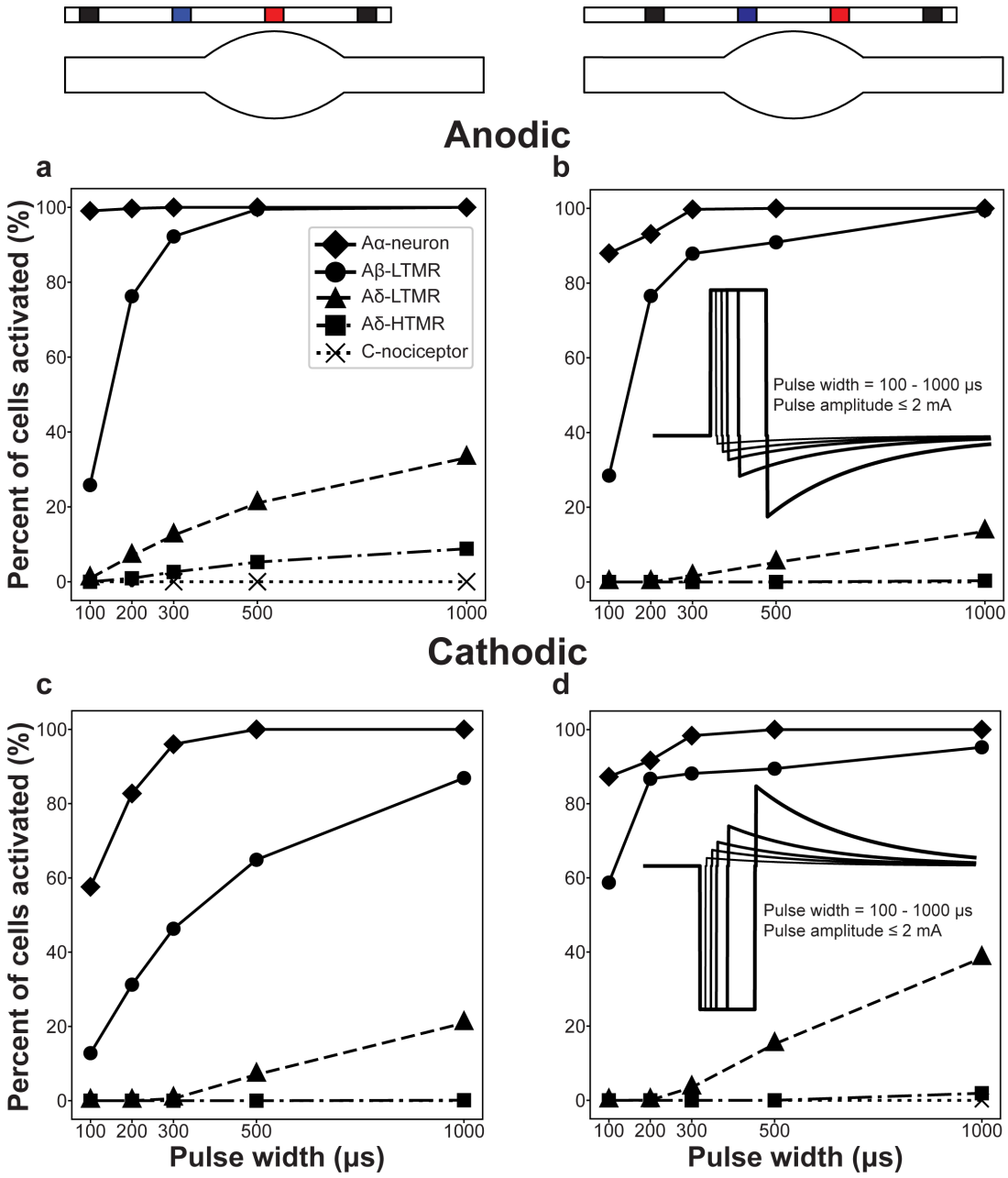

Figure 5.6 Effect of pulse width on neural activation during DRGS. Each plot shows the percentage of each neuron type that generated action potentials in response to DRGS with a pulse width between 100 and 1000 µs, and an amplitude 2 mA or less. We examined the effects of pulse width on neural activation for several electrode positions and stimulus polarities. a,c. The active (red) contact centered above the ganglion. b,d. The active and return (blue) contacts straddling the ganglion. a,b. Anodic-first DRGS. c,d. Cathodic-first DRGS. DRGS, dorsal root ganglion stimulation.

For amplitudes within the clinical range, we did not observe activation of nonmyelinated C-nociceptors for any pulse width. However, we did observe activation of small-diameter thinly myelinated Aδ-neurons. When the active contact was centered above the ganglion, the minimum

pulse widths for anodic-first DRGS (**Figure 5.6a**) to activate one or more Aδ-LTMRs or Aδ-HTMRs were 100 and 200 μs, respectively, while the minimum pulse widths for cathodic-first DRGS (**Figure 5.6c**) to activate one or more Aδ-LTMRs or Aδ-HTMRs were 300 and 1000 μs, respectively. When the active and return contacts straddled the ganglion, the minimum pulse widths for anodic-first DRGS to activate one or more Aδ-LTMRs or Aδ-HTMRs were 300 and 1000 μs, respectively (**Figure 5.6b**), while the minimum pulse widths for cathodic-first DRGS to activate one or more Aδ-LTMRs or Aδ-HTMRs were 200 and 1000 μs, respectively (**Figure 5.6d**). DRGS always recruited more Aδ-LTMRs than Aδ-HTMRs, regardless of pulse width or stimulus polarity.

We observed Aα- and Aβ-neuron activation by clinical DRGS for all pulse widths. Increasing the stimulus pulse width increased the percentage of Aα- and Aβ-neurons activated, regardless of stimulus pulse polarity or position of the active and return contact relative to the ganglion. For stimulus pulse widths below 300 μs, cathodic-first DRGS applied with the active and return contacts straddling the ganglion activated the largest percentage of Aβ-LTMRs (59–87%) (**Figure 5.6d**). For stimulus pulse widths greater than or equal to 300 μs, anodic-first DRGS applied with the active contact centered above the ganglion activated the largest percentage of Aβ-LTMRs (92–100%) (**Figure 5.6a**). Anodic-first DRGs applied with the active contact centered above the ganglion always activated the largest percentage of Aα-neurons (99–100%) (**Figure 5.6a**) For all pulse widths and stimulus polarities, there was always a larger percentage of Aα- and Aβ-neurons activated by clinical DRGS than any other neuron type.

5.4.3 Effect of stimulus pulse frequency

Stimulus pulse frequency is an important parameter during neurostimulator programming, and recent innovations in neurostimulation for pain have focused chiefly on this parameter (e.g.,

10 kHz SCS).[33] DRGS is, on average, applied at 20 Hz, but can be applied as low as 4 Hz or as high as 80 Hz.[77] Presently, we do not understand the physiologic effect of varying stimulus pulse frequency, nor how those effects translate to clinical outcomes. Therefore, we applied anodic- and cathodic-first DRGS with a pulse amplitude of 1 mA, a pulse width of 300 μs, and examined the time-varying membrane potential of different neural compartments (e.g., soma, axons) in response to DRGS applied at different pulse frequencies.

Regardless of pulse frequency, we did not observe activation of nonmyelinated C-nociceptors for any stimulus pulse frequency, for DRGS applied within standard clinical parameter ranges. We observed minimal activation of both thinly myelinated Aδ-LTMRs and Aδ-HTMRs (a maximum of 12 and 3%, respectively). As the majority of our data suggests that DRGS predominantly activates large myelinated neurons, and Aβ-LTMRs are believed to play an important role in both DRGS-induced pain relief and physiologic pain inhibition in the spinal cord,[190118] we focused the rest of our analyses on Aβ-LTMRs.

Figure 5.7 shows the average response frequency of different Aβ-LTMR compartments (i.e., soma, stem axon, centrally projecting axon, peripherally projecting axon) to DRGS applied at different frequencies, for Aβ-LTMRs that responded to DRGS applied with a 1-mA stimulus pulse. For most stimulus polarities and positions of active and return contacts, all Aβ-LTMR compartments responded in a one-to-one fashion with the DRGS pulse (i.e., one action potential for each stimulus pulse). However, in response to anodic-first DRGS with the active contact centered above the ganglion, the stem axon's response frequency was slightly larger than unity, while all other compartments' response frequencies were slightly below unity (**Figure 5.7a**). The increase in stem axon response frequency was caused by a rebound action potential propagating down the stem axon following a somatic action potential, which fails to propagate passed the T-

junction. The decrease in the average response frequencies in other compartment was attributed to neurons with activation thresholds near 1 mA. For those neurons, some DRGS pulses elicited an action potential, while some pulses failed to induce an action potential.

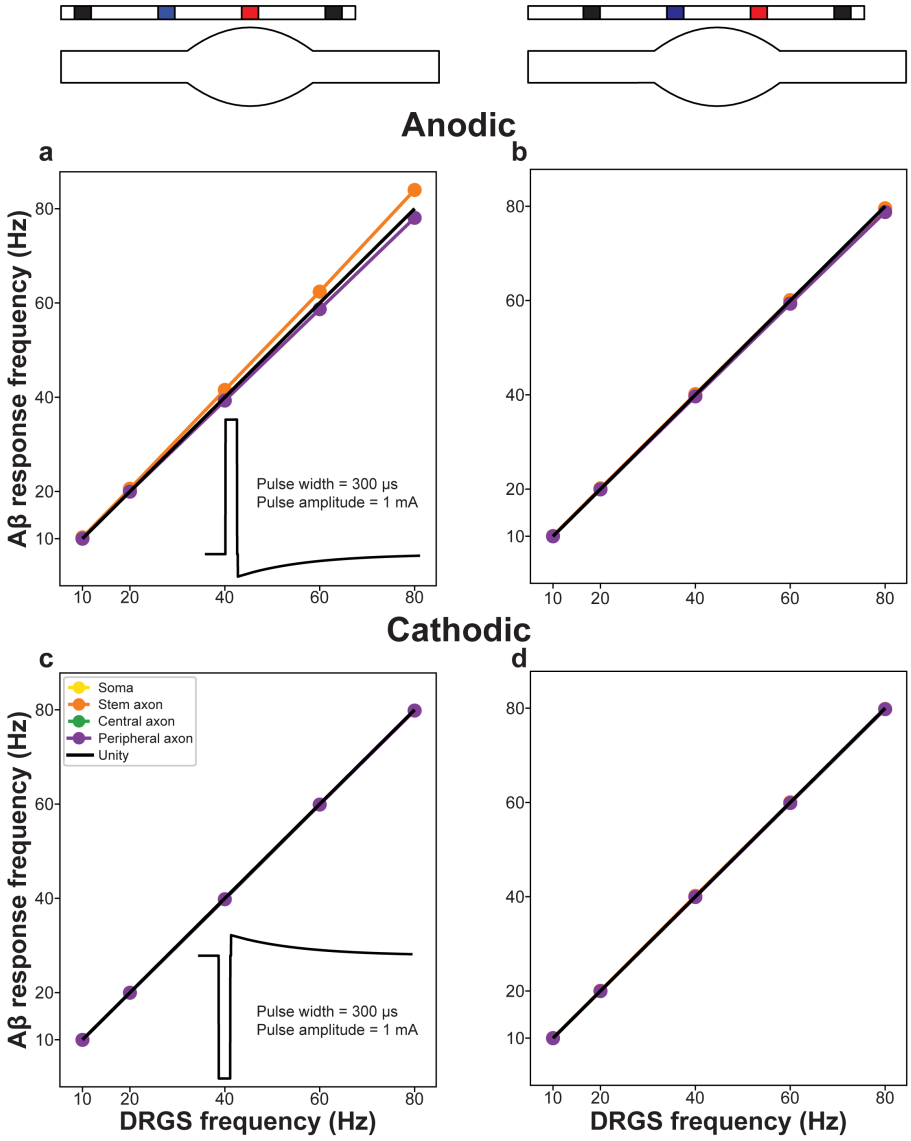

Figure 5.7 Effect of pulse frequency on different Aβ-LTMR compartment response frequencies during DRGS. Each plot shows the average response frequency (i.e., the frequency of action potential generation in response to DRGS) of Aβ-LTMR somata (blue), stem axons (orange), centrally projecting axons (green), and peripherally projecting axons (red). The black lines indicate unity (i.e., the neural compartment is responding in a one-to-one fashion with the stimulus train). We examined the effects of pulse frequency on several electrode positions and stimulus polarities. a,c. The active (red) contact centered above ganglion. b,d. The active and return contacts straddling the ganglion. a,b. Anodic-first DRGS. c,d. Cathodic-first DRGS. Note: some data are not visible due to many compartments having the same response frequency. DRGS, dorsal root ganglion stimulation; LTMR, low-threshold mechanoreceptor.

5.4.4 Effect of bipole placement

Clinical DRGS utilizes a bipolar stimulation configuration in which the cathode is typically placed directly beneath the pedicle.[77] However, the position of the DRG within the foramen varies across patients and spinal level.[95,222] X-ray fluoroscopy, the imaging modality used to visualize electrode position relative to bony structures during DRGS electrode implantation, is unable to resolve neural tissue, implying that clinicians are unable to precisely determine the position of the ganglia relative to the active contact. Therefore, the position of the stimulating contacts relative to the DRG is likely variable across patients, warranting investigation into how bipole placement relative to the ganglion affects neural activation during DRGS.

Figure 5.8 shows the percentage of modeled Aβ-LTMRs activated by various bipolar DRGS configurations. For bipolar configurations where the active and return contacts were adjacent to each other (**Figure 5.8a**), cathodic-first DRGS (light gray bars) typically activated more Aβ-LTMRs than anodic-first DRGS (dark gray bars), except when the active contact was centered above the ganglion. Cathodic-first DRGS applied with the return contact centered above the ganglion, and the active contact above the peripheral nerve root, activated the largest percentage of modeled Aβ-LTMRs (99%). Anodic-first DRGS applied with the active electrode above the spinal nerve root activated the smallest percentage of modeled Aβ-LTMRs (40%). In general, placing the cathode near the peripheral nerve root, or placing the anode near the ganglion, maximized Aβ-LTMR activation.

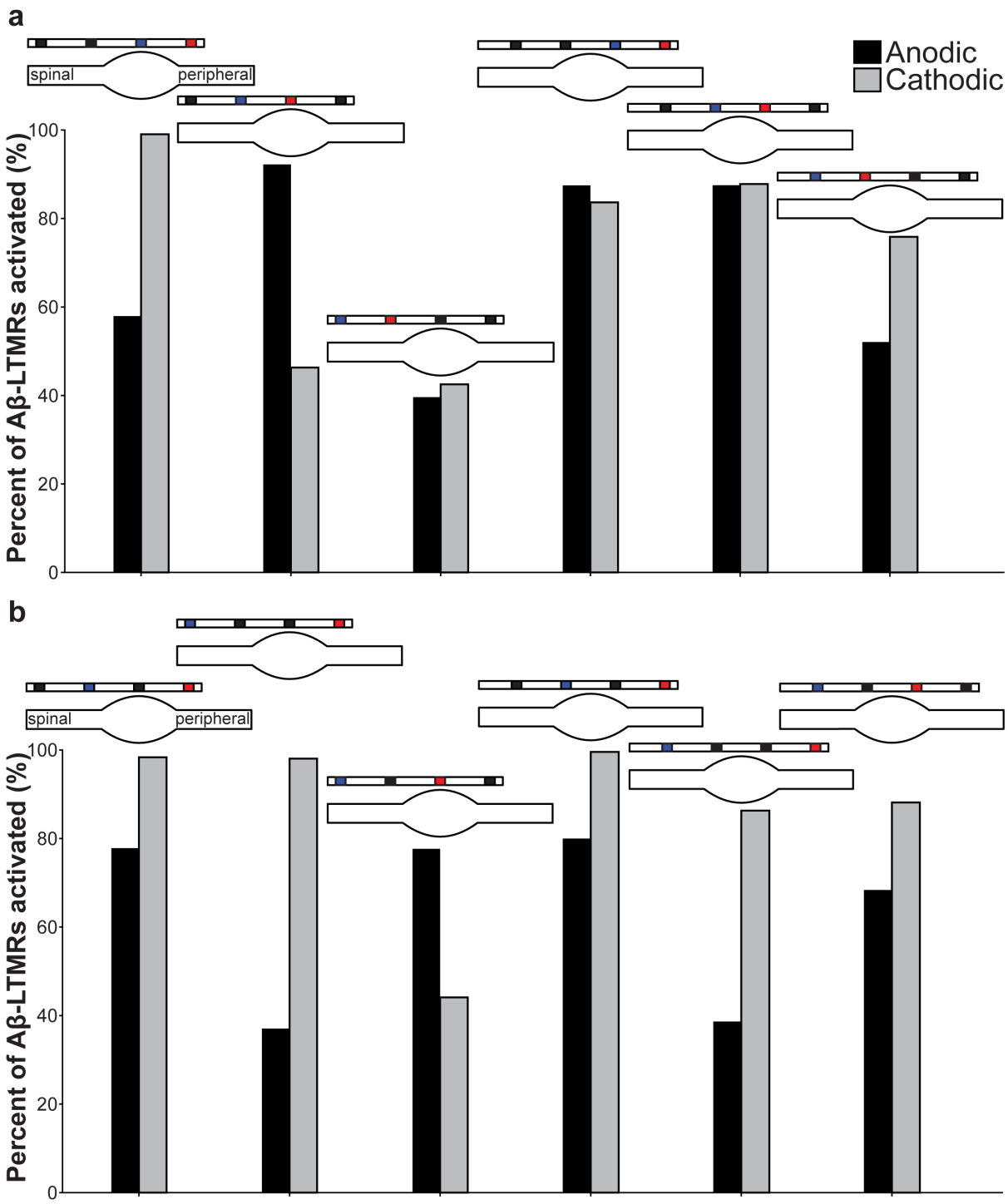

Figure 5.8 Effect of bipole configuration on neural activation during DRGS. Each plot shows the percentage of modeled Aβ-LTMRs activated by different bipolar DRGS configurations. For each pair of bars, the black and gray bars indicate the percentage of Aβ-LTMRs activated by anodic-first and cathodic-first DRGS, respectively. For the schematics above each pair of bars, the red, blue, and black contacts indicate the active, return, and inactive contacts, respectively. Left-most schematics indicate spinal and peripheral nerve roots. a. Percentage of modeled Aβ-LTMRs activated by adjacent bioples. b. Percentage of modeled Aβ-LTMRs activated by bipoles with one or more inactive contacts separating the active and return contacts. DRGS, dorsal root ganglion stimulation; LTMR, low-threshold mechanoreceptor.

For bipolar configurations with one or more inactive contacts separating the active and return contacts (i.e., separated bipoles; **Figure 5.8b**), cathodic-first DRGS typically activated more Aβ-LTMRs than anodic-first DRGS. For separated bipole configurations, anodic-first DRGS only activated more Aβ-LTMRs than cathodic-first DRGS when the active contact was centered above the ganglion, similar to bipolar DRGS with adjacent active and return contacts. Three separated bipole configurations activated more than 98% of modeled Aβ-LTMRs, each of which applied cathodic-first DRGS with the active contact above the peripheral nerve root, and the return contact as either the first or second most proximal contact. Anodic-first DRGS applied with a distal active contact and proximal return contact (i.e., placing the active contact above the peripheral nerve root and the return contact above the spinal root) activated the smallest percentage of modeled Aβ-LTMRs (37%). Similar to adjacent bipole configurations, placing the cathode near the peripheral nerve root, or placing the anode near the ganglion, maximized Aβ-LTMR activation. However, except for the case when the active electrode was centered above the ganglion, cathodic-first DRGS using a separated bipole configuration always activated more than 80% of modeled Aβ-LTMRs, while only half of the adjacent bipole configurations activated more than 80% of modeled Aβ-LTMRs.

5.4.5 Effect of the guarded cathode stimulation configuration

Guarded cathode configurations are commonly used in clinical SCS,[69] but to our knowledge have not been documented in DRGS studies. Therefore, we examined neural activation patterns resultant from DRGS applied with guarded contact stimulation configurations. We again observed no activation of nonmyelinated C-nociceptors, and minimal activation of Aδ-LTMRs and Aδ-HTMRs (a maximum of 12 and 3%, respectively), and therefore we focused our analysis on Aβ-LTMRs.

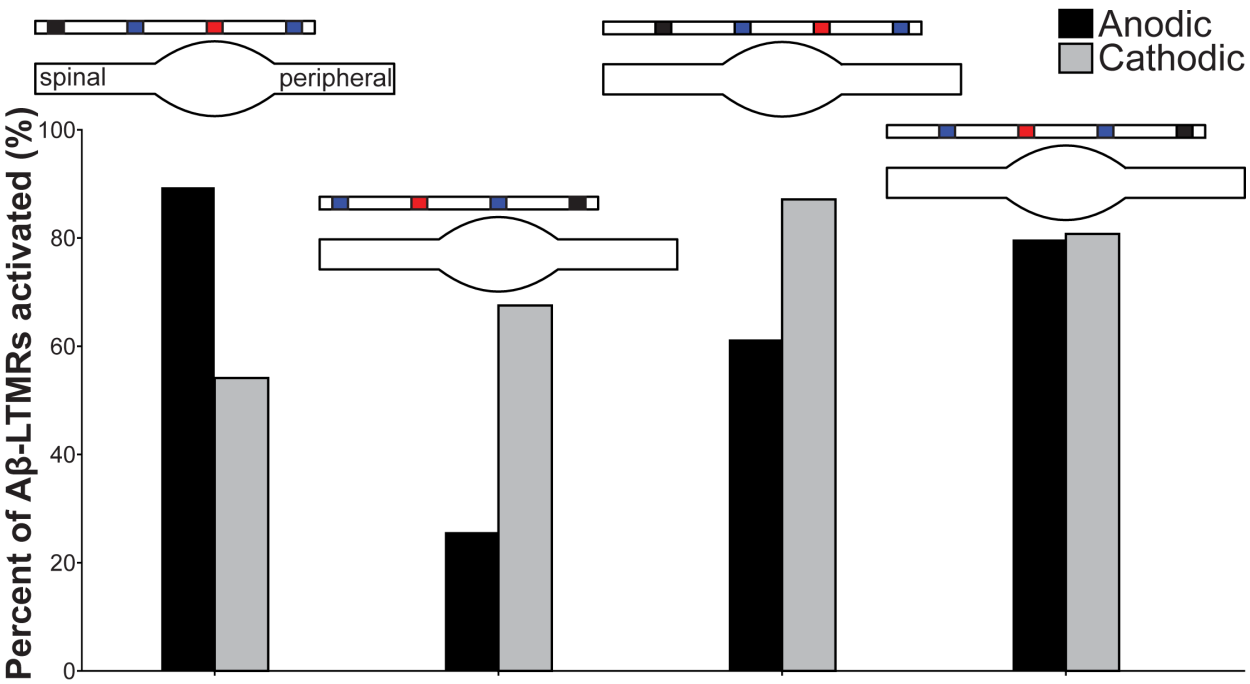

Figure 5.9 Effect of guarded active contact configurations on neural activation during DRGS. For each pair of bars, the black and gray bars indicate the percentage of Aβ-LTMRs activated by anodic-first and cathodic-first DRGS, respectively. For the schematics above each pair of bars, the red, blue, and black contacts indicate the active, return, and inactive contacts, respectively. Left-most schematic indicates spinal and peripheral nerve roots. DRGS, dorsal root ganglion stimulation; LTMR, low-threshold mechanoreceptor.

Figure 5.9 shows the percentage of modeled Aβ-LTMRs activated by various guarded contact DRGS configurations. Similar to conventional and longitudinal bipole configurations, anodic-first DRGS applied with a guarded active contact activated more Aβ- LTMRs than cathodic-first DRGS only when the active contact was centered above the ganglion. When the active contact was close to a nerve root, or when the active contact and one of the return contacts straddled the ganglion, cathodic-first DRGS activated more Aβ-LTMRs than anodic-first DRGS. For guarded active contact configurations, applying anodic-first DRGS with the active contact centered above the ganglion maximized Aβ-LTMR activation (89%). For cathodic-first DRGS applied with a guarded active contact configuration, placing the active contact near the peripheral nerve root maximized Aβ-LTMR activation (87%).

5.5 Discussion

DRGS is a safe and effective therapy for chronic pain that is refractory to conventional medical management. To ensure accurate delivery of electrical stimulation to the DRG, several clinically controllable parameters, such as the position of the active and return contacts and the shape of the stimulus pulse, must be carefully tuned to maximize pain relief without producing uncomfortable sensations. It is presently unclear how varying each of these parameters affects which types of sensory neurons are directly activated by DRGS. Our data suggest that DRGS applied with stimulation amplitudes within a clinical range (i.e., ≤ 2 mA) predominantly activates large-diameter myelinated afferents (e.g., Aα- and Aβ-neurons). Furthermore, our results indicate that the position of the active and return contacts relative to the ganglion has the greatest effect on DRGS-induced Aβ-LTMR activation.

5.5.1 Implications for mechanisms of DRGS

Our data suggest that clinical DRGS directly activates myelinated neurons, regardless of electrode position, stimulation configuration, and stimulus pulse parameters (i.e., frequency, pulse width). This corroborates our previous study's findings that clinical DRGS is likely driving the activity of large-diameter myelinated Aβ-LTMRs, without directly activating small-diameter nonmyelinated C-nociceptors[118] and is supported by recent experimental findings that DRGS applied with nonpenetrating electrode arrays activates neurons with conduction velocities in the Aδ- to Aβ-axon range.[311] Furthermore, our data also suggest that clinical DRGS activates Aα-neurons, and may activate Aδ-neurons, though in a considerably smaller proportion than Aα- and Aβ-neurons. Based on these findings, DRGS may provide pain relief by driving pain-gating mechanisms in the dorsal horn, via postsynaptic activation of inhibitory interneurons which receive input from large myelinated afferents. This hypothesis suggests similarities between the

mechanisms of DRGS and SCS. Previous animal studies of SCS demonstrated increased levels of γ-amino butyric acid (GABA), an inhibitory neurotransmitter, in the spinal cord,[312] and increased paw withdrawal thresholds in animals that responded to SCS[313] predominantly driven through the $GABA_B$ receptor.[80,314] However, a recent study in rats concluded that DRGS does not cause GABA release in the dorsal horn,[122] indicating DRGS may provide pain relief through other mechanisms.

Koetsier and colleagues suggested that instead of driving GABAergic inhibition in the dorsal horn, DRGS may provide pain relief by inducing GABAergic inhibition through GABA signaling within the DRG.[122] Du and colleagues concluded that in rats, activating small-, medium-, or large-diameter DRG neurons can induce GABA release in the DRG, and that nearly all small-diameter DRG neurons (putative nociceptors) can respond to GABA.[123] Furthermore, they demonstrated that vesicular inhibitory amino acid transporter (VGAT), the primary transporter for inhibitory neurotransmitter reuptake, was commonly found in DRG neurons that co-expressed 200 kDa neurofilament, a marker of myelinated afferents in rats and mice. Optogenetically stimulating VGAT expressing DRG neurons produced a marked reduction in nocifensive behavior, and $GABA_A$ receptor antagonists increased nocifensive behavior even when no noxious stimuli were present, suggesting that a GABAergic pain-gating system exists at the level of the DRG. Taking these findings in context with our model predictions, it is possible that clinical DRGS provides pain relief by directly activating medium- and large-diameter myelinated afferents, causing local GABA release in the DRG to inhibit nociceptive afferents, thereby preventing pain signals from reaching the central nervous system.

However, GABA is not the only inhibitory neurotransmitter in the spinal dorsal horn. Many dorsal horn neurons that release GABA co-release glycine, with some inhibitory postsynaptic currents in superficial dorsal horn laminae mediated exclusively by glycine.[315] Recent studies have

identified a glycinergic feedforward dorsal horn circuit that gates mechanical allodynia, mediated by paravalbumin (PV) expressing interneurons in lamina IIi and III of the dorsal horn, which silence lamina II PKCγ+ interneurons that form excitatory synapses on projection neurons in lamina I.[124,316,317] These PV+ interneurons receive afferent input from both Aβ- and Aδ-axons,[317] and gate mechanical pain via pre- and post-synaptic inhibition of primary afferents and lamina II excitatory interneurons, respectively.[316,317] Subsequent studies uncovered novel neural circuits involved in, and further somatosensory functions of, glycinergic inhibition. Foster and colleagues demonstrated that selective ablation of dorsal horn interneurons which express GlyT2, the glycine transporter expressed in the spinal cord and brainstem, facilitates mechanical, heat, and cold hyperalgesia, and can induce spontaneous pain behaviors.[318] Cui and colleagues identified a separate subpopulation of deep laminae (III–V), predominantly glycinergic interneurons which receive monosynaptic and polysynaptic input from both A- and C-axons, and form a feed-forward gate to silence pain transmission from PKCγ+ and somatostatin+ superficial dorsal horn neurons.[319] The results of these studies emphasize the complexity of sensory processing in the dorsal horn, and taken together with the data presented in this work, suggest that DRGS may provide pain relief through a combination of glycinergic inhibition in the dorsal horn and GABAergic inhibition within the DRG itself. To fully elucidate the mechanisms of action of DRGS, we must uncover how innocuous and noxious stimuli are processed in dorsal horn and supraspinal structures in healthy and pathologic states, and how the pattern of DRGS-induced afferent activity augments or abrogates neural activity throughout the neuraxis.

5.5.2 Importance of electrode lead placement

The location of the DRGS electrode lead relative to the DRG likely varies across patients, depending on the size of the patients' neuroforamina, the position of their DRG within the

foramen,[95,222] and the implanting physician's placement of the electrode lead relative to the patient's DRG. The NACC suggests that straddling the second and third contacts across the medial and lateral borders of the pedicle is the optimal position of the lead in the foramen.[77] This positioning likely resembles our models where the second and third contacts are straddling the ganglion, as lumbar DRG are typically located in the "foraminal zone" (i.e., beneath the pedicle).[95] Martin and colleagues found that power consumption by the implanted pulse generator (IPG) was minimized by electrodes placed superodorsally in the foramen, a similar position to what the NACC suggests to be optimal.[308] However, Martin and colleagues found that clinical outcomes were not dependent on the position of the electrode in the foramen. That study suggests that DRGS is able to activate analgesic mechanisms with the electrode placed anywhere in the foramen, at the cost of additional power consumption, though the optimal electrode positioning would result in straddling the ganglion with the active and return contacts.

Our modeling results, and our hypothesis that DRGS provides pain relief by driving the activity of large-diameter myelinated afferents, corroborate these notions. We demonstrated that DRGS consistently activates Aα- and Aβ-neurons regardless of the positioning of active and return contacts relative to the ganglion, selection of stimulus parameters, and distance between the electrode lead body and the ganglion (**Figure 5.5**). Furthermore, we showed that straddling the active and return contacts across the ganglion maximizes Aβ-LTMR activation (**Figure 5.5d**). Straddling the DRG with the active and return contacts, and placing the electrode lead in close proximity to the ganglion, would therefore enable consistent DRGS-induced analgesia while minimizing IPG power consumption, thereby reducing the need for battery replacement surgeries.

5.5.3 Importance of stimulator programming

Programming a patient's DRG stimulator is a crucial and often time-consuming process, as the stimulus parameter space is large and cannot be fully explored in a single programming session. This process is further complicated by the fact that we do not fully understand how varying each parameter, such as pulse width, pulse frequency, and the placement of cathodes and anodes, affects neural recruitment during DRGS. The median DRGS pulse width and pulse frequency reported by the ACCURATE trial were 300 μs and 20 Hz, respectively, and the NACC highlights that pulse widths utilized by patients typically decrease over time, and that shorter pulse widths maximize the therapeutic window.[77] Our results again corroborate the NACC recommendations; we demonstrated that regardless of pulse width, DRGS is predominantly activating Aβ-LTMRs, especially with shorter pulse widths (**Figure 5.6**). However, when using 500 or 1000 μs pulse widths, our models predicted increased activation of both Aδ-LTMRs and Aδ-HTMRs (**Figure 5.6a,d**). Activation of smaller diameter axons in response to longer pulse widths has also been reported in SCS studies, where increased pulse widths increased activation of small diameter myelinated axons in the medial DCs.[298,300] Increased activation of Aδ-neurons, particularly Aδ-HTMRs, could explain why some patients report uncomfortable or painful sensations in response to DRGS of longer pulse widths. Therefore, shorter pulse widths (i.e., ≤ 300 μs) may maximize activation of target neurons (i.e., Aβ-LTMRs), while minimizing activation of nociceptive neurons, increasing the therapeutic window of DRGS.

From the ACCURATE clinical trial, the median DRGS pulse frequency was 20 Hz, and the maximum frequency across the DRGS patient cohort did not exceed 50 Hz at any time point.[90] Our data demonstrate that in general, DRGS elicits one-to-one action potential generation in most Aβ-LTMRs (**Figure 5.7**), suggesting DRGS consistently sends propagating action potentials to the dorsal horn via Aβ-LTMRs. However, our data do not explain why DRGS patients typically

utilize lower frequencies (around 20 Hz on average) compared to SCS patients (around 50 Hz on average),[320] especially considering the two therapies may operate through similar mechanisms (i.e., driving the activity of Aβ-LTMRs in the DRG vs. in the DCs). Future experimental and clinical studies are necessary to understand the effect of DRGS pulse frequency both on the mechanisms of the therapy and on clinical outcomes.

As described above, the NACC suggests straddling the second and third contacts across the target pedicle and applying bipolar, cathodic-first DRGS. However, it is currently unknown how selecting contacts as anodes and cathodes affects neural activation during DRGS. We showed that regardless of which contacts were set to be active, DRGS activated a substantial portion (~40%) of modeled Aβ-LTMRs (**Figure 5.8**). Generally, placing an anode near the body of the ganglion, or placing a cathode near a nerve root, particularly near the peripheral nerve root which contains larger-diameter axons, maximized Aβ-LTMR activation. This agrees with our previous findings,[118] and follows conventional neurostimulation theory that anodic stimulation results in lower activation thresholds when the electrode is near a cell body, and cathodic stimulation results in lower activation thresholds when the electrode is near an axon of passage.[51]

Guarded cathode configurations, placing an anode on either side of a cathode, are commonly used in traditional SCS. Because traditional SCS putatively targets the DCs—axons of passage running parallel to the implanted electrode—guarded cathodes are thought to maximize the therapeutic window of SCS by maximizing the activating function along DC axons.[321] We explored if DRGS applied with a guarded active contact configuration would provide greater Aβ-LTMR activation than other stimulus configurations. However, we did not find any added benefit of the guarded cathode configuration compared to bipolar configurations, regardless of stimulus polarity (**Figure 5.8** and **Figure 5.9**). As DRG neurons are not axons of passage, but instead have

pseudounipolar morphologies,[97] the guarded cathode configuration is unlikely to maximize neural activation during DRGS. Our data again add support to the NACC recommendation that "complex programming arrays are not necessary, as simple bipolar arrays can achieve optimal activation of the DRG."[77]

5.5.4 Limitations

Although we built our models using previously published clinical and experimental data, there are several limitations to our approach. The FEM of a human L5 DRG used in this study represented several anatomical compartments (e.g., foraminal bone, intraforaminal tissue) as largely concentric cylinders. Although the method of representing anatomical compartments as simplified concentric shapes has been commonly used to study other clinical neurostimulation therapies,[33,53] recent work demonstrated that the complex anatomy of bony structures in the spine can affect model predictions of SCS-induced neural activation.[31] Future studies could employ a patient-specific modeling approach, similar to previous studies of SCS,[73] which could elucidate how the complex anatomy of the spinal column affects DRGS model predictions.

Human lumbar DRG somata are typically located around the dorsal edge of the ganglion.[45] To study how DRGS would affect a specific cell type at any location in the DRG, we homogeneously distributed each cell type throughout the DRG, with their cell bodies placed around the dorsal edge of the ganglion. However, the actual distribution of functional subpopulations of DRG neurons (e.g., Aα-neurons) is likely not homogeneous. Our data suggest DRGS causes widespread activation of large-diameter Aα-neurons, which carry proprioceptive and stretch receptor information from the muscles. However, a recent study in mice lumbar DRG showed that only 0.6% of DRG neurons were PV+, a marker of proprioceptive primary afferents,[140] and our recent histologic data suggests that only 3.6% of axons in human lumbar DRG

have diameters greater than or equal to 12 μm, an approximate lower limit of Aα-axon diameters.[45,225,322] Furthermore, human lower leg muscles contain on the order of hundreds of muscle spindles,[323] while there are tens of thousands of neurons in human DRG.[45] These data suggest that Aα-neurons may sparsely populate the DRG, and therefore our model may be overestimating the amount of Aα-neuron activation during clinical DRGS. However, prolonged activation of muscle afferents could be another source of DRGS-induced discomfort, in addition to the activation of Aδ- neurons with longer stimulus pulse widths described above. Future studies should examine the functional organization of cells within human DRG and the corresponding implications for DRGS.

We modeled several classes of neurons important to the transmission of painful and non-painful stimuli: Aα-, Aβ-, Aδ-, and C-neurons. However, we ignored the potential effects of DRGS on non-neuronal DRG cells, such as satellite glial cells (SGCs), the glial cell type found in DRG. Glial cells in the central nervous system are known to play an important role in regulating both normal nociceptive pain processing and pathologic chronic pain states.[324,325] Furthermore, recent work has highlighted the contributions of SGCs to chronic pain, including visceral pain.[326] To date, there are few studies examining the influence of clinical neurostimulation therapies on glial activity, though the effect of SCS-induced electric fields on glial cell function is a growing area of study.[177,327,328] Glial cells express voltage-gated ion channels, the molecular targets by which neurostimulation therapies influence neural activity.[116] Though SGCs do not contain voltage-gated sodium channels, the channel chiefly responsible for the generation of propagating action potentials, SGCs do express voltage-gated potassium channels.[175] The extent to which DRGS affects voltage-gated channels in SGCs is unclear, though it is possible that DRGS could indirectly induce a myriad of potassium-mediated intracellular signaling cascades within SGCs. This notion

is supported by recent studies highlighting the importance of glial cells in the development and maintenance of chronic pain at multiple levels of the nervous system, such as Schwann cells in the periphery,[329] SGCs themselves in the DRG,[174] and microglia in the spinal dorsal horn.[330]

Finally, we examined the direct neural response to DRGS, that is, which neurons are directly activated by one DRGS pulse or a short train of DRGS pulses. Clinically, DRGS is applied tonically, ideally over a period of years. In our multicompartment neuron models, we included models of voltage-gated sodium and potassium channels, but ignored the contributions of other types of ion channels, such as calcium channels. We believe that this simplification is justified for examining the direct neural response to DRGS, as voltage-gated sodium and potassium channels are predominantly responsible for the generation of action potentials.[331] However, due to this simplification, we were unable to study the long-term effects of tonic DRGS, as these channels activate and inactivate on time scales ranging from a few to tens of milliseconds. Furthermore, computational demands are prohibitive in simulating more than a second of neural activity. To complete the picture of the effect of DRGS on primary afferents, future experimental studies should study the effect of long-term DRGS on physiologic processes mediated by ion channels that operate on long timescales, and on how tonic DRGS may cause upregulation or downregulation of different genes.[332]

5.6 Conclusions

DRGS is a valuable clinical tool for managing intractable focal pain. Currently, we do not understand the physiologic mechanisms of action of DRGS, nor how the clinical implementation of DRGS (e.g., lead placement, stimulator programming) affects the utilization of these mechanisms. In this work, we studied how clinically controllable parameters affect neural

activation during DRGS. Firstly, our data support the hypothesis that DRGS provides pain relief by directly activating Aβ-LTMRs, leading to postsynaptic activation of pain-gating mechanisms in the dorsal horn and possibly pain-gating mechanisms within the DRG itself. Based on this hypothesis, our data corroborate several NACC recommendations: 1) straddling the active and return contacts across the pedicle (and presumably, the ganglion) may be the optimal electrode positioning in the foramen, 2) shorter pulse widths are preferred, based on maximizing activation of innocuous neurons while minimizing activation of potentially nociceptive neurons, and 3) conventional bipolar stimulation is sufficient to achieve analgesia, without the need for more complex programming configurations. Although the data presented here are pivotal to understanding the direct neural response to DRGS, future experimental and clinical studies are necessary to understand the downstream mechanisms of DRGS and how such effects influence long-term success with the therapy.

Chapter 6 – Neuromodulatory Effects of DRGS on C-neurons

6.1 Abstract

Dorsal root ganglion stimulation (DRGS) is a neurostimulation therapy for intractable neuropathic pain. Currently, we do not understand the physiological mechanisms of DRGS-induced pain relief, limiting our ability to innovate the therapy to improve patient outcomes. In this work, we investigate the effects of DRGS on C-neurons – nonmyelinated, putatively nociceptive sensory neurons. We implemented a Markov Chain Monte Carlo method to generate populations of biophysically distinct multi-compartment C-neuron models. We then simulated the effects of DRGS on this population of C-neurons by calculating the extracellular potentials generated by DRGS using a finite element method model. In general, DRGS only augmented T-junction filtering in C-neurons when we added L-type calcium channels and calcium-activated potassium channels to the stem axon and central and peripheral processes. Our model population exhibited activation thresholds ranging between 4 and 14 mA, depending on biophysical parameters (e.g., M-type potassium conductance), number of applied pulses, and stimulus pulse polarity. Larger current densities produced by small preclinical DRGS electrode arrays may be partially responsible for the lower C-neuron thresholds observed in *in vivo* studies. However, other features of DRG neurons, such as their complex stem axon trajectories, may also contribute to this phenomenon.

6.2 Introduction

Chronic pain is a debilitating neurological disorder that affects more than one hundred million Americans.[10] Secondary effects of the prevalence of chronic pain include more than 600 billion dollars in healthcare costs each year and contributing to the ongoing opioid epidemic.[15,333] Dorsal root ganglion stimulation (DRGS) is a non-addictive third-line treatment for managing pain that is refractory to conventional medical management. DRGS is achieved by implanting a small electrode array in the intraforaminal space on the dorsal side of a dorsal root ganglion (DRG).[287] The electrode array applies brief electrical impulses to modulate the activity of primary sensory neurons (PSNs) in the DRG. However, DRGS fails to provide adequate pain relief in all patients, leaving them with few other treatment options. Improving the clinical implementation of DRGS may help reduce the enormous burden of chronic pain.

One of the factors precluding our ability to improve DRGS is that we do not understand the physiological mechanisms of action behind DRGS-induced pain relief.[46] Computational studies have suggested that DRGS likely drives the activity of Aβ-neurons, possibly driving feed-forward pain-gating circuitry in the spinal cord dorsal horn.[118,119] Work from other computational and preclinical studies suggests that DRGS may act chiefly upon C-neurons.[48,76,121,146] However, it is well understood that extracellular electrical stimulation, like that utilized by DRGS, preferentially activates myelinated axons over nonmyelinated axons and cell bodies.[57,58,116,291] Computational studies of clinical DRGS corroborate this notion. Aβ-neuron activation thresholds (i.e., the current amplitude needed to generate an action potential (AP)) have been reported on the order of several hundred μA,[118,119] whereas C-neuron activation thresholds have been reported on the order of several mA.[76,118,119] Clinically, therapeutic DRGS is typically applied with pulse

amplitudes less than 1 mA.[43,77] This suggests that Aβ-neurons may be the predominant substrate of DRGS-induced pain relief.

However, a recent study using a rat model of DRGS demonstrated that when stimulating a DRG, the activation thresholds of C-neurons were only approximately 1.5 times greater than the activation thresholds of Aβ-neurons.[121] This ratio of C-neuron to Aβ-neuron activation thresholds was considerably lower than the ratio of C-axon to Aβ-axon activation thresholds when stimulating the sciatic nerve.[121] Though these data contrast with conventional neurostimulation intuition, they also suggest that there may be features unique to DRG neurons that facilitate the activation of nonmyelinated neurons at comparably smaller pulse amplitudes. Understanding these features will be crucial to understanding not only the mechanisms of DRGS, but also how extracellular electrical stimulation may modulate the activity of nonmyelinated neurons.

The goal of this work was to investigate which features of DRG neurons may facilitate the activation of C-neurons at comparable pulse amplitudes to Aβ-neurons. We coupled a finite element method (FEM) model of DRGS to a multi-compartment model of a C-neuron to simulate the neural response to DRGS. We corroborated previous findings that DRGS applied at high stimulus pulse amplitudes (e.g., 10 mA) can induce T-junction filtering in C-neurons. We found that the maximal conductances used to parametrize an individual C-neuron model can have a significant influence on its activation threshold, which are generally greater than 4 mA. In particular, the net conductance of potassium channels underlying the M-current may play an important role in setting the C-neuron's activation threshold. Future work should incorporate novel C-neuron morphological models with complex stem axon trajectories to investigate the role of morphological peculiarities on the neural response to stimulation.

6.3 Methods

6.3.1 FEM model of DRGS

We implemented a previously published FEM model of a human L5 DRG with an explicit representation of a clinical four-contact cylindrical DRGS electrode array.[119] The geometry of the model was based on imaging and cadaver studies of human DRG and the surrounding anatomy.[95,96,256,257] We set the conductivity of each tissue to the values used in our previous studies of DRGS.[118,119] We modeled all conductivities as isotropic, with the exception of the white matter in the nerve roots. We built the FEM model in the commercially available 3-matic module within the Mimics Innovation Suite (Materialise, Brussels, Belgium). We oriented the electrode array above the DRG such that the middle of the active contact (the second contact relative to the tip of the electrode array) was oriented above the midpoint of the DRG. We surrounded the electrode array with a 300 μm thick encapsulation layer to represent the foreign body response to implanted objects.[259] In some cases, we examined the effect of simulating an electrode array similar to those used in preclinical experiments of DRGS. **Table 6.1** reports the contact lengths, electrode lead diameters, and edge-to-edge contact spacing used by clinical DRGS cylindrical electrode arrays and those approximated from preclinical reports.[96,146]

We imported the FEM model into COMSOL Multiphysics (COMSOL, Inc., Burlington, MA, USA). We simulated bipolar DRGS by applying a unit current stimulation boundary condition (i.e., 1 A) to the active electrode contact and grounded (i.e., 0 V) the return contact. We modeled the electrode lead shaft as a perfect insulator and modeled inactive electrode contacts as equipotential with zero net current across their surface. To calculate the voltage distribution generated by DRGS, we used the conjugate gradient method to solve Laplace's equation. To calculate model impedances, we divided the average voltage measured at the surface of the active

contact by the applied stimulus current. The FEM reproduced bipolar impedances similar to those reported clinically (i.e., 1458.9 ± 714.5 Ω).[77]

6.3.2 Multi-compartment C-neuron model

We modified a previously published model of a C-neuron.[118] The model was validated on its ability to reproduce somatic AP characteristics of experimentally measured DRG neurons.[118,265,283] The rough morphology of the model was based on a previously published model of a C-neuron.[135]

We made several modifications to the morphology of the model. First, we set the diameters of the centrally projecting axon and peripherally projecting axon to 0.6 μm and 1.3 μm, respectively. These values are closer to the average values measured from cat DRG.[183] Furthermore, larger diameter axons have lower activation thresholds than smaller diameter axons,[58,291] improving the likelihood we would see C-neuron activation in response to DRGS. We also decreased the stem axon diameter from 1.4 μm to 1.3 μm, to better reproduce experimentally measured following frequencies (see below). Following frequency is the maximum frequency at which APs can propagate through a branch point (e.g., the T-junction). Finally, we shortened the stem axon from 869 μm to 150 μm, to increase potential electrotonic effects of hyperpolarization at the soma on the T-junction (the proposed mechanism of augmented T-junction filtering).[76]

We also made changes to the active ion channels included in the model. We included several ion channel mechanisms represented in the Sundt model that may be critical in producing T-junction filtering.[76,135] Specifically, we included representations of the outward potassium M-current, an L-type voltage-gated calcium channel, and the small conductance calcium-activated potassium channel (SK).[135] Typically, these additional channels were only expressed in the soma. However, where noted below, we also included these ion channels in the stem axon and the first

50 compartments of the peripheral and central axons. We also removed the representation of $Na_v1.9$ from our model to reduce computational complexity and dimensionality during model population generation (see below). We set the decay time constant of intracellular calcium concentration to 5 seconds to reflect values measured in DRG tissue.[120] None of these modifications produced significant effects on the AP characteristics (e.g., amplitude, duration) used to validate the original model.

6.3.3 Parametrizing a population of C-neuron models

We implemented Goodman and Weare's Affine-Invariant Markov Chain Monte Carlo method (MCMC) using the emcee Python package (https://emcee.readthedocs.io) to generate a population of C-neuron models each with a unique set of maximal ion channel conductances.[334,335] Typically, MCMC methods use Bayes' theorem to estimate posterior probabilities of a set of parameter values describing a given system based on prior assumptions about the distribution of each parameter's values and experimental data. We assumed uniform distributions for each parameter as priors, and we constrained each distribution relative to physiologic ranges (e.g., conductances must be greater than or equal to zero). In this work, we implemented the MCMC method to simulate and validate thousands of possible parameter sets (in this work, combinations of maximal ion channel conductances). Each parameter set was evaluated on its ability to produce somatic AP characteristics (e.g., amplitude, duration) described by previous preclinical experiments with C-neurons (**Table 6.2**).[265,283] We calculated the normalized distance between each parameter set's AP characteristic values and the mean values reported by previous experiments. We averaged the normalized distance across all metrics to calculate a "score" for each parameter set. A lower score indicates a parameter set produces model AP characteristics that

are closer to the mean of the experimentally measured characteristics' values. We selected 100 models with the lowest scores for analysis in this study.

To ensure the MCMC method fully explored each parameter space, we ran the algorithm four times, with each successive run injecting progressively increasing variance of gaussian noise in the initial guess for each parameter value. Each run utilized 400 individual Markov chains (i.e., 'walkers') which were allowed to iterate their parameter values 25 times per run.

Table 6.1 Clinical and preclinical DRGS electrode array specifications.

	Diameter (mm)	**Contact length (mm)**	**Contact edge-to-edge spacing (mm)**	**Contact surface area (mm^2)**
Clinical	1.0	1.25	5	3.92
Preclinical (rat)	0.45	0.5	0.5	1.41

6.3.4 Simulating the neural response to DRGS

We interpolated the extracellular potentials calculated by the FEM onto the center of each neural compartment in our C-neuron model using the NEURON simulation environment within the Python programming language.[261,280] We calculated each compartment's time-varying membrane voltage in response to DRGS using a backward Euler implicit integration method with a time step of 5 μs. We calculated activation thresholds, the minimum pulse amplitude required to elicit one or more action potentials in a C-neuron model, using a binary search algorithm with a precision of 0.1 μA. We calculated the activation threshold in response to one, three, or five DRGS pulses. In each case, we calculated the amplitude required to induce one-to-one activation, i.e., each applied pulse elicits one AP from the C-neuron. Unless otherwise stated, we simulated DRGS pulses with a 300 μs pulse width.[77]

6.4 Results

6.4.1 C-neuron population characteristics

We first compared our model C-neuron population's ranges for each AP characteristic with those reported by the experimental literature (**Table 6.2**). In general, the model population ranges typically overlapped with the experimentally reported ranges. In some cases (e.g., amplitude), the model range extended beyond the experimental range, while in other cases (e.g., duration, rise time), the model range covered more of the left tail of the experimental range. Therefore, we believe that our 100 models represent a reasonable portion of the experimental population's AP characteristics.

Table 6.2 Comparing model population and experimental ranges for C-neuron somatic action potential metrics. Model population data are represented [minimum, maximum].

	Model population range	**Experimental range**	**Reference**
Amplitude	[75.7, 100.2] mV	81.6 ± 6.9 mV	[265]
Duration (base)	[2.2, 2.9] ms	4.97 ± 2.16 ms	[265]
Rise time	[0.7, 1.3] ms	2.5 ± 0.89 ms	[283]
Fall time	[1.4, 2.2] ms	4.61 ± 3.5	[283]
AHP amplitude	[10.6, 17.3] mV	8.2 ± 5.1 mV	[265]
AHP 80	[0.0, 43.1] ms	14.4 ± 9.2 ms	[283]

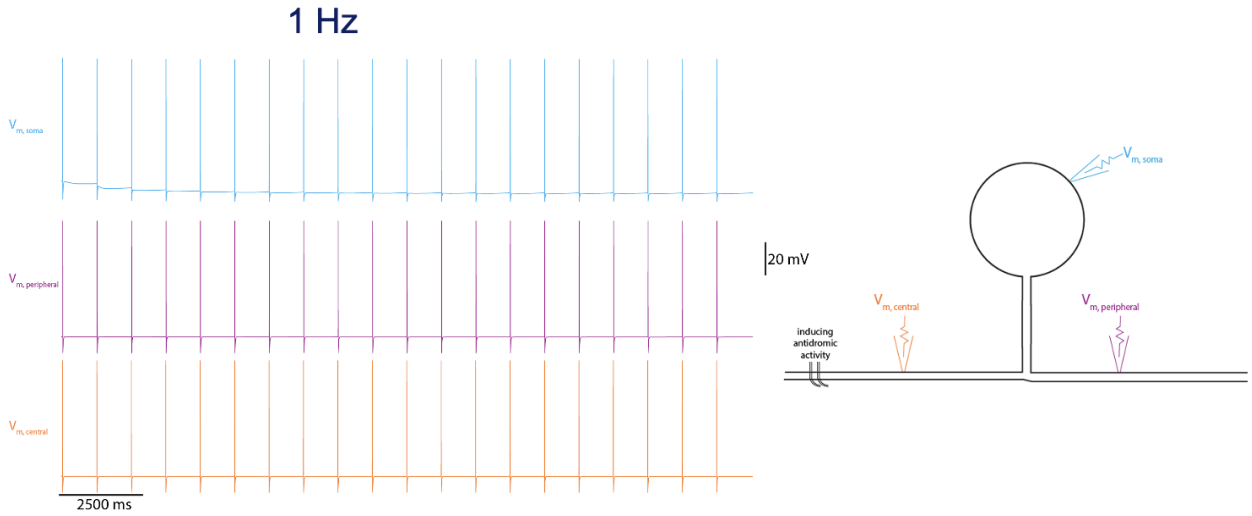

Figure 6.1 Action potential propagation in C-neurons. We simulated 1 Hz antidromically propagating afferent traffic in the central axon of a representative C-neuron model. (Left) Membrane potential recordings from the soma (blue, top), peripheral axon (purple, middle), and central axon (orange, bottom). (Right) Cartoon representation of a C-neuron model's pseudounipolar morphology, and locations where membrane potential is recorded (color coded to corresponding traces on left). All 20 APs initiated in the central axon propagated into the peripheral axon and invaded the soma.

We next examined the ability of our model population to filter propagating APs at the T-junction. We induced antidromically propagating APs in the central axon and recorded how many APs propagated into the peripheral axon.[336,337] In general, model populations allowed only low frequency trains of APs to propagate through the T-junction, while increasing the frequency of propagating APs resulted in a low-pass filtering effect. For example, **Figure 6.1** shows 20 APs initiated at 1 Hz in the central axon of a representative C-neuron model. Each of the 20 APs successfully propagates into the peripheral axon. However, when increasing the AP initiation frequency to 2 Hz (**Figure 6.2**), the model demonstrates several APs which fail to propagate into the peripheral axon (note the electrotonic residues in the somatic membrane potential trace).

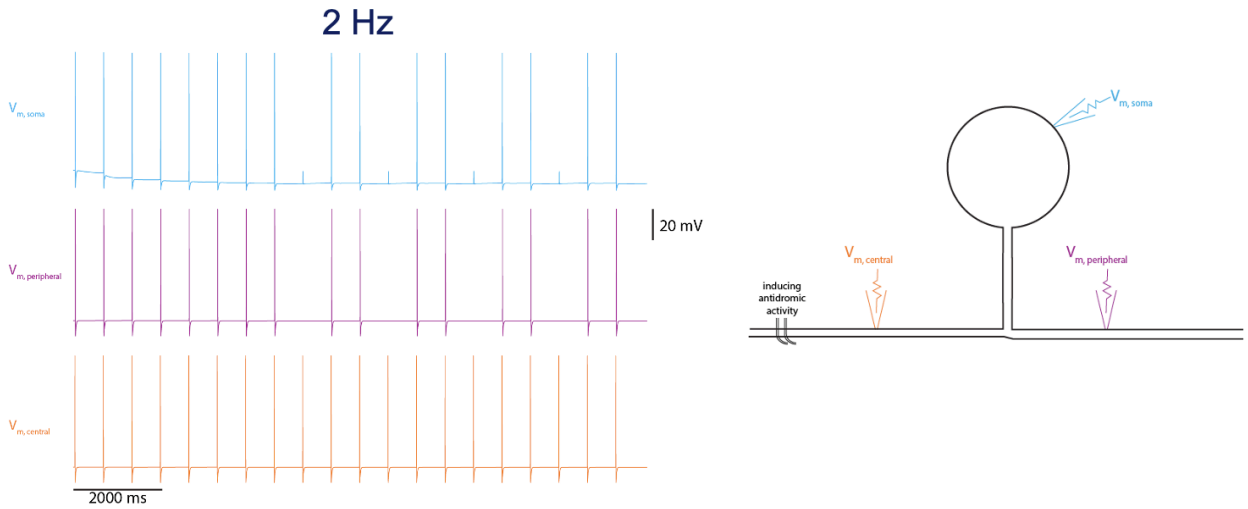

Figure 6.2 T-junction filtering in C-neurons. We simulated 2 Hz antidromically propagating afferent traffic in a representative C-neuron model. (Left) Membrane potential recordings from the soma (blue, top), peripheral axon (purple, middle), and central axon (orange, bottom). (Right) Cartoon representation of a C-neuron model's pseudounipolar morphology, and locations where membrane potential is recorded (color coded to corresponding traces on left). We initiated 2 Hz activity in the central axon. At this frequency, not all pulses propagated from the central axon into the peripheral axon and soma, demonstrating low-pass filtering of APs at the T-junction.

We next examined if DRGS augmented T-junction filtering. We initiated APs at a frequency of 20 Hz in the peripheral axon to simulate painful afferent traffic propagating to the spinal cord.[121] After 500 ms of afferent traffic, we applied DRGS and examined if action potentials ceased propagating into the central axon. None of our C-neuron models demonstrated augmented T-junction filtering as a result of DRGS. However, including active ion channels, specifically SK and Ca_L, in the axons of the C-neuron produced DRGS-enhanced T-junction filtering in many C-neuron models. **Figure 6.3** shows a representative model in response to 40 Hz cathodic DRGS applied with a 10 mA pulse amplitude,[76] with a maximal axonal SK conductance of 10 mS/cm^2 and a maximal axonal Ca_L conductance of 0.03 mS/cm^2. DRGS initiated APs in the soma of the C-neuron, and fully filtered orthodromically propagating action potentials after a brief (~200 ms) wash-in period.

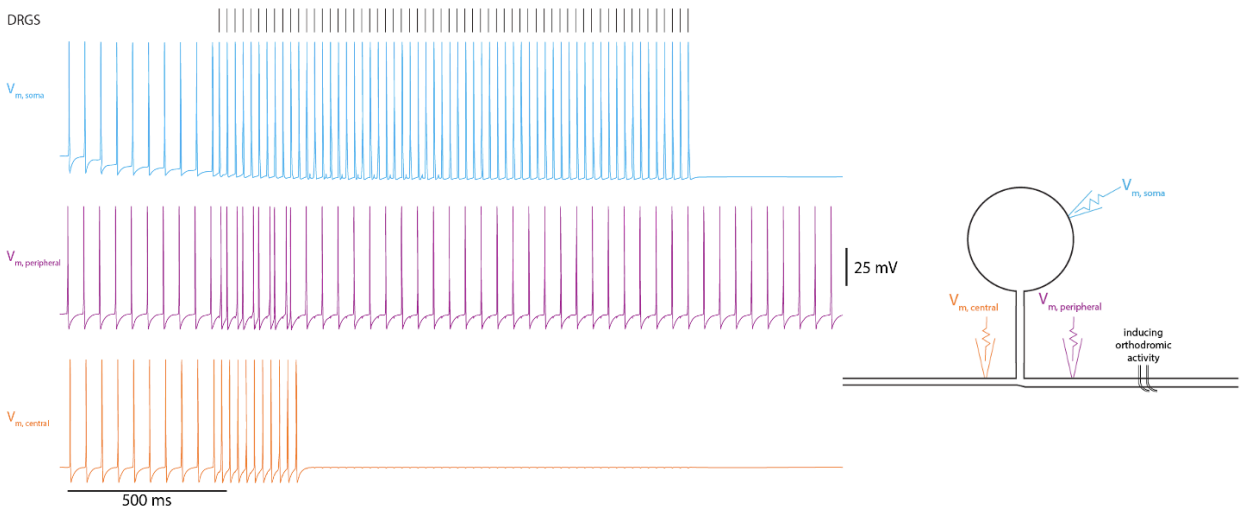

Figure 6.3 DRGS-induced T-junction filtering in C-neurons. When including SK and L-type calcium channels in the stem, peripheral, and central axons, 40 Hz cathodic DRGS applied with a pulse amplitude of 10 mA and pulse duration of 300 μs (top, black tick marks) induced T-junction filtering. We initiated 20 Hz afferent traffic in the peripheral axon (purple trace) and recorded the somatic (blue) and central axon (orange) responses before, during, and after DRGS. DRGS augmented the somatic hyperpolarization that began in response to putatively painful AP generation in the soma. DRGS induced T-junction filtering after a brief wash-in period, precluding orthodromic propagation of APs through the T-junction.

6.4.2 Effect of physiologic variability on C-neuron activation thresholds

We next examined whether variability in the ion channel expression profiles of C-neurons affected their activation thresholds in response to DRGS. **Figure 6.4** compares the activation thresholds of each C-neuron model in our population in response to anodic and cathodic DRGS applied at 20 Hz and 40 Hz.[76,77] Cathodic DRGS (**Figure 6.4A,B**) activation thresholds ranged between approximately 7 mA and 14 mA across the model population. Anodic DRGS (**Figure 6.4C,D**) thresholds ranged between approximately 4 mA and 12 mA. Generally, activation thresholds for cathodic DRGS were similar in response to one, three, or five pulses. However, anodic DRGS thresholds generally increased as the number of applied pulses (and therefore, the number of APs elicited at threshold) increased.

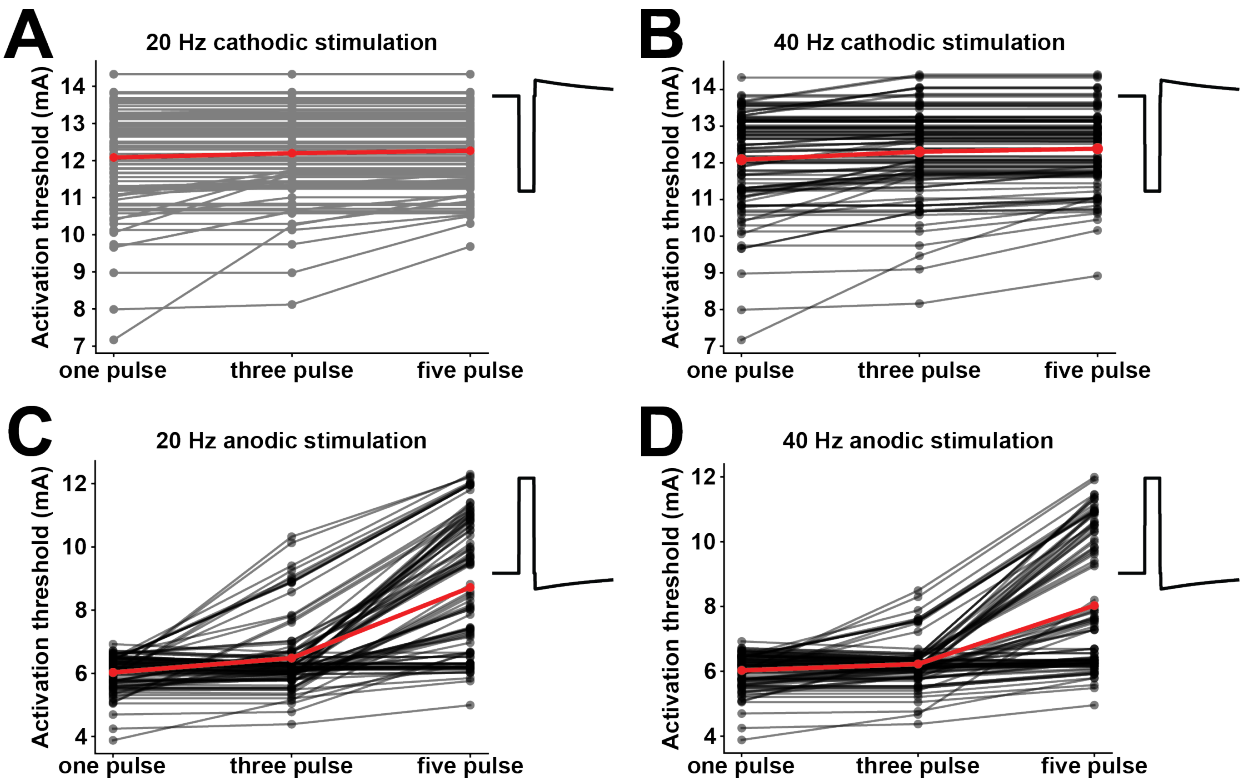

Figure 6.4 C-neuron activation thresholds during DRGS. We calculated the stimulation amplitudes necessary to induce one-to-one activation in all 100 C-neuron models in response to one, three, and five stimulus pulses. Gray lines represent each C-neuron model. Red lines indicate the mean population threshold. We calculated thresholds in response to cathodic (A, B) and anodic DRGS (C, D) applied at 20 Hz (A, C) and 40 Hz (B, D).

Next, we examined if there were any relations in the biophysical properties of our C-neuron model population and their resulting activation thresholds. Generally, we did not observe trends between maximal ion channel conductances (e.g., $Na_v1.8$) and activation threshold. However, **Figure 6.5** compares each model's activation threshold in response to five cathodic DRGS pulses applied at 20 Hz to its maximal M-current potassium conductance. There appears to be a trend between increased maximal M-current potassium conductance and model activation threshold. This trend is present in response to cathodic DRGS applied at 40 Hz, and anodic DRGS applied at 20 Hz and 40 Hz (data not shown).

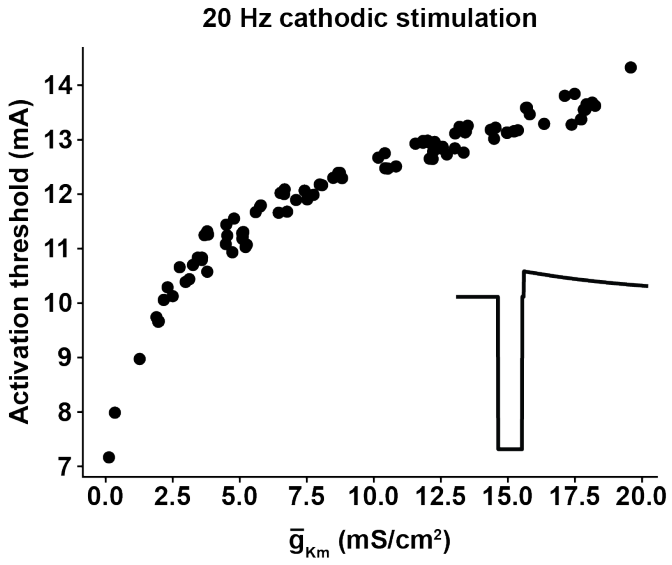

Figure 6.5 Activation thresholds compared to M-type potassium conductances. We compared each model's activation threshold and maximal M-type potassium conductance in response to five pulses of 20 Hz cathodic DRGS. There appears to be a trend between increased model M-type potassium conductance and increased activation threshold.

6.4.3 Effect of electrode array size on C-neuron response to DRGS

Lastly, we wanted to examine the apparent discrepancy between C-neuron activation thresholds found in previous computational modeling studies of clinical DRGS and those found in preclinical studies.[118,121] We compared each C-neuron model's activation threshold in response to five DRGS pulses applied with a clinical electrode array compared to an electrode array scaled down to mimic the arrays used in preclinical experiments in rats (**Figure 6.6**).[146] Regardless of stimulus pulse polarity or pulse frequency, each C-neuron's activation threshold decreased when stimulating with the preclinical electrode array.

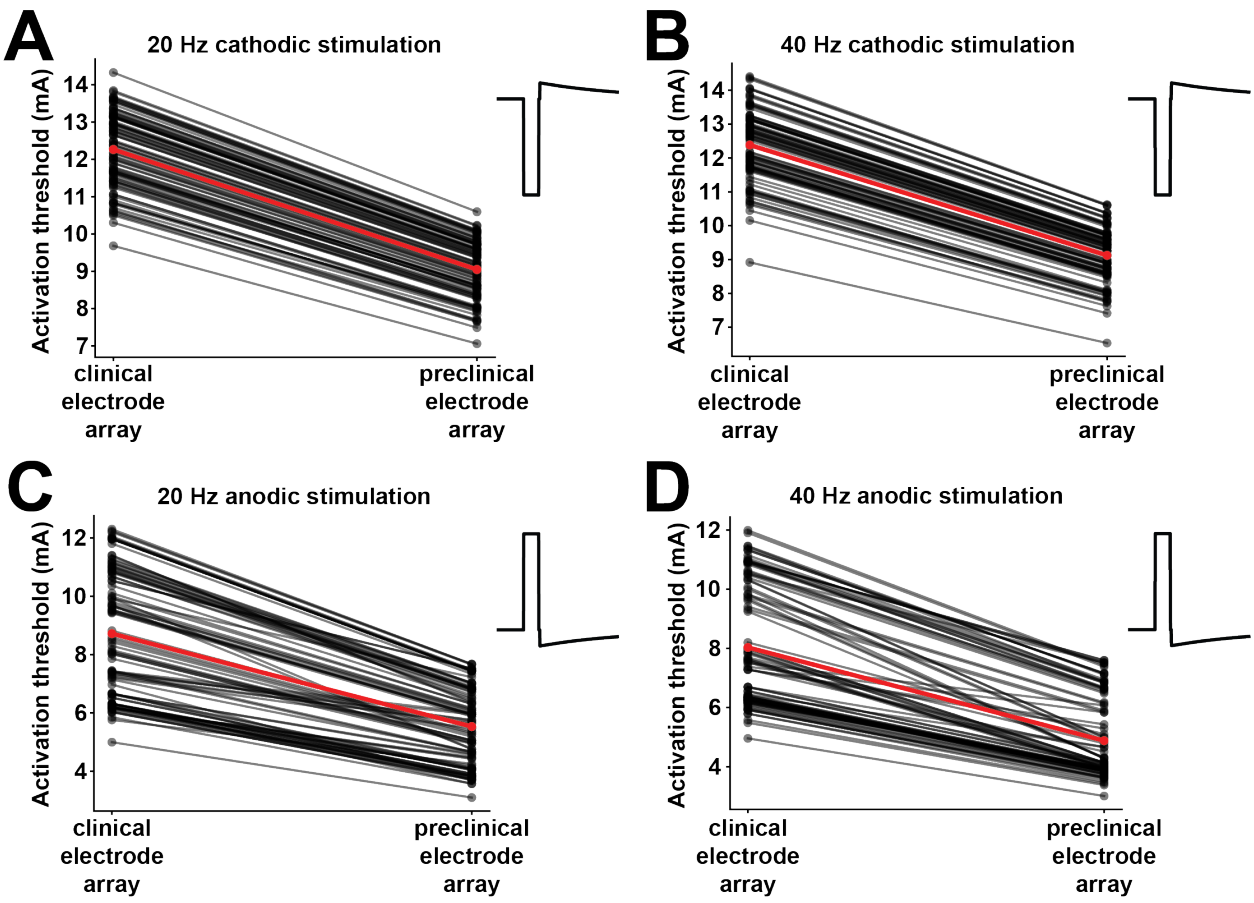

Figure 6.6 C-neuron activation thresholds in response to clinical and preclinical electrode arrays. We compared C-neuron activation thresholds in response to DRGS applied with electrodes with spatial dimensions representing clinical electrode arrays and electrode arrays used in preclinical experiments (**Table 6.1**). Gray lines represent each C-neuron model. Red lines indicate the mean population threshold.

6.5 Discussion

6.5.1 Augmenting T-junction filtering in C-neurons as a mechanism of action of DRGS

Several previous studies demonstrated that filtering painful APs at the T-junction of C-neurons in DRG may be a primary mechanism of DRGS.[76,121] However, computational studies suggest that the stimulation amplitudes required to produce this effect are outside of the ranges used clinically.[76,118,119] Recent preclinical work demonstrated that contrary to the estimates of

computational modeling studies, the activation thresholds of Aβ- and C-neurons when stimulating a DRG are more comparable than when stimulating peripheral nerves.[121]

Preclinical studies of DRGS necessarily utilize small electrodes capable of stimulating comparably smaller DRG (**Table 6.1**).[82,121,146] The electrode contacts utilized by Yu and colleagues had surface areas nearly one-third the surface area of electrode contacts used clinically (1.41 mm^2 and 3.92 mm^2, respectively).[146] Smaller electrode contacts suggest that the current densities produced by electrode arrays used in preclinical experiments are larger than those used clinically, possibly lowering the activation threshold of nonmyelinated C-neurons. Therefore, we investigated the effect of smaller electrode arrays on C-neuron thresholds. Our models suggest that smaller preclinical electrode arrays likely produce a noticeable decrease in C-neuron thresholds compared to clinical electrode arrays (**Figure 6.6**). However, the C-neuron thresholds did not reduce to levels comparable to Aβ-neurons, which are on the order of hundreds of microamps.[118,119] Therefore, there may be other features of DRG neurons not accounted for in our models that reduce thresholds further.

For example, we implemented a modified (increased axon diameter) version of our previously published morphological model of a C-neuron with a linear stem axon trajectory.[118,135] *In vivo*, stem axon trajectories are complex, winding paths which may produce complex spatial distributions of extracellular potentials during DRGS. Our biophysical intuition for neural activation during extracellular stimulation traditionally comes from studies of long axons in peripheral nerves.[57,58,181] Therefore, investigation into the effects of complex axonal trajectories on the neural response to extracellular stimulation may be warranted.[338]

A recent study found that large-diameter DRG neurons positive for 200 kDa neurofilament (putatively Aβ-neurons) release the inhibitory neurotransmitter gamma-aminobutyric acid

(GABA), and that stimulating these neurons reduced chronic pain-related behaviors.[123] It is possible that DRGS predominantly directly activates Aβ-neurons, which then release GABA to activate surrounding C-neurons. Primary afferent DRG neurons have higher internal concentrations of chloride than external concentrations.[180] Therefore, activating the ionotropic $GABA_A$ receptor would cause a C-neuron to depolarize, potentially triggering filtering at the T-junction. Such a finding would suggest that DRGS may provide pain relief by modulating both Aβ- and C-neuron input into the spinal cord.

Finally, it is possible that there may be a component of the long-term threshold in response to tonic stimulation that cannot be captured by modeling the effects of only five stimulus pulses on a cell model simulating biological processes which occur on time scales of milliseconds to tens or hundreds of milliseconds. Chao and colleagues found that DRGS-induced T-junction filtering has a wash-in time of approximately 30 seconds.[121] It seems plausible that there could be homeostatic mechanisms or other biological processes which operate on time scales of seconds to minutes which modulate a neuron's response to extracellular stimulation.[86] Interdisciplinary approaches combining systems neuroscience with electrical biophysics may be useful in exploring such possibilities.

6.5.2 Modeling the response of populations of biophysically distinct neurons to electrical stimulation

Our C-neuron model population exhibited a range of activation thresholds in response to DRGS (**Figure 6.4**). In response to cathodic pulses, thresholds ranged between approximately 7 mA and 14 mA. In response to anodic pulses, thresholds ranged between approximately 4 and 12 mA. We did not see a significant difference in results between the two tested stimulation frequencies. However, anodic thresholds were consistently lower than cathodic thresholds. We

believe this is due to the cell body being oriented directly below the active contact. When placing an electrode near a cell body, anodic stimulation will induce APs in neurons at lower stimulus pulse amplitudes than cathodic stimulation.[51]

We also compared activation thresholds in response to different numbers of stimulus pulses (**Figure 6.4**). We are particularly interested in the pain-relieving effects of DRGS in the long-term, i.e., after patients have been living with the therapy for many months or years. Unfortunately, simulating only a few seconds of the neural response to DRGS is computationally demanding. Our data suggest that cathodic thresholds may be consistent in response to different numbers of stimulus pulses, while anodic thresholds increase with larger numbers of applied pulses. We hypothesize that this difference may result from axons having shorter chronaxies than somas (50-200 μs for axons, 200-700 μs for somas).[291,339] Cathodic stimuli typically produce lower activation thresholds when placed near axonal compartments, while anodic stimuli typically produce lower activation thresholds when placed near a soma.[51] In this work, we used a 300 μs stimulus pulse duration, which may favor axonal excitation over somatic excitation.[51] Therefore, the greater excitability of axonal compartments at the pulse duration used in this study may produce consistent thresholds in response to different numbers of applied cathodic stimuli. Longer pulse durations (e.g., ≥ 700 μs) may produce a similar effect on different numbers of applied anodic stimuli. Further study is needed to understand the long-term response to therapeutic electrical stimulation, and how technical factors, such as stimulus pulse polarity and pulse duration may lead to different long-term responses.

We also found an apparent trend between maximal M-type potassium conductance and activation threshold (**Figure 6.5**). Should this finding stand up to further analysis, it would demonstrate some utility in modeling populations of biophysical models in studying

neurostimulation. Our data suggest that increased maximal M-type potassium conductance also brings about an increase in C-neuron activation thresholds. This population modeling framework may allow for interpreting the biophysical underpinnings (e.g., variable M-current) of experimental results (e.g., variable activation thresholds within a cell population).

6.5.3 Limitations

The experiments of Lüscher and colleagues showed that the following frequencies of orthodromically propagating APs should be the same as antidromically propagating APs.[336,337] However, action potentials propagating through a branch point from a small-diameter axon to a large-diameter axon would have a higher likelihood of failure at a junction. According to Smith, geometric ratios (GRs) – relating the diameters of parent and daughter branches – larger than 10 suggest propagation is likely to fail.[340] Sundt and colleagues showed that C-neurons with axons near the diameter ranges used here and in previous DRGS studies can produce GRs greater than or equal to 10 for antidromically propagating APs, but less than 4 for orthodromically propagating APs.[76,135] Furthermore, some data suggest that the central processes of cat DRG neurons are consistently smaller in diameter than the peripheral processes.[183] Therefore, further experiments are needed to determine: 1) how consistent central and peripheral process diameter differences are across species (e.g., rats, humans), and 2) whether differences in antidromic and orthodromic following frequencies exist across species. An in-depth understanding of the physiological mechanisms which affect a neuron's following frequency is crucial to understanding how DRGS and other therapies may augment such mechanisms.

We parametrized our model populations to reproduce characteristics of somatic APs. None of the resulting models exhibited T-junction filtering of orthodromically propagating pulses in response to DRGS. One reason for the absence of T-junction filtering in our models is we did not

include a following frequency as a component of each model's "score." Unfortunately, repeatedly simulating following frequency scenarios is not computationally feasible when using 400 walkers in the MCMC algorithm due to the large number of simulations with long simulation times. To ensure sufficient exploration of model parameter space with the MCMC method and reduce computational demand, we excluded following frequency metrics from our model "score." With sufficient computational resources, including following frequency metrics may produce models with robust filtering properties.

Another explanation is that our C-neuron model might be missing one or more ionic mechanisms (e.g., currents which produce a net hyperpolarization), that are important to producing robust T-junction filtering. Sundt and colleagues hypothesized that a slow outward cation current, such as the SK current, could be responsible for T-junction filtering. However, their model included SK only as an illustrative example.[135] There may be one or more additional molecular constituents of T-junction filtering not accounted for in our present model population.

A previous computational study of DRGS showed DRGS-induced somatic activation produced a net hyperpolarization effect on the T-junction mediated by slowly decaying outward currents.[76] Though we included the same somatic active ion channels as Kent and colleagues[76] in our model populations, none of our models exhibited T-junction filtering in response to DRGS. We had to include SK and Ca_L channels in the stem, central, and peripheral axons to produce this effect in our previously published model (**Figure 6.3**).[118,119] We believe there are several possible explanations for the discrepancy between our findings and those of Kent and colleagues.[76] For example, we modeled explicit representations of different sodium and potassium channel currents (e.g., $Na_v1.7$, $Na_v1.8$, K_A, K_{DR}), while Kent and colleagues modeled the lumped effects of each

isoform.[76,118] It is possible that accounting for the dynamics between explicit ion channel isoforms affects cumulative model behaviors, such as T-junction filtering.

6.6 Conclusion

DRGS is an important tool in a clinician's clinical algorithm for managing neuropathic pain. In this work, we demonstrated that DRGS may augment T-junction filtering in C-neurons to provide pain relief, but do not yet understand the biophysical basis of DRGS producing significant effects on nonmyelinated neurons. Simulating preclinical electrodes with larger current densities than their clinical counterparts reduced C-neuron activation thresholds, but not to the level predicted by preclinical studies. Other possible avenues for exploration include the complex morphology of DRG neuron stem axons, the possibility of "postsynaptic" GABAergic activation of C-neurons by directly stimulating Aβ-neurons, and exploring the long-term physiological effects of tonic electrical stimulation. Modeling populations of biophysically distinct neurons which reproduce variability in experimental measures may be a useful tool in understanding the neural response to extracellular electrical stimulation.

Chapter 7 – A Patient-Specific Modeling Framework for Studying Neural Activation During Spinal Cord Stimulation

7.1 Abstract

Despite several decades of experience, there have been limited improvements in the clinical outcomes of spinal cord stimulation (SCS) for managing chronic pain. One factor limiting our ability to improve the clinical implementation of SCS is our lack of understanding of how inter-patient variability affects the neural response to SCS. Patient-specific field-cable models provide a computational approach to estimating the neural response to SCS in individual patients. In this work, we developed a framework for constructing and analyzing patient-specific models of patients receiving SCS to manage intractable chronic pain. This framework could be used to compare the neural response to SCS across many patients. Here, we demonstrate this approach by comparing the neural response to SCS in two patients. We compare model-predicted axonal thresholds to clinically measured sensory and discomfort thresholds. This study demonstrates the utility of the patient-specific modeling approach in studying the mechanisms of action and implementation of SCS and lays the groundwork for future high-powered studies pairing computational modeling and clinical data. Such interdisciplinary studies are vital to improving our understanding and implementation of SCS.

7.2 Introduction

Spinal cord stimulation (SCS) is a mainstay third-line neurostimulation therapy for managing neuropathic pain that does not respond to conventional medical management.[88] SCS is achieved by implanting an electrode array in the dorsal epidural space of the spinal column. Conventional SCS applies electrical impulses at frequencies of approximately 40-60 Hz to the dorsal columns of the spinal cord, while some novel SCS modalities apply stimulation in bursts of electrical impulses, or at frequencies in the kilohertz range.[25] Unfortunately, the success of SCS is highly variable across patients, and improvements in patient outcomes over time have been limited.[29] Two contributing factors limiting the success of SCS are: 1) we do not understand the physiological mechanisms of SCS-induced pain relief, and 2) we do not understand the patient-specific factors that affect SCS's ability to target pain-relieving mechanisms.

Computational modeling has been critical in advancing our understanding of the mechanisms of SCS. These studies suggest that SCS likely provides pain relief by inducing action potentials in axons in the dorsal columns, which may activate inhibitory circuitry in the spinal cord gray matter.[65,67,341] These findings were supported by subsequent preclinical studies which demonstrated SCS may induce inhibitory signaling within the spinal cord dorsal horn.[288,312] Computational approaches have also been used to develop novel electrode technologies and configurations to preferentially target the dorsal columns.[342,343] Despite these advancements, SCS outcomes have not improved. We believe that insight into how patient-specific factors (e.g., anatomy, stimulator programming) affect the neural response to SCS is critical to improving the therapy.[189]

Patient-specific modeling has been a useful approach in studying the effects of other neurostimulation therapies, such as deep brain stimulation.[344,345] To date, there have been relatively

few studies using patient-specific models to study the effects of SCS. Preliminary studies found that compared to canonical SCS models, patient-specific SCS models predict axonal activation at amplitudes consistent with corresponding clinical thresholds.[73,346] However, these studies simplified various aspects of the spinal column anatomy such as the spine.[73] Recent work has demonstrated that the position of active electrode contacts relative to bony structures affects the pulse amplitude needed to induce action potentials in the dorsal columns.[136] Therefore, patient-specific models which account for patient-specific differences in the complex anatomy of the spinal column may provide deeper insights into the mechanisms of action of SCS.

In this work, we present a novel framework for creating patient-specific SCS models which captures the complex anatomy of the spinal column. We implement this framework to compare the neural response of SCS in two patients receiving SCS as part of their standard clinical care. We conclude by discussing the utility of the patient-specific modeling approach, and highlight areas of future research which may help understand the variability in the neural response to SCS across patients. This knowledge will be crucial to improving the clinical implementation of SCS.

7.3 Methods

7.3.1 Participant information

This study was reviewed and approved by the University of Michigan medical Institutional Review Board. We included two adult participants who were receiving SCS to manage their chronic pain as part of their standard clinical care. Both participants cleared a standard psychological evaluation. Both participants provided written informed consent prior to study participation. **Table 7.1** presents information related to each patient's pain diagnosis and electrode array.

Table 7.1 Patient pain diagnosis and electrode array information.

	Pain diagnosis	Implant level	Electrode array type
P1	Lumbar FBSS	T7-T9	16-contact paddle lead
P2	Lumbar FBSS	T9-T10	16-contact paddle lead

FBSS = failed back surgery syndrome; T7 = seventh thoracic spine vertebrae number

7.3.2 Patient-specific finite element models of SCS

We developed patient-specific field-cable models of spinal cord stimulation using a similar approach to Lempka and colleagues.[73] We extended this approach to incorporate realistic representations of each participant's spine geometry. There are three steps in creating a patient-specific field-cable model. The first step is to calculate the extracellular potentials generated in the participant's spinal cord during SCS. Therefore, we developed finite element method (FEM) models of each participant's spinal column anatomy.

Medical image segmentation and co-registration

We used preoperative magnetic resonance imaging (MRI) to segment each participant's spinal cord, cerebrospinal fluid (CSF), intervertebral discs, and vertebrae. We used a postoperative X-ray computed tomography (CT) to segment the participant's spine and SCS electrode array. We then co-registered the segmented surfaces from the MRI and CT images using common anatomical landmarks on the vertebrae to define the patient-specific FEM model. We also included a 300-μm domain surrounding the electrode array to represent the encapsulation layer resulting from the foreign body response to implanted materials.[259,347] We used the software packages Mimics and 3-matic within the Mimics Innovation Suite (Materialise, Brussels, Belgium) to perform the image segmentation and co-registration, respectively. **Figure 7.1** shows the construction of the patient-specific model for P1.

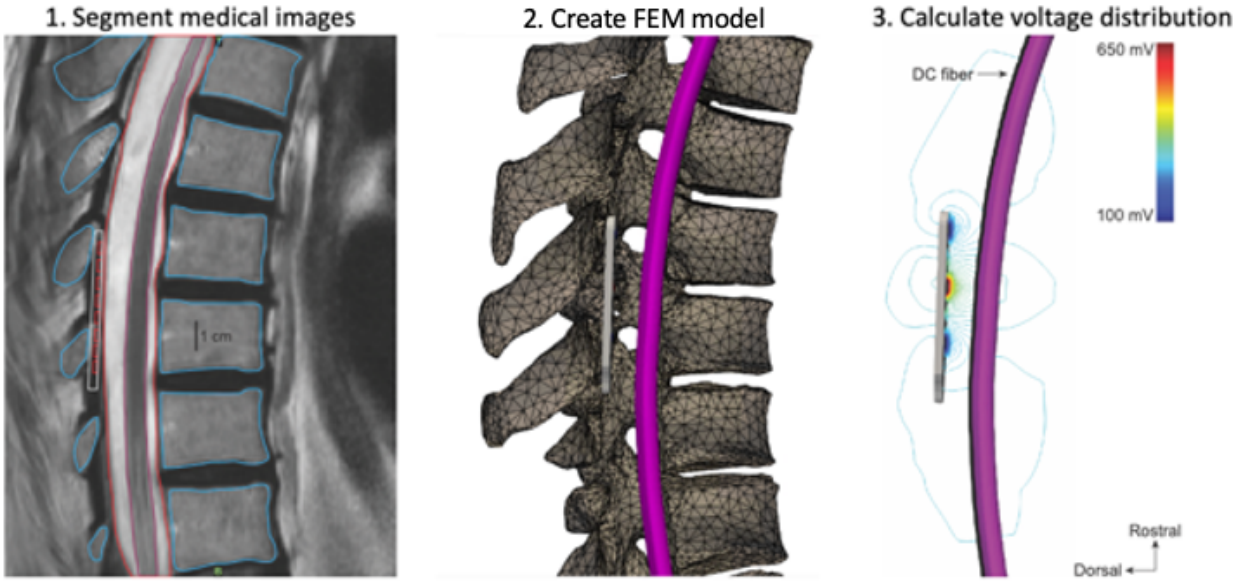

Figure 7.1 Constructing a patient-specific FEM model. (Left) Segmenting the spinal column anatomy from pre-operative MRI images, and SCS electrode array from post-operative CT images. (Middle) Creating a three-dimensional FEM model from the segmented surfaces. Only the spine, spinal cord, and electrode array are shown. (Right) Isopotential lines representing the extracellular potentials generated by SCS calculated from the FEM model.

We were not able to discern the boundaries between the gray and white matter of each participant's spinal cord. Therefore, we needed a method to represent the gray and white matter dimensions at each level of the participant's cord. First, we determined which spinal vertebrae was closest to the participant's cathode as part of their clinically effective programming. If the participant had more than one cathode, we selected the vertebrae nearest the greatest number of cathodes. Due to the anatomy of the lower thoracic spinal cord, we assumed that the effects of that participant's SCS system were predominantly focused on the spinal cord segment two levels caudal to the vertebral level nearest the cathode(s).[348] For example, if a participant's T9 vertebrae was nearest their cathode(s), we simulated the relative gray and white matter dimensions at the T11 spinal cord level.[349] We then scaled these relative gray and white matter dimensions to match the dorsoventral and mediolateral dimensions of the participant's spinal cord at 5 mm increments along the trajectory of the participant's segmented spinal cord surface.

Meshing and tissue conductivity assignment

We then imported the co-registered surfaces into COMSOL Multiphysics (v5.6; COMSOL, Inc., Burlington, MA, USA). The complex anatomy of the participant's spinal bone, and the close apposition of the intervertebral discs to the vertebral bodies, prevented us from creating a tractable finite element mesh. We developed a method for representing geometrically complex surfaces (e.g., the highly resistive spine) in the FEM model's tissue conductivity stiffness matrix. First, we created a large cylindrical general thorax domain centered around the rostro caudal axis of the participant's electrode array. This thorax domain completely encompassed all other anatomical domains of the patient-specific model. We excluded the spine and intervertebral discs from the initial meshing process. We then created an initial volume mesh of this cylinder containing all anatomical compartments (i.e., electrode array, encapsulation layer, CSF, spinal cord) except for the spine and intervertebral discs.

We imported a list of each node in the initial volume mesh's three-dimensional coordinates into MATLAB (MathWorks, Natick, MA, USA). We iterated through each node in the list and then determined if each node's three-dimensional coordinate resided within one of the surfaces representing the participant's spine or intervertebral discs. If a node resided within one of these surfaces, we assigned that node's conductivity value equal to that tissue's electrical conductivity. Electrical conductivities used for the anatomical domains in each patient-specific model are reported in **Table 7.2**. We then imported the resulting list of nodes and conductivities back into COMSOL. We re-calculated the volume mesh, and included a smoothing function to increase mesh resolution in regions where differences in neighboring node conductivities are large (i.e., near the boundaries between various tissue compartments). We obtained a final FEM mesh by repeating this process of conductivity assignment and volume mesh calculation three times, to

ensure an accurate representation of the boundary between each participant's various tissue compartments.

Table 7.2 Electrical conductivities used in each tissue domain in the FEM.

Parameter	Value	Reference
Gray matter	0.23 S/m	[258]
White matter (longitudinal)	0.6 S/m	[258]
White matter (transverse)	0.083 S/m	[258]
Dura mater	0.03 S/m	[295]
Bone	0.02 S/m	[260]
General thorax	0.25 S/m	[258]
Encapsulation	0.17 S/m	[259]
Intervertebral disc	0.65 S/m	[350]

Calculate the potential field generated by SCS

We used the final FEM mesh to calculate the extracellular potentials generated by SCS. Generally, we applied 1 V and 0 V boundary conditions to the participant's active and return contacts, respectively. We modeled the electrode lead body and outer boundary of the thorax domain as perfect insulators. We modeled the surface of all inactive electrode contacts as equipotential with zero net current across their surface. Then, we solved Laplace's equation to calculate the extracellular potentials generated by SCS. Some SCS systems can fractionalize the applied current over multiple independent electrode contacts. In participant models utilizing those systems, we calculated the extracellular potentials generated by a monopolar source at each individual electrode contact with the outer surface of the thorax domain set to ground (i.e., 0 V). For an arbitrary stimulation configuration (i.e., combination of active contacts), we scaled each utilized contact's solution by the percentage of current flowing through the contact, and summed all corresponding scaled solutions using the principle of superposition to create the final distribution of extracellular potentials. We then scaled this spatial distribution by the time-

dependent output of a typical implanted pulse generator (IPG) to obtain the spatiotemporal distribution of extracellular potentials.[281]

7.3.3 Distribute axon models in the spinal cord

Multi-compartment model of a dorsal column axon

The next step in creating a field-cable model is to distribute neuron models within the anatomy of interest (i.e., the spinal cord). In this work, we examined the effect of SCS on axons in the white matter of the spinal cord (e.g., the dorsal columns). We implemented a previously published model of an Aβ-axon.[118] We modeled axon diameters between 5.7 μm and 11.5 μm, similar to the diameter ranges found in human dorsal columns.[31,351] The morphology and passive electrical properties of each axon was represented using the McIntyre-Richardson-Grill (MRG) myelinated axon model.[263] The active electrical properties (i.e., the voltage-gated ion channels) were based on the Gaines model of a sensory axon,[264] with modifications made to reproduce electrophysiological properties of Aβ-neurons in the DRG (from where dorsal column axons originate) (**Figure 7.2**, left).[118]

Distributing axons in the spinal cord white matter

We next aimed to determine the density of axons in each participant's spinal cord. We calculated the point on the surface of the participant's spinal cord with the largest value of the activating function[58] in response to the participant's clinically effective programming. The activating function, the second spatial difference of extracellular potentials along an axon,[58] is an approximation for the activation of axons, such as those that makeup the dorsal columns. Therefore, we assumed that the participant's clinically effective SCS programming is likely predominantly activating dorsal column axons in the region of the spinal cord where the activating function is largest. We calculated the cross-sectional area of the participant's spinal cord at the

point where the activating function was largest. We used this cross-sectional area to calculate the density of axons of a given diameter as described previously,[136] using previously published axon densities in the superficial dorsal columns.[351]

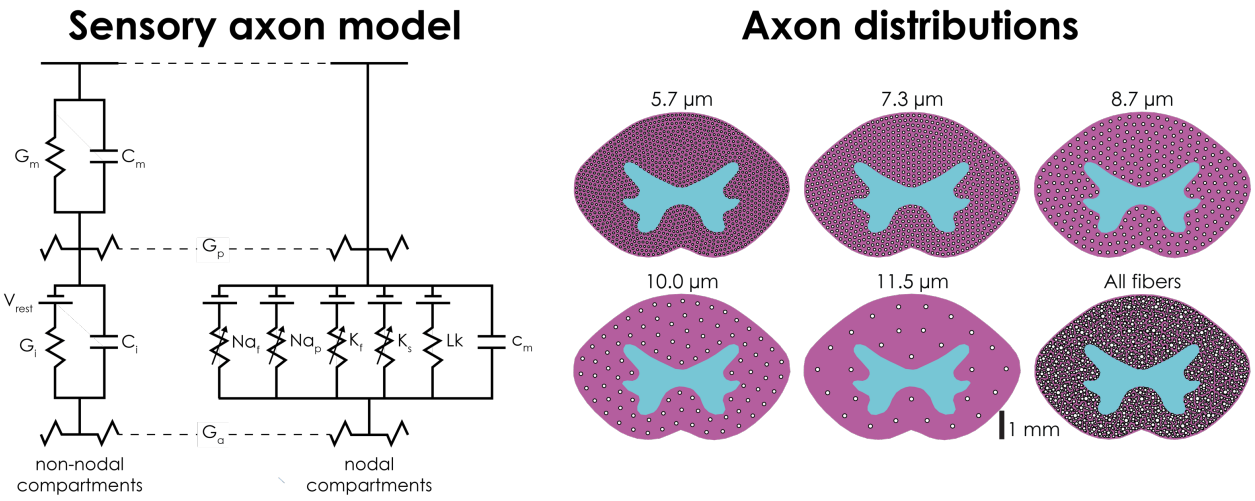

Figure 7.2 Multi-compartment models of dorsal column axons. (Left) Circuit schematic representing the nodal and internodal compartments. (Right) Relative densities of axon diameters constituting the dorsal column axons. Adapted from the work of Zander and colleagues.[136]

Because the dimensions of a spinal cord vary with spinal level,[349] it is difficult to mathematically define a single canonical trajectory which could be distributed throughout the white matter to constitute the dorsal columns. Therefore, we employed a physics-based approach to generating axonal trajectories through the participant's white matter. We applied a 10 V boundary condition to the caudal face of the participant's spinal cord, and a 0 V (i.e., ground) boundary condition to the rostral face of the participant's spinal cord. We then calculated the electric potential distribution through the participant's spinal cord as described above. We then used COMSOL's Streamline function to calculate uniformly distributed streamlines current paths leading from the caudal face of the cord to the rostral face. By setting the number of streamlines equal to the number of axons of a given diameter, we generated several sets of uniformly distributed white matter axon trajectories. **Figure 7.2** shows representative densities of axons within the spinal cord white matter.

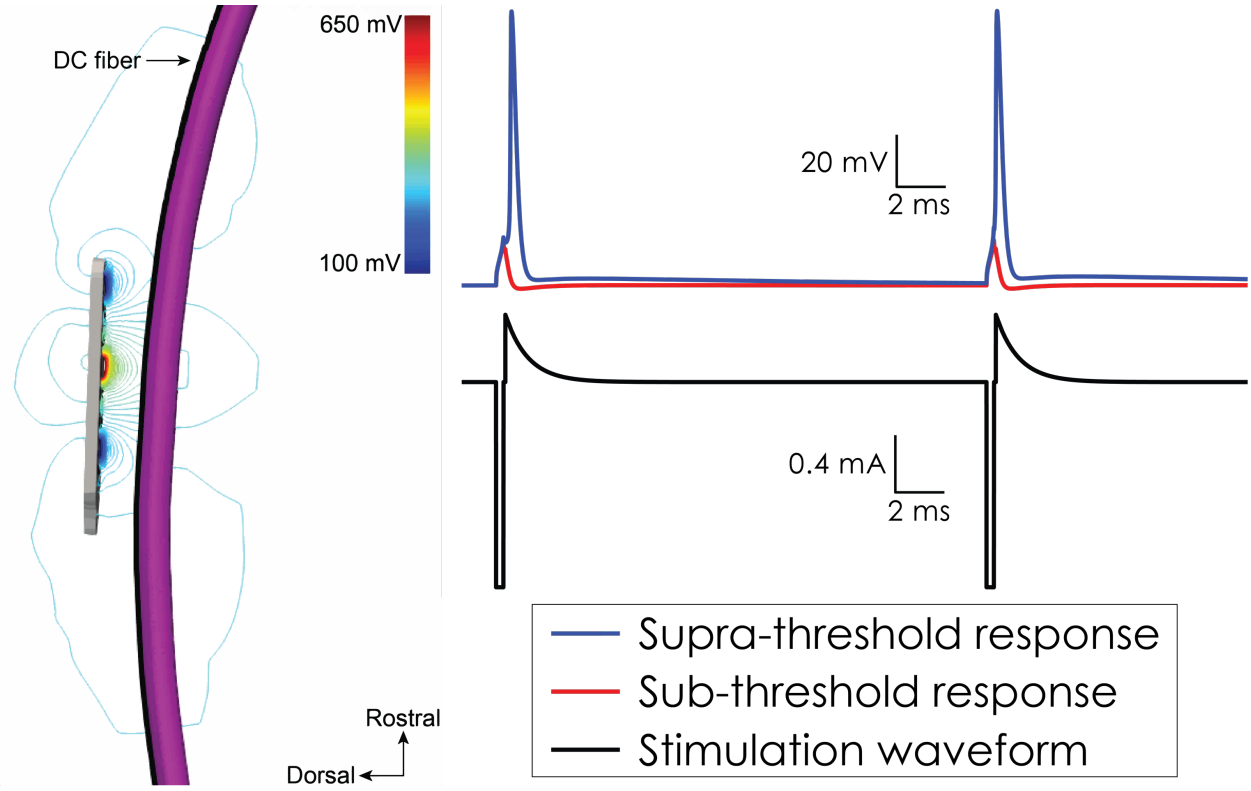

Figure 7.3 Simulating the neural response to SCS. (Left) Isopotential lines representing the extracellular potentials generated by SCS which are interpolated onto the three-dimensional trajectory of dorsal column (DC) fibers. (Right) Example neural responses in response to SCS (black trace) applied at current intensities above (blue) and below (red) the threshold to initiate action potentials. Adapted from the work of Zander and colleagues.[136]

7.3.4 Simulate the neural response to SCS

The third and final step of the field-cable modeling approach was to simulate the neural response to SCS (**Figure 7.3**). We interpolated the spatiotemporal extracellular potentials calculated from the FEM and IPG output onto the center of each axonal compartment. For a given set of stimulation parameters (e.g., stimulus pulse width, pulse frequency), we calculated the activation threshold for each axon in each participant's spinal cord. In this work, we defined the activation threshold as the minimum pulse amplitude at which the axon will generate one or more action potentials in response to each pulse in a train of three stimulus pulses.[352] To calculate an activation threshold, we implemented a bisection algorithm with a precision of 20 μA. We used a

backward Euler implicit integration method with a time step of 5 μs to calculate each neural compartment's time-varying membrane potential in response to SCS.

7.3.5 Clinical testing

We compared model predictions of neural activation to clinically measured SCS-induced evoked sensations. Specifically, we measured each participant's sensory, comfort, and discomfort thresholds. First, we set the participant's stimulus pulse amplitude to 0 mA. We then increased the stimulus pulse amplitude by 0.1 mA increments until the participant reported feeling SCS-induced paresthesias. We then decreased the pulse amplitude until the participant reported they no longer felt paresthesias. We then increased the pulse amplitude until the participant reported feeling SCS-induced paresthesias, and we defined that amplitude as the sensory threshold (ST). We then increased the stimulus pulse amplitude until the participant reported that the SCS-induced sensations became uncomfortable, and we defined that amplitude as the discomfort threshold (DT). We then reduced the stimulation amplitude from the DT until the SCS-induced sensations became an intensity that the participant could tolerate long-term, and we defined that amplitude as the comfort threshold (CT). We defined the therapeutic window (TW) as the difference between DT and ST.

7.4 Results

We developed a framework for constructing patient-specific field-cable models of participants receiving SCS to manage their chronic pain. The rationale for this approach is that accounting for differences between participants, such as differences in anatomy (e.g., CSF layer thickness), in field-cable models may provide key insights into how the neural response to SCS

varies across participants. This framework would allow for the comparison of model-predicted neural activation with clinically measured phenomena (e.g., sensory thresholds). **Figure 7.4** shows qualitatively that this patient-specific modeling framework can capture key anatomical differences which could affect neural activation. Specifically, P1 has a noticeably thicker layer of CSF on the dorsal side of the spinal cord than P2. Dorsal CSF thickness is known to produce significant shunting of current away from the spinal cord, and may affect neural activation during SCS.[67,68]

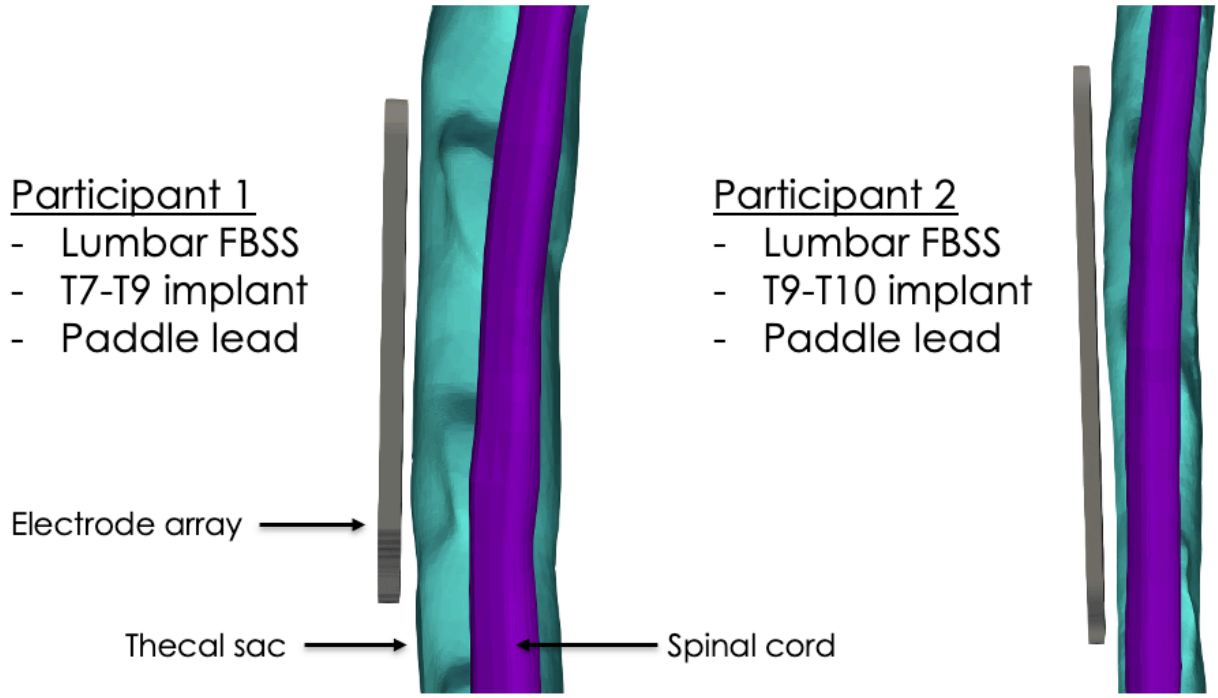

Figure 7.4 Anatomical differences captured by patient-specific modeling framework. The patient-specific model is able to capture anatomical differences that may impact the neural response to SCS. Participant 1 has a noticeably thicker layer of CSF on the dorsal side of the spinal cord than Participant 2.

7.4.1 Effect of pulse width on model and clinical thresholds

We first aimed to compare model predictions of neural activation with clinically measured thresholds. We compared model dorsal column axon activation thresholds with clinically measured sensory thresholds (**Figure 7.5**). In both participants, we compared the minimum activation thresholds to activate one axon model of a given diameter with clinical STs in response

to three different stimulus pulse widths: 60 µs, 300 µs, and 1000 µs. The clinically measured sensory thresholds are reported in **Table 7.3**. Both participants' sensory thresholds decreased in response to increased stimulus pulse widths. For each pulse width, P1's sensory thresholds were higher than P2's sensory thresholds.

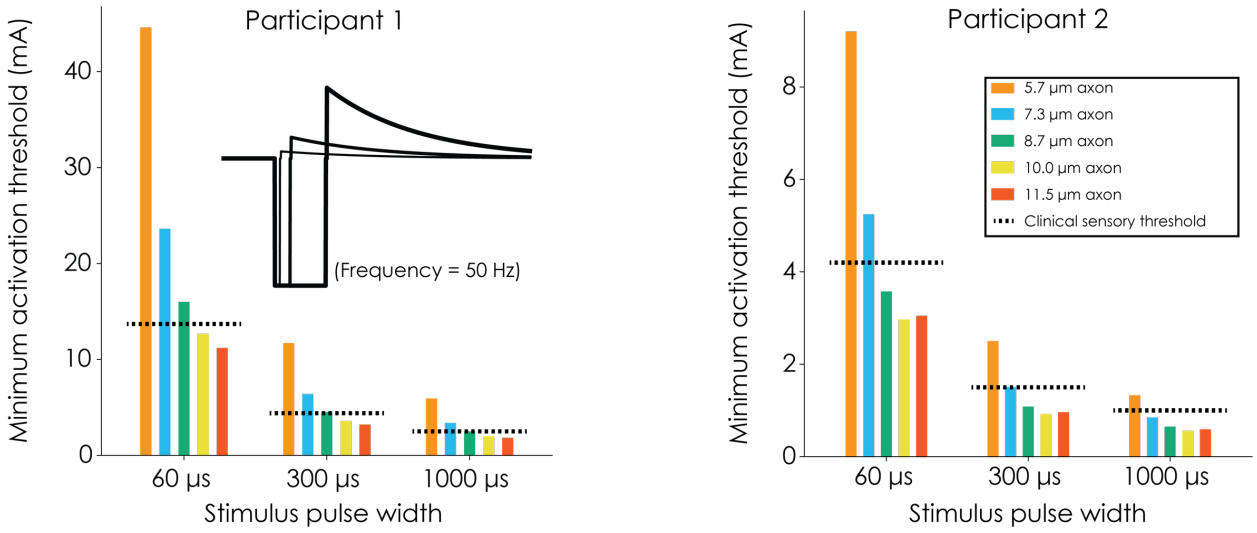

Figure 7.5 Dorsal column and sensory thresholds in response to different SCS pulse widths. Minimum activation thresholds for model dorsal column axons of varying diameters (color-coded bars). Horizontal dashed black lines indicate clinically measured sensory thresholds. Note the different y-axis scales between P1 (left) and P2 (right).

Table 7.3 Sensory thresholds in response to different stimulus pulse durations.

	Sensory thresholds (mA)		
	60 µs	**300 µs**	**1000 µs**
P1	13.7	4.4	2.5
P2	4.2	1.5	1.0

As expected, larger-diameter dorsal column axons had lower minimum activation thresholds than smaller-diameter axons. Similarly, increasing stimulus pulse width produced a decrease in minimum activation threshold of dorsal column axons. Interestingly, the clinically measured STs were generally similar to the minimum activation thresholds for large-diameter (i.e.,

≥ 8.7 µm) dorsal column axons. Notably, P2 had consistently lower thresholds (both the clinically measured ST, and model dorsal column axon thresholds) than P1.

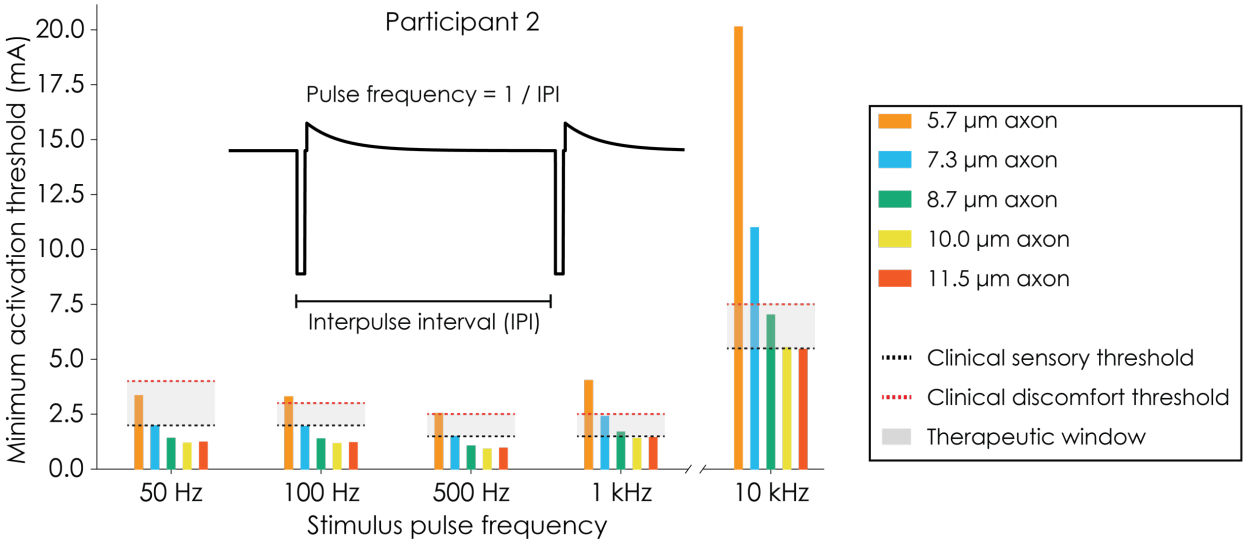

Figure 7.6 Dorsal column, sensory, and discomfort thresholds in response to different SCS frequencies. Minimum activation thresholds for model dorsal column axons of varying diameters (color-coded bars). Horizontal dashed black and red lines represent clinically measured sensory and discomfort thresholds, respectively. Gray shaded region indicates the therapeutic window.

7.4.2 Effect of frequency on model and clinical thresholds

In P2, we performed a preliminary analysis into the effects of stimulus pulse frequency on clinically measured STs and DTs, and minimum model activation thresholds across dorsal column axon diameters. We tested the following stimulus pulse frequencies: 50 Hz, 100 Hz, 500 Hz, 1,000 Hz, and 10,000 Hz. For frequencies less than 10,000 Hz, the stimulus pulse width was 200 µs. When stimulating at 10,000 Hz, the stimulus pulse width was 30 µs, with an interphase gap of 20 µs.

Table 7.4 reports P2's clinically measured STs and DTs and the resulting TW. **Figure 7.6** shows the effect of stimulus pulse frequency on the minimum activation threshold of dorsal column axons across diameters. Generally, increasing stimulus frequency did not significantly affect dorsal column axon minimum thresholds. However, applying SCS with a stimulus pulse

frequency of 10,000 Hz considerably increased minimum dorsal column thresholds. In this preliminary analysis of a single participant, stimulating at 50 Hz or 10,000 Hz resulted in a therapeutic window of 2.0 mA, while stimulating at 100 Hz, 500 Hz, or 1,000 Hz resulted in a therapeutic window of 1.0 mA.

Table 7.4 P2's clinically measured sensory and discomfort thresholds and therapeutic windows in response to SCS applied at different stimulation frequencies.

	Clinically measured thresholds (mA)				
	50 Hz	**100 Hz**	**500 Hz**	**1,000 Hz**	**10,000 Hz**
ST	2.0	2.0	1.5	1.5	5.5
DT	4.0	3.0	2.5	2.5	7.5
TW	2.0	1.0	1.0	1.0	2.0

7.5 Discussion

The goal of this study was to develop a patient-specific field-cable modeling framework for participants receiving SCS to manage their chronic pain. We believe the utility of this approach lies in its ability to: 1) compare neural activation profiles during SCS across participants, and 2) to compare model predictions with clinical data collected from that participant. The bulk of this work focused on developing the methodology for creating anatomically realistic patient-specific models of SCS. We then demonstrated the utility of this approach in a small cohort of two participants. In general, both patient-specific models reproduced expected biophysical trends during extracellular electrical stimulation. Specifically, increases in myelinated axon diameter produced lower activation thresholds, and increasing stimulus pulse width reduced activation thresholds.[57,58,61,291,310] Going forward, this patient-specific modeling framework can be applied to

scientific studies with large participant cohorts to examine the mechanisms of action of SCS and sources of inter-patient variability in the neural response to SCS.

7.5.1 Sources of paresthesia and discomfort during SCS

One of the interesting findings of this work is that the clinically measured STs closely resemble the minimum activation thresholds for dorsal column axons greater than or equal to 8.7 μm in diameter (**Figure 7.5**, **Table 7.3**). Currently, it is unknown how many Aβ-axons must be activated to produce a paresthetic sensation. Some studies applying microstimulation to peripheral nerve axons suggest that activating a single axon can produce a percept.[353] A previous study using patient-specific modeling of SCS suggested that clinical sensory thresholds track well with the pulse amplitude needed to activate 10% of modeled axons.[73] Continued analysis of the dataset presented in this work should more rigorously examine both the percentage of axons activated at ST, as well as the spatial distribution and diameters of axons activated.

We also examined the activation of dorsal column axons at DT in one participant (**Figure 7.6**). Though this investigation is preliminary, these data suggest stimulating at DT likely activates many dorsal column axons, including small-diameter dorsal column axons (i.e., ≤ 7.3 μm). We also examined the TW in response to SCS applied at different stimulus pulse frequencies (**Figure 7.6**). Interestingly, the TW was largest when using the lowest (50 Hz) and highest (10,000 Hz) frequencies. The physiological reasons for different TWs in response to various SCS frequencies are unknown. We must emphasize that we cannot draw conclusions from this investigation in a single participant. However, we believe our results suggest examining the TW in response to different SCS parameters (stimulus pulse frequencies, electrode configurations, etc.) is a worthy avenue of future research.

7.5.2 Inter-patient variability during SCS

Figure 7.4 shows qualitative differences in the thecal sacs and spinal cords of P1 and P2. P1 has noticeably more CSF on the dorsal side of their spinal cord than P2. **Figure 7.5** shows that the STs and amplitude ranges required for dorsal column activation is higher in P1 than in P2. For example, in response to a 60 μs stimulus pulse, all of P1's dorsal column axons have activation thresholds greater than 10 mA, while the minimum thresholds for P2's dorsal column axons are all below 10 mA. It is well understood that the presence of highly conductive CSF causes much of the current generated by SCS to be shunted away from the cord.[67,68] Therefore, our patient-specific modeling framework is able to capture the effect of anatomical differences on differences in neural activation during SCS. This modeling framework could be extended to study the influence of other anatomical variabilities, such as the curvature of the spinal cord, on the neural response to SCS.

7.5.3 Limitations and future work

Though this work represents an advancement in the patient-specific field-cable modeling approach to SCS, there are several limitations to our work. The major limitation of this work as currently presented is the inclusion of only two participants. We believe that demonstrating this approach in two preliminary participants underscores the utility of patient-specific modeling and helps validate the approach. It will be necessary to include a larger cohort of participant models and corresponding clinical data to draw rigorous conclusions.

Constructing a single patient-specific model is time consuming. However, we believe it is feasible to develop a cohort of ten to twenty models for a single study. The most time-consuming step in the model construction process is segmenting and co-registering the three-dimensional surfaces representing the participant's anatomy and SCS system. Interestingly, machine-learning based tools have been developed to automatically segment cervical spinal anatomy.[354,355] Extending these approaches to account for the anatomy of the thoracic spine, and developing

similar tools for automatically segmenting SCS electrode arrays could eliminate or significantly reduce the time necessary to construct a single participant model. Such a tool would be useful in scientific studies aiming to compare model predictions across participants and could form the basis for developing a clinical decision support system for guiding the clinical implementation of SCS. Similar systems have found great success in assisting the implementation of other neurostimulation therapies, such as deep brain stimulation.[356]

In this work, we compared model-predicted neural activation with clinically measured sensory and discomfort thresholds. Though such comparisons may provide insight into the neural substrates of sensations evoked by SCS, there are other clinical data which merit comparison to patient-specific model data. For example, one could compare predicted neural activation profiles with patient reported outcomes of pain relief, such as changes in the pain numerical rating scale (NRS). By comparing predicted neural activation profiles in participants that responded well to SCS (i.e., participants that had a considerable reduction in NRS) with those that did not respond to SCS may provide insights into the physiological mechanisms of SCS-induced pain relief. Furthermore, quantitative sensory testing[139] and clinical electrophysiology measures (e.g., electromyography)[357] could be combined with patient-specific SCS models.

Finally, we examined the effect of SCS only on Aβ-axons in the dorsal columns. Though it is generally believed that conventional SCS provides pain relief by directly activating the dorsal columns,[23,33,67] there are many other types of neurons in the spinal cord which could be modulated by SCS.[110,190,358] However, a recent study using a canonical computer model of SCS demonstrated that across stimulus waveforms (i.e., conventional, burst, high-frequency), clinical SCS is likely applied at insufficient intensities to modulate local neurons in the dorsal horn.[32] It would be

interesting to investigate the effects of SCS on local cells across patients, to determine if local cell modulation by SCS is more feasible in some patients and not in others.

7.6 Conclusions

Spinal cord stimulation is an effective therapy for chronic pain. To maximize the positive impact of the next generation of SCS technologies, we must understand how inter-patient variability affects the neural response to SCS. This understanding, paired with a concise understanding of the mechanisms of SCS-induced pain relief, is crucial to maximizing pain relief in all patients. Combining the patient-specific modeling framework described here with clinical data (e.g., patient-reported outcomes, clinical electrophysiology measures) may be a powerful tool in realizing that goal.

Chapter 8 – Modeling the Molecular Determinants of Central Sensitization in Chronic Itch

The work presented in this chapter was in collaboration with Drs. Bo Duan, Hankyu Lee, and Ehsan Mirzakhalili. This work is currently under preparation for peer-reviewed publication.

The work presented in this chapter has been adapted to reflect my contributions to the larger work. My contributions specifically relate to implementing a Markov Chain Monte Carlo method to develop populations of conductance-based neuron models. Further, I used these model populations to examine which experimentally measured changes in mRNA expression likely contributed to the changes in single-cell and network excitability under chronic itch conditions.

8.1 Abstract

Chronic itch is a common clinical symptom that can have significant negative effects on one's quality of life. We do not understand the physiological mechanisms governing the development of chronic itch, and therefore cannot develop targeted therapies to manage clinical itch conditions. Recent work highlighted the importance of two populations of spinal interneurons in chronic itch development: excitatory neurons expressing Urocortin 3 (Ucn3) and inhibitory neurons expressing neuropeptide Y (NPY) which typically inhibit Ucn3 neurons. Experiments performed by our collaborators, but outside the scope of this dissertation, have identified several changes in ion channel expression in Ucn3 and NPY neurons which may affect the development of chronic itch. In Ucn3 neurons, the expression of mRNA coding for the voltage-gated sodium channel $Na_v1.6$ and voltage-gated R-type calcium channels increased, while expression of mRNA coding for the calcium-activated potassium channel SK decreased. In NPY neurons, the expression

of mRNA coding for Nav1.6 and the voltage- and calcium-activated potassium channel BK decreased. We simulated these changes in populations of multi-compartment conductance-based cable models of spinal interneurons. We leveraged a Markov Chain Monte Carlo method to generate populations of models which reproduce characteristics of the experimentally measured population. Our data suggest that changes in the expression levels of $Na_v1.6$ are likely the greatest contributor to changes in the excitability (e.g., rheobase) of Ucn3 and NPY neurons observed under chronic itch conditions. Furthermore, decreased expression of $Na_v1.6$ specifically in NPY neurons may be a key component of opening the mechanical itch gate. The results of our study suggest therapies aimed at augmenting Nav1.6 function in NPY neurons may be effective in managing chronic itch symptoms. Future experimental work will be critical to test the predictions of our model population data.

8.2 Introduction

Chronic itch is an unpleasant persistent feeling of needing to scratch the skin, clinically defined as an itch sensation lasting longer than six weeks.[359] Chronic itch may be a symptom of dermatological disease, neurological disease, drug use, or systemic disease.[360–363] It is estimated that approximately 23% of the general population has experienced chronic itch at some point in their lives.[364] Unfortunately, chronic itch conditions can have significant negative impacts on one's sleep and is associated with mood disturbances, such as anxiety and depression.[365] Unfortunately, chronic itch, especially neuropathic rather than histaminergic itch, is difficult to manage clinically. Current therapeutics for chronic itch range from topical therapies and anesthetics to opioids and anticonvulsants.[366] Presently, our understanding of the pathophysiological mechanisms of chronic

itch are incomplete, precluding our ability to develop targeted therapeutics for alleviating chronic itch sensations.[367]

Recent work highlighted key interneurons involved in both the transition of mechanical itch sensations, and the development of pathological chronic itch.[107] Pan and colleagues demonstrated that dorsal horn interneurons expressing Urocortin 3 (Ucn3) are a crucial node in transmitting mechanical itch sensations. Furthermore, Ucn3 neurons are typically under tight inhibitory control from dorsal horn interneurons expressing neuropeptide Y (NPY), and that this inhibitory tone is reduced under chronic itch conditions.[107] Currently, we do not understand the molecular mechanisms contributing to chronic itch pathogenesis.

Multi-compartment models use Hodgkin-Huxley dynamics to simulate neural activity. Previous work used multi-compartment models to study the biophysical mechanisms of sensory transmission and disease pathogenesis, and investigate how therapeutics may alter the activity of diseased neural circuits.[78,368] However, such models are typically parametrized to reproduce the means of experimental data, which may not represent a real neuron from a sampled experimental population.[85] Furthermore, studying the effects of potential therapeutics on only one model, while real instantiations of the therapy would putatively be affecting populations of many neurons, suggests that we may be missing effects of therapies on diverse populations.

In this work, we implemented a Markov Chain Monte Carlo (MCMC) method to generate populations of multi-compartment models representing Ucn3 and NPY neurons. We used these model populations to simulate how experimentally measured changes in ion channel expression may affect changes in excitability at both the single-cell (e.g., rheobase) and circuit (e.g., Ucn3 neuron spiking) level.

8.3 Methods

We employed a multi-compartment cable modeling approach to investigate how changes in ion channel expression led to the biophysical changes (e.g., change in rheobase) observed during calcipotriol-induced chronic itch pathogenesis. We extended a previously published model of a superficial dorsal horn interneuron to include explicit representations of the ion channels we found in Ucn3 and NPY neurons in our qRT-PCR experiments in calcipotriol-treated mice. We developed populations of biophysically plausible multi-compartment cable models of Ucn3 and NPY neurons, where each model had a unique parameter set of maximal ion channel conductances. Second, we simulated experimentally measured changes in ion channel expression in each neuron model to determine which changes in ion channel expression were chiefly responsible for changes in single-cell excitability metrics (e.g., rheobase). Lastly, we simulated changes in ion channel expression in networks of Ucn3 and NPY neuron models to determine which pathological changes contributed to the opening of the mechanical itch gate.

8.3.1 Biophysical model of superficial dorsal horn interneurons

We constructed all Ucn3 and NPY multi-compartment cable models with the NEURON simulation environment (v7.7) within the Python programming language.[261,280] We used a temperature of 23 degrees Celsius and an integration time step of 20 μs in each simulation.

We implemented a previously published multi-compartment cable model of a superficial dorsal horn interneuron[369,370] to model Ucn3 and NPY neurons (**Figure 8.1A**). The model utilized a simplified ball-and-stick morphology to accurately reproduce morphological and electrophysiological features of spinal cord interneurons (e.g., cell body size, equivalent dendrite impedance) without increasing computational demand. We implemented all morphological

parameters described by Melnick and colleagues,[369] with the addition of a myelinated axon with 41 nodes of Ranvier (**Figure 8.1A**).

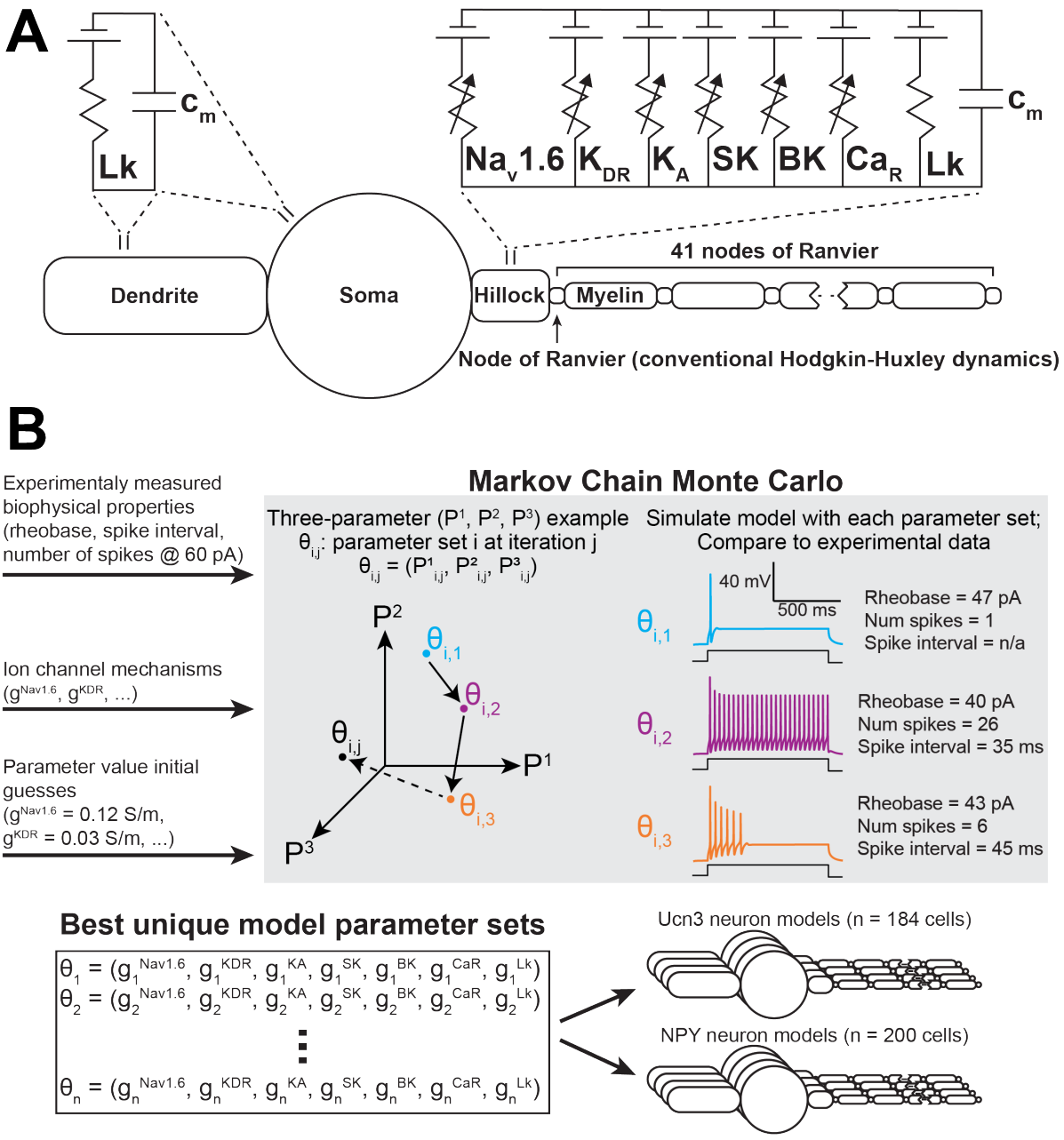

Figure 8.1 Spinal interneuron model and model population parametrization. (A) Multi-compartment model of a superficial dorsal horn interneuron expressing the ion channels found to be up- or down-regulated in response to calcipotriol. (B) Markov Chain Monte Carlo (MCMC) method for parametrizing populations of Ucn3 and NPY neuron models. An example with three unknown parameters (P_1, P_2, P_3) is shown for visualization purposes. Our implementation of the MCMC algorithm had seven unknown parameters ($g_{Nav1.6}$, g_{KDR}, g_{KA}, g_{SK}, g_{BK}, g_{CaR}, g_{Lk}). The MCMC algorithm produced 184 unique models of Ucn3 neurons, and 200 unique models of NPY neurons.

The original spinal interneuron model contained a voltage-gated sodium channel and a delayed-rectifier potassium channel which reproduced tonic- and adapting-firing behavior seen in some superficial dorsal horn interneurons.[369,370] However, we aimed to determine which specific ion channels found in our study contribute to the biophysical features of chronic itch pathogenesis. Therefore, we removed the original ion channel models and instead included explicit representations of the voltage-gated sodium channel $Na_v1.6$,[371] a delayed rectifier potassium channel,[372] an A-type potassium channel,[373] a small-conductance calcium-activated (SK) potassium channel,[372] an R-type voltage-gated calcium channel,[374] a big conductance calcium- and voltage-activated (BK) potassium channel,[375] and a linear leak conductance. To reduce dimensionality during model parametrization and computational demand during single-cell and network simulations (see below; **Figure 8.1B**), we expressed these ion channels only in the axon hillock (**Figure 8.1A**). We modeled the dendritic and somatic compartments as passive cables with only a linear leak conductance and membrane capacitance. The 41 nodal compartments in the axon consisted of NEURON's built-in Hodgkin-Huxley dynamics (i.e., the 'hh' mechanism in NEURON) to facilitate action potential propagation in the axon.

Our goal was to use this biophysical neuron modeling approach to simulate which experimentally measured changes in ion channel expression were predominantly responsible for calcipotriol-induced changes in neuronal excitability. However, this biophysical modeling approach does not directly account for mRNA expression. To mimic experimentally measured changes in mRNA expression, we instead changed the maximal conductance of a given ion channel according to its percent change in mRNA expression under chronic itch conditions. We assumed that an increase in mRNA expression of a given channel likely corresponded to an increase in the number of those channels inserted into the neural membrane. Similarly, we assumed that a

decrease in mRNA expression corresponded to a decrease in the number of channels inserted into the membrane. Therefore, increasing or decreasing the maximal conductance of a given ion channel in our modeling framework mimics an increase or decrease in mRNA expression, respectively.

8.3.2 Simulating the mechanical itch network

We wanted to examine how changes in ion channel expression affected the output of the mechanical itch network. In other words, we wanted to examine how changes in ion channel expression affected whether Ucn3 neurons generated action potentials in response to physiological Aβ-fiber input.[107] Therefore, in some simulations, we modeled synaptic connections between Ucn3 and NPY neuron models and simulated how calcipotriol-induced changes in ion channel expression affected network behavior.

We modeled all synaptic connections as alpha functions using NEURON's built-in Exp2Syn mechanism. We modeled the inhibitory synapse from the last node of Ranvier in an NPY neuron onto the somata of Ucn3 neurons with a 0.1 ms rise time, a 20 ms decay time constant, and a reversal potential of -75 mV.[78,376]

We modeled Aβ-fiber input as point processes onto the middle of the dendrite of both Ucn3 and NPY neurons. We modeled the excitatory Aβ-fiber input using a rise time of 0.1 ms, a 5 ms decay constant, and a reversal potential of 0 mV.[78] The latency of monosynaptic input from Aβ-fibers onto Ucn3 neurons is longer than the latency of Aβ-fiber input onto NPY neurons. Therefore, we modeled Aβ-fiber input onto Ucn3 and NPY neurons with latencies of 4.0 ms and 2.2 ms, respectively. We set the conductance of all excitatory and inhibitory synapses such that they produced evoked postsynaptic currents of similar amplitude to those previously measured in the mechanical itch network.[107]

8.3.3 Parametrization of populations of Ucn3 and NPY neuron models

To generate populations of Ucn3 and NPY neuron models with variable ion channel expression profiles, we implemented Goodman and Weare's Affine-Invariant Markov Chain Monte Carlo method (MCMC; **Figure 8.1B**) using the emcee Python package (https://emcee.readthedocs.io).[334,335] MCMC methods have previously been used to simultaneously estimate the values of several ion current parameters in a biophysical neuron model.[377] We extended this approach to generate de novo combinations of maximal ion channel conductances with which to parametrize our Ucn3 and NPY models.

MCMC methods use Bayes' theorem to estimate the posterior probabilities of a given set of parameter values describing a system based on experimental data and prior probabilities of each parameter's value. One of the benefits of the MCMC algorithm is that it preferentially samples parameter combinations with greater likelihoods (i.e., parameter combinations which better describe our experimental data). However, the goal of our study was not to estimate plausible distributions of each ion channel's conductances in Ucn3 and NPY neurons. Rather, we were interested in how populations of Ucn3 and NPY neuron models that were differently parametrized, but still representative of experimentally measured populations, respond to calcipotriol-induced pathophysiological changes. Therefore, we utilized the MCMC algorithm to simulate and evaluate thousands of possible parameter sets (i.e., combinations of maximal ion channel conductances) on their ability to reproduce experimentally measured biophysical characteristics of Ucn3 and NPY neurons. Specifically, we calculated rheobase, number of spikes generated during 60 pA current clamp stimulation, and spike interval during 60 pA current clamp stimulation, for each parameter set. We then calculated the normalized distance between each parameter set's calculated biophysical characteristics and the experimentally measured means for both Ucn3 and NPY

neurons. We assigned each tested model a "score" by averaging the normalized distances between each metric, where a lower score indicates the model's biophysical properties more closely recapitulate the biophysical properties of an experimentally measured cell.

For each run of the MCMC algorithm, we simulated 400 individual Markov chains (i.e., walkers) of parameter sets. We allowed each walker to modify and re-evaluate its parameter values 25 times per run (i.e., 25 iterations). We ensured sufficient exploration of parameter space by running the MCMC algorithm four times for each cell type (i.e., Ucn3 and NPY neurons), and injecting Gaussian noise in each walker's initial guesses for each parameter value during each run. We chose uniform distributions constrained within physiologic ranges (e.g., conductances cannot be negative) as priors for each parameter. This process resulted in thousands of possible parameter combinations which could parametrize a Ucn3 or NPY neuron model. We removed parameter sets which poorly matched experimentally measured biophysical characteristics (e.g., rheobase) by excluding models above a score threshold (i.e., a normalized distance greater than 0.6) from analysis. The final result of this process was 184 parameter sets which described Ucn3 neuron models, and 200 parameter sets which described NPY neuron models (**Figure 8.1B**).

8.4 Results

8.4.1 Model population characteristics

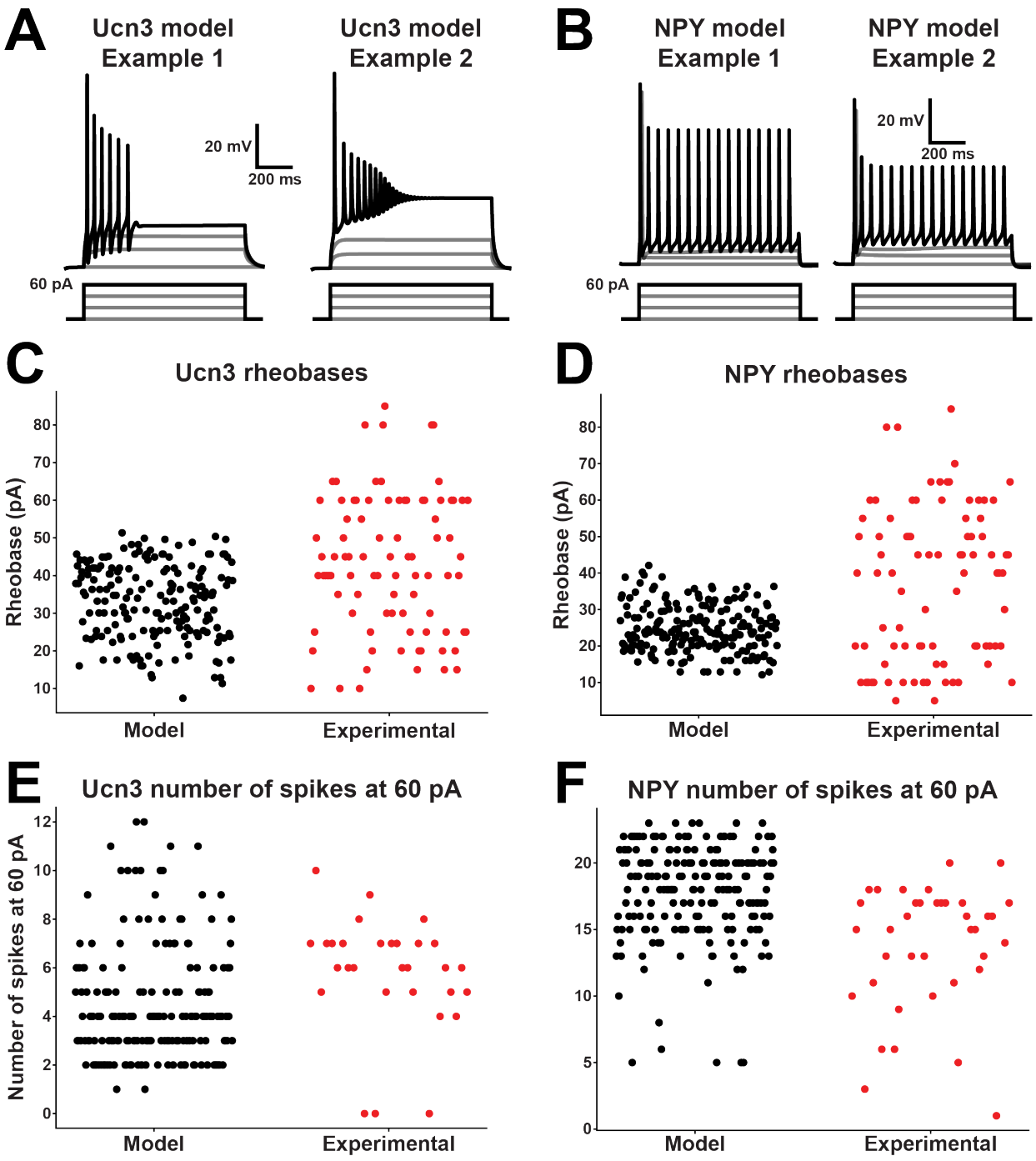

Figure 8.2 Ucn3 and NPY neuron model population characteristics. (A) Example Ucn3 neuron model firing patterns during current injection. Ucn3 neuron models demonstrated initial bursting patterns similar to experimentally measured cells. (B) Example NPY neuron model firing patterns during current injection. NPY neuron models demonstrated tonic firing patterns similar to our experimentally measured cells. (C) Comparison of Ucn3 neuron model rheobases (black) with experimentally measured Ucn3 neuron rheobases (red). (D) Comparison of NPY neuron model rheobases (black) with experimentally measured NPY neuron rheobases (red). (E) Comparison of Ucn3 neuron model number of spikes generated in response to 60 pA current injection (black) with those of experimentally measured Ucn3 neurons (red). (F) Comparison of NPY neuron model number of spikes generated in response to 60 pA current injection (black) with those of experimentally measured NPY neurons (red).

Our implementation of the MCMC algorithm generated 184 models of Ucn3 neurons, and 200 models of NPY neurons (**Figure 8.1B**). These models produced current-clamp responses similar to those seen experimentally (**Figure 8.2A,B**). The distributions of the model populations' biophysical properties (i.e., rheobase, number of spikes generated at 60 pA) resembled the distribution of biophysical properties measured from our experimental population (**Figure 8.2C-F**). Our model populations appear to resemble the more-excitable cells observed in our experimental population of neurons. For example, the Ucn3 (**Figure 8.2C**) and NPY (**Figure 8.2D**) neuron model populations produced rheobases up to 51.4 pA and 42.1 pA, respectively. However, a few experimentally measured cells from both populations had rheobases greater than 80 pA (**Figure 8.2C,D**). It is possible that mechanical itch circuits comprised of the most excitable population of each cell type may be most susceptible to chronic itch-induced changes. Therefore, we believe that our Ucn3 and NPY model populations could provide crucial insight into the mechanisms of chronic itch pathogenesis.

8.4.2 Effect of ion channel conductance on single-cell biophysical properties

As described above, we observed several concurrent changes in the biophysical properties and ion channel expression levels of Ucn3 and NPY neurons in chronic itch conditions. We next aimed to determine which changes in ion channel expression were chiefly responsible for the changes in single-cell biophysical properties observed in calcipotriol-treated mice. We mimicked the experimentally measured changes in ion channel mRNA expression by systematically increasing or decreasing the conductance of the corresponding ion channel in each of our Ucn3 and NPY models. We then calculated the biophysical properties of each cell model (e.g., rheobase) to determine how changes in ion channel expression affected the excitability of neurons in the mechanical itch network.

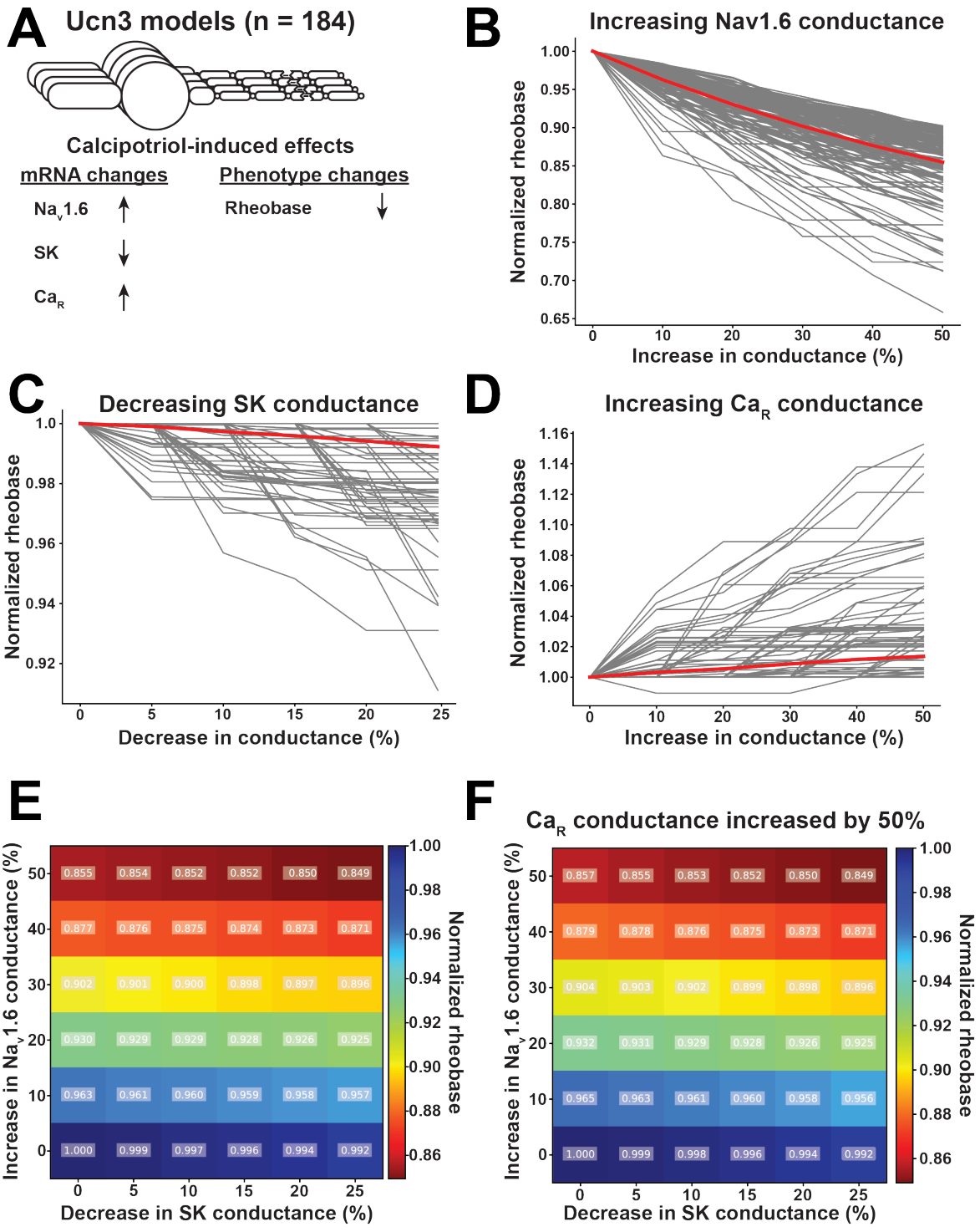

Figure 8.3 Effect of calcipotriol-induced changes in ion channel expression on Ucn3 excitability. (A) Calcipotriol-induced effects on Ucn3 neurons observed experimentally. (B) Effect of increasing $Na_v1.6$ conductance on Ucn3 neuron model rheobases. (C) Effect of decreasing SK conductance on Ucn3 neuron model rheobases. (D) Effect of increasing Ca_R conductance on Ucn3 neuron model rheobases. (E) Effect of simultaneously increasing $Na_v1.6$ conductance and decreasing SK conductance on Ucn3 neuron model rheobases. (F) Effect of simultaneously increasing $Na_v1.6$ conductance, decreasing SK conductance, and increasing Ca_R conductance by 50% on Ucn3 neuron model rheobases.

In calcipotriol-treated mice, the rheobase of Ucn3 neurons decreased, the expression of $Na_v1.6$ and CaR increased, and the expression of SK decreased (**Figure 8.3A**). When increasing $Na_v1.6$ conductance in Ucn3 neuron models by 50%, Ucn3 neuron models experienced between a 9.8% and 34.2% reduction in rheobase, with an average reduction in rheobase of 14.5% (**Figure 8.3B**). When decreasing SK conductance in Ucn3 neuron models by 25%, Ucn3 neuron models experienced between a 0% and 8.9% reduction in rheobase, with an average reduction in rheobase of 0.8% (**Figure 8.3C**). When increasing Ca_R conductance in Ucn3 neuron models by 50%, Ucn3 neuron models experienced between a 0% and 15.3% increase in rheobase, with an average increase in rheobase of 1.4% (**Figure 8.3D**). Interestingly, one Ucn3 neuron model exhibited a 1.1% decrease in rheobase in response to an increase in Ca_R conductance between 10% and 30% (**Figure 8.3D**).

We next examined how varying the conductance of multiple ion channels simultaneously affected the rheobase of Ucn3 neuron models (**Figure 8.3E,F**). Generally, rheobase was most significantly affected by increasing the conductance of $Na_v1.6$. When increasing $Na_v1.6$ conductance by 50% and decreasing SK conductance by 25%, Ucn3 neuron models experienced between a 9.8% and 41.5% reduction in rheobase, with an average reduction in rheobase of 15.1% (**Figure 8.3E**). When additionally increasing Ca_R conductance by 50%, Ucn3 neuron models experience between a 9.8% and 38.3% reduction in rheobase, with an average reduction in rheobase of 15.1% (**Figure 8.3F**). The average reduction in rheobase when maximally varying the conductance of multiple ion channels (i.e., 15.1%) was comparable to that of increasing $Na_v1.6$ conductance by 50% alone (i.e., 14.5%).

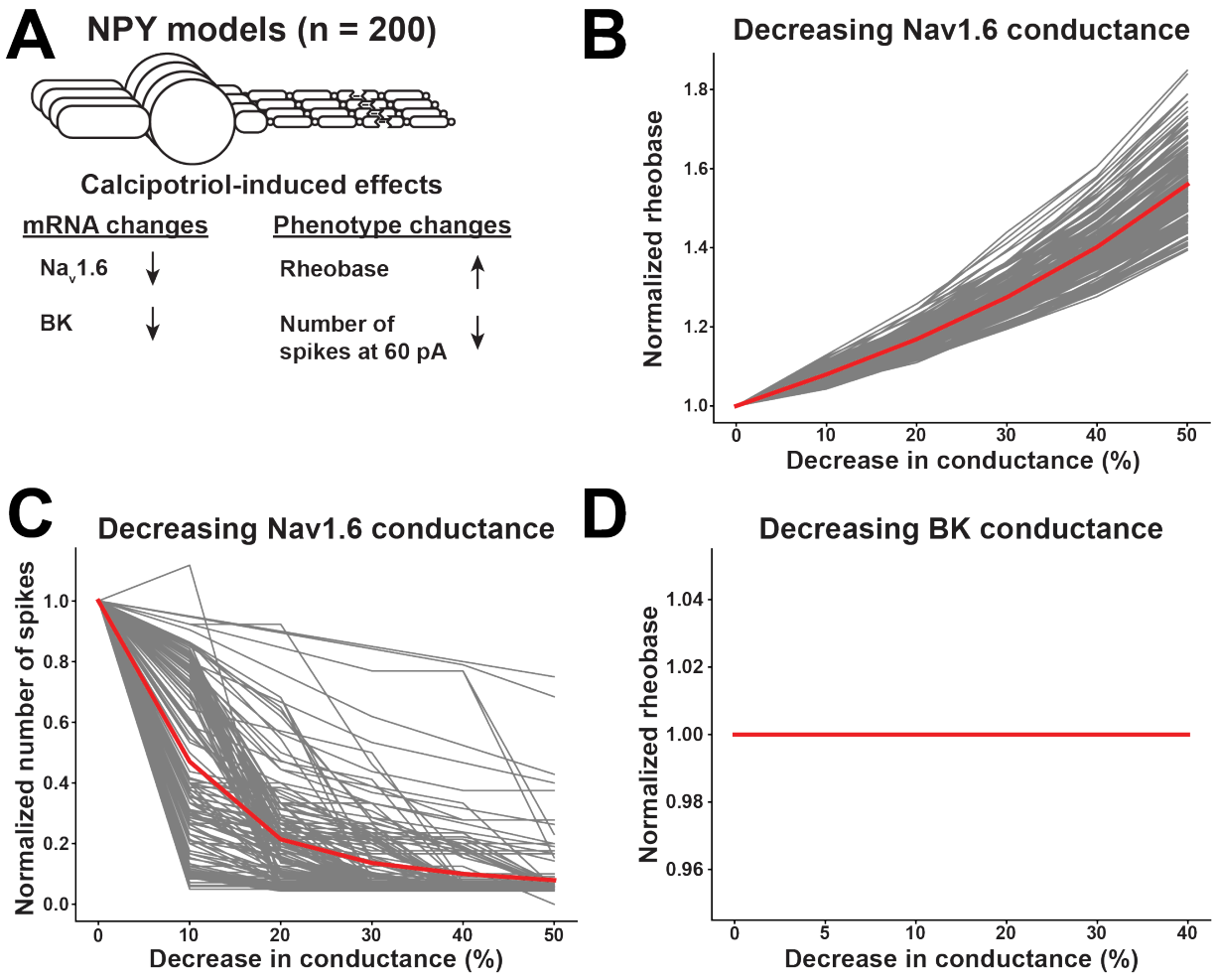

Figure 8.4 Effect of calcipotriol-induced changes in ion channel expression on NPY excitability. (A) Calcipotriol-induced effects on NPY neurons observed experimentally. (B) Effect of decreasing $Na_v1.6$ conductance on NPY neuron model rheobases. (C) Effect of decreasing $Na_v1.6$ conductance on NPY neuron model numbers of spikes generated in response to 60 pA current injection. (D) Effect of decreasing BK conductance on NPY neuron model rheobases.

In calcipotriol-treated mice, the rheobase of NPY neurons increased, the number of spikes generated in response to 60 pA current clamp stimulation decreased, and the expression of $Na_v1.6$ and BK decreased (**Figure 8.4A**). When decreasing $Na_v1.6$ conductance in NPY neuron models by 50%, NPY neuron models experienced between a 39.3% and 84.9% increase in rheobase, with an average increase in rheobase of 56.0% (**Figure 8.4B**). In addition, a 50% decrease in $Na_v1.6$ conductance in NPY models produced between a 25.0% and 100.0% reduction in the number of spikes generated during 60 pA current clamp stimulation, with an average decrease of 92.1%

(**Figure 8.4C**). Interestingly, in one NPY neuron model, a 10% decrease in $Na_v1.6$ conductance produced an 11.8% increase in the number of spikes generated during 60 pA current clamp stimulation. However, further decreases in $Na_v1.6$ conductance in that model decreased the number of spikes generated during 60 pA current clamp stimulation. Decreasing BK conductance by up to 40% had no effect on any NPY neuron model rheobase (**Figure 8.4D**) or number of spikes generated during 60 pA current clamp stimulation (data not shown). We did not vary the conductance of $Na_v1.6$ and BK simultaneously in our NPY neuron models because changing BK conductance alone did not produce an effect on the excitability metrics found to be significantly altered by chronic itch pathogenesis.

8.4.3 Effect of ion channel conductance on gating mechanical itch

We next aimed to understand how calcipotriol-induced changes in ion channel expression led to the opening of the mechanical itch gate. In our models, we investigated which changes in ion channel conductance prevented NPY neurons from inhibiting action potential generation in Ucn3 neurons. We simulated each permutation of the 200 NPY neuron models and 184 Ucn3 neuron models for a total of 36,800 individual networks (**Figure 8.5A**). We then increased or decreased ion channel conductance as described above to determine how molecular changes affected action potential generation in Ucn3 neurons in response to physiologic Aβ-fiber input.

We first simulated how changes in the conductance of single ion channels affected the mechanical itch gate. Interestingly, decreasing $Na_v1.6$ conductance in NPY neuron models was the only calcipotriol-induced change that affected action potential generation in Ucn3 neurons (**Figure 8.5B**). Increasing $Na_v1.6$ conductance by 50% in NPY neuron models resulted in 43.9% of simulated networks (16,148 out of 36,800 total networks) having a Ucn3 neuron model generating an action potential in response to physiologic Aβ-fiber input.

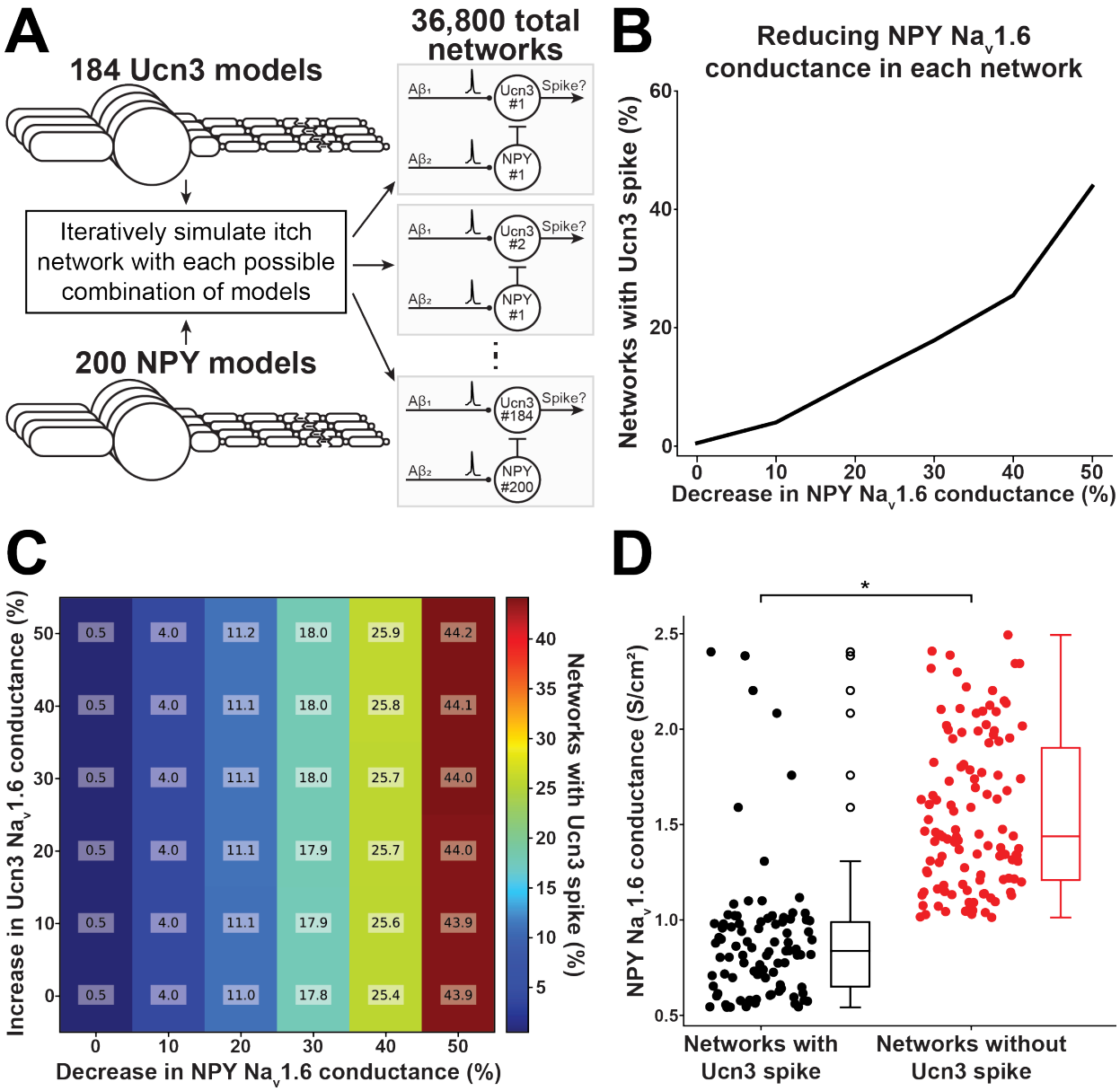

Figure 8.5 Effect of calcipotriol-induced changes in ion channel expression on mechanical itch network excitability. (A) Simulating every permutation of the mechanical itch network with our 184 Ucn3 neuron models and 200 NPY neuron models. In total, we simulated 36,800 distinct networks. (B) Effect of decreasing $Na_v1.6$ conductance in the NPY neuron model on the percentage of networks producing a spike in its Ucn3 neuron model. (C) Effect of simultaneously decreasing $Na_v1.6$ conductance in the NPY neuron model and increasing $Na_v1.6$ conductance in the Ucn3 neuron model on the percentage of networks producing a spike in its Ucn3 neuron model. (D) Comparing the baseline $Na_v1.6$ conductance in NPY neuron models present in networks which produced a spike in the Ucn3 neuron model (black) and networks which did not produce a spike in the Ucn3 neuron model (red). (*$p < 0.001$)

Decreased expression of $Na_v1.6$ in NPY neurons and increased expression of $Na_v1.6$ in Ucn3 neurons produced the greatest magnitude of change in excitability in each cell under chronic itch conditions (**Figure 8.3B**, **Figure 8.4B**). Therefore, we examined how concurrent changes in

$Na_v1.6$ conductance in both Ucn3 and NPY neuron models affected action potential generation in Ucn3 neurons (**Figure 8.5C**). In general, decreasing $Na_v1.6$ conductance in NPY neuron models had the greatest effect on opening the mechanical itch gate. Simultaneously decreasing $Na_v1.6$ conductance in NPY neuron models by 50% and increasing $Na_v1.6$ conductance in Ucn3 neuron models by 50% resulted in 44.2% of simulated networks (16,258 out of 36,800 total networks) producing an action potential in the Ucn3 neuron model (**Figure 8.5C**). Simultaneously varying $Na_v1.6$ conductance in Ucn3 and NPY neuron models produced only a slight increase in the percentage of networks producing a Ucn3 neuron spike compared to decreasing $Na_v1.6$ conductance in NPY neuron models alone (44.2% and 43.9%, respectively).

Lastly, we examined if there were differences between the neurons in mechanical itch networks with an open gate compared to a closed gate. We compared the biophysical properties of Ucn3 and NPY neuron models in itch networks that produced a Ucn3 spike (i.e., gate open) with Ucn3 and NPY neuron models in networks that did not produce a Ucn3 spike (i.e., gate closed). NPY neuron models in networks that produced a Ucn3 neuron spike had significantly lower $Na_v1.6$ conductances than networks that did not produce a Ucn3 neuron spike ($*p < 0.001$. Mann-Whitney U rank test; **Figure 8.5D**). This suggests that NPY neurons with lower levels of baseline $Na_v1.6$ expression may be the chief constituents of disinhibition in response to chronic itch pathogenesis.

8.5 Discussion

8.5.1 $Na_v1.6$ conductance contributes to changes in the excitability of Ucn3 and NPY neurons in chronic itch conditions

Our experimental recordings demonstrated that under chronic itch conditions, Ucn3 neurons become more excitable and NPY neurons become less excitable. We aimed to determine

which changes in ion channel expression were predominantly responsible for these changes in excitability under chronic itch conditions. We simulated calcipotriol-induced changes in mRNA expression in Ucn3 and NPY neurons by increasing or decreasing the conductance of the corresponding ion channel type in our Ucn3 (**Figure 8.3**) and NPY (**Figure 8.4**) neuron models. For both cell types, calcipotriol-induced changes in $Na_v1.6$ conductance produced the greatest effect on rheobase (**Figure 8.3B, Figure 8.4B**) and number of spikes generated during 60 pA current injection (**Figure 8.4C**). In general, decreasing SK conductance (**Figure 8.3C**) and increasing Ca_R conductance (**Figure 8.3D**) produced modest effects on Ucn3 neuron model rheobase. Decreasing BK conductance had no effect on NPY neuron model rheobase (**Figure 8.4D**) or number of spikes generated during 60 pA current injection. These modeling data suggest that changes in $Na_v1.6$ mRNA expression may be predominantly responsible for chronic itch-induced changes in excitability of Ucn3 and NPY neurons.

8.5.2 Decreased $Na_v1.6$ conductance in NPY neurons opens the mechanical itch gate

A key feature of chronic itch pathogenesis in the dorsal horn is the reduction of inhibitory control of NPY neurons onto Ucn3 neurons.[107] We aimed to investigate which calcipotriol-induced changes in ion channel expression contribute to the reduction of inhibition from NPY neuron models onto Ucn3 neuron models. Our results suggest that a reduction in $Na_v1.6$ conductance in NPY neuron models has the greatest effect on Ucn3 neurons generating a spike in response to physiologic Aβ-fiber input. Concurrently varying $Na_v1.6$ conductance in both NPY and Ucn3 neuron models produced only slight changes in the percentage of networks with a Ucn3 neuron spike compared to varying $Na_v1.6$ conductance in NPY models neuron alone. Therefore, decreased expression of $Na_v1.6$ in NPY neurons may be a key contributor to the disinhibition underlying the development of chronic itch. Novel therapeutics aimed towards upregulating the expression of

$Na_v1.6$ or augmenting the activity of existing $Na_v1.6$ may be worth exploring for managing chronic itch conditions. However, continued study of the spinal and supraspinal mechanisms of pathological itch are needed to ensure such therapies would be effective without producing undesired side effects.

8.5.3 Modeling populations of biophysically distinct neurons

Typically, multi-compartment neuron models are parametrized (e.g., maximal ion channel conductances) such that the singular model reproduces the means of experimentally measured properties (e.g., rheobase). However, inherent biological variability between neurons (e.g., varying expression levels of different ion channels) suggests that neurons parametrized to reproduce the means of experimental data may not represent an actual neuron from the sampled population.[85] Furthermore, disparate combinations of maximal ion channel conductances can produce similar model cell behaviors (e.g., similar firing patterns in response to current-clamp stimulation).[85,86] It is unclear if similarly behaving but biophysically distinct cells are differentially affected by the physiological changes observed during pathogenesis. It is also unclear if such pathological changes differentially affect the activity of networks comprised of biophysically distinct cells. Understanding the effects of biological variability on the behavior of single neurons and neural networks during pathogenesis is critical to understanding which physiological parameters contribute to disease phenotypes across neuronal populations.

In this work, we modeled populations of Ucn3 and NPY neuron models. We sought to understand how changes in ion channel expression affected both the excitability of each single-cell model, and the output of the mechanical itch network when constructed with different permutations of cell combinations. In general, many individual neuron models responded similarly to changes in ion channel conductance. For example, all Ucn3 neuron models experienced a

reduction in rheobase in response to increased $Na_v1.6$ conductance (**Figure 8.3B**), though some Ucn3 models experienced a greater reduction in rheobase than other Ucn3 models. However, there were two instances where individual cell models responded differently to a change in conductance than the rest of the population. One Ucn3 model experienced a reduction in rheobase in response to a 10% to 30% increase in Ca_R conductance while all other cells only experienced increases in rheobase (**Figure 8.3D**). Similarly, one NPY neuron model experienced an increase in the number of spikes generated during 60 pA current injection when $Na_v1.6$ conductance was increased by 10% while all other cells experienced only decreases (**Figure 8.4C**). Though these are only two examples out of hundreds of cells, this example highlights that simulating many distinct neurons could reveal subpopulations of cells which respond differently to the same physiological stimulus.

Many, but not all, networks of Ucn3 and NPY neuron models saw an opening of the mechanical itch gate in response to decreased $Na_v1.6$ conductance in NPY neurons (**Figure 8.5B,C**). Interestingly, networks which produced a Ucn3 spike were comprised of NPY neurons with lower baseline values of maximal $Na_v1.6$ conductance than networks which did not produce a Ucn3 spike. This suggests that simulating the network with many different biophysically distinct neurons allowed us to determine which intrinsic properties indicate a neuron is a likely node contributing to disease development. Modeling the effects of disease phenomena on a population of models which reproduce the desired characteristics of an experimental population could provide crucial insights into the mechanisms of disease. Such a framework could also provide a testbed for the design of novel therapeutics.

8.5.4 Limitations

Our model populations are currently simulating the most excitable subset of our experimentally measured Ucn3 and NPY neurons (**Figure 8.2**). This suggests that there may be

significant outward currents present in Ucn3 and NPY neurons in vivo that our models are not currently accounting for, but which may contribute to producing neurons with rheobases greater than approximately 50 pA. Furthermore, our models predicted an average reduction in Ucn3 rheobase of approximately 15%, whereas our experiments suggested the average reduction in Ucn3 rheobase was approximately 28%. Similarly, our models predicted a minimum increase in NPY rheobase of approximately 39%, whereas our experiments found an average increase in NPY rheobase of approximately 24%. Failing to capture the subpopulation of cells that are less excitable in our model populations may lead to inaccurate estimation in the average reduction in rheobase, as less excitable cells may experience a greater change in rheobase in response to up- or down-regulation of sodium channels. However, we believe our model populations still provide critical insight into which ion channels are responsible for the qualitative trends in biophysical changes. Including other outward ion currents in these models may lead to more accurately capturing the quantitative changes in excitability induced by chronic itch.

To simulate experimentally measured changes in ion channel expression, we systematically increased or decreased the conductance of each ion channel present in our cell models. However, measuring changes in mRNA expression is not a direct measurement of functional protein insertion into the cell membrane. Therefore, it is difficult to surmise if a 50% increase in the expression of $Na_v1.6$ mRNA corresponds to a 50% increase in $Na_v1.6$ conductance. Novel methods for measuring the spatiotemporal profiles of ion channel insertion into neural membranes could provide crucial data with which to parametrize multi-compartment neuron models like those used in this study. Such a pairing of experimental measurement and model design could provide insights into the biophysical mechanisms of disease pathogenesis and assist the design of novel targeted therapeutics.

8.6 Conclusions

Understanding the mechanisms of chronic itch pathogenesis is crucial to developing safe and effective therapeutics. Our data suggest that changes in $Na_v1.6$ conductance are predominantly responsible for changes in the excitability of Ucn3 and NPY neurons in the mechanical itch circuit. Furthermore, decreased expression of $Na_v1.6$ in NPY neurons may be a key mechanism of opening the mechanical itch gate. Novel therapeutics aiming to augment the activity of $Na_v1.6$ in NPY neurons may be tractable methods of managing clinical chronic itch conditions. This population-based modeling approach could be leveraged to investigate the utility of non-pharmaceutical therapies (e.g., electrical stimulation) in managing chronic itch.

Chapter 9 – Discussion

9.1 Summary of main findings and implications

This dissertation aimed to provide insight into the mechanisms of action of dorsal root ganglion stimulation (DRGS) in managing chronic pain and how variability across multiple scales of the nervous system may affect the neural response to extracellular stimulation (e.g., spinal cord stimulation (SCS)). These results have advanced our understanding of the neural substrates of stimulation-induced pain relief and could assist the systematic design and testing of novel treatment strategies for managing the symptoms of neurological disorders.

9.1.1 Cytoarchitecture of human lower-lumbar DRG

This project first examined the location of different neural structures – cell bodies and axons – in human lumbar dorsal root ganglia (DRG). This project analyzed serial histology slices with a semi-automated image processing algorithm to develop statistical models of neural element location in human DRG. The results show a higher density of cell bodies in the dorsomedial region of the DRG, while axons are more homogeneously distributed throughout the ganglion. This suggests that the cell bodies and stem axons around the dorsomedial edge of the DRG may receive the strongest electrical currents from clinical DRGS. Furthermore, it suggests that recording electrode arrays placed on the dorsomedial surface of the DRG may be able to acquire signals with high signal-to-noise ratios from the large membrane currents produced by cell bodies. Interestingly, the results also showed a lower density of small-diameter (putatively nociceptive) axons in the dorsal region of the DRG compared to larger-diameter axons. This suggests that when

stimulating the dorsal region of the DRG, stimulation may naturally avoid driving the activity of pain-sensing neurons. This project also demonstrated a method for creating computer models constructed from serial histology slices of the DRG and ventral root. Such models could be used for computer-aided design of novel neurotechnologies for utilizing electrical stimulation, electrical recordings, or both.

9.1.2 Feedforward pain-gating as a potential analgesic mechanism of DRGS

This project examined which subtypes of neurons in the DRG are activated during clinical DRGS. This project coupled a finite element method model of the potential distribution generated by DRGS to multi-compartment models of DRG neurons. The results show that during clinical DRGS (i.e., pulse amplitudes $\leq$ 1 mA, 200-300 μs pulse widths),[77] large-diameter myelinated afferents, such as Aβ-neurons, are activated while small-diameter nonmyelinated afferents are not. Tonic activation of tactile afferents suggests that DRGS may provide pain relief in part by engaging inhibitory circuitry in the dorsal horn of the spinal cord as suggested by the Gate Control Theory of Pain. Furthermore, this project suggested that direct activation of Aδ-neurons may be one source of discomfort produced by DRGS. This project also examined possible modulatory effects of DRGS on C-neurons. The results support the notion that DRGS may be able to augment T-junction filtering in nonmyelinated nociceptors. However, DRGS had to be applied with high stimulation amplitudes outside of amplitudes used clinically to produce this effect. Continued study is needed to determine if there are specific features of DRG neurons that facilitate clinical DRGS engaging this phenomenon.

9.1.3 Variability of neural activation across patients during SCS

This project developed a framework for constructing patient-specific computer models of patients receiving SCS to manage chronic pain. Such models can be used to compare neural activation patterns across SCS patients. By comparing model-predicted neural activation with clinically measured phenomena (e.g., patient reported outcomes), one could gain insight into the differences between the neural response of patients that respond well to SCS (i.e., receive adequate pain relief) versus patients that do not. Furthermore, one could understand patient-specific features (e.g., anatomical features, stimulator programming) that facilitate or abrogate therapeutic neural activation patterns. This project applied this patient-specific modeling framework to two patients and showed that patient-specific differences in anatomy (e.g., the amount of cerebrospinal fluid) captured by the modeling framework may affect the activation thresholds of dorsal column axons. Furthermore, this project showed that in both patients, the minimum stimulation amplitudes required to elicit paresthesias compared well with the minimum activation thresholds of large-diameter (i.e., ≥ 8.7 μm) dorsal column axons. The results of this project suggest that paresthesias may be produced by activating relatively small populations of large-diameter dorsal column axons.

9.1.4 Effect of physiologic variability on the neural response to extracellular stimulation

This project examined how extracellular electrical stimulation, such as DRGS, may differentially affect neurons of the same sub-type depending on variability in their expression of ion channels. This project implemented a population of 100 biophysical models of C-neurons and found that the baseline expression of ion channels in a given cell can significantly affect its activation threshold in response to DRGS. Interestingly, there appeared to be a trend between a C-neuron's maximal M-current potassium conductance and its activation threshold in response to DRGS. This project demonstrated that modeling populations of cells, rather than a single cell that reproduces the mean of experimental data, may provide more realistic insight into the neural

response to electrical stimulation. Furthermore, this framework may be useful in determining the biophysical underpinnings (e.g., variable M-currents) of experimental observations (e.g., populations of C-neurons with different activation thresholds). Such knowledge is crucial to understanding how a therapy modulates the activity of populations of neurons, rather than just the "average" neuron.

9.1.5 Molecular mechanisms of chronic itch pathogenesis

This project examined which chronic itch-induced changes in ion channel expression were likely responsible for the changes in excitability of the mechanical itch network. This project implemented populations of biophysical models of both excitatory and inhibitory neuron subtypes involved in chronic itch pathogenesis. Generally, the data suggest that changes in the expression of the voltage-gated sodium channel $Na_v1.6$ is a key contributor to changes in single-cell and network excitability measures observed experimentally. Changes in $Na_v1.6$ expression in the inhibitory interneurons which make up the mechanical itch circuit seem particularly crucial to opening the mechanical itch gate. This project also demonstrated the utility of parametrizing populations of biophysical neuron models to study disease pathogenesis. The data suggest that inhibitory interneurons with lower baseline expression levels of $Na_v1.6$ may be more susceptible to producing circuit behaviors indicative of chronic itch conditions.

9.2 Future directions

9.2.1 Three-dimensional characterization of human DRG functional cellular anatomy

This study demonstrated that cell bodies typically congregate around the dorsomedial edge of human lumbar DRG, while axons are more homogeneously distributed throughout the structure.

Unfortunately, the data presented in this project did not provide insight into possible somatotopy or functional organization in human DRG. DRG neurons are comprised of neurochemically distinct subpopulations which correlate with its functional role (e.g., cold sensing). If, as suggested by this dissertation, direct activation of Aβ-mechanoreceptors is the principal mechanism of DRGS, understanding typical spatial distributions of Aβ-mechanoreceptors could inform the optimal placement of DRGS electrode arrays. Elucidating the functional anatomy of the nervous system is critical to any neural therapy which relies on delivering a therapeutic dose (electrical, chemical, mechanical, etc.) to a particular structure in 3D space.

9.2.2 Patient-specific models as a clinical decision-making support system

This project developed a framework for creating patient-specific models of SCS. The motivation for this work was developing patient-specific models to investigate the therapeutic mechanisms of SCS. However, the patient-specific modeling approach could form the basis of a clinical decision-making support system. Such a system could be used to calculate optimal stimulation parameters (e.g., pulse amplitude, pulse width, electrode configuration) which maximize pain relief. However, this approach is not currently feasible due to the considerable time necessary to create a patient-specific field-cable model. Modern machine learning algorithms focused on medical image segmentation and co-registration could automate and significantly speed up the model-construction process, making such a system clinically feasible.

Patient-specific models could also aid in the design and characterization of novel neurostimulation technologies. For example, one could test a novel electrode geometry in patient-specific models representing different patient demographics, spinal column anatomies, and possible contraindications to SCS. Furthermore, one could simulate the neural response to a novel stimulus waveform aiming to engage a particular neural phenomenon, and compare how that

response may differ across patient anatomies. Pairing patient-specific modeling predictions with other forms of clinical neuroscience data could allow for cross-scale comparison of stimulation-induced phenomena.

9.2.3 A systems neuroscience approach to studying and designing neurostimulation therapies

This work provided insight into which DRG neurons are predominantly activated during DRGS. However, the neurons modulated directly by the electric fields generated by therapeutic neurostimulation are only the first step in a presumed series of changes which lead to symptom management. Neurons project to and affect the activity of many downstream neurons and neural networks. This suggests that therapeutically altering neural activity produces changes in not only the activity of the neurons which are being stimulated, but also the neurons and networks to which they provide synaptic input. Because DRG contain neurons which receive input from only one source (i.e., the periphery), DRGS may be a particularly useful test case for studying how downstream networks process therapeutic stimuli. The ability to remove peripheral input and record the activity of spinal networks receiving input from DRGS may provide key insights into how artificially generated neural signals are integrated by downstream networks. Such insight is crucial to understanding how all therapeutics, not just electrical stimulation, provide clinical benefit.

Since the turn of the century, the advent of experimental techniques, such as optogenetics, has provided neuroscientists with unprecedented spatiotemporal control of neural dynamics. Furthermore, novel techniques for monitoring the activity of large populations of neurons in awake behaving preclinical models (e.g., *in vivo* calcium imaging, high-density electrophysiology) allow for the correlation of the activity of large neural networks with animal behavior. Implementing these techniques to study how neurostimulation therapies affect the activity of the neural circuits

governing neurological disorders could provide insight into the postsynaptic mechanisms of neurostimulation therapies. Furthermore, such techniques could serve as an experimental testbed for the systematic design of novel therapies that target specific circuit mechanisms of disease.

9.3 Final conclusion

This dissertation contributed to our understanding of the mechanisms of action of DRGS and sources of variability that could affect the neural response to therapeutic neurostimulation. Continued interdisciplinary study is needed to fully elucidate the effects of neurostimulation on the entire neuraxis. A clear understanding of the mechanisms of action of a therapeutic effect is critical to developing novel therapies which act principally upon those mechanisms. Such advancements are critical to lessening the impact of neurological disorders on the human condition.

Bibliography

1. Testerman RL, Rise MT, Stypulkowski PH. Electrical stimulation as therapy for neurological disorders: The basics of implantable neurological stimulators. *IEEE Eng Med Biol Mag*. 2006;25(5):74-78. doi:10.1109/MEMB.2006.1705750
2. Johnstone DM, Hamilton C, Gordon LC, et al. Exploring the Use of Intracranial and Extracranial (Remote) Photobiomodulation Devices in Parkinson's Disease: A Comparison of Direct and Indirect Systemic Stimulations. *J Alzheimer's Dis*. 2021;83(4):1399-1413. doi:10.3233/JAD-210052
3. Guo H, Offutt SJ, Hamilton M, et al. Ultrasound does not activate but can inhibit in vivo mammalian nerves across a wide range of parameters. *Sci Rep*. 2022;12(1):1-14. doi:10.1038/s41598-022-05226-7
4. Russo CM, Brose WG. Chronic pain. *Annu Rev Med*. 1998;49:123-133.
5. Raja SN, Carr DB, Cohen M, et al. The revised International Association for the Study of Pain definition of pain: concepts, challenges, and compromises. *Pain*. 2020;161(9):1976-1982. doi:10.1097/j.pain.0000000000001939
6. Melzack R. From the gate to the neuromatrix. *Pain Suppl 6*. Published online 1999:S121-S126. doi:10.1016/S0304-3959(99)00145-1
7. Melzack R. The McGill Pain Questionnaire. *Anesthesiology*. 2005;103:199-202. doi:10.1097/00000542-200507000-00028
8. Holmes A, Christelis N, Arnold C. Depression and chronic pain. *Med J Aust*. 2013;199(6):S17-S20. doi:10.5694/mja12.10589
9. Asmundson GJG, Katz J. Understanding the co-occurrence of anxiety disorders and chronic pain: State-of-the-art. *Depress Anxiety*. 2009;26(10):888-901. doi:10.1002/da.20600
10. Kuehn BM. Chronic pain prevalence. *JAMA*. 2018;319:1632. doi:10.1001/jama.2018.7441
11. Nahin RL. Estimates of pain prevalence and severity in adults: United States, 2012. *J Pain*. 2015;16(8):769-780. doi:10.1016/j.jpain.2015.05.002
12. Paulozzi LJ, Jones CM, Mack KA, Rudd RA. Vital signs: Overdoses of prescription opioid pain relievers - United States, 1999-2008. *MMWR Morb Mortal Wkly Rep*. 2011;60(43):1487-1492.
13. Rudd RA, Aleshire N, Zibbell JE, Gladden RM. Increases in drug and opioid overdose deaths - United States, 2000-2014. *MMWR Morb Mortal Wkly Rep*. 2016;64:1378-1382.
14. Scholl L, Seth P, Kariisa M, Wilson N, Baldwin G. Drug and opioid-involved overdose deaths - United States, 2013-2017. *MMWR Morb Mortal Wkly Rep*. 2019;67:1419-1427. doi:10.15585/mmwr.mm675152e1
15. Gaskin DJ, Richard P. The economic costs of pain in the United States. *J Pain*. 2012;13(8):715-724. doi:10.1016/j.jpain.2012.03.009
16. Finnerup NB, Otto M, McQuay HJ, Jensen TS, Sindrup SH. Algorithm for neuropathic pain treatment: An evidence based proposal. *Pain*. 2005;118(3):289-305. doi:10.1016/j.pain.2005.08.013
17. Hayek SM, Shah A. Nerve blocks for chronic pain. *Neurosurg Clin N Am*.

2014;25(4):809-817. doi:10.1016/j.nec.2014.07.006
18. Soloman M, Mekhail MN, Mekhail N. Radiofrequency treatment in chronic pain. *Expert Rev Neurother*. 2010;10(3):469-474. doi:10.1586/ern.09.153
19. Willems PC, Staal JB, Walenkamp GHIM, De Bie RA. Spinal fusion for chronic low back pain: Systematic review on the accuracy of tests for patient selection. *Spine J*. 2013;13(2):99-109. doi:10.1016/j.spinee.2012.10.001
20. Melzack R, Wall PD. Pain mechanisms: A new theory. *Science*. 1965;150(3699):971-979. doi:10.1016/S1082-3174(96)80062-6
21. Mendell LM. Constructing and deconstructing the gate theory of pain. *Pain*. 2014;155(2):210-216. doi:10.1016/j.pain.2013.12.010
22. Wall PD, Sweet WH. Temporary abolition of pain in man. *Science*. 1967;155(3758):108-109.
23. Shealy CN, Mortimer JT, Reswick JB. Electrical inhibition of pain by stimulation of the dorsal columns: Preliminary clinical report. *Anesth Analg*. 1967;46(4):489-491. doi:10.3109/15360288.2012.678473
24. Sdrulla AD, Guan Y, Raja SN. Spinal cord stimulation: Clinical efficacy and potential mechanisms. *Pain Pract*. Published online 2018. doi:10.1111/papr.12692
25. Lempka SF, Patil PG. Innovations in spinal cord stimulation for pain. *Curr Opin Biomed Eng*. 2018;8:51-60. doi:10.1016/j.cobme.2018.10.005
26. Kemler MA, Barendse GAM, van Kleef M, et al. Spinal cord stimulation in patients with chronic reflex sympathetic dystrophy. *N Engl J Med*. 2000;343:618-624.
27. Kumar K, Taylor RS, Jacques L, et al. The effects of spinal cord stimulation in neuropathic pain are sustained: A 24-month follow-up of the prospective randomized controlled multicenter trial of the effectiveness of spinal cord stimulation. *Neurosurgery*. 2008;63(4):762-768. doi:10.1227/01.NEU.0000325731.46702.D9
28. Sears NC, Machado AG, Nagel SJ, et al. Long-term outcomes of spinal cord stimulation with paddle leads in the treatment of complex regional pain syndrome and failed back surgery syndrome. *Neuromodulation*. 2011;14:312-318. doi:10.1111/j.1525-1403.2011.00372.x
29. Titus ND, Gilbert JE, Grill WM. Biophysics and Mechanisms of Spinal Cord Stimulation for Chronic Pain. In: *Handbook of Neuroengineering*. ; 2021:1-45. doi:10.1007/978-981-15-2848-4_99-2
30. Mekhail N, Levy RM, Deer TR, et al. Long-term safety and efficacy of closed-loop spinal cord stimulation to treat chronic back and leg pain (Evoke): A double-blind, randomised, controlled trial. *Lancet Neurol*. 2019;4422(19):1-12. doi:10.1016/S1474-4422(19)30414-4
31. Anaya CJ, Zander HJ, Graham RD, Sankarasubramanian V, Lempka SF. Evoked potentials recorded from the spinal cord during neurostimulation for pain: A computational modeling study. *Neuromodulation*. 2020;23(1):64-73. doi:10.1111/ner.12965
32. Rogers ER, Zander HJ, Lempka SF. Neural Recruitment During Conventional, Burst, and 10-kHz Spinal Cord Stimulation for Pain. *J Pain*. 2021;00(00). doi:10.1016/j.jpain.2021.09.005
33. Lempka SF, McIntyre CC, Kilgore KL, Machado AG. Computational analysis of kilohertz frequency spinal cord stimulation for chronic pain management. *Anesthesiology*. 2015;122(6):1362-1376. doi:10.1097/ALN.0000000000000649
34. Lee KY, Bae C, Lee D, et al. Low-intensity, Kilohertz Frequency Spinal Cord Stimulation

Differently Affects Excitatory and Inhibitory Neurons in the Rodent Superficial Dorsal Horn. *Neuroscience*. 2020;428:132-139. doi:10.1016/j.neuroscience.2019.12.031
35. Vallejo R, Kelley CA, Gupta A, Smith WJ, Vallejo A, Cedeño DL. Modulation of neuroglial interactions using differential target multiplexed spinal cord stimulation in an animal model of neuropathic pain. *Mol Pain*. 2020;16. doi:10.1177/1744806920918057
36. Zannou AL, Khadka N, Truong DQ, et al. Temperature increases by kilohertz frequency spinal cord stimulation. *Brain Stimul*. 2019;12(1):62-72. doi:10.1016/j.brs.2018.10.007
37. Khadka N, Bikson M. Neurocapillary-Modulation. *Neuromodulation*. 2020;2020. doi:10.1111/ner.13338
38. Kumar K, Rizvi S, Bnurs SB. Spinal cord stimulation is effective in management of complex regional pain syndrome I: Fact or fiction. *Neurosurgery*. 2011;69(3):566-578. doi:10.1227/NEU.0b013e3182181e60
39. Deer TR, Pope JE. Dorsal root ganglion stimulation approval by the Food and Drug Administration: Advice on evolving the process. *Expert Rev Neurother*. 2016;16(10):1123-1125. doi:10.1080/14737175.2016.1206817
40. Eldabe S, Espinet A, Wahlstedt A, et al. Retrospective case series on the treatment of painful diabetic peripheral neuropathy with dorsal root ganglion stimulation. *Neuromodulation*. 2018;21:787-792. doi:10.1111/ner.12767
41. Eldabe S, Burger K, Moser H, et al. Dorsal root ganglion (DRG) stimulation in the treatment of phantom limb pain (PLP). *Neuromodulation*. 2015;18:610-617. doi:10.1111/ner.12338
42. Morgalla MH, Bolat A, Fortunato M, Lepski G, Chander BS. Dorsal root ganglion stimulation used for the treatment of chronic neuropathic pain in the groin: A single-center study with long-term prospective results in 34 cases. *Neuromodulation*. 2017;20:753-760. doi:10.1111/ner.12713
43. Deer TR, Levy RM, Kramer J, et al. Dorsal root ganglion stimulation yielded higher treatment success rate for CRPS and causalgia at 3 and 12 months. *Pain*. 2017;158(4):669-681. doi:10.1097/j.pain.0000000000000814
44. Morgalla MH, Fortunato M, Lepski G, Chander BS. Dorsal root ganglion stimulation (DRGS) for the treatment of chronic neuropathic pain: A single-center study with long-term prospective results in 62 Cases. *Pain Physician*. 2018;21(4):E377-E388.
45. Sperry ZJ, Graham RD, Peck-Dimit N, Lempka SF, Bruns TM. Spatial models of cell distribution in human lumbar dorsal root ganglia. *J Comp Neurol*. 2020;528(10):1644-1659. doi:10.1002/cne.24848
46. Graham RD, Sankarasubramanian V, Lempka SF. Dorsal root ganglion stimulation for chronic pain: Hypothesized mechanisms of action. *J Pain*. 2021;23(2):196-211. doi:10.1016/j.jpain.2021.07.008
47. Koopmeiners AS, Mueller S, Kramer J, Hogan QH. Effect of electrical field stimulation on dorsal root ganglion neuronal function. *Neuromodulation*. 2013;16(4):304-311. doi:10.1111/ner.12028
48. Gemes G, Koopmeiners A, Rigaud M, et al. Failure of action potential propagation in sensory neurons: Mechanisms and loss of afferent filtering in C-type units after painful nerve injury. *J Physiol*. 2013;591(4):1111-1131. doi:10.1113/jphysiol.2012.242750
49. Pan B, Yu H, Fischer GJ, Kramer JM, Hogan QH. Dorsal root ganglionic field stimulation relieves spontaneous and induced neuropathic pain in rats. *J Pain*. 2016;17(12):1349-1358. doi:10.1016/j.jpain.2016.09.004

50. Rattay F. The basic mechanism for the electrical stimulation of the nervous system. *Neuroscience*. 1999;89(2):335-346. doi:10.1016/S0306-4522(98)00330-3
51. McIntyre CC, Grill WM. Excitation of central nervous system neurons by nonuniform electric fields. *Biophys J*. 1999;76(2):878-888. doi:10.1016/S0006-3495(99)77251-6
52. McIntyre CC, Grill WM, Sherman DL, Thakor N V. Cellular effects of deep brain stimulation: Model-based analysis of activation and inhibition. *J Neurophysiol*. 2004;91(4):1457-1469. doi:10.1152/jn.00989.2003
53. Datta A, Elwassif M, Battaglia F, Bikson M. Transcranial current stimulation focality using disc and ring electrode configurations: FEM analysis. *J Neural Eng*. 2008;5(2):163-174. doi:10.1088/1741-2560/5/2/007
54. Raspopovic S, Capogrosso M, Micera S. A computational model for the stimulation of rat sciatic nerve using a transverse intrafascicular multichannel electrode. *IEEE Trans Neural Syst Rehabil Eng*. 2011;19(4):333-344. doi:10.1109/TNSRE.2011.2151878
55. Verma N, Graham RD, Mudge J, et al. Augmented Transcutaneous Stimulation Using an Injectable Electrode: A Computational Study. *Front Bioeng Biotechnol*. 2021;9:1-19. doi:10.3389/fbioe.2021.796042
56. Hodgkin AL, Huxley AF. A quantitative description of membrane current and its application to conduction and excitation in nerve. *J Physiol*. 1952;117:500-544. doi:10.1109/ICCCT2.2017.7972284
57. McNeal DR. Analysis of a model for excitation of myelinated nerve. *IEEE Trans Biomed Eng*. 1976;BME-23(4):329-337. doi:10.1109/TBME.1976.324593
58. Rattay F. Analysis of models for external stimulation of axons. *IEEE Trans Biomed Eng*. 1986;BME-33(10):974-977. doi:10.1109/TBME.1986.325670
59. Benabid AL, Benazzouz A, Gao D, et al. Chronic electrical stimulation of the ventralis intermedius nucleus of the thalamus and of other nuclei as a treatment for Parkinson's disease. *J Neurosurg*. 1996;94:203-214. doi:10.1097/00127927-199905010-00003
60. McIntyre CC, Grill WM. Selective microstimulation of central nervous system neurons. *Ann Biomed Eng*. 2000;28(3):219-233. doi:10.1114/1.262
61. McIntyre CC, Grill WM. Extracellular stimulation of central neurons: Influence of stimulus waveform and frequency on neuronal output. *J Neurophysiol*. 2002;88(4):1592-1604. doi:DOI 10.1152/jn.00147.2002
62. Coburn B. Electrical stimulation of the spinal cord: two-dimensional finite element analysis with particular reference to epidural electrodes. *Med Biol Eng Comput*. 1980;18(5):573-584. doi:10.1007/BF02443129
63. Sin WK, Coburn B. Electrical stimulation of the spinal cord : a further analysis relating to anatomical factors and tissue properties Medical & Biological Engineering & Computing May 1983. *Med Biol Eng Comput*. 1983;21:264-269.
64. Coburn B, Sin WK. A theoretical study of epidural electrical stimulation of the spinal cord part I: Finite element analysis of stimulus fields. *Biomed Eng IEEE Trans*. 1985;BME-32(11):971-977. doi:10.1109/tbme.1985.325648
65. Coburn B. A Theoretical Study of Epidural Electrical Stimulation of the Spinal Cord—Part II: Effects on Long Myelinated Fibers. *IEEE Trans Biomed Eng*. 1985;BME-32(11):978-986. doi:10.1109/TBME.1985.325649
66. Struijk JJ, Holsheimer J, van der Heide GG, Boom HBK. Recruitment of dorsal column fibers in spinal cord stimulation: Influence of collateral branching. *IEEE Trans Biomed Eng*. 1992;39(9):903-912.

67. Holsheimer J. Which neuronal elements are activated directly by spinal cord stimulation. *Neuromodulation*. 2002;5(1):25-31. doi:10.1046/j.1525-1403.2002._2005.x
68. Holsheimer J, Struijk JJ. How do geometric factors influence epidural spinal cord stimulation? *Stereotact Funct Neurosurgery1*. 1991;56:234-249.
69. Holsheimer J, Wesselink WA. Optimum electrode geometry for spinal cord stimulation: The narrow bipole and tripole. *Med Biol Eng Comput*. 1997;35:493-497. doi:10.1007/BF02525529
70. Struijk JJ, Holsheimer J. Transverse tripolar spinal cord stimulation: Theoretical performance of a dual channel system. *Med Biol Eng Comput*. 1996;34(4):273-279. doi:10.1007/BF02511237
71. Sankarasubramanian V, Buitenweg JR, Holsheimer J, Veltink P. Triple leads programmed to perform as longitudinal guarded cathodes in spinal cord stimulation: A modeling study. *Neuromodulation*. 2011;14(5):401-411. doi:10.1111/j.1525-1403.2011.00383.x
72. Capogrosso M, Wenger N, Raspopovic S, et al. A computational model for epidural electrical stimulation of spinal sensorimotor circuits. *J Neurosci*. 2013;33(49):19326-19340. doi:10.1523/JNEUROSCI.1688-13.2013
73. Lempka SF, Zander HJ, Anaya CJ, Wyant A, Ozinga JG, Machado AG. Patient-specific analysis of neural activation during spinal cord stimulation for pain. *Neuromodulation*. 2020;23(5):572-581. doi:10.1111/ner.13037
74. Rowald A, Komi S, Demesmaeker R, et al. Activity-dependent spinal cord neuromodulation rapidly restores trunk and leg motor functions after complete paralysis. *Nat Med*. 2022;28(February):21-23. doi:10.1038/s41591-021-01663-5
75. Bourbeau DJ, Hokanson JA, Rubin JE, Weber DJ. A computational model for estimating recruitment of primary afferent fibers by intraneural stimulation in the dorsal root ganglia. *J Neural Eng*. 2011;8(5):056009. doi:10.1088/1741-2560/8/5/056009
76. Kent AR, Min X, Hogan QH, Kramer JM. Mechanisms of dorsal root ganglion stimulation in pain suppression: A computational modeling analysis. *Neuromodulation*. 2018;21:234-246. doi:10.1111/ner.12754
77. Deer TR, Pope JE, Lamer TJ, et al. The neuromodulation appropriateness consensus committee on best practices for dorsal root ganglion stimulation. *Neuromodulation*. 2019;22(1):1-35. doi:10.1111/ner.12845
78. Zhang TC, Janik JJ, Grill WM. Mechanisms and models of spinal cord stimulation for the treatment of neuropathic pain. *Brain Res*. 2014;1569:19-31. doi:10.1016/j.brainres.2014.04.039
79. Song Z, Ansah OB, Meyerson BA, Pertovaara A, Linderoth B. Exploration of supraspinal mechanisms in effects of spinal cord stimulation: Role of the locus coeruleus. *Neuroscience*. 2013;253:426-434. doi:10.1016/j.neuroscience.2013.09.006
80. Cui J-G, O'Connor WT, Ungerstedt U, Linderoth B, Meyerson BA. Spinal cord stimulation attenuates dorsal horn release of excitatory amino acids in mononeuropathy via a GABAergic mechanism. *Pain*. 1997;73:87-95.
81. Howell B, Lad SP, Grill WM, Glorioso JC. Evaluation of intradural stimulation efficiency and selectivity in a computational model of spinal cord stimulation. *PLoS One*. 2014;9(12):1-25. doi:10.1371/journal.pone.0114938
82. Pan B, Zhang Z, Chao D, Hogan QH. Dorsal root ganglion field stimulation prevents inflammation and joint damage in a rat model of rheumatoid arthritis. *Neuromodulation*. 2018;21:247-253. doi:10.1111/ner.12648

83. Ostrowski AK, Sperry ZJ, Kulik G, Bruns TM. Quantitative models of feline lumbosacral dorsal root ganglia neuronal cell density. *J Neurosci Methods*. 2017;290:116-124. doi:10.1016/j.jneumeth.2017.07.018
84. Holsheimer J, Den Boer JA, Struijk JJ, Rozeboom AR. MR assessment of the normal position of the spinal cord in the spinal canal. *Am J Neuroradiol*. 1994;15(5):951-959.
85. Marder E, Taylor AL. Multiple models to capture the variability in biological neurons and networks. *Nat Neurosci*. 2011;14(2):133-138. doi:10.1038/nn.2735
86. Marder E, Goaillard JM. Variability, compensation and homeostasis in neuron and network function. *Nat Rev Neurosci*. 2006;7(7):563-574. doi:10.1038/nrn1949
87. Prinz AA, Bucher D, Marder E. Similar network activity from disparate circuit parameters. *Nat Neurosci*. 2004;7(12):1345-1352. doi:10.1038/nn1352
88. Kumar K, Caraway DL, Rizvi S, Bishop S. Current challenges in spinal cord stimulation. *Neuromodulation*. 2014;17(SUPPL. 1):22-35. doi:10.1111/ner.12172
89. Deer TR, Grigsby E, Weiner RL, Wilcosky B, Kramer JM. A prospective study of dorsal root ganglion stimulation for the relief of chronic pain. *Neuromodulation*. 2013;16(1):67-72. doi:10.1111/ner.12013
90. Deer TR, Levy RM, Kramer J, et al. Dorsal root ganglion stimulation yielded higher treatment success rate for complex regional pain syndrome and causalgia at 3 and 12 months: A randomized comparative trial. *Pain*. 2017;158(4):669-681. doi:10.1097/j.pain.0000000000000814
91. Jensen MP, Chodroff MJ, Dworkin RH. The impact of neuropathic pain on health-related quality of life: review and implications. *Neurology*. 2007;68(15):1178-1182. doi:10.1212/01.wnl.0000259085.61898.9e
92. Mekhail NA, Cheng J, Narouze S, Kapural L, Mekhail MN, Deer T. Clinical applications of neurostimulation: Forty years later. *Pain Pract*. 2010;10(2):103-112. doi:10.1111/j.1533-2500.2009.00341.x
93. Haberberger RV, Barry C, Dominguez N, Matusica D. Human dorsal root ganglia. *Front Cell Neurosci*. 2019;13:1-17. doi:10.3389/fncel.2019.00271
94. Brierley JB. The penetration of particulate matter from the cerebrospinal fluid into the spinal ganglia, peripheral nerves, and the perivascular spaces of the central nervous system. *J Neurol Neurosurg Psychiatry*. 1950;13(3):203-215.
95. Hasegawa T, Mikawa Y, Watanabe R, An HS. Morphometric analysis of the lumbrosacral nerve roots and dorsal root ganglia by magnetic resonance imaging. *Spine*. 1996;21(9):1005-1009.
96. Amirdelfan K, Kramer J, Cusack WF, Burton AW. *Advanced Neuromodulation Techniques: Dorsal Root Ganglion Stimulation*.; 2018.
97. Devor M. Unexplained peculiarities of the dorsal root ganglion. *Pain Suppl 6*. Published online 1999:S27-S35.
98. Lawson SN, Fang X, Djouhri L. Nociceptor subtypes and their incidence in rat lumbar dorsal root ganglia (DRGs): focussing on C-polymodal nociceptors, Aβ-nociceptors, moderate pressure receptors and their receptive field depths. *Curr Opin Physiol*. 2019;11:125-146. doi:10.1016/j.cophys.2019.10.005
99. Hu L, Cai MM, Xiao P, Luo F, Iannetti GD. Human brain responses to concomitant stimulation of Aδ and C nociceptors. *J Neurosci*. 2014;34(34):11439-11451. doi:10.1523/JNEUROSCI.1355-14.2014
100. Wang F, Bélanger E, Côté SL, et al. Sensory afferents use different coding strategies for

heat and cold. *Cell Rep*. 2018;23(7):2001-2013. doi:10.1016/j.celrep.2018.04.065
101. Sharif B, Ase AR, Ribeiro-da-Silva A, Séguéla P. Differential coding of itch and pain by a subpopulation of primary afferent neurons. *Neuron*. 2020;106(6):940-951.e4. doi:10.1016/j.neuron.2020.03.021
102. Löken LS, Wessberg J, Morrison I, McGlone F, Olausson H. Coding of pleasant touch by unmyelinated afferents in humans. *Nat Neurosci*. 2009;12(5):547-548. doi:10.1038/nn.2312
103. Boyd IA, Kalu KU. Scaling factor relating conduction velocity and diameter for myelinated afferent nerve fibres in the cat hind limb. *J Physiol*. 1979;289:277-297.
104. Abraira VE, Ginty DD. The sensory neurons of touch. *Neuron*. 2013;79(4):618-639. doi:10.1016/j.neuron.2013.07.051
105. Arcourt A, Gorham L, Dhandapani R, et al. Touch receptor-derived sensory information alleviates acute pain signaling and fine-tunes nociceptive reflex coordination. *Neuron*. 2017;93(1):179-193. doi:10.1016/j.neuron.2016.11.027
106. Djouhri L, Lawson SN. Aβ-fiber nociceptive primary afferent neurons: A review of incidence and properties in relation to other afferent A-fiber neurons in mammals. *Brain Res Rev*. 2004;46(2):131-145. doi:10.1016/j.brainresrev.2004.07.015
107. Pan H, Fatima M, Li A, et al. Identification of a spinal circuit for mechanical and persistent spontaneous itch. *Neuron*. 2019;103(6):1135-1149.e6. doi:10.1016/j.neuron.2019.06.016
108. Djouhri L. Aδ-fiber low threshold mechanoreceptors innervating mammalian hairy skin: A review of their receptive, electrophysiological and cytochemical properties in relation to Aδ-fiber high threshold mechanoreceptors. *Neurosci Biobehav Rev*. 2016;61:225-238. doi:10.1016/j.neubiorev.2015.12.009
109. Braz J, Solorzano C, Wang X, Basbaum A. Transmitting pain and itch messages: A contemporary view of the spinal cord circuits that generate gate control. *Neuron*. 2014;82(3):522-536. doi:10.1016/j.neuron.2014.01.018
110. Todd AJ. Neuronal circuitry for pain processing in the dorsal horn. *Nat Rev Neurosci*. 2010;11:823-836. doi:10.1038/nrn2947
111. Vuka I, Vučić K, Repić T, Ferhatović Hamzić L, Sapunar D, Puljak L. Electrical stimulation of dorsal root ganglion in the context of pain: A systematic review of in vitro and in vivo animal model studies. *Neuromodulation*. 2018;21(3):213-224. doi:10.1111/ner.12722
112. Esposito MF, Malayil R, Hanes M, Deer T. Unique characteristics of the dorsal root ganglion as a target for neuromodulation. *Pain Med*. 2019;20:S23-S30. doi:10.1093/pm/pnz012
113. Krames ES. The dorsal root ganglion in chronic pain and as a target for neuromodulation: A review. *Neuromodulation*. 2015;18(1):24-32. doi:10.1111/ner.12247
114. Harrison C, Epton S, Bojanic S, Green AL, FitzGerald JJ. The efficacy and safety of dorsal root ganglion stimulation as a treatment for neuropathic pain: A literature review. *Neuromodulation*. 2018;21(3):225-233. doi:10.1111/ner.12685
115. Niu J, Ding L, Li JJ, et al. Modality-based organization of ascending somatosensory axons in the direct dorsal column pathway. *J Neurosci*. 2013;33(45):17691-17709. doi:10.1523/JNEUROSCI.3429-13.2013
116. Rattay F. The basic mechanism for the electrical stimulation of the nervous system. *Neuroscience*. 1999;89(2):335-346. doi:10.1016/S0306-4522(98)00330-3

117. Capogrosso M, Lempka SF. A computational outlook on neurostimulation. *Bioelectron Med*. 2020;6(10):1-7. doi:10.1186/s42234-020-00047-3
118. Graham RD, Bruns TM, Duan B, Lempka SF. Dorsal root ganglion stimulation for chronic pain modulates Aβ-fiber activity but not C-fiber activity: A computational modeling study. *Clin Neurophysiol*. 2019;130(6):941-951. doi:10.1016/j.clinph.2019.02.016
119. Graham RD, Bruns TM, Duan B, Lempka SF. The effect of clinically controllable factors on neural activation during dorsal root ganglion stimulation. *Neuromodulation*. 2021;24(4):655-671. doi:10.1111/ner.13211
120. Gemes G, Rigaud M, Koopmeiners AS, Poroli MJ, Zoga V, Hogan QH. Calcium signaling in intact dorsal root ganglia: New observations and the effect of injury. *Anesthesiology*. 2010;113(1):134-146. doi:10.1097/ALN.0b013e3181e0ef3f
121. Chao D, Zhang Z, Mecca CM, Hogan QH, Pan B. Analgesic dorsal root ganglionic field stimulation blocks conduction of afferent impulse trains selectively in nociceptive sensory afferents. *Pain*. 2020;161(12):2872-2886. doi:10.1097/j.pain.0000000000001982
122. Koetsier E, Franken G, Debets J, et al. Mechanism of dorsal root ganglion stimulation for pain relief in painful diabetic polyneuropathy is not dependent on GABA release in the dorsal horn of the spinal cord. *CNS Neurosci Ther*. 2020;26(1):136-143. doi:10.1111/cns.13192
123. Du X, Hao H, Yang Y, et al. Local GABAergic signaling within sensory ganglia controls peripheral nociceptive transmission. *J Clin Invest*. 2017;127(5):1741-1756. doi:10.1172/JCI86812
124. Lu Y, Dong H, Gao Y, et al. A feed-forward spinal cord glycinergic neural circuit gates mechanical allodynia. *J Clin Invest*. 2013;123(9):4050-4062.
125. Bruns TM, Weber DJ, Gaunt RA. Microstimulation of afferents in the sacral dorsal root ganglia can evoke reflex bladder activity. *Neurourol Urodyn*. 2015;34:65-71. doi:10.1002/nau
126. Ayers CA, Fisher LE, Gaunt RA, Weber DJ. Microstimulation of the lumbar DRG recruits primary afferent neurons in localized regions of lower limb. *J Neurophysiol*. 2016;116(1):51-60. doi:10.1152/jn.00961.2015
127. Fisher LE, Ayers CA, Ciollaro M, Ventura V, Weber DJ, Gaunt RA. Chronic recruitment of primary afferent neurons by microstimulation in the feline dorsal root ganglia. *J Neural Eng*. 2014;11(3):036007. doi:10.1088/1741-2560/11/3/036007
128. Gaunt RA, Hokanson JA, Weber DJ. Microstimulation of primary afferent neurons in the L7 dorsal root ganglia using multielectrode arrays in anesthetized cats: Thresholds and recruitment properties. *J Neural Eng*. 2009;6(5):055009. doi:10.1088/1741-2560/6/5/055009
129. King KW, Cusack WF, Nanivadekar AC, et al. DRG microstimulation evokes postural responses in awake, standing felines. *J Neural Eng*. 2020;17(1):016014. doi:10.1088/1741-2552/ab50f4
130. Nanivadekar A, Ayers CA, Gaunt RA, Weber D, Fisher LE. Selectivity of afferent microstimulation at the DRG using epineural and penetrating electrode arrays. *J Neural Eng*. 2020;17:016011. doi:10.1088/1741-2552/ab4a24
131. Spencer PS, Raine CS, WiśNiewski H. Axon diameter and myelin thickness - unusual relationships in dorsal root ganglia. *Anat Rec*. 1973;176(2):225-243. doi:10.1002/ar.1091760209

132. Ha H. Axonal bifurcation in the dorsal root ganglion of the cat: A light and electron microscopic study. *J Comp Neurol*. 1970;140:227-240. doi:10.1002/cne.901400206
133. Amir R, Devor M. Electrical excitability of the soma of sensory neurons is required for spike invasion of the soma, but not for through-conduction. *Biophys J*. 2003;84(4):2181-2191. doi:10.1016/S0006-3495(03)75024-3
134. Amir R, Devor M. Extra spike formation in sensory neurons and the disruption of afferent spike patterning. *Biophys J*. 2003;84(April):2700-2708. doi:10.1016/S0006-3495(03)75075-9
135. Sundt D, Gamper N, Jaffe DB. Spike propagation through the dorsal root ganglia in an unmyelinated sensory neuron: A modeling study. *J Neurophysiol*. 2015;114(6):3140-3153. doi:10.1152/jn.00226.2015
136. Zander HJ, Graham RD, Anaya CJ, Lempka SF. Anatomical and technical factors affecting the neural response to epidural spinal cord stimulation. *J Neural Eng*. 2020;17(3):036019. doi:10.1088/1741-2552/ab8fc4
137. Falowski SM, Dianna A. A prospective analysis of neuromonitoring for confirmation of lead placement in dorsal root ganglion stimulation. *Oper Neurosurg*. 2018;14(6):654-659. doi:10.1093/ons/opx172
138. Mekhail NA, Deer TR, Kramer J, et al. Paresthesia-free dorsal root ganglion stimulation: An ACCURATE study sub-analysis. *Neuromodulation*. 2020;23(2):185-195. doi:10.1111/ner.12942
139. Sankarasubramanian V, Chiravuri S, Mirzakhalili E, et al. Quantitative sensory testing of spinal cord and dorsal root ganglion stimulation in chronic pain patients. *Neuromodulation*. 2021;24(4):672-684. doi:10.1111/ner.13329
140. Giacobassi MJ, Leavitt LS, Raghuraman S, et al. An integrative approach to the facile functional classification of dorsal root ganglion neuronal subclasses. *Proc Natl Acad Sci*. 2020;117(10):1-8. doi:10.1073/pnas.1911382117
141. Devor M, Govrin-Lippmann R. Neurogenesis in adult rat dorsal root ganglia. *Neurosci Lett*. 1985;61:189-194. doi:10.1016/0304-3940(85)90423-9
142. Puigdellívol-Sánchez A, Prats-Galino A, Ruano-Gil D, Molander C. Sciatic and femoral nerve sensory neurones occupy different regions of the L4 dorsal root ganglion in the adult rat. *Neurosci Lett*. 1998;251(3):169-172. doi:10.1016/S0304-3940(98)00518-7
143. Serra J, Bostock H, Solà R, et al. Microneurographic identification of spontaneous activity in C-nociceptors in neuropathic pain states in humans and rats. *Pain*. 2012;153(1):42-55. doi:10.1016/j.pain.2011.08.015
144. Amir R, Liu CN, Kocsis JDK, Devor M. Oscillatory mechanism in primary sensory neurones. *Brain*. 2002;125(2):421-435. doi:10.1093/brain/awf037
145. Campbell JN, Raja SN, Meyer RA, Mackinnon SE. Myelinated afferents signal the hyperalgesia associated with nerve injury. *Pain*. 1988;32(1):89-94. doi:10.1016/0304-3959(88)90027-9
146. Yu G, Segel I, Zhang Z, Hogan QH, Pan B. Dorsal root ganglion stimulation alleviates pain-related behaviors in rats with nerve injury and osteoarthritis. *Anesthesiology*. 2020;133(2):408-425. doi:10.1097/ALN.0000000000003348
147. Ghosh A, Greenberg ME. Calcium signaling in neurons: Molecular mechanisms and cellular consequences. *Science*. 1995;268:239-247.
148. Sankarasubramanian V, Harte SE, Chiravuri S, et al. Objective measures to characterize the physiological effects of spinal cord stimulation in neuropathic pain: A literature

review. *Neuromodulation*. 2019;22(2):127-148. doi:10.1111/ner.12804
149. Chapman KB, van Roosendaal BK, Yousef TA, Vissers KC, van Helmond N. Dorsal root ganglion stimulation normalizes measures of pain processing in patients with chronic low-back pain: A prospective pilot study using quantitative sensory testing. *Pain Pract*. 2020;21(5):1-10. doi:10.1111/papr.12992
150. Kinfe T, von Willebrand N, Stadlbauer A, et al. Quantitative sensory phenotyping in chronic neuropathic pain patients treated with unilateral L4-dorsal root ganglion stimulation. *J Transl Med*. 2020;18(1):1-14. doi:10.1186/s12967-020-02566-8
151. Eide PK. Wind-up and the NMDA receptor complex from a clinical perspective. *Eur J Pain*. 2000;4:5-15. doi:10.1053/eujp.1999.0154
152. Campbell CM, Buenaver LF, Raja SN, et al. Dynamic pain phenotypes are associated with spinal cord stimulation-induced reduction in pain: A repeated measures observational pilot study. *Pain Med*. 2015;16(7):1349-1360. doi:10.1111/pme.12732
153. De Andrade DC, Bendib B, Hattou M, Keravel Y, Nguyen JP, Lefaucheur JP. Neurophysiological assessment of spinal cord stimulation in failed back surgery syndrome. *Pain*. 2010;150(3):485-491. doi:10.1016/j.pain.2010.06.001
154. Biurrun Manresa JA, Sörensen J, Andersen OK, Arendt-Nielsen L, Gerdle B. Dynamic changes in nociception and pain perception after spinal cord stimulation in chronic neuropathic pain patients. *Clin J Pain*. 2015;31(12):1046-1053. doi:10.1097/AJP.0000000000000209
155. García-Larrea L, Sindou M, Mauguière F. Nociceptive flexion reflexes during analgesic neurostimulation in man. *Pain*. 1989;39(2):145-156. doi:10.1016/0304-3959(89)90002-X
156. Song Z, Ansah OB, Meyerson BA, Pertovaara A, Linderoth B. The rostroventromedial medulla is engaged in the effects of spinal cord stimulation in a rodent model of neuropathic pain. *Neuroscience*. 2013;247:134-144. doi:10.1016/j.neuroscience.2013.05.027
157. Song Z, Meyerson BA, Linderoth B. Spinal 5-HT receptors that contribute to the pain-relieving effects of spinal cord stimulation in a rat model of neuropathy. *Pain*. 2011;152(7):1666-1673. doi:10.1016/j.pain.2011.03.012
158. Song Z, Ultenius C, Meyerson BA, Linderoth B. Pain relief by spinal cord stimulation involves serotonergic mechanisms: An experimental study in a rat model of mononeuropathy. *Pain*. 2009;147(1-3):241-248. doi:10.1016/j.pain.2009.09.020
159. Pawela CP, Kramer JM, Hogan QH. Dorsal root ganglion stimulation attenuates the BOLD signal response to noxious sensory input in specific brain regions: Insights into a possible mechanism for analgesia. *Neuroimage*. 2017;147(July 2016):10-18. doi:10.1016/j.neuroimage.2016.11.046
160. Kiriakopoulos ET, Tasker RR, Nicosia S, Wood ML, Mikulis DJ. Functional magnetic resonance imaging: A potential tool for the evaluation of spinal cord stimulation: Technical case report. *Neurosurgery*. 1997;41(2):501-504. doi:10.1097/00006123-199708000-00042
161. Moens M, Sunaert S, Mariën P, et al. Spinal cord stimulation modulates cerebral function: An fMRI study. *Neuroradiology*. 2012;54(12):1399-1407. doi:10.1007/s00234-012-1087-8
162. Stančák A, Kozák J, Vrba I, et al. Functional magnetic resonance imaging of cerebral activation during spinal cord stimulation in failed back surgery syndrome patients. *Eur J Pain*. 2008;12(2):137-148. doi:10.1016/j.ejpain.2007.03.003

163. Meuwissen KP V, Toorn A Van Der, Gu JW, Zhang TC, Dijkhuizen RM, Joosten EAJ. Active recharge burst and tonic spinal cord stimulation engage different supraspinal mechanisms: A functional magnetic resonance imaging study in peripherally injured chronic neuropathic rats. *Pain Pract*. 2020;20(5):510521. doi:10.1111/papr.12879
164. Parker T, Huang Y, Raghu ALB, Fitzgerald JJ, Green AL, Aziz TZ. Dorsal root ganglion stimulation modulates cortical gamma activity in the cognitive dimension of chronic pain. *Brain Sci*. 2020;10(2):1-13. doi:10.3390/brainsci10020095
165. De Ridder D, Vanneste S. Burst and tonic spinal cord stimulation: Different and common brain mechanisms. *Neuromodulation*. 2016;19(1):47-59. doi:10.1111/ner.12368
166. De Ridder D, Plazier M, Kamerling N, Menovsky T, Vanneste S. Burst spinal cord stimulation for limb and back pain. *World Neurosurg*. 2013;80(5):642-649.e1. doi:10.1016/j.wneu.2013.01.040
167. Buonocore M, Bodini A, Demartini L, Bonezzi C. Inhibition of somatosensory evoked potentials during spinal cord stimulation and its possible role in the comprehension of antalgic mechanisms of neurostimulation for neuropathic pain. *Minerva Anestesiol*. 2012;78:297-302.
168. Lang E, Krainick JU, Gerbershagen HU. Spinal cord transmission of impulses during high spinal anesthesia as measured by cortical evoked potentials. *Anesth Analg*. 1989;69(1):15-20. doi:10.1213/00000539-198907000-00004
169. Larson SJ, Sances A, Riegel DH, Meyer GA, Dallmann DE, Swiontek T. Neurophysiological effects of dorsal column stimulation in man and monkey. *J Neurosurg*. 1974;41(2):217-223. doi:10.3171/jns.1974.41.2.0217
170. Poláček H, Kozák J, Vrba I, Vrána J, Stančák A. Effects of spinal cord stimulation on the cortical somatosensory evoked potentials in failed back surgery syndrome patients. *Clin Neurophysiol*. 2007;118(6):1291-1302. doi:10.1016/j.clinph.2007.02.029
171. Morgalla MH, de Barros Filho MF, Chander BS, Soekadar SR, Tatagiba M, Lepski G. Neurophysiological effects of dorsal root ganglion stimulation (DRGS) in pain processing at the cortical level. *Neuromodulation*. 2019;22:36-43. doi:10.1111/ner.12900
172. Malaga KA, Schroeder KE, Patel PR, et al. Data-driven model comparing the effects of glial scarring and interface interactions on chronic neural recordings in non-human primates. *J Neural Eng*. 2015;13:016010. doi:10.1088/1741-2560/13/1/016010
173. Hanani M, Spray DC. Emerging importance of satellite glia in nervous system function and dysfunction. *Nat Rev Neurosci*. 2020;21(9):485-498. doi:10.1038/s41583-020-0333-z
174. Costa FAL, Neto FLM. Satellite glial cells in sensory ganglia: Its role in pain. *Brazilian J Anesthesiol*. 2015;65(1):73-81. doi:10.1016/j.bjane.2013.07.013
175. Huang L-YM, Gu Y, Chen Y. Communication between neuronal somata and satellite glial cells in sensory ganglia. *Glia*. 2013;61:1571-1581. doi:10.1002/glia.22541
176. Ruiz-Sauri A, Orduña-Valls JM, Blasco-Serra A, et al. Glia to neuron ratio in the posterior aspect of the human spinal cord at thoracic segments relevant to spinal cord stimulation. *J Anat*. 2019;235(5):997-1006. doi:10.1111/joa.13061
177. Vallejo R, Bradley K, Kapural L. Spinal cord stimulation in chronic pain. *Spine*. 2017;42(14):S53-S60. doi:10.1097/BRS.0000000000002179
178. Tilley DM, Lietz CB, Cedeno DL, Kelley CA, Li L, Vallejo R. Proteomic modulation in the dorsal spinal cord following spinal cord stimulation therapy in an in vivo neuropathic pain model. *Neuromodulation*. 2021;24(1):22-32. doi:10.1111/ner.13103
179. Vallejo R, Tilley DM, Cedeño DL, Kelley CA, DeMaegd M, Benyamin R. Genomics of

the effect of spinal cord stimulation on an animal model of neuropathic pain. *Neuromodulation*. 2016;19(6):576-586. doi:10.1111/ner.12465
180. Price TJ, Cervero F, Gold MS, Hammond DL, Prescott SA. Chloride regulation in the pain pathway. *Brain Res Rev*. 2009;60(1):149-170. doi:10.1016/j.brainresrev.2008.12.015
181. Rattay F. Analysis of models for extracellular fiber stimulation. *IEEE Trans Biomed Eng*. 1989;36(7):676-682. doi:10.1109/10.32099
182. Amir R, Michaelis M, Devor M. Membrane potential oscillations in dorsal root ganglion neurons: Role in normal electrogenesis and neuropathic pain. *J Neurosci*. 1999;19(19):8589-8596.
183. Lee KH, Chung K, Chung JM, Coggeshall RE. Correlation of cell body size, axon size, and signal conduction velocity for individually labelled dorsal root ganglion cells in the cat. *J Comp Neurol*. 1986;243(3):335-346. doi:10.1002/cne.902430305
184. Yoshida S, Matsuda Y. Studies on sensory neurons of the mouse with intracellular-recording and horseradish peroxidase-injection techniques. *J Neurophysiol*. 1979;42(4):1134-1145. doi:10.1152/jn.1979.42.4.1134
185. Finn KE, Zander HJ, Graham RD, Lempka SF, Weiland JD. A patient-specific computational framework for the Argus II implant. *IEEE Open J Eng Med Biol*. 2020;1:190-196. doi:10.1109/ojemb.2020.3001563
186. Tveito A, Jæger KH, Lines GT, et al. An evaluation of the accuracy of classical models for computing the membrane potential and extracellular potential for neurons. *Front Comput Neurosci*. 2017;11:1-18. doi:10.3389/fncom.2017.00027
187. Bennett DL, Clark AJ, Huang J, Waxman SG, Dib-Hajj SD. The role of voltage-gated sodium channels in pain signaling. *Physiol Rev*. 2019;99:1079-1151. doi:10.1152/physrev.00052.2017
188. Tsantoulas C, McMahon SB. Opening paths to novel analgesics: The role of potassium channels in chronic pain. *Trends Neurosci*. 2014;37(3):146-158. doi:10.1016/j.tins.2013.12.002
189. Lempka SF. Can patient-specific computer models help in pain clinics using spinal cord stimulation? *Bioelectron Med*. 2020;3(1):1-4.
190. Duan B, Cheng L, Ma Q. Spinal circuits transmitting mechanical pain and itch. *Neurosci Bull*. 2018;34(1):186-193. doi:10.1007/s12264-017-0136-z
191. Wercberger R, Basbaum AI. Spinal cord projection neurons: a superficial, and also deep analysis. *Curr Opin Physiol*. 2019;11:109-115. doi:10.1016/j.cophys.2019.10.002
192. Koetsier E, Franken G, Debets J, et al. Effectiveness of dorsal root ganglion stimulation and dorsal column spinal cord stimulation in a model of experimental painful diabetic polyneuropathy. *CNS Neurosci Ther*. 2019;25(3):367-374. doi:10.1111/cns.13065
193. Bruns TM, Wagenaar JB, Bauman MJ, Gaunt RA, Weber DJ. Real-time control of hind limb functional electrical stimulation using feedback from dorsal root ganglia recordings. *J Neural Eng*. 2013;10(2). doi:10.1088/1741-2560/10/2/026020
194. Holinski BJ, Everaert DG, Mushahwar VK, Stein RB. Real-time control of walking using recordings from dorsal root ganglia. *J Neural Eng*. 2013;10(5):1-15. doi:10.1088/1741-2560/10/5/056008
195. Ouyang Z, Sperry ZJ, Barrera ND, Bruns TM. Real-time bladder pressure estimation for closed-loop control in a detrusor overactivity model. *IEEE Trans Neural Syst Rehabil Eng*. 2019;27(6):1209-1216. doi:10.1109/TNSRE.2019.2912374
196. Umeda T, Seki K, Sato M aki, Nishimura Y, Kawato M, Isa T. Population coding of

forelimb joint kinematics by peripheral afferents in monkeys. *PLoS One*. 2012;7(10). doi:10.1371/journal.pone.0047749
197. Weber DJ, Stein RB, Everaert DG, Prochazka A. Limb-state feedback from ensembles of simultaneously recorded dorsal root ganglion neurons. *J Neural Eng*. 2007;4(3). doi:10.1088/1741-2560/4/3/S04
198. Kashkoush AI, Gaunt RA, Fisher LE, Bruns TM, Weber DJ. Recording single- and multi-unit neuronal action potentials from the surface of the dorsal root ganglion. *Sci Rep*. 2019;9(1):1-12. doi:10.1038/s41598-019-38924-w
199. Sperry ZJ, Na K, Parizi SS, et al. Flexible microelectrode array for interfacing with the surface of neural ganglia. *J Neural Eng*. 2018;15(3). doi:10.1088/1741-2552/aab55f
200. Aoyagi Y, Stein RB, Branner A, Pearson KG, Normann RA. Capabilities of a penetrating microelectrode array for recording single units in dorsal root ganglia of the cat. *J Neurosci Methods*. 2003;128:9-20. doi:10.1016/S0165-0270(03)00143-2
201. Kneist W, Kauff DW, Schröder M, Koch KP, Lang H. Percutaneous nerve evaluation based on electrode placement under control of autonomic innervation. *Tech Coloproctol*. 2014;18(8):725-730. doi:10.1007/s10151-014-1160-x
202. Dubin AE, Patapoutian A. Nociceptors: the sensors of the pain pathway. *J Clin Invest*. 2010;120(11):3760-3772. doi:10.1172/JCI42843.3760
203. Winter DL. Receptor characteristics and conduction velocities in bladder afferents. *J Psychiatr Res*. 1971;8(3-4):225-235. doi:10.1016/0022-3956(71)90021-5
204. Gardner EP, Johnson KO. The somatosensory system: Receptors and central pathways. In: *Principles of Neural Science, Fifth Edition*. McGraw-Hill Education; 2014:475-497.
205. Burton H, McFarlane JJ. The organization of the seventh lumbar spinal ganglion of the cat. *J Comp Neurol*. 1986;149:215-232.
206. Kausz M, Rethelyi M. Lamellar arrangement of neuronal somata in the dorsal root ganglion of the cat. *Somatosens Res*. 1985;2(3):193-204. doi:10.1080/19397030902947041
207. Peyronnard J -M, Messier J -P, Dubreuil M, Charron L, Lebel F. Three-dimensional computer-aided analysis of the intraganglionic topography of primary muscle afferent neurons in the rat. *Anat Rec*. 1990;227(4):405-417. doi:10.1002/ar.1092270404
208. Prats-Galino A, Puigdellívol-Sánchez A, Ruano-Gil D, Molander C. Representations of hindlimb digits in rat dorsal root ganglia. *J Comp Neurol*. 1999;408(1):137-145. doi:10.1002/(SICI)1096-9861(19990524)408:1<137::AID-CNE10>3.0.CO;2-3
209. Wessels WJT, Feirabend HKP, Marani E. Somatotopic organization in the sensory innervation of the rat hindlimb during development, using half dorsal root ganglia as subsegmental units. *Eur J Morphol*. 1990;28(2-4):394-403.
210. Wessels WJT, Feirabend HKP, Marani E. Evidence for a rostrocaudal organization in dorsal root ganglia during development as demonstrated by intra-uterine WGA-HRP injections into the hindlimb of rat fetuses. *Dev Brain Res*. 1990;54(2):273-281. doi:10.1016/0165-3806(90)90150-W
211. Sato M, Austin G. Intracellular potentials of mammalian dorsal root ganglion cells. *J Neurophysi*. 1961;24(6):569-582.
212. Bossy J. *Atlas of Neuroanatomy and Special Sense Organs*. 1st ed. WB Saunders; 1970.
213. Miletic V, Lu G-W. Characteristics of action potentials recorded from cat spinal ganglion neurons in vivo. *Brain Res Bull*. 1993;31(5):531-538. doi:10.1016/0361-9230(93)90120-Z
214. Rostock C, Schrenk-Siemens K, Pohle J, Siemens J. Human vs. mouse nociceptors -

similarities and differences. *Neuroscience*. 2018;387:13-27. doi:10.1016/j.neuroscience.2017.11.047
215. Vega JA, Humara JM, Naves FJ, Esteban I, Valle ME Del. Immunoreactivity for phosphorylated 200-kDa neurofilament subunit is heterogeneously expressed in human sympathetic and primary sensory neurons. *Anat Embryol (Berl)*. 1994;190:453-459.
216. Liu YT, Zhou XJ, Ma J, Ge Y Bin, Cao X. The diameters and number of nerve fibers in spinal nerve roots. *J Spinal Cord Med*. 2015;38(4):532-537. doi:10.1179/1079026814Z.000000000273
217. Wienert S, Heim D, Saeger K, et al. Detection and segmentation of cell nuclei in virtual microscopy images: A minimum-model approach. *Sci Rep*. 2012;2(503):1-7. doi:10.1038/srep00503
218. Taha AA, Hanbury A. Metrics for evaluating 3D medical image segmentation: Analysis, selection, and tool. *BMC Med Imaging*. 2015;15(1). doi:10.1186/s12880-015-0068-x
219. Al-Kofahi Y, Lassoued W, Lee W, Roysam B. Improved automatic detection and segmentation of cell nuclei in histopathology images. *IEEE Trans Biomed Eng*. 2010;57(4):841-852. doi:10.1109/TBME.2009.2035102
220. Peikari M, Martel AL. Automatic cell detection and segmentation from H and E stained pathology slides using colorspace decorrelation stretching. *Proc SPIE 9791, Med Imaging 2016 Digit Pathol*. 2016;9791. doi:10.1117/12.2216507
221. Offord K, Ohta M, Oenning RF, Dyck PJ. Method of morphometric evaluation of spinal and autonomic ganglia. *J Neurol Sci*. 974;22:65-71.
222. Silverstein MP, Romrell LJ, Benzel EC, Thompson N, Griffith S, Lieberman IH. Lumbar dorsal root ganglia location: An anatomic and MRI assessment. *Int J Spine Surg*. 2015;9. doi:10.14444/2003
223. Josephson A, Widenfalk J, Trifunovski A, Widmer HR, Olson L, Spenger C. GDNF and NGF family members and receptors in human fetal and adult spinal cord and dorsal root ganglia. *J Comp Neurol*. 2001;440(2):204-217. doi:10.1002/cne.1380
224. Flegal KM, Carroll D, Kit BK, Ogden CL. Prevalence of obesity and trends in the distribution of body mass index among US adults, 1999-2010. *JAMA - J Am Med Assoc*. 2012;307(5):491-497. doi:10.1001/jama.2012.39
225. Peck-Dimit N, Sperry ZJ, Graham RD, Lempka SF, Bruns TM. Human DRG 3D cross section analysis. Open Science Framework. doi:10.17605/OSF.IO/TQRFZ
226. St. Wecker PGR, Farel PB. Hindlimb sensory neuron number increases with body size. *J Comp Neurol*. 1994;342(3):430-438. doi:10.1002/cne.903420309
227. Devor M, Govrin-Lippmann R. Neurogenesis in adult rat dorsal root ganglia: On counting and the count. *Somatosens Mot Res*. 1991;8(1):9-12. doi:10.3109/08990229109144724
228. Pover CM, Barnes MC, Coggeshall RE. Do primary afferent cell numbers change in relation to increasing weight and surface area in adult rats? *Somatosens Mot Res*. 1994;11(2):163-167. doi:10.3109/08990229409028869
229. Aldskogius H, Risling M. Number of dorsal root ganglion neurons and axons in cats of different ages. *Exp Neurol*. 1989;106(1):70-73. doi:10.1016/0014-4886(89)90145-3
230. Aldskogius H, Risling M. Effect of sciatic neurectomy on neuronal number and size distribution in the L7 ganglion of kittens. *Exp Neurol*. 1981;74(2):597-604. doi:10.1016/0014-4886(81)90194-1
231. Chung K, Coggeshall RE. The ratio of dorsal root ganglion cells to dorsal root axons in sacral segments of the cat. *J Comp Neurol*. 1984;225(1):24-30.

232. Langford LA, Coggeshall RE. Branching of sensory axons in the dorsal root and evidence for the absence of dorsal root efferent fibers. *J Comp Neurol*. 1979;184:193-204.
233. Langford LA, Coggeshall RE. Branching of sensory axons in the peripheral nerve of the rat. *J Comp Neurol*. 1981;203:745-750.
234. Risling M, Aldskogius H, Hildebrand C, Remahl S. Effects of sciatic nerve resection on L7 spinal roots and dorsal root ganglia in adult cats. *Exp Neurol*. 1983;82(3):568-580. doi:10.1016/0014-4886(83)90081-X
235. Davenport HA, Bothe RT. Cells and fibers in spinal nerves. *J Comp Neurol*. 1934;59:167-174.
236. Shen J, Wang H-Y, Chen J-Y, Liang B-L. Morphologic analysis of normal human lumbar dorsal root ganglion by 3D MR imaging. *AJNR Am J Neuroradiol*. 2006;27(10):2098-2103. http://www.ncbi.nlm.nih.gov/pubmed/17110675
237. Hope J, Vanholsbeeck F, McDaid A. A model of electrical impedance tomography implemented in nerve-cuff for neural-prosthetics control. *Physiol Meas*. 2018;39(4):1-17. doi:10.1088/1361-6579/aab73a
238. Moffitt MA, McIntyre CC. Model-based analysis of cortical recording with silicon microelectrodes. *Clin Neurophysiol*. 2005;116(9):2240-2250. doi:10.1016/j.clinph.2005.05.018
239. Fowler CJ. Bladder afferents and their role in the overactive bladder. *Urology*. 2002;59(Supplement 5A):37-42. doi:10.1016/S0090-4295(02)01544-3
240. West CA, McKay Hart A, Terenghi G, Wiberg M. Sensory neurons of the human brachial plexus: A quantitative study employing optical fractionation and in vivo volumetric magnetic resonance imaging. *Neurosurgery*. 2012;70(5):1183-1194. doi:10.1227/NEU.0b013e318241ace1
241. Chang W, Berta T, Kim YH, Lee S, Lee S-Y, Ji R-R. Expression and role of voltage-gated sodium channels in human dorsal root ganglion neurons with special focus on Nav1.7, species differences, and regulation by paclitaxel. *Neurosci Bull*. 2018;34(1):4-12. doi:10.1007/s12264-017-0132-3
242. Kramer J, Liem L, Russo M, Smet I, Van Buyten JP, Huygen F. Lack of body positional effects on paresthesias when stimulating the dorsal root ganglion (DRG) in the treatment of chronic pain. *Neuromodulation*. 2015;18(1):50-57. doi:10.1111/ner.12217
243. Schu S, Gulve A, Eldabe S, et al. Spinal cord stimulation of the dorsal root ganglion for groin pain - a retrospective review. *Pain Pract*. 2014;15(4):293-299. doi:10.1111/papr.12194
244. Mol FMU, Roumen RMH. DRG spinal cord stimulation as solution for patients with severe pain due to anterior cutaneous nerve entrapment syndrome: A case series. *Neuromodulation*. 2018;21(3):317-319. doi:10.1111/ner.12692
245. Devor M. Ectopic discharge in Aβ afferents as a source of neuropathic pain. *Exp Brain Res*. 2009;196(1):115-128. doi:10.1007/s00221-009-1724-6
246. Djouhri L, Koutsikou S, Fang X, McMullan S, Lawson SN. Spontaneous pain, both neuropathic and inflammatory, is related to frequency of spontaneous firing in intact C-fiber nociceptors. *J Neurosci*. 2006;26(4):1281-1292. doi:10.1523/JNEUROSCI.3388-05.2006
247. Kajander KC, Bennett GJ. Onset of a painful peripheral neuropathy in rat: A partial and differential deafferentation and spontaneous discharge in Aβ and Aδ primary afferent neurons. *J Neurophysiol*. 1992;68(3):734-744.

248. Liu CN, Wall PD, Ben-Dor E, Michaelis M, Amir R, Devor M. Tactile allodynia in the absence of C-fiber activation: Altered firing properties of DRG neurons following spinal nerve injury. *Pain*. 2000;85(3):503-521. doi:10.1016/S0304-3959(00)00251-7
249. Kovalsky Y, Amir R, Devor M. Simulation in sensory neurons reveals a key role for delayed Na+ current in subthreshold oscillations and ectopic discharge: Implications for neuropathic pain. *J Neurophysiol*. 2009;102(3):1430-1442. doi:10.1152/jn.00005.2009.
250. Prescott SA, Ma Q, De Koninck Y. Normal and abnormal coding of somatosensory stimuli causing pain. *Nat Neurosci*. 2014;17(2):183-191. doi:10.1038/nn.3629
251. Blumberg H, Jänig W. Discharge pattern of afferent fibers from a neuroma. *Pain*. 1984;20(4):335-353. doi:10.1016/0304-3959(84)90111-8
252. Welk E, Leah JD, Zimmermann M. Characteristics of A- and C-fibers ending in a sensory nerve neuroma in the rat. *J Neurophysiol*. 1990;63(4):759-766.
253. Liu CN, Michaelis M, Amir R, Devor M. Spinal nerve injury enhances subthreshold membrane potential oscillations in DRG neurons: Relation to neuropathic pain. *J Neurophysiol*. 2000;84(1):205-215. doi:10.1152/jn.2000.84.1.205
254. Azeem N, Attias MD. Neuromodulation: Mechanisms of action. In: *Advanced Procedures for Pain Management: A Step-by-Step Atlas*. Springer International Publishing; 2018:93-103.
255. Bendinger T, Plunkett N. Dorsal root ganglion stimulation vs. conventional spinal cord stimulation - efficacy and patient experience of two neurostimulation methods for the treatment of Complex Regional Pain Syndrome type II: A case report. *J Obs Pain Med*. 2015;1(5):42-47.
256. Hogan Q. Size of human lower thoracic and lumbosacral nerve roots. *Anesthesiology*. 1996;85:37-42. doi:10.1167/8.5.1.
257. Reina MA, Villanueva MC, López A, De Andrés JA. Grasa dentro de los manguitos durales de las raices nerviosas de la columna lumbar humana. *Rev Esp Anestesiol Reanim*. 2007;54:297-301.
258. Geddes LA, Baker LE. The specific resistance of biological material - a compendium of data for the biomedical engineer and physiologist. *Med Biol Eng*. 1967;5(3):271-293. doi:10.1007/BF02474537
259. Grill WM, Mortimer JT. Electrical properties of implant encapsulation tissue. *Ann Biomed Eng*. 1994;22:23-33. doi:10.1007/BF02368219
260. Gabriel S, Lau RW, Gabriel C. The dielectric properties of biological tissues: III. Parametric models for the dielectric spectrum of tissues. *Phys Med Biol*. 1996;41(11):2271-2293. doi:10.1088/0031-9155/41/11/003
261. Hines ML, Carnevale NT. The NEURON simulation environment. *Neural Comput*. 1997;9:1179-1209. doi:10.1162/neco.1997.9.6.1179
262. Ito M, Takahashi I. Impulse conduction through spinal ganglion. In: *Electrical Activity of Single Cells*. ; 1960:159-179.
263. McIntyre CC, Richardson AG, Grill WM. Modeling the excitability of mammalian nerve fibers: Influence of afterpotentials on the recovery cycle. *J Neurophysiol*. 2002;87:995-1006. doi:10.1152/jn.00353.2001
264. Gaines JL, Finn KE, Slopsema JP, Heyboer LA, Polasek KH. A model of motor and sensory axon activation in the median nerve using surface electrical stimulation. *J Comput Neurosci*. 2018;45(1):29-43. doi:10.1007/s10827-018-0689-5
265. Harper AA, Lawson SN. Electrical properties of rat dorsal root ganglion neurones with

different peripheral nerve conduction velocities. *J Physiol*. 1985;359(1):47-63. doi:10.1113/jphysiol.1985.sp015574
266. Villière V, McLachlan EM. Electrophysiological properties of neurons in intact rat dorsal root ganglia classified by conduction velocity and action potential duration. *J Neurophysiol*. 1996;76(3):1924-1941.
267. Matsumoto E, Rosenbluth J. Plasma membrane structure at the axon hillock, initial segment and cell body of frog dorsal root ganglion cells. *J Neurocytol*. 1985;14(5):731-747.
268. Sheets PL, Jackson JO, Waxman SG, Dib-hajj SD, Cummins TR. A Nav 1.7 channel mutation associated with hereditary erythromelalgia contributes to neuronal hyperexcitability and displays reduced lidocaine sensitivity. *J Physiol*. 2007;581(3):1019-1031. doi:10.1113/jphysiol.2006.127027
269. Huang J, Han C, Estacion M, et al. Gain-of-function mutations in sodium channel Nav1.9 in painful neuropathy. *Brain*. 2014;137(6):1627-1642. doi:10.1093/brain/awu079
270. Waxman SG, Ritchie JM. Organization of ion channels in the myelinated nerve fiber. *Science*. 1985;228(4707):1502-1507.
271. Amir R, Kocsis JD, Devor M. Multiple interacting sites of ectopic spike electrogenesis in primary sensory neurons. *J Neurosci*. 2005;25(10):2576-2585. doi:10.1523/JNEUROSCI.4118-04.2005
272. Xiao H-S, Huang Q-H, Zhang F-X, et al. Identification of gene expression profile of dorsal root ganglion in the rat peripheral axotomy model of neuropathic pain. *Proc Natl Acad Sci U S A*. 2002;99(12):8360-8365. doi:10.1073/pnas.122231899
273. Dawes JM, Weir GA, Middleton SJ, et al. Immune or genetic-mediated disruption of CASPR2 causes pain hypersensitivity due to enhanced primary afferent excitability. *Neuron*. 2018;97(4):806-822. doi:10.1016/j.neuron.2018.01.033
274. Hunt MA, Nascimento DSM, Bersellini Farinotti A, Svensson CI. Autoantibodies hurt: Transfer of patient-derived CASPR2 antibodies induces neuropathic pain in mice. *Neuron*. 2018;97(4):729-731. doi:10.1016/j.neuron.2018.02.008
275. Ishikawa K, Tanaka M, Black J a, Waxman SG. Changes in expression of voltage-gated potassium channels in dorsal root ganglion neurons following axotomy. *Muscle Nerve*. 1999;22(4):502-507. doi:10.1002/(SICI)1097-4598(199904)22:4<502::AID-MUS12>3.0.CO;2-K [pii]
276. Waxman SG. The molecular pathophysiology of pain: Abnormal expression of sodium channel genes and its contributions to hyperexcitability of primary sensory neurons. *Pain*. 1999;82(Supplement 6):S133-40. doi:10.1016/S0304-3959(99)00147-5
277. Devor M. Sodium channels and mechanisms of neuropathic pain. *J Pain*. 2006;7(1S):S3-S12. doi:10.1016/j.jpain.2005.09.006
278. Devor M, Govrin-Lippmann R, Raber P. Corticosteroids suppress ectopic neural discharge originating in experimental neuromas. *Pain*. 1985;22(2):127-137. doi:10.1016/0304-3959(85)90173-3
279. Song XJ, Hu SJ, Greenquist KW, Zhang JM, LaMotte RH. Mechanical and thermal hyperalgesia and ectopic neuronal discharge after chronic compression of dorsal root ganglia. *J Neurophysiol*. 1999;82(6):3347-3358.
280. Hines ML, Davison AP, Muller E. NEURON and Python. *Front Neuroinform*. 2009;3:1-12. doi:10.3389/neuro.11.001.2009
281. Lempka SF, Howell B, Gunalan K, Machado AG, McIntyre CC. Characterization of the

stimulus waveforms generated by implantable pulse generators for deep brain stimulation. *Clin Neurophysiol*. 2018;129(4):731-742. doi:10.1016/j.clinph.2018.01.015
282. Huxley AF, Stämpfli R. Direct determination of membrane resting potential and action potential in single myelinated nerve fibres. *J Physiol*. 1951;112(3-4):476-495.
283. Djouhri L, Bleazard L, Lawson SN. Association of somatic action potential shape with sensory receptive properties in guinea-pig dorsal root ganglion neurones. *J Physiol*. 1998;513(3):857-872. doi:10.1111/j.1469-7793.1998.857ba.x
284. Zhang JM, Donnelly DF, Lamotte RH. Patch clamp recording from the intact dorsal root ganglion. *J Neurosci Methods*. 1998;79(1):97-103. doi:10.1016/S0165-0270(97)00164-7
285. Howells J, Trevillion L, Bostock H, Burke D. The voltage dependence of Ih in human myelinated axons. *J Physiol*. 2012;590(7):1625-1640. doi:10.1113/jphysiol.2011.225573
286. Harper AA, Lawson SN. Conduction velocity is related to morphological cell type in rat dorsal root ganglion neurones. *J Physiol*. 1985;359(1):31-46. doi:10.1113/jphysiol.1985.sp015573
287. Vancamp T, Levy RM, Peña I, Pajuelo A. Relevant anatomy, morphology, and implantation techniques of the dorsal root ganglia at the lumbar levels. *Neuromodulation*. 2017;20(7):690-702. doi:10.1111/ner.12651
288. Guan Y. Spinal cord stimulation: Neurophysiological and neurochemical mechanisms of action. *Curr Pain Headache Rep*. 2012;16(3):217-225. doi:10.1007/s11916-012-0260-4
289. Duan B, Cheng L, Bourane S, et al. Identification of spinal circuits transmitting and gating mechanical pain. *Cell*. 2014;159(6):1417-1432. doi:10.1016/j.cell.2014.11.003
290. Cheng L, Duan B, Huang T, et al. Identification of spinal circuits involved in touch-evoked dynamic mechanical pain. *Nat Neurosci*. 2017;20(6):804-814. doi:10.1038/nn.4549
291. Ranck JB. Which elements are excited in electrical stimulation of mammalian central nervous system: A review. *Brain Res*. 1975;98(3):417-440. doi:10.1097/SHK.0000000000000692
292. Kikuchi S, Sato K, Konno S, Hasue M. Anatomic and radiographic study of dorsal root ganglia. *Spine*. 1994;19(1):6-11.
293. Tandrup T. A method for unbiased and efficient estimation of number and mean volume of specified neuron subtypes in rat dorsal root ganglion. *J Comp Neurol*. 1993;329(2):269-276. doi:10.1002/cne.903290208
294. McIntyre CC, Savasta M, Kerkerian-Le Goff L, Vitek JL. Uncovering the mechanism(s) of action of deep brain stimulation: Activation, inhibition, or both. *Clin Neurophysiol*. 2004;115(6):1239-1248. doi:10.1016/j.clinph.2003.12.024
295. Struijk JJ, Holsheimer J, Boom HBK. Excitation of dorsal root fibers in spinal cord stimulation: A theoretical study. *IEEE Trans Biomed Eng*. 1993;40(7):632-639.
296. Lawson SN. The peripheral sensory nervous system: Dorsal root ganglion neurons. In: *Peripheral Neuropathy*. Elsevier Inc.; 2005:163-202. doi:10.1016/B978-0-7216-9491-7.50010-7
297. Nissen M, Ikäheimo T-M, Huttunen J, Leinonen V, von und zu Fraunberg M. Long-term outcome of spinal cord stimulation in failed back surgery syndrome: 20 years of experience with 224 consecutive patients. *Neurosurgery*. 2019;84(5):1011-1018. doi:10.1093/neuros/nyy194
298. Lee D, Hershey B, Bradley K, Yearwood T. Predicted effects of pulse width programming in spinal cord stimulation: A mathematical modeling study. *Med Biol Eng Comput*.

2011;49:765-774. doi:10.1007/s11517-011-0780-9
299. Holsheimer J, Wesselink WA. Effect of anode-cathode configuration on paresthesia coverage in spinal cord stimulation. *Neurosurgery*. 1997;41(3):654-660. doi:10.1097/00006123-199709000-00030
300. Holsheimer J, Buitenweg JR, Das J, De Sutter P, Manola L, Nuttin B. The effect of pulse width and contact configuration on paresthesia coverage in spinal cord stimulation. *Neurosurgery*. 2011;68(5):1452-1461. doi:10.1227/NEU.0b013e31820b4f47
301. Stebbing MJ, Eschenfelder S, Acosta MC, et al. Changes in the action potential in sensory neurones after peripheral axotomy in vivo. *Neuroreport*. 1999;10:201-206.
302. Black JA, Dib-Hajj S, McNabola K, et al. Spinal sensory neurons express multiple sodium channel α-subunit mRNAs. *Mol Brain Res*. 1996;43:117-131. doi:10.1016/S0169-328X(96)00163-5
303. Djouhri L, Newton R, Levinson SR, Berry CM, Carruthers B, Lawson SN. Sensory and electrophysiological properties of guinea-pig sensory neurones expressing Nav 1.7 (PN1) Na+ channel α subunit protein. *J Physiol*. 2003;546(2):565-576. doi:10.1113/jphysiol.2002.026559
304. Djouhri L, Fang X, Okuse K, Wood JN, Berry CM, Lawson SN. The TTX-resistant sodium channel Nav1.8 (SNS/PN3): Expression and correlation with membrane properties in rat nociceptive primary afferent neurons. *J Physiol*. 2003;550(3):739-752. doi:10.1113/jphysiol.2003.042127
305. Capogrosso M, Gandar J, Greiner N, et al. Advantages of soft subdural implants for the delivery of electrochemical neuromodulation therapies to the spinal cord. *J Neural Eng*. 2018;15:1-15. doi:10.1088/1741-2552/aaa87a
306. Mainen ZF, Sejnowski TJ. Dendritic structure modulates firing pattern in model neocortical neurons. *Nature*. 1996;382:363-366.
307. Waddell PJ, Lawson SN. Electrophysiological properties of subpopulations of rat dorsal root ganglion neurons in vitro. *Neuroscience*. 1990;36(3):811-822. doi:10.1016/0306-4522(90)90024-X
308. Martin S, Hadjipavlou G, Garcia Ortega R, et al. The importance of the location of dorsal root ganglion stimulator electrodes within the nerve root exit foramen. *Neuromodulation*. 2020;23(2):245-251.
309. Falowski SM, Conti KR, Mogilner AY. Analysis of S1 DRG programming to determine location of the DRG and ideal anatomic positioning of the electrode. *Neuromodulation*. 2020;23(2):252-257.
310. Yearwood TL, Hershey B, Bradley K, Lee D. Pulse width programming in spinal cord stimulation: a clinical study. *Pain Physician*. 2010;13:321-335.
311. Nanivadekar AC, Ayers CA, Gaunt RA, Weber DJ, Fisher LE. Selectivity of afferent microstimulation at the DRG using epineural and penetrating electrode arrays. *J Neural Eng*. 2020;17(1):016011. doi:10.1088/1741-2552/ab4a24
312. Linderoth B, Stiller C-O, Gunasekera L, O'Connor WT, Ungerstedt U, Brodin E. Gamma-aminobutyric acid is released in the dorsal horn by electrical spinal cord stimulation: An in vivo microdialysis study in the rat. *Neurosurgery*. 1994;34:484-489. doi:10.1017/CBO9781107415324.004
313. Janssen SP, Gerard S, Raijmakers ME, Truin M, Van Kleef M, Joosten EA. Decreased intracellular GABA levels contribute to spinal cord stimulation-induced analgesia in rats suffering from painful peripheral neuropathy: The role of KCC2 and GABAA receptor-

mediated inhibition. *Neurochem Int*. 2012;60:21-30. doi:10.1016/j.neuint.2011.11.006
314. Cui J-G, Linderoth B, Meyerson BA. Effects of spinal cord stimulation on touch-evoked allodynia involve GABAergic mechanisms. An experimental study in the mononeuropathic rat. *Pain*. 1996;66(2-3):287-295. doi:10.1016/0304-3959(96)03069-2
315. Todd AJ. Identifying functional populations among the interneurons in laminae I-III of the spinal dorsal horn. *Mol Pain*. 2017;13:1-19. doi:10.1177/1744806917693003
316. Petitjean H, Pawlowski SA, Fraine SL, et al. Dorsal horn parvalbumin neurons are gate-keepers of touch-evoked pain after nerve injury. *Cell Rep*. 2015;13(6):1246-1257. doi:10.1016/j.celrep.2015.09.080
317. Boyle KA, Gradwell MA, Yasaka T, et al. Defining a spinal microcircuit that gates myelinated afferent input: Implications for tactile allodynia. *Cell Rep*. 2019;28(2):526-540.e6. doi:10.1016/j.celrep.2019.06.040
318. Foster E, Wildner H, Tudeau L, et al. Targeted ablation, silencing, and activation establish glycinergic dorsal horn neurons as key components of a spinal gate for pain and itch. *Neuron*. 2015;85(6):1289-1304. doi:10.1016/j.neuron.2015.02.028
319. Cui L, Miao X, Liang L, et al. Identification of early RET+ deep dorsal spinal cord interneurons in gating pain. *Neuron*. 2016;91(5):1137-1153. doi:10.1016/j.neuron.2016.07.038
320. Miller JP, Eldabe S, Buchser E, Johanek LM, Guan Y, Linderoth B. Parameters of Spinal Cord Stimulation and Their Role in Electrical Charge Delivery: A Review. *Neuromodulation*. 2016;19(4):373-384. doi:10.1111/ner.12438
321. Moffitt MA, Lee DC, Bradley K. *Spinal Cord Stimulation: Engineering Approaches to Clinical and Physiological Challenges*.; 2009. doi:10.1007/978-0-387-77261-5
322. Hunt CC. Relation of function to diameter in afferent fibers of muscle nerves. *J Gen Physiol*. 1954;38(1):117-131. doi:65.1678.208-a
323. Banks RW. An allometric analysis of the number of muscle spindles in mammalian skeletal muscles. *J Anat*. 2006;208(6):753-768. doi:10.1111/j.1469-7580.2006.00558.x
324. Ji RR, Berta T, Nedergaard M. Glia and pain: Is chronic pain a gliopathy? *Pain*. 2013;154(SUPPL. 1):S10-S28. doi:10.1016/j.pain.2013.06.022
325. Ji RR, Donnelly CR, Nedergaard M. Astrocytes in chronic pain and itch. *Nat Rev Neurosci*. 2019;20(11):667-685. doi:10.1038/s41583-019-0218-1
326. Hanani M. Role of satellite glial cells in gastrointestinal pain. *Front Cell Neurosci*. 2015;9:1-10. doi:10.3389/fncel.2015.00412
327. Vallejo R, Gupta A, Kelley CA, et al. Effects of Phase Polarity and Charge Balance Spinal Cord Stimulation on Behavior and Gene Expression in a Rat Model of Neuropathic Pain. *Neuromodulation*. 2020;23(1):26-35. doi:10.1111/ner.12964
328. Caylor J, Reddy R, Yin S, et al. Spinal cord stimulation in chronic pain: evidence and theory for mechanisms of action. *Bioelectron Med*. 2019;5(1):1-41. doi:10.1186/s42234-019-0023-1
329. Abdo H, Calvo-Enrique L, Lopez JM, et al. Specialized cutaneous Schwann cells initiate pain sensation. *Science*. 2019;365:695-699. doi:10.1126/science.aax6452
330. Zhou LJ, Peng J, Xu Y-N, et al. Microglia are indispensable for synaptic plasticity in the spinal dorsal horn and chronic pain. *Cell Rep*. 2019;27:3844-3859.e6. doi:10.1016/j.celrep.2019.05.087
331. Bean BP. The action potential in mammalian central neurons. *Nat Rev Neurosci*. 2007;8(6):451-465. doi:10.1038/nrn2148

332. North RY, Li Y, Ray P, et al. Electrophysiological and transcriptomic correlates of neuropathic pain in human dorsal root ganglion neurons. *Brain*. Published online 2019:1-12. doi:10.1093/BRAIN/AWZ063
333. Manchikanti L, Helm S, Fellows B, et al. Opioid epidemic in the United States. *Pain Physician*. 2012;15(3 Suppl):ES9-38. doi:10.1016/j.emc.2015.11.002
334. Goodman J, Weare J. Ensemble Samplers With Affine. *Commun Appl Math Comput Sci*. 2010;5(1):65-80.
335. Foreman-Mackey D, Hogg DW, Lang D, Goodman J. emcee : The MCMC Hammer . *Publ Astron Soc Pacific*. 2013;125(925):306-312. doi:10.1086/670067
336. Lüscher C, Streit J, Quadroni R, Luscher HR. Action potential propagation through embryonic dorsal root ganglion cells in culture. I. Influence of the cell morphology on propagation properties. *J Neurophysiol*. 1994;72(2):622-633. doi:10.1152/jn.1994.72.2.634
337. Lüscher C, Streit J, Lipp P, Luscher HR. Action potential propagation through embryonic dorsal root ganglion cells in culture. II. Decrease of conduction reliability during repetitive stimulation. *J Neurophysiol*. 1994;72(2):634-643. doi:10.1152/jn.1994.72.2.634
338. Kish KE, Graham RD, Wong KY, Weiland JD. The effect of axon trajectory on retinal ganglion cell activation with epiretinal stimulation. *Int IEEE/EMBS Conf Neural Eng NER*. 2021;2021-May:263-266. doi:10.1109/NER49283.2021.9441073
339. Nowak LG, Bullier J. Axons, but not cell bodies, are activated by electrical stimulation in cortical gray matter. I. Evidence from chronaxie measurements. *Exp Brain Res*. 1998;118(4):477-488. doi:10.1007/s002210050304
340. Smith DO. Morphological aspects of the safety factor for action potential propagation at axon branch points in the crayfish. *J Physiol*. 1980;301:261-269.
341. Wesselink WA, Holsheimer J, Boom HB. A model of the electrical behaviour of myelinated sensory nerve fibres based on human data. *MedBiolEng Comput*. 1999;37(0140-0118 (Print)):228-235. doi:10.1007/BF02513291
342. Holsheimer J, Struijk JJ, Tas NR. Effects of electrode geometry and combination on nerve fibre selectivity in spinal cord stimulation. *Med Biol Eng Comput*. 1995;33:676-682. doi:10.1007/BF02510785
343. Anderson DJ, Kipke DR, Nagel SJ, et al. Intradural spinal cord stimulation: Performance modeling of a new modality. *Front Neurosci*. Published online 2019. doi:10.3389/fnins.2019.00253
344. Butson CR, Cooper SE, Henderson JM, McIntyre CC. Patient-specific analysis of the volume of tissue activated during deep brain stimulation. *Neuroimage*. 2007;34(2):661-670. doi:10.1016/j.neuroimage.2006.09.034
345. Gunalan K, Howell B, McIntyre CC. Quantifying axonal responses in patient-specific models of subthalamic deep brain stimulation. *Neuroimage*. 2018;172(December 2017):263-277. doi:10.1016/j.neuroimage.2018.01.015
346. Solanes C, Durá JL, ngeles Canós M, De Andrés J, Martí-Bonmatí L, Saiz J. 3D patient-specific spinal cord computational model for SCS management: potential clinical applications. *J Neural Eng*. 2021;18(3). doi:10.1088/1741-2552/abe44f
347. Im S, Son B chul. Long-Term Changes in Thecal Sac Compression and Decreased Cerebrospinal Fluid Space Following Paddle Lead Spinal Cord Stimulation at T9: A Long-Term Follow-Up via Three-Dimensional Myelographic Computed Tomography. *Neuromodulation*. 2021;2021. doi:10.1111/ner.13491

348. Kim JH, Lee CW, Chun KS, Shin WH, Bae HG, Chang JC. Morphometric relationship between the cervicothoracic cord segments and vertebral bodies. *J Korean Neurosurg Soc*. 2012;52(4):384-390. doi:10.3340/jkns.2012.52.4.384
349. Kameyama T, Hashizume Y, Sobue G. Morphologic features of the normal human cadaveric spinal cord. *Spine*. 1996;21(11):1285-1290. doi:10.1097/00007632-199606010-00001
350. Jackson AR, Yuan TY, Huang CY, Gu WY. Measurement of ion diffusivity in intervertebral disc using a two-point electrical conductivity approach. *IFMBE Proc*. 2009;24(24):171-172. doi:10.1007/978-3-642-01697-4_62
351. Feirabend HKP, Choufoer H, Ploeger S, Holsheimer J, Van Gool JD. Morphometry of human superficial dorsal and dorsolateral column fibres: Significance to spinal cord stimulation. *Brain*. 2002;125(5):1137-1149. doi:10.1093/brain/awf111
352. Howell B, Choi KS, Gunalan K, Rajendra J, Mayberg HS, McIntyre CC. Quantifying the axonal pathways directly stimulated in therapeutic subcallosal cingulate deep brain stimulation. *Hum Brain Mapp*. 2019;40(3):889-903. doi:10.1002/hbm.24419
353. Macefield G, Gandevia SC, Burke D. Perceptual responses to microstimulation of single afferents innervating joints, muscles, and skin of the human hand. *J Physiol*. 2009;429(1990):113-129.
354. Yiannakas MC, Mustafa AM, De Leener B, et al. Fully automated segmentation of the cervical cord from T1-weighted MRI using PropSeg: Application to multiple sclerosis. *NeuroImage Clin*. 2016;10:71-77. doi:10.1016/j.nicl.2015.11.001
355. Asgari Taghanaki S, Abhishek K, Cohen JP, Cohen-Adad J, Hamarneh G. *Deep Semantic Segmentation of Natural and Medical Images: A Review*. Vol 54. Springer Netherlands; 2021. doi:10.1007/s10462-020-09854-1
356. Noecker AM, Frankemolle-Gilbert AM, Howell B, et al. StimVision v2: Examples and Applications in Subthalamic Deep Brain Stimulation for Parkinson's Disease. *Neuromodulation*. 2021;24(2):248-258. doi:10.1111/ner.13350
357. Falowski SM. An observational case series of spinal cord stimulation waveforms visualized on intraoperative neuromonitoring. *Neuromodulation Technol Neural Interface*. Published online 2018. doi:10.1111/ner.12781
358. Wercberger R, Basbaum AI. Spinal cord projection neurons: A superficial, and also deep analysis. *Curr Opin Physiol*. 2019;11:109-115. doi:10.1016/j.cophys.2019.10.002
359. Ständer S, Weisshaar E, Mettang T, et al. Clinical classification of itch: A position paper of the international forum for the study of itch. *Acta Derm Venereol*. 2007;87(4):291-294. doi:10.2340/00015555-0305
360. Sommer F, Hensen P, Böckenholt B, Metze D, Luger TA, Ständer S. Underlying diseases and co-factors in patients with severe chronic pruritus: A 3-year retrospective study. *Acta Derm Venereol*. 2007;87(6):510-516. doi:10.2340/00015555-0320
361. DeShazo RD, Kemp SF. Allergic reactions to drugs and biologic agents. *J Am Med Assoc*. 1997;278(22):1895-1906. doi:10.1001/jama.278.22.1895
362. Mazeh D, Melamed Y, Cholostoy A, Aharonovitzch V, Weizman A, Yosipovitch G. Itching in the psychiatric ward. *Acta Derm Venereol*. 2008;88(2):128-131. doi:10.2340/00015555-0406
363. Zirwas MJ, Seraly MP. Pruritus of unknown origin: A retrospective study. *J Am Acad Dermatol*. 2001;45(6):892-896. doi:10.1067/mjd.2001.117732
364. Matterne U, Strassner T, Apfelbacher CJ, Diepgen TL, Weisshaar E. Measuring the

prevalence of chronic itch in the general population: Development and validation of a questionnaire for use in large-scale studies. *Acta Derm Venereol*. 2009;89(3):250-256. doi:10.2340/00015555-0641
365. Zachariae R, Lei U, Haedersdal M, Zachariae C. Itch severity and quality of life in patients with pruritus: Preliminary validity of a danish adaptation of the itch severity scale. *Acta Derm Venereol*. 2012;92(5):508-514. doi:10.2340/00015555-1221
366. Leslie TA, Greaves MW, Yosipovitch G. Current topical and systemic therapies for itch. In: *Handbook of Experimental Pharmacology*. Vol 226. ; 2015:337-356. doi:10.1007/978-3-662-44605-8_18
367. Fowler E, Yosipovitch G. Chronic itch management: therapies beyond those targeting the immune system. *Ann Allergy, Asthma Immunol*. 2019;123(2):158-165. doi:10.1016/j.anai.2019.01.016
368. Medlock L, Sekiguchi K, Hong S, Dura-Bernal S, Lytton W, Prescott SA. Multiscale computer model of the spinal dorsal horn reveals changes in network processing associated with chronic pain. *J Neurosci*. Published online 2022. https://www.biorxiv.org/content/10.1101/2021.06.09.447785v1%0Ahttps://www.biorxiv.org/content/10.1101/2021.06.09.447785v1.abstract
369. Melnick I V., Santos SFA, Szokol K, Szucs P, Safronov B V. Ionic basis of tonic firing in spinal substantia gelatinosa neurons of rat. *J Neurophysiol*. 2004;91(2):646-655. doi:10.1152/jn.00883.2003
370. Melnick I V., Santos SFA, Safronov B V. Mechanism of spike frequency adaptation in substantia gelatinosa neurones of rat. *J Physiol*. 2004;559(2):383-395. doi:10.1113/jphysiol.2004.066415
371. Hu W, Tian C, Li T, Yang M, Hou H, Shu Y. Distinct contributions of Nav1.6 and Nav1.2 in action potential initiation and backpropagation. *Nat Neurosci*. 2009;12(8):996-1002. doi:10.1038/nn.2359
372. Traub RD, Wong RKS, Miles R, Michelson H. A model of a CA3 hippocampal pyramidal neuron incorporating voltage-clamp data on intrinsic conductances. *J Neurophysiol*. 1991;66(2):635-650. doi:10.1152/jn.1991.66.2.635
373. Choi J, Waxman SG. Physiological interactions between Nav1.7 and Nav1.8 sodium channels: a computer simulation study. *J Neurophysiol*. 2011;21(20):7909-7918. doi:10.1523/JNEUROSCI.1101-06.2006
374. Markaki M, Orphanoudakis S, Poirazi P. Modelling reduced excitability in aged CA1 neurons as a calcium-dependent process. *Neurocomputing*. 2005;65-66(SPEC. ISS.):305-314. doi:10.1016/j.neucom.2004.10.023
375. Gidon A, Zolnik TA, Fidzinski P, et al. Dendritic action potentials and computation in human layer 2/3 cortical neurons. *Science*. 2020;367(6473):83-87. doi:10.1126/science.aax6239
376. Moraud EM, Capogrosso M, Formento E, et al. Mechanisms Underlying the Neuromodulation of Spinal Circuits for Correcting Gait and Balance Deficits after Spinal Cord Injury. *Neuron*. 2016;89(4):814-828. doi:10.1016/j.neuron.2016.01.009
377. Adams C, Stroberg W, Defazio RA, Schnell S, Moenter SM. Gonadotropin-releasing hormone (GnRH) neuron excitability is regulated by estradiol feedback and kisspeptin. *J Neurosci*. 2018;38(5):1249-1263. doi:10.1523/JNEUROSCI.2988-17.2017